Numerical reconstruction of the Dallery organ in the Chapelle de la Sorbonne

Gonzalo Villegas Curulla

To cite this version:

Gonzalo Villegas Curulla. Numerical reconstruction of the Dallery organ in the Chapelle de la Sorbonne. Musicology and performing arts. Sorbonne Université, 2023. English. NNT : 2023SORUS243 . tel-04233895

HAL Id: tel-04233895

https://theses.hal.science/tel-04233895v1

Submitted on 9 Oct 2023

SORBONNE UNIVERSITÉ

École doctorale Sciences Mécaniques, Acoustique, Électronique et Robotique

THÈSE DE DOCTORAT
SPÉCIALITÉ ACOUSTIQUE

Numerical reconstruction of the Dallery organ in the Chapelle de la Sorbonne

---

Reconstruction numérique de l'orgue Dallery

de la Chapelle de la Sorbonne

Presentée par **Gonzalo VILLEGAS CURULLA**

pour obtenir le grade de Docteur de Sorbonne Université

à l'Institut Jean Le Rond ∂'Alembert, Sorbonne Université, CNRS, UMR 7190

Soutenue le 3/07/2023 devant le jury composé de :

M. Patricio de la CUADRA BANDERAS	Professeur	Rapporteur
M. Christophe VERGEZ	Directeur de Recherche	Rapporteur
Mme. Soizic TERRIEN	Chargée de Recherche	Examinatrice
M. Christophe d'ALESSANDRO	Directeur de Recherche	Examinateur[†]
M. Murray D. CAMPBELL	Professeur émérite	Invité
M. Benoît FABRE	Professeur	Directeur de Thèse
M. Brian F. G. KATZ	Directeur de Recherche	Co-Directeur de Thèse

[†] Président du Jury

Reconstruction numérique de l'orgue Dallery de la Chapelle de la Sorbonne

Résumé: Dans cette thèse, nous étudions des outils théoriques et numériques pour reconstruire le son d'instruments historiques, en particulier d'orgues à tuyaux. L'accent est mis, tout d'abord, sur la source élémentaire: le tuyau de l'orgue et son système d'alimentation. La nature des sources aéro-acoustiques a fait l'objet des études spécifiques depuis les années 1950, avec les contributions majeures de Lighthill et Powell. Jusqu'à la date actuelle, le mécanisme excitateur de ces sources élémentaires manquait d'une condition initiale vraisemblable et d'un lien avec les conditions de pression du système de ventilation des orgues à tuyaux. Nous rassemblons, incorporons, implémentons et étendons les aspects du modèle qui sont apparus après le travail de Verge dans les années 1990. Dans la deuxième partie, nous étudions le rôle de l'enceinte de la cavité du buffet. L'imbrication fréquentielle et spatiale d'un réseau arbitraire de sources élémentaires à l'intérieur du buffet constitue un aspect crucial de la complexité de l'orgue par rapport aux autres instruments de musique. Les cavités de l'orgue sont, elles-mêmes, des résonateurs et, en tant que telles, une version réduite de la salle avec laquelle elles sont intrinsèquement couplées. Par conséquent, leur entité est divisée en éléments de modélisation plus petits et plus réalisables. Nous considérons un problème de champ diffusé à l'intérieur de la cavité de l'orgue et étudions sa transmission et couplage avec l'extérieur. Nous considérons l'état du champ de pression en plusieurs points de la fente individuelle dans une façade idéalisée et simplifiée, et le dimensionement du modèle de rayonnement acoustique d'une à plusieurs ouvertures entre tuyaux de la facade. Les étapes de la démarche de validation du modèle couvrent différentes étapes de simplification des problèmes et d'identification des preuves dans les cas type, ce qui englobe les travaux réalisés dans les domaines suivants: adaptation des parties d'instruments équivalents disponibles, mesures des cas idéalisés dans des conditions contrôlées, modélisation de sources idéalisées, simulation numériquedes des modèles de tuyaux et des réseaux diffractants, mesures d'instruments pseudo-idéaux et d'instruments réels.

Mots-clés: orgue, tuyau, écoulement unidimensionnel, rayonnement acoustique, source cylindrique, diffusion

Numerical reconstruction of the Dallery organ in the Chapelle de la Sorbonne

Abstract: In this thesis, we study theoretical and numerical tools for retrieving the sound of historical instruments, specifically pipe organs. The focus is, first,set on the elementary source: the organ pipe and its air supply driving system. The nature of the aero-acoustic sources has been investigated specifically since the 1950s, with leading contributions by Lighthill and Powell. Up to the current date, the driving mechanism of said elementary sources lacked plausible initial conditions and a link with the pressure supplied by the ventilation system of pipe organs. We gather, incorporate, implement, and extend pipe model aspects that appeared after the work by Verge in the 1990s. In the second part, we investigate the role of the *buffet* cavity enclosure. The spectral and spatial imbrication of an arbitrary array of elementary sources inside the *buffet* constitutes a crucial complexity aspect of the organ compared to other musical instruments. Organ cavities are a resonator themselves and, as such, a smaller version of the room with which they are intrinsically coupled. Therefore, their entity is split into smaller, manageable, and predictable modeling elements. We consider a scattered field problem in the organ's cavity interior and study the radiation into the exterior. Consideration is given to the state of the pressure field at multiple points of the single slit in an idealized, simplified *facade*, and the scaling of the acoustic radiation model from one to multiple apertures between the pipes of the *facade*. The stages of the model validation process span different steps in problem simplification and sign identification in application cases, which encompasses work carried out in the following: adaptation of available equivalent instrument parts, idealized problem measurements under controlled conditions, idealized source modeling, numerical simulation of pipe and scattering problems, measurements of pseudo-ideal real instruments, and actual instruments.

Keywords: organ, pipe, one-dimensional flow, acoustic radiation, cylindrical source, scattering problem

Acknowledgements

Working with Benoît and Brian to form a triad has proven to be an invaluable strategy for giving structure and coherence to this complex research project. I have attempted to reciprocate the confluence of your wisdom, experience and guidance with my effort and genuine dedication.

The doctorate life, early shaken under COVID-19 conditions, would not have been as pleasant should I not had the friendly and stimulating company of Serena, Tomas and Lyes in the same office. Having Sarabeth, Elliot and Piergiovanni as accomplices in experimental endeavours led to plenty of slendid memories and enriching discussions. Special thanks go to Antoine, with whom my learning during these years has benefited from his remarkably skillful insight in both numerical and experimental fields.

My gratitude extends to all of those that have volunteered support and ideas from many different angles: friends, colleagues, organists, manufacturers, professors and researchers. Amongst others, it is worth mentioning Pierre, whose vast knowledge of the instrument concerned in this work represented access to priceless information

I am grateful that Clément, Albert, Adrià, Jordi, Josep, and Alex persevered in observing with me a work-life balance beyond the walls of Sorbonne.

This work would not have been possible without the financial support of the Institut des Sciences du Calcul et des Données (ISCD), under grant FED 3 – 2019/7/2.

The unwavering support and patience of my family and Holly merit my deepest acknowledgement.

Contents

Résumé i
Abstract ii
Acknowledgements iii
List of Figures ix

Introduction **1**

1 Context: Chapelle Sorbonne and its organ **3**
1.1 Prelude 3
1.2 Sorbonne 4
1.2.1 The historic Sorbonne 4
1.2.2 The turn of the 19th century 5
1.2.3 From the new Sorbonne to Sorbonne University 6
1.3 La Chapelle de la Sorbonne 7
1.4 The Dallery organ 9
1.5 A restauration project 13
1.6 Summary and concluding remarks 14

2 Methods and state of the art **17**
2.1 Prelude 17
2.2 On wind supply and reservoirs 19
2.3 On the organ pipe 21
2.3.1 The controversy that started it all 22
2.3.2 Specific modeling elements of the flue organ pipe 26
2.4 On instrument radiation and scattering 29
2.5 On room acoustics 30
2.6 Summary 31

I Developments on flue organ pipes **33**

3 A model for pressure-rise time prediction in organ pipes **35**
3.1 Introduction 36
3.2 Operation of organ pipes and supply systems 38
3.2.1 Organ pipe models: a recapitulation 39
3.2.2 The coupling of the supply system and the pipe 40
3.3 The reservoir and the foot 42
3.3.1 Supply system: continuous model 42
3.3.2 Pallet-box and initialization of the system 44
3.3.3 Analysis towards a non-dimensional model 45
3.4 Measurements 48

3.4.1 Setup of the laboratory measurements 49
3.4.2 Setup of the measurements in Pinchi organs 49
3.4.3 Results 52
3.4.4 Steady-state results in real organs 54
3.5 Discussion 58
3.6 Conclusions 62
3.7 Future perspectives 65
3.8 Summary 68

4 Numerical methods for organ pipe and supply system simulation 69
4.1 Introduction 69
4.2 On the continuous model 70
4.2.1 The windchest air supply system 70
4.2.2 The pipe system 72
4.2.3 The coupling of air supply and pipe 74
4.3 Continuous-time system analysis 75
4.3.1 Stability of the open loop 76
4.4 Implementation 77
4.4.1 State space formulation 77
4.4.2 Semi-discrete model 80
4.4.3 Discrete model 82
4.4.4 Temporal finite difference operators 83
4.4.5 Forward Euler 83
4.4.6 Second-order trapezoid and 1st order backwards-difference . . 84
4.4.7 Störmer-Verlet scheme 84
4.5 Validation 84
4.5.1 Numerical stability 84
4.5.2 Measurements 85
4.6 Summary and future perspectives 87

II Developments on buffet radiation and spaces 89

5 Design of specific sources for the study of the cavities and radiation of organs 91
5.1 Introduction 91
5.2 Cylindrical wave propagation 93
5.3 Thiele-Small parameters 94
5.4 Application case 96
5.5 Cylindrical source 1: 1m speaker array 100
5.5.1 Directivity 100
5.6 Cylindrical source 2: for Notre-Dame de Paris, 2m speaker array . . 105
5.7 Summary 110

6 Organ buffet radiation 111
- 6.1 Prelude . . . 111
- 6.2 Introduction . . . 112
  - 6.2.1 Hypothesis, approximations, and methods . . . 114
- 6.3 Theoretical apparatus . . . 116
  - 6.3.1 [Step 1] Closed cavity, lossless, and rigid walls . . . 117
  - 6.3.2 [Step 2] Closed cavity, losses, non-rigid walls . . . 120
  - 6.3.3 [Step 3] Semi-open cavity: façade and slits . . . 122
- 6.4 Measurements . . . 130
  - 6.4.1 Measurement setup in ideal conditions (anechoic) . . . 131
  - 6.4.2 Cavity field and wall impedance estimation . . . 133
  - 6.4.3 Directivity measurements with the idealized organ . . . 143
- 6.5 Application case: Notre-Dame de Paris . . . 146
  - 6.5.1 The NDP tribune organ buffet measurements . . . 147
- 6.6 Numerical experiments: finite-volume finite-difference . . . 151
- 6.7 Future perspectives . . . 154
  - 6.7.1 Sainte-Élisabeth de Hongrie . . . 156
- 6.8 Conclusion and summary . . . 158

7 Bringing everything together: virtualizing the Dallery organ 161
- 7.1 Documentation . . . 161
  - 7.1.1 Reports and inventories . . . 161
  - 7.1.2 Interpolated pipe diameters . . . 168
  - 7.1.3 Modal parameter extraction . . . 172
- 7.2 Chapelle de la Sorbonne . . . 172
  - 7.2.1 Prelude . . . 172
  - 7.2.2 GA model of Chapelle Sorbonne . . . 175
- 7.3 The sound of the organ in the Chapelle Sorbonne . . . 178
- 7.4 Summary and future perspectives . . . 180

A Speaker technical specifications 183

B Organ radiation 187

C Radiated pressure in the empty organ of NDP 209

D Numerical directivity of an organ-like cavity geometry 215

E A sample instrument file 221

Bibliography 225

Glossary 245

List of Figures

1.1 North view of the Chapelle de la Sorbonne as seen from the Cour d'Honneur . . . 5
1.2 View and plan of Chapelle Sorbonne . . . 6
1.3 Layout of the buffet of the Orgue Dallery . . . 9
1.4 View of the keyboards of the Dallery organ . . . 10
1.5 View of the disparition extent of the pipework in the Dallery organ . 11
1.6 Dynasty of Dallery organ builders. . . . 12
1.7 Tribune of Dallery organ in Chapelle Sorbonne supported with scaffolding . . . 13

2.1 Organ overview and flue organ pipe samples . . . 18
2.2 Diagram of the entire system to reconstruct. . . . 19
2.3 Measured wind supply responses at different valve opening times and sizes . . . 20
2.4 Electric wind supply system example . . . 20
2.5 Depiction of the pipe and mouth geometry, together with the illustration of the 1D acoustic analogy . . . 26
2.6 Schieleren visualization of the jet and instability wavenumber . . . 28
2.7 Three-dimensional view and Nyquist plot of computed input admittance for a test pipe . . . 29
2.8 Magnitude and phase of computed input admittance of a test pipe . 29

3.1 Diagram of reservoirs and organ pipe . . . 40
3.2 Feedback loop system in self-sustained oscillation . . . 41
3.3 Measured pressure overview during transient and data deviation . . . 42
3.4 Pipe diameter scaling rules . . . 46
3.5 Measurement setup in the laboratory and sample test pipes 1-5 . . . 50
3.6 Interior view of the pallet-box . . . 50
3.7 Measurement setup of the workshop organ . . . 51
3.8 Reduced jet velocity as measured in test pipes 1-5 . . . 53
3.9 Fourier coefficient ratios of the first three modes in measured pressure for test pipes 1-5 . . . 56
3.10 Measured pressure for different number of stops coupled . . . 57
3.11 Zoom plot of measured pressure in test pipe 5 at the workshop Pinchi organ . . . 57
3.12 Time-domain numerical solutions of the groove and pipe foot as per the physical and fitted models . . . 59
3.13 Solution errors of computed pressure in the groove and pipe foot as per physical and fitted models . . . 59
3.14 Foot volume estimation . . . 60

3.15 Non-dimensional pressure-rise time steepness as a function of cavity volume ratios . . . 61
3.16 Pressure amplitude responses by distance and valve opening . . . 64
3.17 Close-up view of interior elements of the wind supply system . . . 66
3.18 Photography, diagrams, and dimensions of the original blowing system installed by Dallery in 1825 in the Chapelle Sorbonne organ . . 67

4.1 Closed loop operation in wind instruments of self-sustained oscillation type . . . 71
4.2 Mouth geometry parameters and one-dimensional analogy . . . 72
4.3 Convergence study of the resonator scheme . . . 85
4.4 Convergence study of the full forward Euler scheme . . . 86
4.5 Input impedance measurement setup and fitting error . . . 86

5.1 Section view of a speaker driver . . . 95
5.2 Setup of the measurement of the cylindrical sources . . . 100
5.3 Measured directivity of the 1 m source at 0.2 m . . . 101
5.4 Directivity of the 1 m source full array measured at 4 m . . . 102
5.5 Measured vertical response of the 1 m source due to the spatial truncation effect . . . 102
5.6 Normalized measured pressure spectra of the 1 m source at 1 m . . . 103
5.7 Pressure of the baffled speaker as a function of distance . . . 104
5.8 Measured pressure decay of the 1 m source as a function of distance . 105
5.9 Directivity of the 2 m source at 1 m: positions 1-2 . . . 107
5.10 Directivity of the 2 m source at 1 m: positions 3-4 . . . 108
5.11 Measured spectra of the 2 m NDP source with closed cabinet . . . 109
5.12 Measured pressure differences of the 2 m source at different alignments 109

6.1 Organ radiation models per frequency ranges . . . 114
6.2 Diagram of the organ-like cavity, its internal elements, and the coordinate system . . . 118
6.3 Mid-frequency range directivity of a façade equivalent array of sources 125
6.4 Computation of radiated field by an array of equaly distributed pulsating sources as per Rossi . . . 126
6.5 Interference models of scattering using the aperture radiation method 129
6.6 Point-source projected scattered pressure . . . 129
6.7 Radiation models and at low frequencies . . . 130
6.8 Radiated pressure measurement setup in the laboratory . . . 132
6.9 Wide span measured spectra overview in the closed cavity . . . 134
6.10 Low modal density range of measured spectra in the closed cavity . . 134
6.11 Measured spectra versus computed lossy Green's solution . . . 135
6.12 Measured internal pressure field for a cavity with no apertures and one aperture . . . 136

6.13 Magnitudes and phases of pressure at the slit for different vertical alignments . . . 138
6.14 Low and mid frequencies of the façade transfer function at a distance of 1.66 m away from the façade . . . 140
6.15 Mid-to-high frequencies of the façade response at 1.66 m away from the façade . . . 141
6.16 High frequencies of the façade response at 1.66 m away from the façade 142
6.17 Relative SPL (dB) and phase measured at 0.2 m from the front boundary with only two lateral walls and no pipes . . . 143
6.18 Relative SPL measured at high density of cylinders behind the façade array at different distances with no walls . . . 143
6.19 Relative SPL measured pressure at different densities near the closed organ cavity . . . 144
6.20 Measured pressure field phase at different densities of forest and different frequencies at 0.2 m of the closed organ cavity . . . 144
6.21 Relative SPL measured at 1.66 m from the idealized organ façade at different forest densities with all the enclosing walls included . . . 145
6.22 NDP buffet internal response as excited by a big balloon explosion compared with the laboratory cavity . . . 149
6.23 Geometry of the NDP tribune organ façade . . . 149
6.24 Selection of measured relative SPL data in the empty organ of Notre-Dame de Paris . . . 150
6.25 Meshed geometry for the 2D FVFDTD simulation of the scattering problem emulating the setup in laboratory condition . . . 152
6.26 Two closed contours in the FVFDTD equivalent implementation of the anechoic measurements of the idealized organ-like cavity at 1.5 m and 4.5 m . . . 153
6.27 Conformal transform mapping of the potential through façade cylinders 155
6.28 Vertical directivity measurement setup of the single slit . . . 156
6.29 Onset detection of noisy, slow organ pipe tones at 65 Hz measured at the Sainte-Élisabeth d'Hongrie tribune organ . . . 158

7.1 Digitalization of instrument file process workflow . . . 161
7.7 Measured diameters from Dallery pipework of the great organ and pedal . . . 169
7.8 Measured diameters from Dallery pipework of the positive . . . 170
7.9 Measured diameters from Dallery pipework of the recit . . . 171
7.10 Chapelle Sorbonne chancel, nave and side chapels as seen from the altar on the East end . . . 173
7.11 Known previous states of the chapelle around the 1940s . . . 174
7.12 Source receiver locations annotated over a floor plan of the Chapelle 175
7.13 View of the GA model of Chapelle Sorbonne in CATT-Acoustic . . . 176
7.14 Clarity and reverberation metrics of Chapelle Sorbonne GA model . 178

7.15 Frequency domain transfer function of the façade element in its 0° response . . . 179
7.16 Sound production chain of the organ sound in Chapelle Sorbonne . . 180

B.1 Interference models of scattering using the aperture radiation method 187
B.2 Computed scattered pressure (normalized dB) in the range 5.5 kHz to 10 kHz as per [Mellow and Kärkkäinen, 2011] model, spanning the width the laboratory setup, with a grid spacing of 2 mm and a frequency bin of 2 Hz. . . . 188
B.3 Representation not to scale of the modal shape projections on the wall aperture losses . . . 188
B.4 Magnitudes of pressure at the slit for different vertical alignments . . 189
B.5 Phases of pressure at the slit for different vertical alignments 190
B.6 Low frequencies of the measured facade pressure transfer function . . 191
B.7 Mid frequencies of the measured facade pressure transfer function . . 192
B.8 High frequencies of the measured facade pressure transfer function . 193
B.9 Lateral organ rigid walls only. Measured pressure, relative SPL dB rms normalized by free propagation reference. . . . 195
B.10 Lateral organ rigid walls only. Measured pressure, relative SPL dB rms normalized by free propagation reference. . . . 196
B.11 Lateral organ rigid walls only. Measured pressure, relative SPL dB rms normalized by free propagation reference. . . . 197
B.12 Façade array of 16 equally distributed cylinders only, no walls of any sort. Measured pressure, relative SPL dB rms normalized by free propagation reference. . . . 198
B.13 Façade array of 16 equally distributed cylinders only, no walls of any sort. Measured pressure, relative SPL dB rms normalized by free propagation reference. . . . 199
B.14 Façade array of 16 equally distributed cylinders and 50% of the total forest cylinders in the cavity space ($n_o = 134$), no walls of any sort. Measured pressure, relative SPL dB rms normalized by free propagation reference. . . . 200
B.15 Façade array of 16 equally distributed cylinders and 100% of the total forest cylinders in the cavity space ($n_o = 134$), no walls of any sort. Measured pressure, relative SPL dB rms normalized by free propagation reference. . . . 201
B.16 Façade array of 16 equally distributed cylinders and 100% of the total forest cylinders in the cavity space ($n_o = 244$), no walls of any sort. Measured pressure, relative SPL dB rms normalized by free propagation reference. . . . 202
B.17 3-walled organ cavity at different densities of cylinders. Measured pressure, relative SPL dB rms normalized by free propagation reference at 0.5 m. . . . 203

B.18 3-walled organ cavity at different densities of cylinders. Measured pressure, relative SPL dB rms normalized by free propagation reference at 0.5 m. 203
B.19 3-walled organ cavity at different densities of cylinders. Measured pressure, relative SPL dB rms normalized by free propagation reference at 0.5 m. 204
B.20 3-walled organ cavity at different densities of cylinders. Measured pressure, relative SPL dB rms normalized by free propagation reference at 2 m. 205
B.21 3-walled organ cavity at different densities of cylinders. Measured pressure, relative SPL dB rms normalized by free propagation reference at 2 m. 206
B.22 3-walled organ cavity at different densities of cylinders. Measured pressure, relative SPL dB rms normalized by free propagation reference at 2 m. 207
B.23 3-walled organ cavity at different densities of cylinders. Measured pressure, relative SPL dB rms normalized by free propagation reference at 2 m. 208

C.1 Measured relative SPL by thirds of octave bands at the empty tribune organ of Notre-Dame de Paris 209
C.2 Twelfth octave bands of relative SPL measured in the empty tribune organ of NDP 210
C.3 Twelfth octave bands of relative SPL measured in empty tribune organ of NDP 211
C.4 Twelfth octave bands of relative SPL measured in the empty tribune organ of NDP 212
C.5 Twelfth octave bands of relative SPL measured in the empty tribune organ of NDP 213

D.1 Numerical simulation of organ façade's scattered field 216
D.2 Numerical simulation of organ façade's scattered field 217
D.3 Scattered pressure spectrum (dB) at the contour of 1.5 m around the organ-like system geometry. 218
D.4 Simulated scattered pressure read at the 4.5 m contour from the origin at different initial window times 219

Introduction

The Chapelle de la Sorbonne has played an iconic role within the history of *Sorbonne* as an institution since the 13th Century. Equaly remarkable is the organ housed in this chapel, which is framed within a strong tradition of French and European organ builders, being highly representative of such tradition and the only instrument remaining that has not suffered posterior alterations, thus being the one piece containing only work by the Dallery (Pierre-François and his son Louis-Paul).

The historical vicissitudes and the lack of maintenance of the chapel and the organ, have rendered them inaccessible to the public nowadays and in perilous state of structural misrepair. The space and instrument have been classified as *monument historique* 1887 for the chapelle and 1980 for the organ, also classified as *patrimoine mobilier* in 1994. However, their current ownership and administrative rights frame the chapel and the organ in a complex net involving: the *chancellerie des Universités*, the *Ville de Paris*, and the *ministère de la culture*.

The organ pipe model The organ pipe is the first elementary source in the sound production chain when one attempts a definition of the organ as an instrument.

The complexity of buffet cavity fields in organs Consideration is needed towards the fact that abstraction may be wished in some modeling stages, where the response of the churches or rooms and the response of the cavities enclosing the windchests of pipes contribute reflections and resonances that one may want to exclude from the analysis. There is, to the best of the author's knowledge and his contributors, no explicit contribution in scientific publication towards modeling of the organ radiation, directivity and phase effects.

Original contributions in this work There has been no model before that proposed driving the jet-drive model with a realistic function or set of equations. Alternatively, options are found in the industry, Modartt, where this problem is overlooked. The extension of this model upstream with one-dimensional flow solver approximations consitute a tool for cultural heritage and historical instrument preservation, as long as documentation or sufficient evidence exists.

In the present work, as long as it has been possible, problems have been examined in three ways: by experimental observation, theoretical approximation, and by numerical simulation.

Outline of the manuscript In Chapter 1, a historical context of the Chapelle Sorbonne and the organ built by the Dallery family are given. We provide the whole picture and the elements to give value and reason to endeavour a digital reconstruction of the organ and chapel.

Chapter 2 summarizes the previous advances in reasearch in the fields of organ wind supply systems, pipe modelling, radiation and room acoustics which will be employed in this work.

Part I of the text is concerned with addressing aspects of pipe modelling and simulation. Especifically, Chapter 3 proposes a geometry-based principle to estimate driving pressures and a form function. The outcome of the latter is used in organ pipe simulations. Chapter 4 investigates the discretization of governing equations and the feasibility of pipe simulations.

While the oscillation of a single pipe is well known, part of the identity of the complete instrument is related to its unique ventilation system. Therefore, the analsysis needs to be developed in the direction of the air supply (Chapter 2 and Chapter 3). On the other hand, the radiation of a single pipe is a somehow known topic (Chapter 3 and Chapter 6); the character of a stop and of a speficifc keyboard may come partly from the fact that all the pipes associated are radiating into a common cavity, with its own acoustic behaviour and a common radiation aperture.

In Part II of the manuscript, the elementary sources developed in Part I are assumed as the element that creates a complex field inside the organ cavity. The aim of Part II is to provide models of the radiated field by a closed organ.

Attention is paid to the design of cylindrical sources in Chapter 5 in order to study the radiation problem as a two-dimensional simplification. Two sources are built for measurements in controlled conditions and in-situ scenarios.

Chapter 6 proposes models for the interior field of the organ cavity, the effect of apertures in the cavity, and radiation models. Results from measured data and numerical simulation are provided alongside with analytical model predictions.

The assembly of all the elements studied is performed in Chapter 7, together with inventory documentation of the organ and some empirical rules from organ building. In addition, a geometrical acoustics model of the Chapelle Sorbonne is presented, which is used to show an example of whole loop that makes the organ sound in the chapel is displayed.

The work concludes with some remarks on the advances that the current work has been able to add to the previous decades of research and its potential applications. Observations are made on those aspects that can attire the attention of further development and some others where our work has overlooked materials pending to process and understand, which may be a useful starting point for further researchers.

Chapter 1

Context: Chapelle Sorbonne and its organ

Contents

1.1 Prelude **3**

1.2 Sorbonne **4**

1.2.1 The historic Sorbonne 4

1.2.2 The turn of the 19th century 5

1.2.3 From the new Sorbonne to Sorbonne University 6

1.3 La Chapelle de la Sorbonne **7**

1.4 The Dallery organ **9**

1.5 A restauration project **13**

1.6 Summary and concluding remarks **14**

In this section we introduce the historical aspects of relevance of the chapel as known today, the context in which the organ was built and used, and the events ocurred since its closure to the public. They frame the pertinence of such work of a digital reconstruction in our concluding remarks.

Content and quotes are largely borrowed from online resources of the (Université Sorbonne, fragments from Hardouin and Dubois [Hardouin, 1980, Dubois, 2016, Dubois and Lueders, 2002], as well as private conversations with M. P. Dubois.

1.1 Prelude

The College of Sorbonne has always had a chapel since the 1326 (currently the *Chapelle Sainte-Ursule*), to welcome the devotion of students at the school of theology and for *festive* events. This former gothic chapel in latin-cross shape was demolished. Studies describe the former chapel of the Sorbonne College [Glorieux, 1966, Glorieux, 1965, Hottin, 1999, Perraut, 2007], whose foundations (found during the reconstruction of Sorbonne in 1897) would nowadays be located in the courtyard of the old University: that is, amidst a dense conglomerate of Faculties in the same block, bounded by rue de la Sorbonne, rue des Écoles, rue Saint-Jacques, and rue Cujas in the today *5ème arrondissement* of Paris. The new chapel as known at the present date by the architect J. Lemercier was built on the site of the former *collège de Calvi*. The works were carried under request of the

Cardinal Richelieu in 1622, commissioned by the prelate himself, *de-facto* starting the works in 1635 and finished the year of the Cardinal's death in 1642.

Its organ has only sounded during two short periods. Firstly, played by Choron from 1825 to 1830 (during which, L. P. Dallery did some interventions), in charge of the direction of the *Institution Royale de Musique Religieuse.* The use of the organ during that time was intended for the accompaniment of chants. Religious chanting stopped with the closure of the Chapelle in 1830, reopening in 1852 for the next only seven years. The appointed organist is then Félix Clément, who showed disapproval of the new profane tendencies in music and thus the use of the organ to serve *effets éloignés de la gravité du culte chrétien*, writes in 1849 a report about the bad status of the religious music in France addressed to M. de Falloux, the minister of the *Public Instruction and Cult.* Some excerpts from that report are representative of the tendency to drift away [again?] from devoutness:

> les développements exagérés de l'orgue n'ont pas peu contribué à affaiblier l'exécution de la musique religieuse dans le choeur de nos églises. Ce instrument, qui autrefois servait pour accompagner les chants liturgiues, est devenu par ses dimensions et l'usage qu'on en fait[,] un hors d'oeuvre dans les offices divins.
>
> [...] les improvisations des organistes, qui absorbent les 2/3 du temps consacré aux offices. [The organist] usurpe le droit au prêtre auquel appartient seul d'élever la voix au nom du peuple. Quant au genre de musique que les organistes ont adopté, ils l'ont tiré des entrailles même de l'art profane. (...)

Inconsistently, Clément requests from L. P. Dallery an extension of the instrument: the addition of a German-style pedal in 1854. In 1859, Clément desists from his position on the grounds of lack of funds: with that being the last time that this organ produced music.

1.2 Sorbonne

1.2.1 The historic Sorbonne

The University of Paris was established in the early 13th century through the emergence of the guild of Parisian teachers and students, who were in competition with the teachings offered in the schools of the cloister of Notre-Dame de Paris. The university had its own regulations and statutes and was organized into four faculties, including liberal arts, law, medicine, and theology. Although it did not have its own buildings at the time, the university was located on the left bank of the Seine.

The Montagne Sainte-Geneviève slopes were home to many colleges that were established to welcome European students grouped together in "nations." The Sorbonne college was founded by Robert de Sorbon, a master of theology, and was recognized by royal power in 1257. The college became the main establishment

Figure 1.1: North view of the Chapelle de la Sorbonne as seen from the Cour d'Honneur North view of the Chapelle de la Sorbonne as seen from the Cour d'Honneur. Image credit: Université Sorbonne website.

of the Faculty of Theology and gained a considerable reputation, contributing to the European influence of the University of Paris. Other teaching places linked to various faculties were scattered around the same district, leading to continuous movement until the 17th century when libraries and lecture halls were created.

In the 17th century, the Sorbonne underwent significant renovations when Cardinal de Richelieu, who became its director in 1622, commissioned the architect Jacques Lemercier to renovate and unite all the separate buildings that made up the college. The renovation included the creation of a baroque-inspired domed chapel at the heart of the Sorbonne. In the latter half of the 18th century, the University moved its headquarters to the Collège Louis-le-Grand premises, which had been left unoccupied after the expulsion of the Jesuits in 1762. Despite this, no significant project has yet revolutionized the place occupied by the various faculties in the Latin Quarter.

1.2.2 The turn of the 19th century

The faculties of the University of Paris were abolished in 1793, but they were reestablished under the Empire in 1806, which became the official founding date of the Faculties of Arts and Sciences. However, it wasn't until the Third Republic that the University of Paris underwent institutional transformation, and a rationalization of the University space finally took place.

In the late 19th century, the democratization of the student body, the gradual inclusion of women in courses, and the creation of research laboratories led to the reorganization of faculties and the spread of universities throughout France. The Sorbonne, which had long suffered from a lack of space, underwent a major renovation under architect Henri-Paul Nénot. The new Sorbonne was built in three

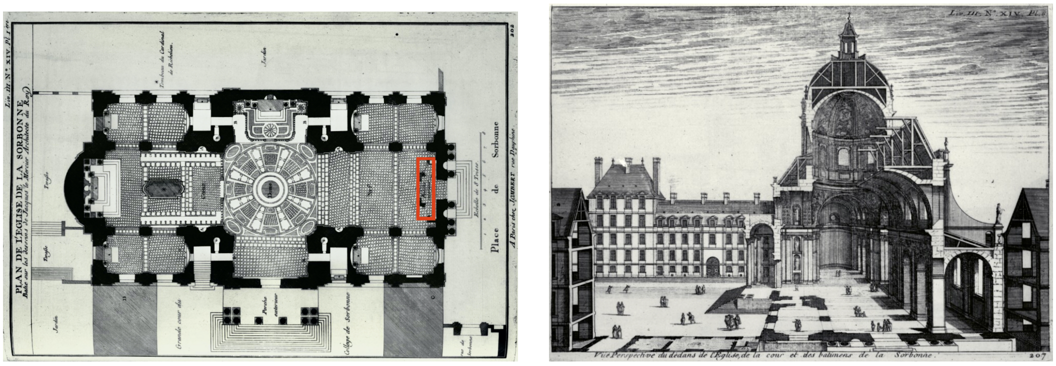

Figure 1.2: View and plan of Chapelle Sorbonne
View and plan of Chapelle Sorbonne. The location of the organ is marked in red.
Source: [Blondel, 1752] and [Marot and Marot, 1727].

phases from 1882 to 1901 and now housed the faculties of Arts and Sciences. The Faculty of Medicine, however, remained in a separate location on the rue de l'Ecole-de-Médecine.

The creation of dedicated chairs for teaching and research contributed to the development of new disciplines and fields of experimentation. For example, marine stations were established in Roscoff and Banyuls-sur-Mer in the late 19th century by Henri de Lacaze-Duthiers, a pioneer in marine biology and director of the experimental zoology laboratory at the Sorbonne. These new courses were supported by the constitution of reference collections and libraries that are still preserved today at Sorbonne University.

1.2.3 From the new Sorbonne to Sorbonne University

The first half of the 20th century saw an increase in the number of students, and the Sorbonne laboratories were at the center of many scientific developments. Marie Curie continued her work on radium at the newly assigned buildings on Rue Cuvier. Several annexes were built between the wars, including the Institute of Geography, the Institute of Art and Archaeology, and the Institute of Hispanic Studies.

After World War II, the Sorbonne's expansion continued with the installation of science laboratories in Orsay, the transfer of part of the Faculty of Arts to Censier and Nanterre, and the allocation of the Halle aux Vins quadrangle to the Faculty of Sciences. The Jussieu campus was launched in 1958 and never really finished, with Edouard Albert taking over the project in 1962, which led to the creation of the famous *grid* and the commissioning of numerous works of art produced under the 1% artistic incentive. The campus is dominated by an 85-meter high tower, the Zamansky Tower.

The *loi Faure*, passed after May 68, granted more autonomy to institutions of higher education, leading to the disappearance of the University of Paris and its faculties. Thirteen universities were created, including Paris-Sorbonne University

(Paris IV) for literature, arts, and humanities, and the University Pierre and Marie Curie (UPMC - Paris VI) for science and medicine. The Faculté de médecine Pitié-Salpêtrière was also created.

Paris-Sorbonne University and University Pierre and Marie Curie collaborated since early 2000s and in 2010, they formed a Pôle de recherche et d'enseignement supérieur (PRES) Sorbonne Universities which later became a Communauté d'Universités et d'établissements (COMUE) in 2015. In 2015, the "Sorbonne Universities in Paris for Education and Research" (SUPER) project was selected as an Excellence Initiative (Idex), leading to the creation of a new multidisciplinary university called Sorbonne University on January 1, 2018.

Evidence exists of decades of attempts to gather the efforts to restore the chapel and the organ [Dubois, 2016]. We offer an English translation of a short excerpt to start providing the institutional context, from *Une situation bloquée* from the same source:

> It is true that it is not uncommon for a project for the construction of a new organ to take about ten years to be completed, but we have been trying for more than 15 years to make the *Ville de Paris*, the *Chancellerie* and the University aware of the pertinence of restoring the Dallery organ in the Sorbonne chapel, without any real progress.
>
> [...] if the 5th *Commission des Monuments Historiques* has ruled on the interest of the instrument, absolutely no decision of restoration has been taken yet, in spite of apparently encouraging declarations of the alerted authorities and of the undoubted interest of the *Chancellerie* for the architectural and real estate heritage of the Sorbonne.
>
> [...] The last visits to the organ have shown that the gallery on which the organ rests is showing worrying signs of subsidence, hence the need for consolidation work if the chapel is to be opened again (the gallery is currently supported by "temporary" scaffolding). [see Figure 1.7]
>
> [...] there is nothing to prevent us from considering the dismantling of the organ and its transfer to a workshop so that its meticulous restoration can be undertaken. [...] The restoration site in a dedicated place could very well entail a pedagogical project for organbuilding apprentices [...]

1.3 La Chapelle de la Sorbonne

The Sorbonne Chapel, built by Jacques Lemercier in 1642-44 at the expense of Cardinal de Richelieu, is considered a masterpiece of early French classical art. Despite its name of *chapel*, it is in fact a building of vast dimensions, topped by a dome. The chapel houses the tomb of Richelieu, sculpted by François Girardon in 1694, which represents Piety and Doctrine mourning the dying prelate. After the closure of the Sorbonne in 1791, a decree attributed in 1808 to the Imperial University all the goods, buildings and rents that had belonged to the former French

Prythaneum. In 1821, this decree was confirmed in the form of a concession of the Sorbonne buildings to the City of Paris on condition that the head office of the Academy of Paris, as well as the faculties of Theology, Science and Letters, etc., would remain there in perpetuity. The church was restored to worship in June 1822 by Bishop Hippolyte de Quélen, then, after another closure from 1830 to 1852, the service of worship was again assured from 1853 to 1885.

For a broader time scale, a succint chronology is provided hereunder:

- 1642-1644: The Sorbonne Chapel is built by Jacques Lemercier at the expense of Cardinal de Richelieu.
- 1791: With the beginning of the French Revolution, the Sorbonne is closed. Later decomissioned in 1792, and target of pillage in December 1793.
- 1808: A decree attributed all the goods, buildings, and rents of the former French Prythaneum to the Imperial University, including the Sorbonne buildings.
- 1821: The Sorbonne buildings are conceded to the *Ville de Paris* on the condition that the head office of the Academy of Paris and the faculties of Theology, Science, and Letters would remain there in perpetuity.
- 1822: Worship is resumed by the Bishop Hippolyte de Quélen under command of Duc of Richelieu.
- 1828: Mass services are celebrated again after a donation from the sister of Duc de Richelieu.
- 1848: The service of worship is interrupted again.
- 1853-1885: The service of worship is resumed.
- 1887: The chapel was declared *monument historique.*
- 1901: Some works on the building. Nature unknown.
- 1906: The chapel is closed to worship due to the *loi de séparation des églises et de l'état.*
- 1921: An exception is granted to celebrate every December an Anniversary Mass.
- 1957: The *tribunal administratif de Paris* decrees the almost complete decomission of the cultual use.
- 1968: Social unrest, revolts, and barricades lead to occupation of Sorbonne and further ransacking.

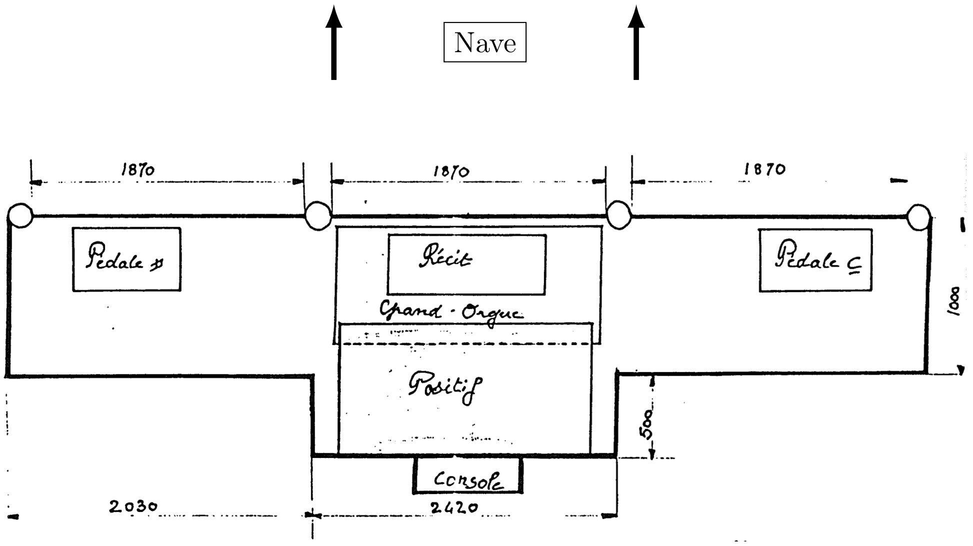

Figure 1.3: Layout of the buffet of the Orgue Dallery. Units in mm. Height of the buffet: 3300 mm. Source: [Dubois and Lueders, 2002].

- Notwithstanding the passing of the *loi Faure*, the Anniversary Mass takes place sporadically until the 1980, when the state of disrepair of the building becomes dangerous.
- The severe storm of December 1999 damages part of the structure. Permanently closed to public access in the 2000s.
- *La Ville de Paris* repairs the latter between 2004 and 2010.

1.4 The Dallery organ

In this section, we reproduce written and visual information that helps situating the relevance of the instrument and its deterioration (see Figure 1.4 and Figure 1.5). Figure 1.3 shows the general shape of the organ and its *plans sonors*, as well as what today would seem the odd location of the organist in the rear side of the instrument. Pierre Dumoulin writes in 2001 for [Dubois and Lueders, 2002], talking about the *sommier de pédal* of the Dallery organ, that

> Deux tuyaux [appartenant à la façade] sont tordus dont un ne repose que par miracle sur un postage et menace de tomber dans la nef.
>
> [...] ce sont les jeux les plus accessibles par l'arrière du buffet qui ont eu souffrir le plus du pillage : les vides du Plein-Jeu en témoignent d'une manière éloquente!
>
> [...] Sur ces seuls jeux, le pourcentage de disparition est en moyenne de 79% avec un maximum de 100% pour le Clairon de Pédale.

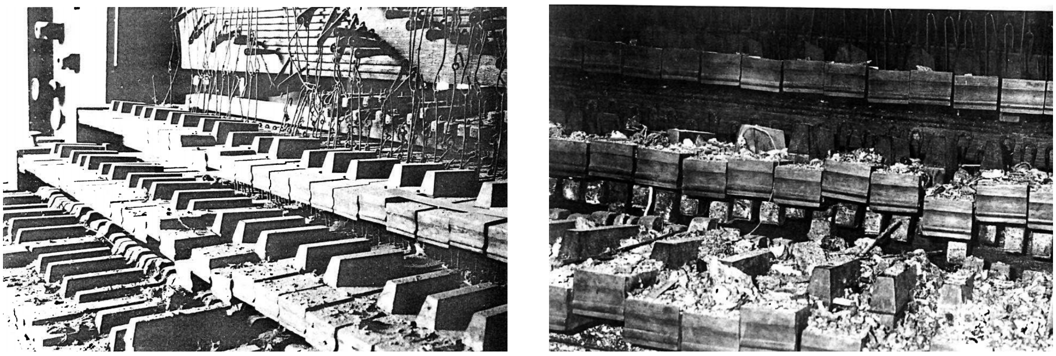

(a) Manuals in 1984 **(b)** Manuals in 1999

Figure 1.4: View of the keyboards of the Dallery organ
View of the keyboards (at the rear of the organ, not in the immedacy of the nave). The console where the organists were seated leads to a small half-rose window that had been broken, thus causing the dispersion of debris everywhere over the organ, while the bellows located in the vertiginously accessible attic have not suffered to the same extent. Image credit: Pierre Dubois.

> [...] *Tout* ce qui est dans l'orgue peut-être réutilisé après une restauration soigneuse; en tout cas, *tout* doit-être conservé.

Figure 1.6 shows an overview of salient organ makers within the French tradition and their links. Of course, a fair list should also mention: Ducroquet, Abbey, Dublaine, and Callinet, amongst others. See also online for further details about the Dallery family and this biography of P. F. Dallery and L. P. Dallery. In the same Figure, we have used the following shorthand notation to summarize the following events: † P. Dallery was first an apprentice of F. H. Clicquot and they later became associates. ‡ Dominique Cavaillé-Coll sends his son Aristide to Paris in September 1833 with a letter to Dallery father asking to show him the best organs in Paris; Dallery father dies next month. ⊛ Dom Bédos' last volume of [Bédos De Celles, 1766] was published in the Roret encyclopedia, modified by Hamel, and the data that was kept was treated as a complement: the consequence of this is that figures and tables show the ancient diapason tuning, while the modifications are made towards a 440 Hz orchestral tuning.

The Sorbonne Chapel's organ was commissioned to Pierre-François Dallery, but his son Louis-Paul built it in 1825 after the restoration of the chapel. The instrument has 23 stops on three manuals and a pedalboard, and the façade was designed by architect Vaudoyer, similar to the case of the church of Sainte-Geneviève. The console is on the west side, and it was used for auditions given by Alexandre Choron with students from the Royal Institution of Religious Music. In 1852, Félix Clément had the instrument restored by Louis-Paul Dallery, and in 1854, he installed the German-style pedalboard. Access to the organ became more difficult after the removal of the staircase leading directly to the organ loft outside the chapel in 1885.

The activity of the last two Dalleries was intense. However, it is worth noting

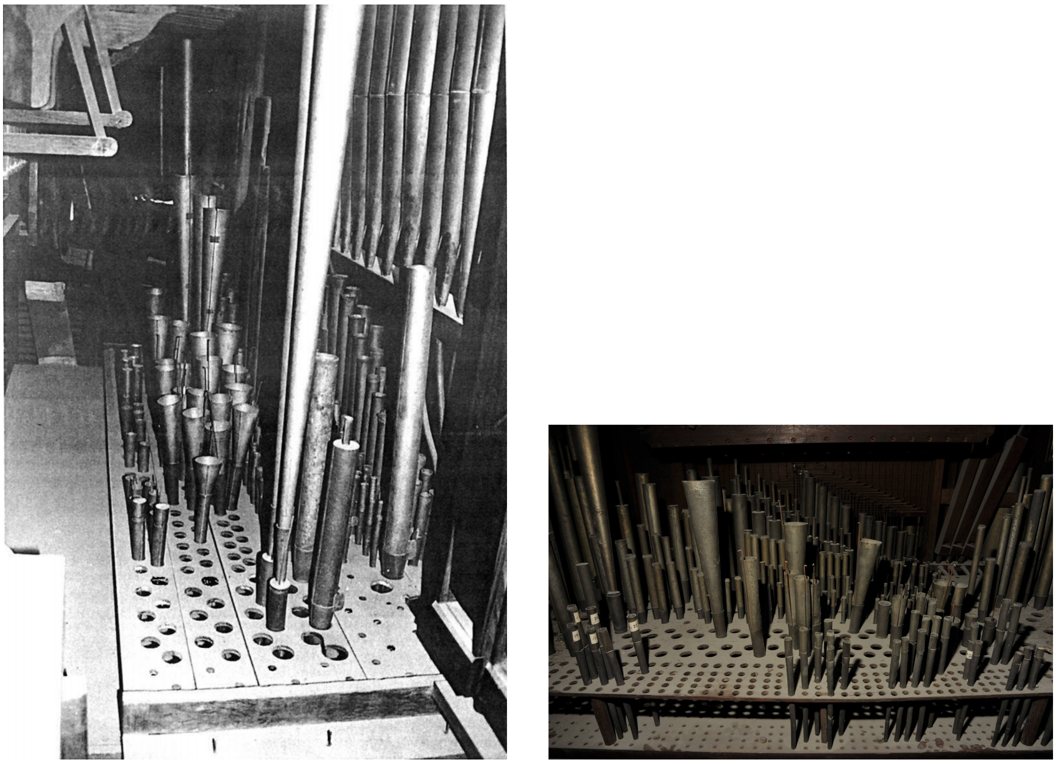

(a) Disappeared pipes as of 1984 in the G.O. **(b)** Disappearance of pipes by 2012

Figure 1.5: View of the disparition extent of the pipework in the Dallery organ. In 1984 the adjacent building to Chapelle was demolished, which may have factored in diminishing the amount of pipes disappearing. Image credit: Jean-Jacques Soin and Pierre Dubois.

that they mainly devoted themselves to restorations, rebuildings and transformations of existing instruments. The organ of the Sorbonne chapel is therefore an important exception, and it is particularly interesting that it has survived unaltered, thus giving us an example of Dallery's know-how at the beginning of the 19th century.

History has mostly remembered the slow decline of the workshop of the last Dallery. Indeed, it does not seem that the quality of the work of Pierre-François and Louis-Paul Dallery, heirs, as we have recalled, of the Clicquot school, was equal to that of their famous predecessor. Often embittered by numerous vicissitudes, Pierre-François wrote vindictive or tearful letters to justify his work, defend his honor and... keep his clients, which at the end of his life he was no longer able to do. Jean-Marc Baffert writes:

> Bricoleur, hâbleur, prétentieux, peut-être bon harmoniste, mais facteur peu capable, Pierre-François fit de « mauvaises affaires », laissant seul son fils en 1826 dans la conduite de l'entreprise. Lorsqu'il mourut « ne laissant à son fils que son nom pour toute fortune », la réputation de l'atelier avait déjà beaucoup décliné.

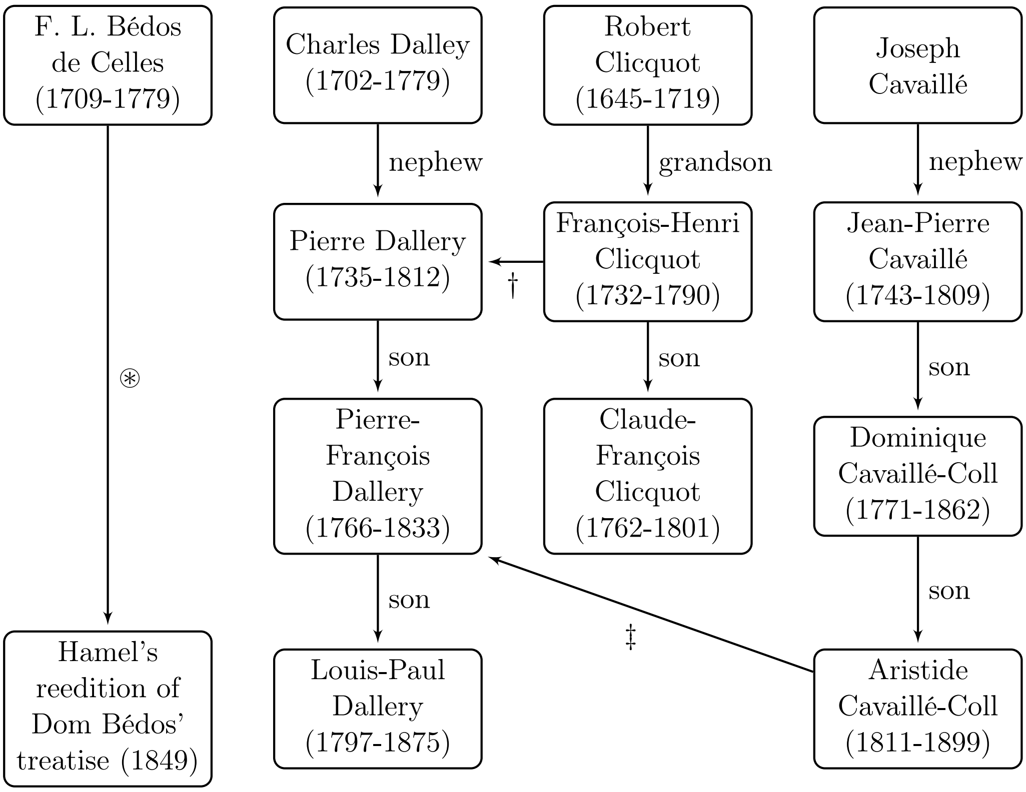

Figure 1.6: Dynasty of the Dallery organ builders in the context of French organ making.

Visited by the musicologists Félix Raugel around 1925, Paul Brunold in 1932, Pierre Hardouin, Dominique Chailley and the organ builder Patrice Bellet in 1971, the organ of the Sorbonne Chapel was described by Pierre Hardouin in [Hardouin, 1980]. A thorough inventory was then made by Pierre Dumoulin, within the framework of the Inventory of the Organs of the Île-de-France, carried out under the aegis of ARIAM-Île-de-France, from May to June 1983. Following the 1983 inventory, the *Bureau des Monuments* of the *Direction des Affaires Culturelles* of the *Ville de Paris* had a complete cleaning of the instrument and the attic where the wind tunnel is located, now protected by a closed shelter. Following Pierre Dumoulin's recommendations, the organ builders Bernard Dargassies and Loïc Martine carried out various urgent safeguarding works - but not restoration, which was considered inappropriate at the time. Bernard Dargassies then wrote a rather detailed survey of the instrument. In a letter dated November 1984, he alerted the Rectorate about the risks incurred by the instrument during the installation and dismantling of exhibitions in the chapel (dented or crushed pipes, even stolen).

Although difficult to access, the organ of the Sorbonne Chapel is not immune to negligent or malicious actions, as Dargassies, Galtier and Dubois were able to see again during a new visit with Pierre Dumoulin, on January 21, 1998, which allowed us to observe the current state of the instrument (now unplayable). An overturned

Figure 1.7: Tribune of Dallery organ in Chapelle Sorbonne supported with scaffolding. Image credit: J.-J. Soin, 2012.

bass pipe had crushed some small pipes of the positive: obviously, the organ had been the object of new degradations since the works of 1984/85, in spite of the protection measures (wooden shelter around the bellows, keys to close the case, etc.). Two other subsequent visits before the colloquium organized at the Sorbonne about this organ in November 2000 (which led to [Dubois and Lueders, 2002]) were to bring further evidence of the degradations that were still taking place. The storm of December 1999 also passed through, leaving rubble on the keyboards that had not been covered due to some negligence. They did not notice any major changes in another visit in 2003, but the organ was of course still in the same state of dirtiness and abandonment.

1.5 A restauration project

This organ, classified as a historical monument, is threatened. Already in 1980, Pierre Hardouin wrote [Hardouin, 1980]:

> A historic instrument if ever there was one! The only classical organ in Paris that is truly unchanged and finally one of the few in France... We thus have, at the Sorbonne, a true testament of the French organ of the XVIIIth century... to save.

> [...] no modernism, even valid, being acceptable in the restoration of an organ located in a chapel that has become a sort of museum today. Indeed, the very fact that the Dallery organ of the Sorbonne is free of any religious constraint and that it is situated in a fertile cultural context allows us to envisage an exemplary, clear, unhurried, and scientifically rigorous approach.

We learned from [Dubois, 2016] that the salvaging efforts by Dubois, Dargassies, Galtier and others have attempted to emphasize the need to protect and preserve the organ of the Sorbonne Chapel, being an important part of French musical heritage. Despite being administratively protected, the organ has lost almost half of its pipework, and there are still threats of further degradation.

One possible approach would be the appointment of a curator, who would be responsible for the organ's physical condition and alert the relevant authorities of any potential threats; followed by conducting a precise survey of the instrument, which would enable the creation of an identical copy in the event of a disaster. The organ making techniques used in the classical era are well-known, and with the existence of vital elements of the organ still intact, such as the mechanics, console, blower, windchests, and faux-sommiers, a restoration of the organ to its original state is possible.

Some may argue in favor of leaving unrestored organs from the past for future generations, however, this instrument cannot produce sounds and allow musical execution. Moreover, the history of the instrument shows that its inability to be played has contributed to its dilapidation and vandalization. In contrast, a regularly used and maintained instrument would escape this inevitable deterioration.

The restoration of the organ would be crucial, given its historical significance as a rare example of the French facture of the *Ancien Régime*. It may be argued that only a scrupulous restoration to the identical is the appropriate course of action, excluding any addition or modification, to ensure the preservation of such instrument without any *improvements*. The restoration of this unique instrument would also give voice to a rare example of Dallery's work, as there are very few traces of their work remaining, and would also contribute to projects of social animation, organ-building training, and research.

1.6 Summary and concluding remarks

It seems to us that, after a few decades of effort in this direction, the administrative blockage is yet more castled than the narration above and the likelihood of an actual restoration is farther from taking place, despite the iconicity of the Chapelle for the University and the *Ville de Paris*.

The work presented here offers a virtual overview of the elements that consitute the sounding heritage, how they may be represented digitally, and finally assembled to render a representative listening experience of the inaccessible chapel and the non-playable instrument.

Such representation has been supported by computational resources, such is the inscription of the project within the *Institute of Computing and Data Sciences* (ISCD), offering great advantage in computation, processing and storage of an inmense collection of information at the crossroads of multiple disciplines: musicology, acoustics, history, engineering, and cultural studies.

Chapter 2

Methods and state of the art

Contents

2.1 **Prelude** . . . 17

2.2 **On wind supply and reservoirs** . . . 19

2.3 **On the organ pipe** . . . 21

2.3.1 The controversy that started it all . . . 22

2.3.2 Specific modeling elements of the flue organ pipe . . . 26

2.4 **On instrument radiation and scattering** . . . 29

2.5 **On room acoustics** . . . 30

2.6 **Summary** . . . 31

2.1 Prelude

The work that we develop here deals with recreating the conditions of sound for an instrument that *de-facto* can be considered extinguished, for now, in a space that is not accessible.

The tools and methods of which one will require to make use include:

- Hydrodynamics for wind supply systems and pipe organ reservoirs
- Fluid dynamics and aero-acoustics of flute-like instruments
- Digital signal processing for implementation of computational models
- Musicological and historically informed reconstruction of instruments and rooms (churches)
- Radiation and scattering in acoustics
- Room response simulation

The items mentioned above can be organized in block diagram such as Figure 2.2. Notice that modeling is gathered in two main issues: firstly, the production of sound and a complex field in the organ's cavity interior; secondly, the transmission of that field into the listening space. Note that the action of the instrument (keyboards and system of trackers, levers, and pulldowns) is not included in the scope of the current work, but literature is available towards the understanding of its operation: for example, *L'art du facteur d'orgue* Dom Bédos [Bédos De Celles, 1766], edited

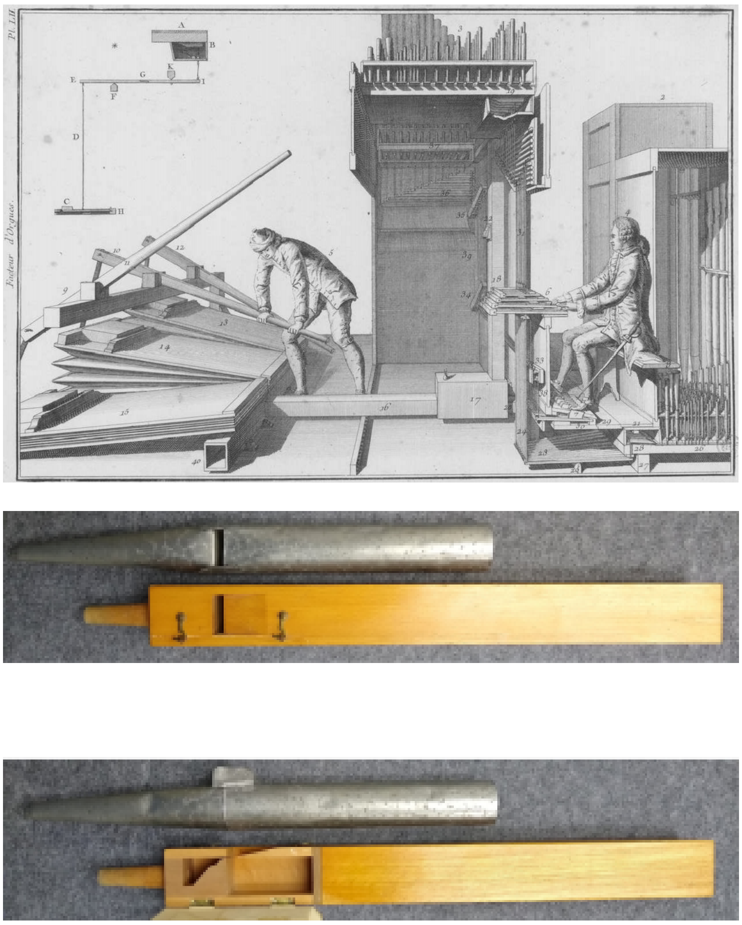

Figure 2.1: Organ overview from [Bédos De Celles, 1766] and flue organ pipe samples.

A. Cavaillé-Coll's *Complete theoretical works* in [Cavaillé-Coll, 1979], and Audsley's *The art of organ building* Volumes 1 and 2 ([Audsley, 1965a], [Audsley, 1965b]). Organ action systems (mechanical-direct, pneumatic, and electric) has been thoroughly examined regarding the effect in the musical performance in [Woolley, 2006].

The understanding of two core elements is crucial for the next investigations: i.e., the flue organ pipe and the mechanical operation of the organ. They are illustrated in Figure 2.1. The illustration from [Bédos De Celles, 1766] shows elements (A)-to-(D) (as per our diagram Figure 2.2) including the wind supply (old manually operated cuneiform bellows), ducts (or *porte vents*), the keyboard, the action mechanism to the windchests, and the pipes.

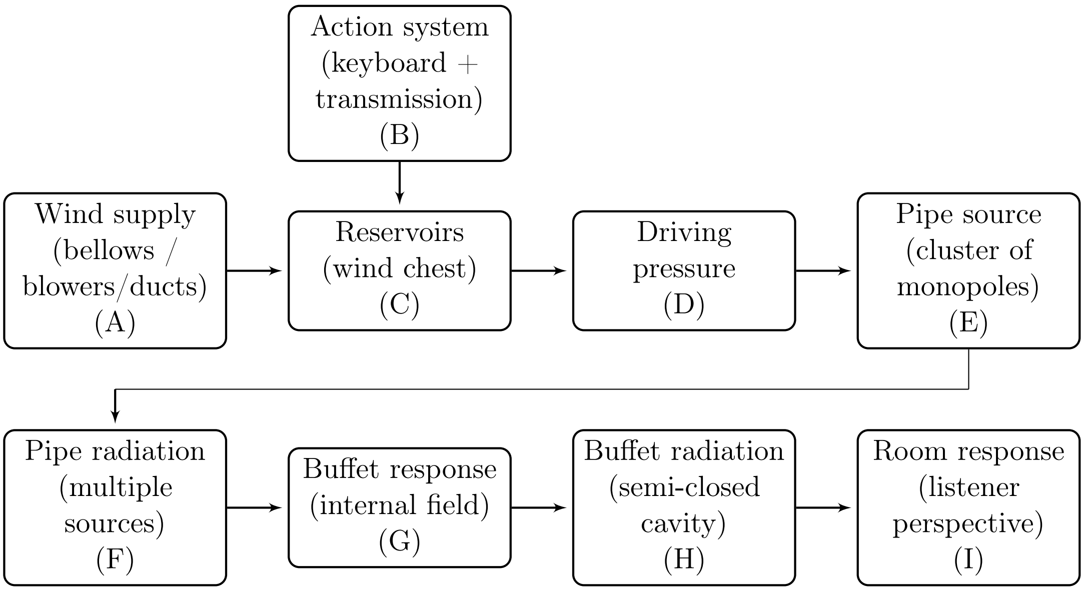

Figure 2.2: Diagram of the entire system to reconstruct.

2.2 Wind supply and reservoirs (A)(C)

Nolle and Finch [Finch and Nolle, 1986, Nolle and Finch, 1992] experimentally compared attack transients obtained with different organ pipes and valve opening times. They attempted to characterize the influence of pipe harmonicity and supply pressure rise time on the frequency content of the transient. Further inspection has been dedicated specifically to the blowing system of the organ electric wind supply, found in the doctoral dissertations of [Ngu, 1995, Carlsson, 2002, Taylor, 2018] and publications such as [Angster et al., 2004a, Angster et al., 2007, Pitsch et al., 2010, Taylor, 2016]. The experimental work of Carlsson offered empirical insights on the different wind supply system responses as is shown in Figure 2.3.

Models of pipe oscillation presented in the literature generally assume a constant pressure or a constant flow at the entrance of the pipe foot, whereas the junction between the wind supply system, reservoirs, and pipe foot still calls for a more detailed analysis. The idea of a Helmholtz resonance in the pipe foot has been introduced by Verge and Fabre [Verge et al., 1994b, Verge et al., 1997a], and studied in more detail by Auvray [Auvray et al., 2012b], Ernoult [Ernoult, 2016], and [Tateishi et al., 2019].

We have shown the traditional manual blowing system in Figure 2.1. However, almost all organs nowadays are provided with an electric system consisting in a centrifugal fan enclosed in a muffled wooden box such as the samples shown in Figure 2.4.

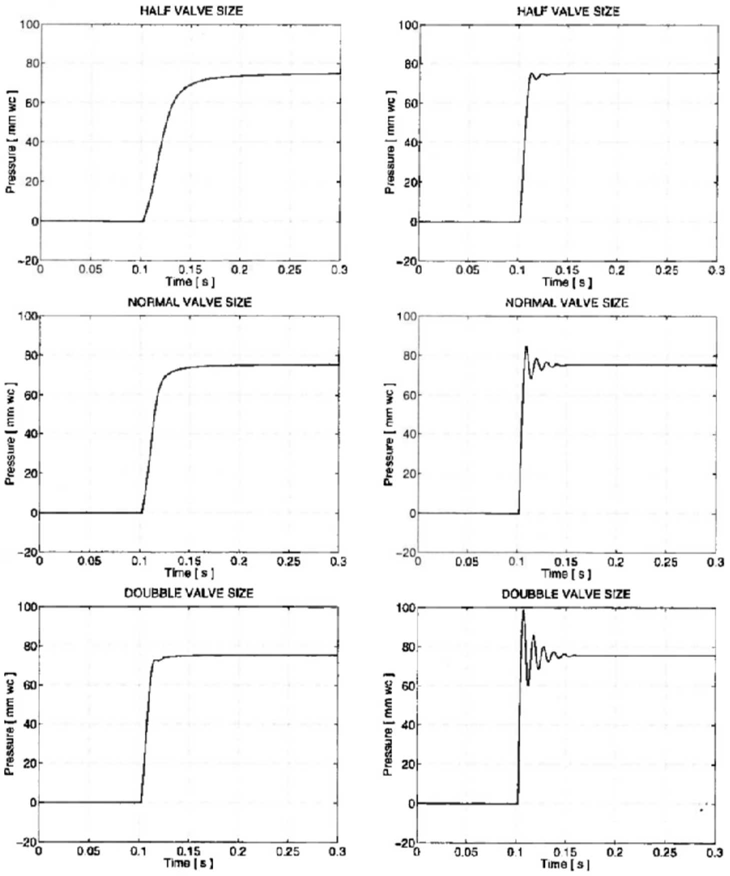

Figure 2.3: Measured wind supply responses at different valve opening times and sizes. Sourced from [Carlsson, 2002].

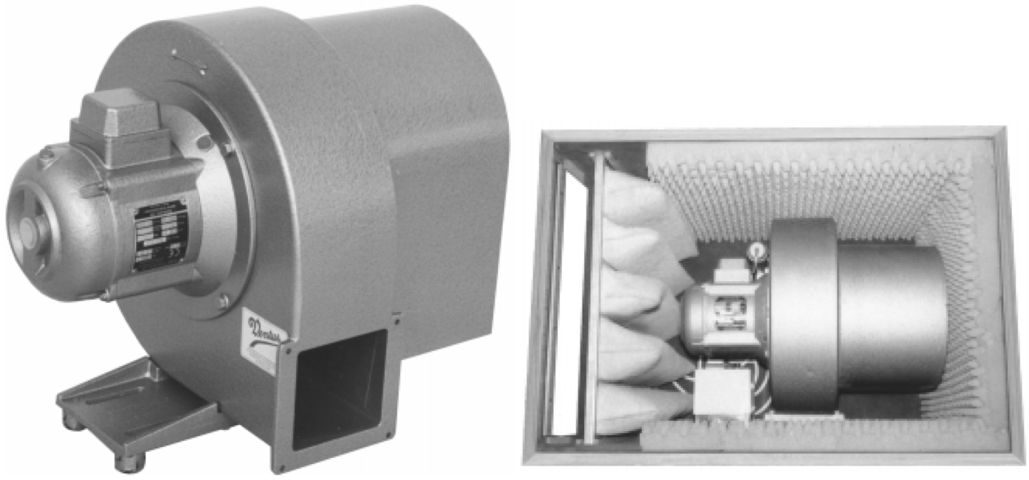

(a) Centrifugal fan **(b)** Muffled case for the fan

Figure 2.4: Electric wind supply system example. Images by Laukhuff Orgelbau.

2.3 On the organ pipe (E)

In acoustics, more specifically in musical acoustics of wind-instruments, one is generally concerned with the equations governing the dynamics of the fluid injected, contained, and surrounding the instrument. Hence, understanding the phenomena at hand and trying to model it have their roots in the complete set of Navier-Stokes (NS) equations. Solving the NS equations has led to intensive computational disciplines such as computational fluid dynamics (CFD), direct numerical simulation (DNS), high-resolution CFD, Reynolds-averaged Navier-Stokes models (RANS), k_ε-k_ω turbulent models amongst others. Such methods can help in finer descriptions of very specific problems when the problem is conditioned with enough detail to be able to interpret results. Some examples of that are: the velocity field at the flue exit or around the labium, the vortices under the mouth inside the pipe's resonator, or thermo-viscous layers effects. Following [Tritton, 2007], Navier-Stokes equations write as

$$\frac{\partial}{\partial t}\rho + \nabla \cdot \rho \mathbf{v} = q \tag{2.1}$$

$$\frac{\partial}{\partial t}\rho \mathbf{v} + (\mathbf{v} \cdot \nabla)\rho \mathbf{v} = -\nabla p + \mathbf{f} + \nabla \sigma_{ij} \tag{2.2}$$

where the velocity field stress tensor σ is

$$\sigma_{ij} = \lambda \nabla \cdot \delta_{ij} \mathbf{v} + \mu \left(\frac{\partial}{\partial x_j} v_i + \frac{\partial}{\partial x_i} v_j \right) \tag{2.3}$$

exploiting $\mathbf{v} = (v_i, v_j)$ as the velocity field, q a mass source, p the pressure, ρ the fluid media density (air), and the Lamé's first and second parameters λ and μ (dynamic viscosity or shear modulus).

However, as long as our musical acoustics definition is contained within wind instruments at low operation amplitudes, linear and weakly non-linear regimes are generally preferred as sufficient descriptors. Some finer elements are borrowed as approximations from in-detail investigations from fields such as those mentioned above. Typical approximations concern compressibility, heat transfer, viscosity, vorticity, and wave-length scale comparison.

The tools utilised in the current work belong to two complementary and incompatible cases. First, the developments on the air supply up to the jet formation will assume incompressible flows including or not viscous effects. Second, the acoustical analysis assumes adiabatic compression and neglects mean flows as well as viscosity, except at specific positions such as walls; nonetheless, they have led to useful methodologies being inherited: this is the case, for example, of the origins of finite-differences in the fields of fluid dynamics and eletrodynamics. We will comment on its application later on this chapter. We consider a departure from the wave (or visco-thermal) equation for our investigations, and as long as it is possible, we will model unsteady Bernoulli flows (between organ cavities) and laminar or piece-wise flows (in regions where the jet operates). In Chapter 6, we will revisit the wave equation with greater attention, reducing Equation (2.2) to

$$\left[\nabla^2 - \frac{1}{c^2}\frac{\partial^2}{\partial t^2}\right]\psi(\mathbf{r},t) = -f(\mathbf{r},t) \tag{2.4}$$

with the addition of visco-thermal terms, with Ψ being the velocity potential of the acoustic field.

2.3.1 The controversy that started it all

The nature of the driving mechanisms discussed today for the pipe models has its origins in a dispute back in the 19th century between J. Rayleigh and H. von Helmholtz, concerning the action type and location of the sources.

The matter of defining aero-acoustic sources is conditioned by being able to define the acoustic field, which is presented in a review paper by [Fabre and Hirschberg, 2000] splitting the subject into the following stages:

- The Rayleigh-Helmholtz controversy
- Sound sources in modern lumped models:[Verge, 1994, Verge et al., 1997b, Howe, 1975, Elder, 1973]
- Edge-tones and turbulence: [Lighthill, 1952, Powell, 1961, Elder, 1978, Miklós and Angster, 2000, Fletcher, 1976, Holger et al., 1980, Howe, 1981]
- Analytical approach to sound source description: [Elder, 1973, Howe, 1998]

The so-called Helmholtz-Rayleigh controversy, as summarized in [Fabre and Hirschberg, 2000]:

> Helmholtz [Helmholtz, 1885] assumed that the oscillating jet injects a volume flow Q_{in} into the pipe below the labium at each sound period. He assumed that the instrument is driven by this monopole source. Rayleigh [Rayleigh, 1894] argued that near an open end, such as the mouth of the pipe, the acoustical pressure p' is small[1], which makes a monopole quite inefficient since the acoustic work performed is given by:
>
> $$\oint p' dV = \int p' Q_{in} dt \approx 0 \tag{2.5}$$
>
> Rayleigh stated that he expected the sound source to be a force and hence have a dipole character. A dipole is much more efficient than a monopole near the open end since the acoustic work is then proportional to the acoustical volume flux, which shows a maximum at such an open end. While Helmholtz agreed with the point of view of Rayleigh in the comments added to the later edition of his book, the controversy reappeared in the 1960s. Cremer [Cremer and Ising, 1968] realized that

---

[1] Think of that as $p' = p_{tot} - p_o$, where p_o is the mean, atmospheric pressure

> the inertance of the acoustic flow in the mouth (corresponding to the so-called end correction) was sufficiently large to support a monopole drive. Coltman [Coltman, 1969] then tried to observe the radiation of the jet flow Q_{out} leaving the pipe. Since this radiation could not be observed, he concluded that the sound source was a dipole as assumed by Rayleigh [Rayleigh, 1894].
>
> Elder [Elder, 1973] explained Coltman's result by stating that obviously the fluctuating part of the two volume flows separated by the labium should be complementary ($Q'_{out} = -Q'_{in}$) because there is no volume creation at the labium and compressibility is locally negligible (compact low Mach number flow). Furthermore, he realized that there was no well defined "inside" or "outside" region of the pipe. The region above the labium is simply a region of lower acoustic impedance than the region under the labium. Hence, only part of the inertance of the mouth is involved. From measurements, Coltman [Coltman, 1976] concluded that the difference in impedance between injection points of the two complementary sources is about half of the total mouth inertance. Verge [Verge, 1994] found a value of about one third of the mouth inertance for the instrument that he studied. He also showed that he could predict this value by assuming an injection of Q_{in} and Q_{out} at a distance from the edge of the labium equal to the jet height h. His theory allows prediction of the influence of the mouth geometry on the effective inertance between the two injection points. However, the exact position of the sources is not predicted by such a theory. This is an essential limitation of lumped models in which the volume injections Q_{in} and Q_{out} are assumed to be localised.

The definition of sources presented by Lighthill [Lighthill, 1952, Lighthill, 1954] was the first of its kind. It is compared with Howe's alternative definition [Howe, 1984], based on Powell's vortex sound theory [Powell, 1964], in Howe's textbook on acoustics [Howe, 1998]. The vortex sound theory can provide an intuitition of the sound production that is related to the phenomenon [Fabre and Hirschberg, 1996, Howe, 1975]. Such step forward moving away from the Helmholtz-Rayleigh dispute takes the name of Lighthill analogy, which can be written, in Einstein notation, as

$$\frac{1}{c_o^2}\frac{\partial^2}{\partial t^2}p' - \frac{\partial^2}{\partial x_i^2}p' = \frac{\partial^2}{\partial_i \partial_j}(\rho v_i v_j - \tau_{ij}) + \frac{\partial^2}{\partial t^2}\left(\frac{p'}{c_o^2} - \rho'\right) + \frac{\partial}{\partial t}q_m - \frac{\partial}{\partial x_i}f_i \qquad (2.6)$$

where p' is the acoustic pressure, defined as the deviation from the mean (atmospheric pressure) as $p' = p - \langle p \rangle$ and analogously, the media density $\rho' = \rho - \langle \rho \rangle$; v, x, τ_{ij}, q are respectively the velocity field, the position vector, the viscous shear stress tensor (Equation (2.2)), and a mass source. The Lighthill stress tensor is finally developed as

$$T_{ij} = \rho v_i v_j - \tau_{ij}(p' - c_o^2 \rho')\delta_{ij} \tag{2.7}$$

The source terms in the right-hand side of Equation (2.6), as explained by Verge in [Verge, 1995], condense the following types of contributions

- Reynolds stress tensor: fluctuations in $\rho v_i v_j$ due to turbulence and vortex shedding.
- Viscous stress: fluctuations of τ_{ij} due to viscous dissipation mostly at the walls.
- Entropy: fluctuation of $p'/c_o^2 - \rho'$ due to heat transfer at walls and to temperature differene between the air blown and that one in the instrument.
- Volume injection: $\partial q_m/\partial t$ (a monopole sound source) represents an unsteady source at a solid wall in the virtual location of the jet's flue exit.
- External force: $-\partial f_i/\partial x_i$ (a dipole sound source) represents external forces acting on the fluid, for instance, due to the presence of the labium amidst the fluid.

1969/70 set a mark for computational musical acoustics: P. M. Ruiz's dissertation [Ruiz, 1970] (followed by [Hiller and Ruiz, 1971a] [Hiller and Ruiz, 1971b]) proposed the use of computers and time-stepping methods to recreate the sound of a vibrating string. This was a milestone, opening possibilities for finite-difference time-domain (FDTD) techniques to be used with musical purposes. The following decades saw the proliferation of computational models for string simulation [Karplus and Strong, 1983, Jaffe and Smith, 1983, Karjalainen et al., 1998].

Acording to Verge, the early model proposed by Cremer and Ising [Cremer and Ising, 1968] is the starting point for most of the literature on the subject of organ pipe tones. This quasi-stationary model of the jet drive has been extended by, amongst others, Coltman (1976), Elder (1973), Fletcher (1976), von Schlosser (1979), Schumacher (1978), Yoshikawa (1980), Nolle (1983) and Mcintyre et al. (1983).

Nowadays, outcomes of Coltman's investigations are extended to flute-like instruments. Spanning from the beginnings of Powell's publications in the 1960 with major publications around the flute subject [Coltman, 1966],[Coltman, 1968b], [Coltman, 1968a], and the crucial [Coltman, 1969] (exploring the radiate difference between both ends of a pipe); up until 2006 with his organ-specific *miter bends* exploration [Coltman, 2006], he proved to be a very inventive and resourceful researcher in wind instrument acoustics.

The first decade of the new millenium provided: C. Ségoufin with numerical resolution of Rayleigh equation to the instability (first described by Mattingly and Criminaly in [Mattingly and Criminale, 1971] and later, within the field of instrument acoustics, by Verge in [Verge et al., 1994a]) and the effect of the channel and flue exit shape on the jet formation velocity profile [Ségoufin, 2000] and

[Ségoufin et al., 2000]. V. Rioux devoted an entire thesis to the perception of organ pipe sound [Rioux, 2000] (and [Rioux, 2001]) at the same time that S. Dequand's thesis on duct acoustics found applications to *musical jets/flows* [Dequand, 2000]; in 2003 she put forward a mouth model simplification [Dequand et al., 2003].

The mouth of the pipe received further attention by P. de la Cuadra, providing feasible approximations with respect to the jet convection and the perturbation amplification wave number (theoretically, frequency-dependant; in practice, such frequency dependance implementation is unwieldy) [De La Cuadra et al., 2008]. Additionally he provided: wave-guide time-domain computation implementations of pipe sound, image-processing tracking of jet footage, and started the extension from the flute-like to the *non-western* flute instruments.

The line of research started by Ruiz has been substantiated by reference books such as *Numerical sound synthesis* by Bilbao ([Bilbao, 2004]) and, closer in methods to the school of Stanford (see Smith and de la Cuadra), in *Wave and scattering methods for numerical simulation* by the same author ([Bilbao, 2009]). F. Blanc closed the decade with research on the influence of the chamfers and flueway geometry [Blanc, 2009] and a complement to Fletcher's scaling rule with [Blanc et al., 2010].

Lefebvre devoted a whole thesis [Lefebvre, 2010] to numerical calculation of impedances in a team well concerned with the description of the embouchoure of reed-instruments ([da Silva et al., 2007, Wang et al., 2021]), with transmission matrix method (TMM) and finite element method (FEM). This finds a continuation by C. Meek with an impedance calculation implementation computational optimization toolbox applied to brass instrument [Meek, 2012]. Toolboxes that have seen major distribution across the acoustics research community include OpenWind (open Wind Instrument Design toolbox, by Makutu team at INRIA) and WIAT (Wind Instrument Acoustic Toolkit, by A. Lefebvre, G. Goudou, and G. Scavone at McGill). More recently, F. Ablitzer has presented a PeakPickingTool utility performing optimization on complex-valued data as per [Ablitzer, 2021] with application to modal expansions of brass instrument impendaces. There is also a limited distribution of two-microphone impedance measurement device which exists principally across French laboratories (*Capteur-Z*, [Le Roux et al., 2012]) with the aim to establish a common benchmark for measurement technique and interpretation.

In the last decade, the recorder-like flue model has received the attention of Auvray, Terrien, and Ernoult with an accent of the transition of regimes ([Auvray, 2013, Terrien, 2014, Ernoult, 2016]). Auvray investigated the time scales for regime transition. Firstly, working out the effect of slow variation of control parameters in Runge-Kutta-like model simulations under quasi-steady regime assumption. Secondly, inspecting the sensitivity of the jet-drive and discrete vortex models under rapid variation of control parameters, e.g. the *vibrato* around a note during musical performance. In the case of Terrien, an analysis of the neutral nature of the delay differential equations involved in the pipe model leads to developing a corpus of numerical continuation of solution branches reporting behaviours not accessible by direct temporal simulation. The work by Ernoult put an emphasis on attack transients, their link with modifications on the performer level: namely, fin-

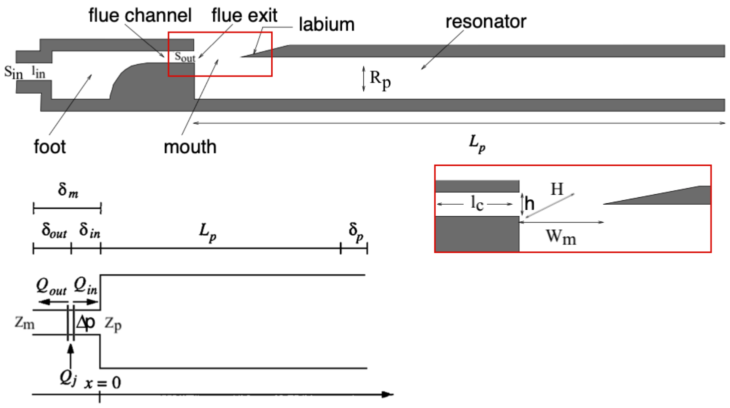

Figure 2.5: Depiction of the pipe and mouth geometry, together with the illustration of the 1D acoustic analogy as appears in [Verge, 1995].

gering, driving pressure, and geometrical and manufacturing parameters; his study to proposed curves of stability leading to a classification and transition behaviour between steady and quasy steady regions of operation, thanks to a great corpus of attack transient measurements of professional and non-professional recorder players.

Two long-standing projects are worth mentioning due to their richness and dedication. Firstly, the team by Angster, Miklós, and Rucz centered around the organ built in the Fraunhofer IBP Institut (Stuttgart, Germany), where [Angster et al., 2019] provides a global overview. Secondly, the Götheborg Organ project, with a high research activity during the 1990s, extending up to the present day.

2.3.2 Specific modeling elements of the flue organ pipe

We propose a succint mention of the modeling aspects that have a role in the modeling of flue recorder-like instruments. A more detail description of them is addressed in Chapter 3 and Chapter 4. The one and two-dimensional representations of the recorder-like instrument in Figure 2.5 will aid in locating each of such elements.

The initial element that puts the instrument in operation is a driving flow. This originates in wind supply systems in organs, and in the mouth of the performer, for recorders and flutes. The performer may change the driving pressure in their mouth, as well as a slight variation of the mouth cavity volume. Both in the organ case and recoders, the flow is not perfectly steady. Indeed, variations may occur, on the one hand, due to the mechanical or anatomical *control system*; on the other hand, due to the coupling of the flow supply with the foot cavity of the instrument, and the resonator of the instrument in self-oscillation operation. With respect to organ case to present, the driving flow of the model has little been described in relation to the geometry and conditions of the supply system (with exceptions mentioned in §2.2). Auvray *et al.* investigated the effect by changes in the vocal tract for the case of flutes and recorders in [Auvray et al., 2015]. See the foot as the first cavity upstream (left to right) in the 2D representation in Figure 2.5.

The air flow going into the instrument foot through an inlet of small cross section attains high Reynolds numbers in the foot and the turbulent flow in the foot has been prolificly described since the 1990s by Verge and Hirschberg, [Verge and Hirschberg, 1995]. A potential flow [Verge et al., 1994b] from the foot, through the flue channel, gives origin to the formation of a jet at the flue exit. As referred before, Ségoufin throughly investigated the evolution of the jet velocity profile along that channel. The jet at the flue exit is affected by the flue geometry (the chamfers), by an impedance jump between the interior and exterior of the pipe (represented uni-dimensionally in Figure 2.5), and by feedback from the pipe (hydrodynamic and acoustic feedback).

The formation of the jet in recorder-like instruments and flue organ pipes is greatly determined by a fixed geometry established at the time of the manufacturing. In cases of similar families of instruments such as transverse flute, pan pipes, quenas, or shakuhachi, amongst others, the performer is in control of geometry parameters: the flue way section (mouth area), the angle and the distance of the jet with respect to the sharp labium. An example of investigations to include these parameters in the flute-like model may be found in [Ernoult et al., 2018].

The so-called *jet receptivity* describes the perturbation of the jet as it emerges from the flue (see Figure 2.6a). The assumption of laminar flow in the mouth makes it possible to model a hydrodynamic instability in the convection of the jet towards the labium. The piece-wise velocity *outside* and *inside* are different. The convection of the jet towards the labium is governed by a hydrodynamic instability, the solutions of which describe in a simplified manner the behaviour of the jet in the mouth (numerical solution of the instability wave numbers are shown in Figure 2.6b). Several modeling approaches have led to considering sound sources by reference to the edge-tone, the vortical sound, and the jet-drive dipole. The resonator acts as a physical filter of frequencies produced by sound sources, the most efficient of which in terms of radiation is the dipole jet-drive as per the discussion above.

Modal decomposition. The modal decomposition technique, for acoutic bores whose reponse is known, has allowed for a computationally inexpensive way of representing the effect of the resonator. Compare it with a brass instrument resolved in finite-difference time-domain (FDTD) simualation to see the advantageous choice (see [Harrison-Harsley, 2018]).

It usually appears as a rational fraction in Laplace or z-domain. As such, they can be implemented as linear time-invariant (LTI) filters or solve the corresponding set of ordinary differential equations (ODEs). Since [Terrien, 2014], it is common to have this representation include a frequencyless mode (or uniform mode) that represents the main flow through the bore and takes the form

$$Y_p(\omega) = \frac{a_o}{j\omega b_o + c_o} + \sum_r \frac{sY_r}{\omega_r^2 + \varepsilon_r \omega_r s + s^2} \tag{2.8}$$

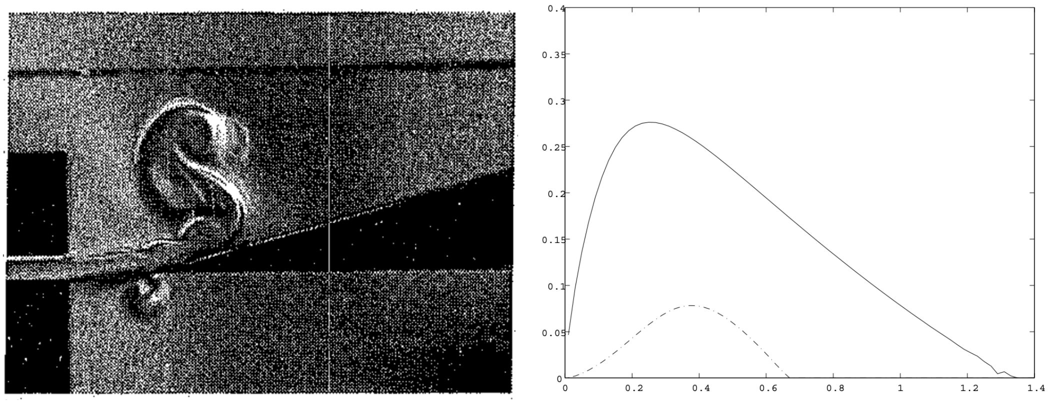

(a) **(b)**

Figure 2.6: (a) Schieleren visualization of the outward jet deflection at the mouth-labium region and vortex pairs. Image credit: B. Fabre and A. Ernoult, 2016. (b) Numerical resolution of Rayleigh's equation in [Verge et al., 1994a, Ségoufin, 2000] showing the dominance of the sinuous modes (antisymmetric) of the perturbation over the varicous ones (symmetric). Data shows the dimensionless spatial amplification $\alpha_i \cdot b$ against dimensionless frequency by the Strouhal number, $Str = \omega b/U_o$. Antisymmetric solution (—) and symmetric solution (- - -).

The resonator equation uses that structure to input the pressure sources at the labium yielding a response in the acoustic velocity in the pipe, taking the form

$$\left[\frac{d^2}{dt^2} + \varepsilon_r \omega_r \frac{d}{dt} + \omega_r^2\right] v_r = Y_r \frac{d}{dt} \Delta p_{tot} \tag{2.9}$$

with the acoustic velocity being the sum of the modal contributions, $v_{ac} = v = \sum_r v_r$; alternatively represented as

$$\frac{d}{dt} v_o = \frac{1}{b_o}(a_o \Delta p_{tot} - c_o v_o) \tag{2.10}$$

$$\frac{d^2}{dt^2} v_r = -\varepsilon_r \omega_r \frac{d}{dt} v_r - \omega_r^2 v_r + Y_r \frac{d}{dt} \Delta p_{tot} \tag{2.11}$$

if the zero-th mode is included. Figures 2.7 and 2.8 illustrate the response differences when the zeroth-mode is included in the bore's acoustic response.

With J. Smith on the lead of digital waveguide sound synthesis since the 1980s, Darabundit and Smith [Darabundit and Smith, 2021] proposed a computationally inexpensive strategy for the organ pipe's bore: a scalable lossy digital waveguide framework, where parameters can be adjusted based on the pipe's geometry.

The resonator under such representation is easily implemented as a linear time-invariant (LTI) filter, whose representation including a zero-frequency uniform mode is reasoned by Terrien [Terrien, 2014]; specifically, it may be seen as second-order section filter, with complex pole-pairs. This will be further examined in Chapter 4.

The three-dimensional plot of the resonator input admittance in Figure 2.7 summarizes all accessible features upon which one may perform numerical modal extrac-

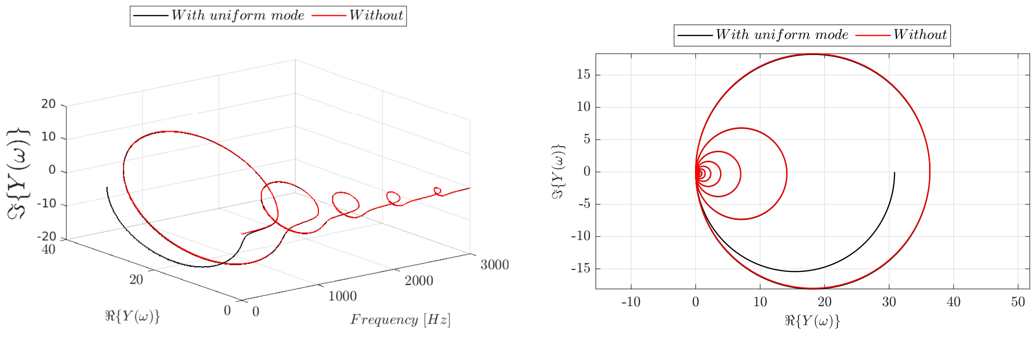

(a) **(b)**

Figure 2.7: (a) Three-dimensional view of a test pipe's computed input admittance. (b) Nyquist plot of $Y(\omega)$.

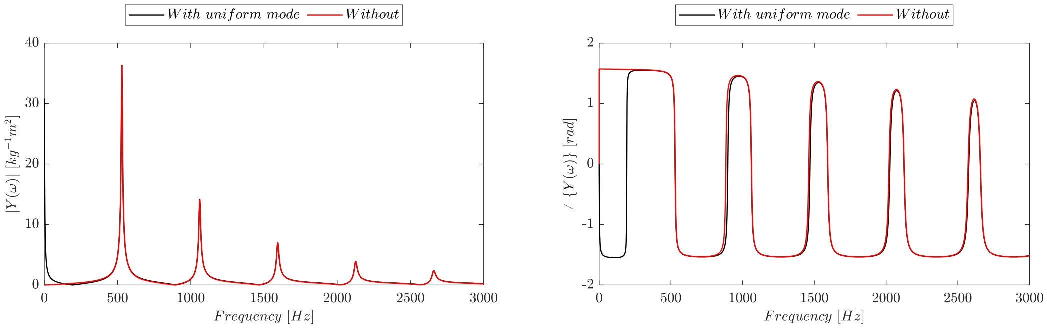

(a) **(b)**

Figure 2.8: (a) magnitude and (b) phase of a test pipe's computed input admittance.

tion. As a demonstation, computed data for the acoustic response of a test organ (test organ pipe 5, see Section 3.4 for geometry details) is projected onto the more common spaces of magnitude, phase, and Nyquist in Figure 2.7 and Figure 2.8. Though the pertinence of including the zero-th mode in analytical loop gain derivation or numerical implementations of pipe simulation is discussed later in this text, we display here the behaviour of both cases.

2.4 On instrument radiation and scattering (F-H)

The publication by Levine and Schwinger [Levine and Schwinger, 1948] has been a foundational keystone for organ pipe radiation (followed four decades later by a contribution on rectangular piston impedance [Levine, 1983]).

The problem of radiation through apertures, has received attention under different approximations and applications: diffuse fields, low modal fields, normal harmonic incident fields, cylindrical and rectangular radiating structures, and finite and infinite apertures [Sauter and Soroka, 1970, Pierce et al., 2002, Linton and Martin, 2005, Mellow, 2006, Sgard et al., 2007, Trompette et al., 2009]. We will refer to more problem-specific publications in Chapter 6, but they all have in common considering the radiation of a single slit.

The complex diffuse field in the organ's buffet cavity in high modal density becomes a problem better suited for statistical representation. Bruneau offers in [Bruneau, 2006] an accessible description to such representation. The directivity of the organ pipe has recently received the attention of Odya *et al.* [Odya et al., 2017] investigating the intensity field near the pipe, along with current work by Kob *et al.* (simultaneously with work on the bassoon [Kob et al., 2022]). Berry *et al.* proposed a low order generalization to estimating the scattered field produced by an array of spaces cylinders in [Berry et al., 2019].

Weber and Katz [Weber and Katz, 2022] implemented the scheme and stability condition published by Bilbao and Hamilton [Bilbao and Hamilton, 2016, Bilbao and Hamilton, 2018]: *Finite Volume Time Domain Room Acoustics Simulation under General Impedance Boundary Conditions* and *Passive volumetric time domain simulation for room acoustics applications.* The application of the work by Weber was to investigate the scattering induced by the presence of columns and piers in the context of room acoustics, especifically in the cathedral of Notre-Dame de Paris.

2.5 On room acoustics (I)

On the least computationally intensive end of room simulation, one finds the field of geometrical acoustics (GA), based on the Sabine's principle of surface material absorption. This approach has lead to developing the ideas of ray tracing, where the room response is computed for a given set of receiver positions, based on a set of finite rays originated at 'fixed' source positions. The core idea to retain is that for a given source emitting with an incident angle θ with respect to the surface normal, there would be a receiver at a position r' with equal angle θ under specular reflection assumption. In such model, the receiver position can be seen as an *image* at the other side of the surface plane with respect to the source side. When the line conneting a source and an *image* crosses one plane, this is equivalent to assuming that the ray is reflected once, thus called first-order reflection. This can be extended to a number N of reflection order, equivalent to considering N *images* of the receiver location with respect to each surface plane. This principle receives the name of Image Source Method (ISM). See [Lehmann and Johansson, 2010] for an introduction.

Reference books covering room acoustics and materials are found, for example, by [Kuttruff, 1991] and [Beranek, 1960, Beranek, 1996, Beranek, 2004]. Savioja and Dalenbäck have proposed overviews in [Savioja and Svensson, 2015] and [Dalenbäck, 2018].

Enhancements of such method start by modeling the properties of the incident wave-plane interaction at the surface, which may be absorbent, reflecting, rough, patterned, multi-layered, perforated, etc. One starts by modeling the absorption properties, transmission, and reflection. Additionally, GA has seen expansions towards scattering (see 1D and 2D Lambert *diffusion* [Dalenbäck, 2011]). See [Dalenbäck, 2016c] and [Svensson et al., 1999, Svensson and Calamia, 2006] on this regard, but in general, scattering phenomena are harder to implement within ray-tracing techniques than it is for wave methods.

At present, widely distributed existing commercial and non-commercial tools to address GA modelling of spaces include: CATT-Acoustics, Odeon, Ramsete, COMSOL Acoustics module, Raven.

Room acoustics has also been tackled by wave-based approaches. Work can be found by Bilbao and Hamilton adding visco-thermal losses, wall impedance, and parameter fitting to material values, as well as adding losses to the airborn propagation [Hamilton, 2021a, Hamilton, 2021b]. Because of the computer intensive nature of FDTD and FVTD methods, work was also developed in collaboration with Webb [Hamilton and Webb, 2014, Hamilton and Webb, 2013] on GPU acceleration for visco-thermal wave-equation schemes, leading to the open source code *PFFDTD* [Hamilton, 2021c]. Compendious context on these approaches can be found in [Hamilton, 2016].

Investigation towards material description for this kind of of approaches is found in previous decades by Beranek and Kuttruff. At present, there is ongoing research on material absorption: a few examples of that are impedance tube-based techniques by L. Jaouen and collaborators ([Arasan et al., 2021, Arasan et al., 2022, Sreekumar et al., 2022], at Matelys enterprise) and non-invasive techniques by B. Briere de la Hosseraye [Briere de la Hosseraye, 2023], who has devoted a doctoral dissertation to the matter. Care has to be taken regarding assumptions on the field nature and the surface incidence when asserting properties of the material that are transferrable to GA models.

2.6 Summary

We have provided in this section a historical overview and the most recent research for elements of the organ modeling, starting with pointers to wind supply systems. Elements of the flue organ pipe model will be revisited in later chapters: the discussion starts by considering what is a *sound source*, which dates now by almost a century and a half. We have later presented tools and contributions that aided in model simplifications, numerical methods and solutions, parameter extraction.

The review adds a few pointers to introduce the considerations of the instrument in space: on the one hand, its radiation within an enclosure, and on the other hand, the radiation of such enclosure into a relevant space from the listening point of view: halls and churches.

As it becomes apparent from existing literature, the creating of a global model of the organ and the church seems like assembling a giant puzzle with missing parts as well as the connection of parts with different hypothesis (e.g. acoustic, hydrodynamics).

Part I

Developments on flue organ pipes

Chapter 3

A model for pressure-rise time prediction in organ pipes

Contents

3.1 Introduction **36**

3.2 Operation of organ pipes and supply systems **38**

3.2.1 Organ pipe models: a recapitulation 39

3.2.2 The coupling of the supply system and the pipe 40

3.3 The reservoir and the foot **42**

3.3.1 Supply system: continuous model 42

3.3.2 Pallet-box and initialization of the system 44

3.3.3 Analysis towards a non-dimensional model 45

3.4 Measurements **48**

3.4.1 Setup of the laboratory measurements 49

3.4.2 Setup of the measurements in Pinchi organs 49

3.4.3 Results 52

3.4.4 Steady-state results in real organs 54

3.5 Discussion **58**

3.6 Conclusions **62**

3.7 Future perspectives **65**

3.8 Summary **68**

In this section we investigate the so-called driving pressure in flue organ pipe models. The foot-pipe coupling is extensively known and equations governing these dynamics have reached reasonable consensus, with some discrepancies related to phenomena in the mouth: namely, loss sources and finer developments of the roles of turbulence. In order to avoid making up the pressure rise in the cavities upstream from the mouth, we examine their geometrical and hydrodynamic "coupling/imbrication", in an attempt to provide an estimate of the time evolution of the driving pressure, whose main application is for simulations.

Reservoir cavities that drive the flue organ pipe are prepended to the model of direct flow injection or jet velocity imposition. Said cavities are the pallet-box, the groove, and the pipe foot. Such reservoirs are considered for modeling the relationship between the air supply system and the pipe operation. When the injection of air triggers the transient in the flue organ pipe, the steepness of the pressure rise affects the response of the resonator and the coupling with the volumes upstream: this comes with changes in the spectra and the volume fill-up time of the pipe foot. Pressure history was measured in the supply system at several locations within the pipe. Non-dimensional transient times of flow velocity growth are ultimately related to the geometry. The continuous equations describe the dynamics of a concatenation of reservoirs and the opening of the pallet valve. An initialization function is proposed, which models the transient after the system has been triggered. Bounds to energy growth are examined, which become useful in deriving further analysis of the system's passivity and energy conservation.

3.1 Introduction

The interest and applications of modeling flue organ pipes span the fields of numerical sound synthesis, organ making and tuning, and instrument design analysis. In line with heritage preservation, pipe models allow for numerical reconstruction of historical organs. We consider one such example in the application of this research.

Attack transients have an outstanding role in the timbre characteristics of sound production. The former greatly depends on the steepness of blowing pressure rise times (BPRT) upstream [Verge et al., 1994b], the distance W_m that the jet has to travel from the flue exit to the collision edge, the window ratio W_m/h, the hydrodynamic feedback of the first pulses reflected from the resonator at the beginning of the transient, and the inwards-outwards leaning tendency of the jet trajectory with respect to an offset y_off of the labium away from being flush with the flue exit. Analysis of the tones during the transient span spectral envelopes of the bore, triggering higher oscillating regimes and changing modal gains, as well as the turbulent noise contribution in the mouth [Mahu et al., 1993, Rioux, 2000, Ernoult and Fabre, 2017a, Hruška and Dlask, 2020]. In sum, acoustic pressure rise times are determined by the blowing and ventilation system and by the foot geometry.

This study proposes a model that predicts the foot pressure rise, taking into account both upstream conditions (blowing system) and downstream conditions (acoustic oscillation in the pipe). Its potential applications are the realistic initialization of pipe simulations, comparison between real organs and experimental organ models, and building bridges in the gap between organ-making enterprises and scientific understanding of the mechanics of this instrument.

The most relevant *recent* works are by Nolle and Finch, first in 1986, examining the response due to reflections in a long pallet-box channel and an organ pipe as a function of pallet opening times [Finch and Nolle, 1986]. In 1992, they further investigated spectral changes during the initial fundamental periods by imposing fast and slow wind supply rise times [Nolle and Finch, 1992]. A few other sparse contributions may be found in the empirically-based investigation of Carlsson with respect to the ducts (*wind trunks*), location of the pipe, and the type of wind blower installed in organs [Carlsson, 2002]. In addition, Pitsch *et al.* ([Pitsch et al., 2010]) produced a CFD model of an organ division for the purpose of estimating temperature gradients that affect pipe detuning; one of their simplifications involved omitting the emmited flow and fan noise by the wind supply system. In collaboration with Angster and Miklós, measured pressure responses were shown as to the harmonic onset under different *slider chest* operation ([Angster et al., 2004b]), the design of devices that would attenuate the drops and pressure fluctuations ([Angster et al., 2007]), and different jet velocities for an experimental flue model with variable angle and distance of the labium ([Außerlechner et al., 2008]).

The pressure in the cavities upstream from the foot can be modeled, represented by a so-called initialization function. Said function encapsulates the target average pressure attained after the rise time, the steepness of the rise time, thus governing the evolution of the jet velocity rise. Those variables depend on the blowing pressure and the geometry of the pipe. The latter implies that for a given set of blowing conditions in the pallet-box and groove reservoirs, the initialization function will be different for each pipe. This results in having different transients across the tessitura and pipes of the same *pitch* that belong to different stops.

In addition to the proposed model, we assess solution techniques to predict the time evolution of the foot pressure that drives the jet. The formulation adds extensions to well-known aspects of the pipe models. We aim to provide a means of reproducing the driving conditions of sound source elements in historical organs for which there exists documentation that makes it possible to estimate their geometry. To that end, we used documentation of the organ in Chapelle de la Sorbonne (Paris, France), built by Louis-Paul Dallery in 1825, and looked at similar pipe ranks in real, fully-functioning organs in Perugia, where we were able to perform measurements. We selected five test pipes available in the laboratory to perform invasive measurements, adapting them to each setup. In the intermediate modeling stage, only one rank of pipes from the organ was considered at a time, thus focusing on one scaling rule for a set of pipes. In our experiments, we first carried out measurements on organ pipes under controlled driving conditions, and later we compared them with those made in real instruments.

Geometry parameter names are indicated henceforth with a capital letter and a subscript (R_p). Pressure and velocity time-series are indicated in lowercase (p_m), which may include amplitudes expressed with a capitalized letter (e.g. P_o). Multiple indications can be given in a subscript to help locate the pressure point: $p_\mathrm{m,rad}$ stands for pressure radiated by the mouth; $p_\mathrm{p,end}$ is the pressure history inside the pipe at the passive end.

A recapitulation of the pipe operation is succinctly mentioned in §3.2 before proceeding with the continuous model equations of the reservoir and foot in §3.3. The measurement setup and presentation of results are described in §3.4, followed by comments and discussion in §3.5. We conclude with some remarks on the current state of this work in §3.6.

3.2 Operation of organ pipes and supply systems

The essential lumped building blocks for a minimal working model can be found in [Fabre and Hirschberg, 2000, Fabre et al., 2012, Chaigne and Kergomard, 2016]. The mechanics of self-sustained oscillation in some wind instruments are enumerated and explained there. The organ pipe is one such type. Losses are carefully reasoned in [Fabre and Hirschberg, 1996], accounting for a non-linear saturation that bounds the oscillation amplitude in the pipe. In [Verge et al., 1994b], inertance-like terms are suggested accounting for end corrections at the passive end of the resonator, ears at each side of the mouth window, and the window impedance itself. Compendious aspects have also been studied at the Fraunhofer IBP Institute [Angster et al., 2019].

Contributions towards modeling this problem significantly started in the 1950s in the field of aeroacoustics, with Lighthill [Lighthill, 1952, Lighthill, 1954] describing the nature of aerodynamically generated acoustic sources given an airflow in the presence of a collision with a rigid body and a resonator. This resulted in coining the term *edge-tone*, which received attention by Powell in the 1950s and 1960s [Powell, 1961] and Holger in the 1970s [Holger et al., 1977], culminating with Coltman picking up the advances and shifting the focus of application towards flutes and flue organ pipes (flute-like instruments) with considerable publications during the 1970s and 1980s [Coltman, 1966, Coltman, 1968b, Coltman, 1969, Coltman, 1971, Coltman, 1973, Coltman, 1976, Coltman, 1979, Coltman, 1981, Coltman, 1984].

Flow visualizations and framing of the jet in terms of the confinement within the flue exit and mouth-window led, on the one hand, to examine vortices as a contribution to sound production and as a source of losses; on the other hand, to the beginning of time-domain models in the 1990s. Hirschberg, Wijnands, Verge and Fabre contributed to these in [Coltman, 1992, Hirschberg et al., 1992, Verge et al., 1994b, Verge and Hirschberg, 1995, Fabre and Hirschberg, 1996, Verge et al., 1997a, Verge et al., 1997b].

Since the 2000s, salient descriptions appeared on the subjects of velocity profile development before the formation of the jet and the influence of the mouth geometry in the sound production, as well as characterizations of the jet receptivity [Ségoufin et al., 2000, de la Cuadra et al., 2004]. Later, oscillation regimes of flute-like instruments were explored, and mouth impedance transfer functions specific to flutes and pipes were proposed [Auvray et al., 2012a, Ernoult and Fabre, 2017b].

The significant parameters affecting sound production are the mouth opening and the pipe's resonator shape. The mouth spans H_m and W_m depth and flue-to-labium length. The flue exit area for the flow is given by h and the same depth H_m as the mouth window. The pipe's resonator with a physical length L_p has a cross-section $S(\mathrm{x})$ for $x \in [0, L_\mathrm{p}]$, which in the simplest case reduces to $S_\mathrm{p} = \pi R_\mathrm{p}^2$ when the resonator is cylindrical.

After initializing the pallet-box and opening the pallet valve by acting on the keyboard, the pressure starts rising in the groove, and the channel lengths of the windways communicating cavities offer resistance to an unsteady initial flow.

In a second time, the pipe's foot volume V_f (see the conical base of the pipe embedded into the reservoir in Figure 3.1) presents a pressure difference between its interior and the pipe mouth, thus starting to drive the flow downstream and outwards. Once the pressure balance reaches the fill-up point of V_f, the flow will transition towards a stationary point, and the energy density in the resonator will establish on a fixed set of modes. We call it the steady-state (SS) operating regime of the system.

In steady flows, the velocity of the flow is proportional to the square root of the pressure drop between adjacent cavities downstream, and mean inflows and outflows of the foot are equivalent. In unsteady flow conditions, however, time-derivative terms will dominate the flow during said initial instances, involving windway lengths and cross-sections. This can be seen as the opposition exerted by a mass of air trapped in the windway. Work by Verge and Ernoult ([Verge et al., 1994b, Ernoult and Fabre, 2017a]), for example, show how the transients affect the order of triggering of modes, the timbre characteristics [Rioux, 2000], the oscillating regime that establishes in steady-state operation (SS), and the transition time to the SS (generally, within a range of 10 to 30 fundamental periods, [Hruška and Dlask, 2020]).

Assuming the blowing system at the beginning of the supply chain provides a sufficient driving flow and reasonably small oscillations around the set value, a steady blowing condition will be reached at some time. Unlike other flue-like instruments, because the blowing pressure does not depend on hand-operation after the action of a note in the organ keyboard, the oscillating regime is expected to remain stable apart from the case of some mechanical organ keyboards where the player may have some control on the note after its onset [Woolley and Campbell, 2017].

3.2.1 Organ pipe models: a recapitulation

The fundamental operation of the so-called closed loop in self-sustained oscillation instruments uses the air supply (with volume flows $q_\text{pallet-box}$ and q_groove) to give rise to aero-acoustic sources (Δp) at the labium (upper lip) level —see Figure 3.1 and §3.2.2. The energy that derives from it is stored near the resonant modes of the bore. Once the pressure supply is initialized, the pressure differences between pallet-box to groove, groove to foot, and foot to mouth start the driving flows downstream. When the flow through the outlet of the foot sees the outside world in the mouth window, an air jet is formed and convected to end up interfering with the sharp-edged labium. A Bickley profile is often considered to approximate the velocity profile of this partially-confined jet [Ségoufin et al., 2000]. The rise time of the pressure in the foot (p_f) may continue to build up during the transient until SS blowing pressure is reached.

As soon as the pressure oscillations start in the resonator, they cause a transverse acoustic flow; therefore, an acoustic velocity transversely impinges on the jet convection line, whose effect in the very vicinity of the flue exit is called *jet-receptivity*. This causes a hydrodynamic instability whose most salient consequence is that the jet convection center-line fluctuates in the transverse direction with elongations η,

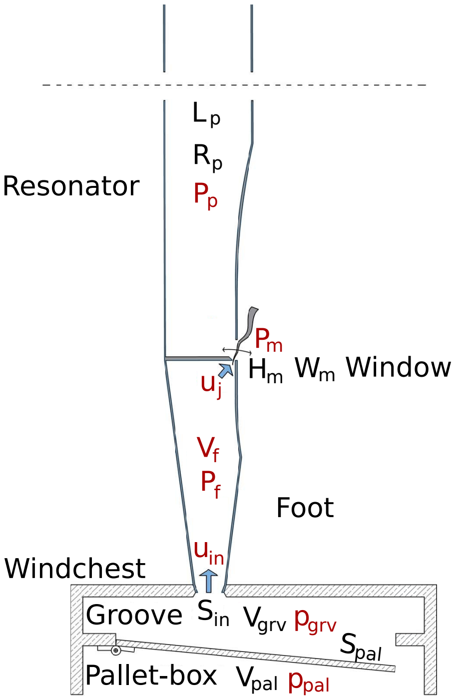

Figure 3.1: Diagram of reservoirs and organ pipe. In red, pressure and velocity variables; in black, geometry parameters. The size of the pallet valve has been increased for visualization purposes only.

thus injecting air inside the resonator and out into the outside world. The alternating character of wafting the labium gives rise to dipole-like aero-acoustic sources (see [Lighthill, 1952, Lighthill, 1954]), also called the jet-drive mechanism. Reciprocally, said alternating character in the acoustic velocity governs the primary source of losses, which acts as a non-linear saturation limit to the modal pressure oscillation amplitudes [Fabre and Hirschberg, 1996]. From the outside perspective of sound production, the pipe is seen as one monopole radiating from the mouth opening and another monopole radiating from the passive open end of the resonator, lengthways and opposite to the mouth at a distance $x = L_{\mathrm{p}}$. Provided that in the jet-drive model, the sound sources depend on the state of the jet at $x = W_{\mathrm{m}}$ (its phase, velocity, and sinuous movement), the time evolution of the pressure imbalance between the foot and the mouth shapes the growth of the jet velocity time-series. Put differently, the pressure rise-time (PRT) in the foot principally governs how the jet ramps up from zero to the SS velocity.

3.2.2 The coupling of the supply system and the pipe

The constituent elements in the feedback loop system of such self-sustained oscillation instruments are summarised in the diagram of Figure 4.1a. These are: the jet center-line velocity (u_{j}) caused by the pressure difference between the foot (p_{f}) and the mouth (p_{m}); the transverse displacement (η) of the jet trajectory away from the

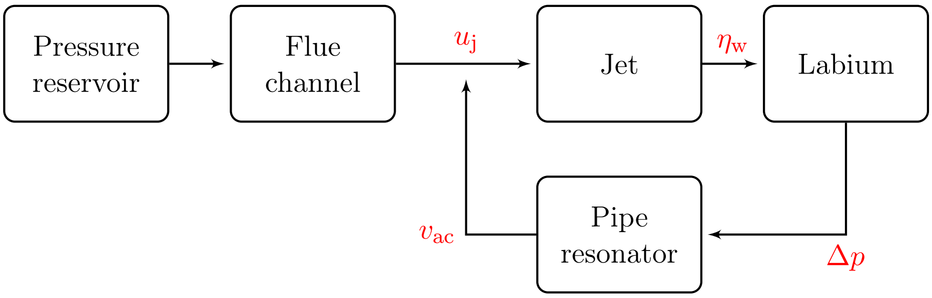

Figure 3.2: Feedback loop system in self-sustained oscillation flue pipe instruments.

center-line which traverses from the flue exit to the labium; said elongations cause the jet wafting on the labium to originate a dipole source with Q_1 and Q_2 inside and outside of the labium, resulting in a Δp term of pressure units. Finally, after accounting for non-linear losses at the mouth, the resonator's modal response yields a total acoustic velocity (v_{ac}) in the mouth region. The latter updates p_{m}, shifted by the delay time it takes for the jet to travel the cut-up distance $x \in [0, W_{\mathrm{m}}]$.

The center-line jet velocity (u_{j}) results from the Bernoulli streamline towards the exit of the foot. In recorder-like instruments, the flow velocity profile evolves along the flue channel, and at the exit, the air jet formation inherits said profile. In lead-tin flue organ pipes, as opposed to wooden ones, the physical flue channel length is short and comparable to the thickness of the tin sheet. Ségoufin *et al.* [Ségoufin et al., 2000] describe the effect of the channel length on the transients of the foot pressure p_{f}, jet velocity u_{j}, and pipe pressure p_{p}. For short channel lengths, the velocity profile of the jet in the mouth is almost trapezoidal, while it develops further towards a Poiseuille profile over more extended channels [Ségoufin, 2000].

In the mouth opening region where the jet is convected towards the labium, the pressure p_{m} constitutes together with the aforementioned p_{f} what physically couples the acoustics of the resonator with the volumes upstream in the foot and the pallet-box and groove. Acoustic pressure in the mouth, velocities, and densities can be decomposed into their steady components and a perturbation or oscillatory term, as shown below:

$$p = \langle p \rangle + p' \tag{3.1}$$

The mean value of the acoustic pressure p_{ac} in the mouth window is neglected, provided that it equals the surrounding atmospheric pressure without undergoing any perturbation, $\langle p_{\mathrm{m,ac}} \rangle \sim 0$. The perturbation term p'_{ac} is retrieved after the modal velocity contributions that depend on $\sum_k v_{\mathrm{k,ac}}$, causing the transverse acoustic flow to go in and out of the resonator. Given a pressure amplitude in the pipe, mapping the region allows one to obtain the oscillation amplitude in the mouth. Based on the work by Stegen and Coltman on this subject [Stegen, 1967, Coltman, 1976], we have verified experimentally that the following approximation can be used in our model:

$$p_{\mathrm{m}} \simeq 0.5\, p_{\mathrm{ac}} \tag{3.2}$$

The pressure decomposition shown in Equation (3.1) can also be performed on density and velocity so that quadratic forms above can be expanded: $u_{\mathrm{in}}^2 = \langle u_{\mathrm{in}} \rangle^2 + u'^2_{\mathrm{in}} + 2\langle u_{\mathrm{in}} \rangle u'_{\mathrm{in}}$.

3.3 The reservoir and the foot

We start by introducing the time-series of a representative measured pressure dataset, shown in Figure 3.3. Before introducing the rest of test pipes and measurement setups, let us consider Pipe 5 measured in the workshop facilities of Perugia University, to help visualize the operation described in §3.2.1. After starting the organ blowing system and triggering the pallet valve opening, one can see the pressure signals corresponding to the pallet-box, the groove, the pipe's foot, the resonator, and the radiated pressure near the mouth (from top to bottom).

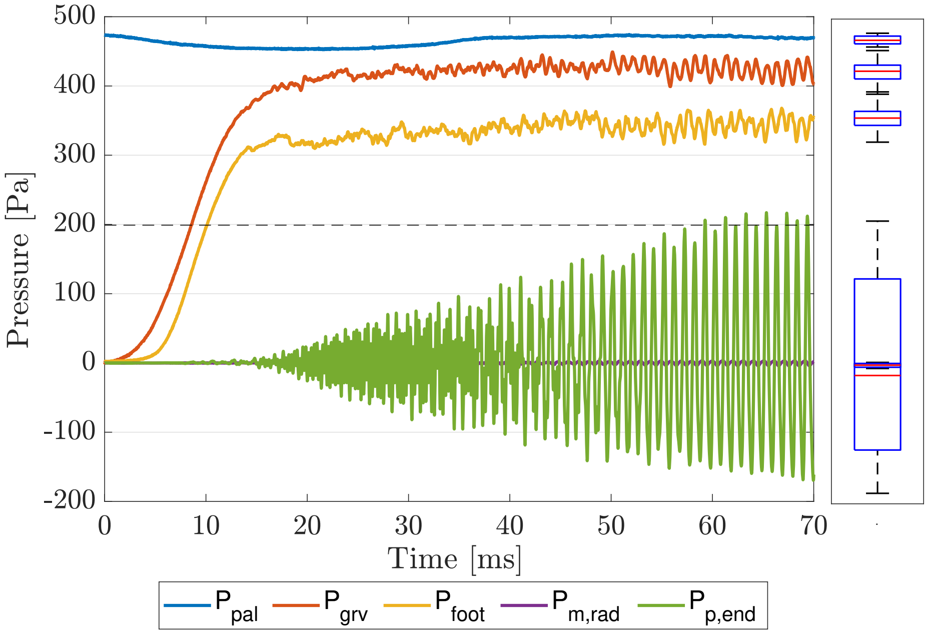

Figure 3.3: Left: overview of measured pressure time-series showing the transient build-up of Pipe 5, with geometry details in Table 3.1. The horizontal dashed line indicates the target pressure amplitude inside the resonator reached in SS. Right: data deviation, over 20 periods in SS.

3.3.1 Supply system: continuous model

Verge *et al.* propose [Verge et al., 1994b] an unsteady Bernoulli potential streamline operating from the inside of an experimental pipe cavity to the outside of the flue channel and an effective channel length. It is further stated that right after the pressure imbalance $p_{\text{foot}} - p_{\text{m}}$ starts, the inertial term $\rho l_{\text{eff}} \partial_t u_{\text{j}}$ initially dominates until the jet gains kinetic energy, $\frac{1}{2}\rho\, u_{\text{j}}^2$. Analogously, the same principle applies throughout the windways upstream in our proposed system.

Here a similarly structured model is proposed, with a streamline progressing from a large reservoir into smaller cavities. In steady-state operation, the flows through the pallet valve q_{pal}, through the foot inlet q_{in}, and the jet flow through the flue exit q_{j} are equal, which is imposed by mass conservation inside these cavities ($\langle q_{\text{res}} \rangle = \langle q_{\text{in}} \rangle = \langle q_{\text{out}} \rangle$).

The underlying assumptions towards feasibility of the model complexity are:

- Time scales considered do not allow for significant heat-exchange
- Adiabatic compressibility regime is considered in the foot
- Flow separation at sharp edges
- Kinetic energy dissipation due to turbulence inside the foot
- The cavities are considered large enough so that the mean flow velocity can be neglected in Bernoulli's equation

The following representation corresponds to modeling (1) a Bernoulli stream-line from the pallet-box to the groove, (2) the continuity in the groove volume, (3) a Bernoulli from the groove to the inlet of the foot, (4) the continuity inside the pipe foot, and (5) the Bernoulli line from the foot to the flue exit:

$$\rho l_{\text{pal}} \frac{d}{dt} u_{\text{pal}} + \frac{1}{2}\rho u_{\text{pal}}^2 = P_{\text{wind}} - p_{\text{grv}} \tag{3.3a}$$

$$\frac{V_{\text{grv}}}{\rho c^2} \frac{d}{dt} p_{\text{grv}} = S_{\text{pal}} u_{\text{pal}} - S_{\text{in}} u_{\text{in}} \tag{3.3b}$$

$$\rho l_{\text{in}} \frac{d}{dt} u_{\text{in}} + \frac{1}{2}\rho u_{\text{in}}^2 = p_{\text{grv}} - p_{\text{f}} \tag{3.3c}$$

$$\frac{V_{\text{f}}}{\rho c^2} \frac{d}{dt} p_{\text{f}} = S_{\text{in}} u_{\text{in}} - S_{\text{j}} u_{\text{j}} \tag{3.3d}$$

$$\rho l_{\text{j}} \frac{d}{dt} u_{\text{j}} + \frac{1}{2}\rho u_{\text{j}}^2 = p_{\text{f}} - p_{\text{m}} \tag{3.3e}$$

exploiting that $p_{\text{pal}}(t) \approx P_{\text{wind}}$ in Equation (3.3a) (see uppermost line in Figure 3.3) and $p' = c_o^2 \rho'$ in the two mass conservation equations (Equations (3.3b) to (3.3d)). Additionally, l_{p} stands for the pallet windway length, and analogously, l_{in} and l_{j} are the effective channel lengths into the pipe foot and out to the jet formation (both of comparable magnitude as the pipe material thickness of tin flue organ pipes). V_{grv} is the groove volume and V_{f} is the pipe's foot volume. Physical parameters c_o and ρ are the sound propagation velocity and the medium density at rest. The variable $u_{\text{pal}}(t)$ expresses the flow velocity through the pallet opening cross-section, from the pallet-box to the groove. Note that in what follows, we may consider solution techniques where the coupling with the pipe's resonator (p_{m}) in Equation (3.3e) will be omitted in some cases.

Although similar analytic solutions are known to the linear and Bernoulli differential equations of the form $\partial_t y = y + Q(t)$ and $\partial_t y = Q(t)y^2 + R(t)$, developing closed-form expressions for implicit solutions for the coupled Bernoulli's in Equation (3.3) is out of the scope of this paper. Throughout the rest of this study, we have prioritized the numerical solution feasibility and model fitting to the expected and measured responses. A simplified foot model discretization is readily examined in [Villegas Curulla and Fabre, 2022]. The non-linear system is time-integrated for one sample rate ($51.2\,\mathrm{kS\,s^{-1}}$). A preliminary comparison is offered for computed pressure versus measured pressure during transients in the laboratory using Pipe 2 and the 4 L reservoir, solving for u_{in}, u_{j}, and p_{foot}.

3.3.2 Pallet-box and initialization of the system

The following description results from modeling the equivalent of having switched on the organ and initialized the pallet-box to a pressure set value $P^{(targ)}_{\mathrm{wind}}$ for p_{pal}, as seen in the topmost of data time-series in Figure 3.3. The windways between cavities couple the downstream sequence: pallet-box, groove, pipe foot, pipe mouth, pipe resonator, and the field surrounding the pipe.

In our system of reservoirs, this can be proposed for the progression from the large pallet-box reservoir (*laye*) to the individual groove (*gravure*), and from the groove to the foot of the pipe. The pallet-box reservoir system is modeled as a Heaviside, followed downstream by smooth functions for the groove and the foot that ramp up from $p_{\mathrm{grv}}(0) = 0$ and $p_{\mathrm{f}}(0) = 0$. As for the pallet-box:

$$p_{\mathrm{pal}} = P^{(targ)}_{\mathrm{wind}}\, H(t) \tag{3.4}$$

with $P^{(targ)}_{\mathrm{wind}} \in \mathbb{R}^{+}$. The target pressures for the groove and foot are defined in SS as the mean value over a window of twenty periods. With respect to the groove and the foot functions (second and third signals from top in Figure 3.3), consider a test solution of the form of a generalized logistic function[1] ramp such that $p_{\mathrm{grv}}(t)$ and $p_{\mathrm{foot}}(t)$ are continuous and differentiable for $t \in \mathbb{R}$:

$$p_{\mathrm{i}}(t) = P^{(targ)}_{\mathrm{i}} \frac{1}{(1 + e^{-\beta(t-t_o)})^{1/\nu}} \tag{3.5}$$

where P_{i} and p_{i} take the values $i = \{\text{groove, foot}\}$. The last term on the right-hand side can be approximated by exponential expansions of `tanh`$(\cdot)$, continuous and differentiable at t_o. t_o is a delay, corresponding to the foot's half fill-up time for the case $\nu = 1$. The steepness parameters β (with units of $\mathrm{s^{-1}}$) and ν can be fitted to measurement data in the groove and foot volume during the transient's pressure rise-time (PRT). At time $t_{\max} = (\beta t_o - ln(\nu))/\beta$, the maximum growth rate is found, and its value follows by substituting into

---

[1] See [Zhang et al., 2022] on trend extraction using logistic functions.

$$\begin{aligned}\frac{d}{dt}p_{\mathrm{i}} &= \left[\frac{\beta e^{-\beta(t-t_o)}}{\nu}\right]\frac{P_{\mathrm{i}}^{(targ)}}{(1+e^{-\beta(t-t_o)})^{(1+1/\nu)}}\\ &= \frac{\beta e^{-\beta(t-t_o)}}{\nu}p_{\mathrm{i}}\end{aligned}\tag{3.6}$$

where $P^{(targ)}\beta$ has units of $[\mathrm{Pa\,s^{-1}}]$ and the rest of the parameters are dimensionless. We show in Figure 3.3, and later in §3.4.3, that the role of ν distinguishes the beginning of transients between the rise of p_{grv} and p_{foot} with an initial quadratic difference in slopes. For $[0 < \nu < 1]$, the maximum growth is found near the initial value, and it occurs before the half-rise time (see p_{foot} in Figure 3.3).

3.3.3 Analysis towards a non-dimensional model

To predict the time evolution of the foot pressure p_{f} given a target pressure $P_{\mathrm{wind}}^{(targ)}$, as explained in §3.3, the geometry of the pipe within a rank is assumed known. All pipes within the same rank will have the same foot height L_{f}, which is imposed by the *faux-sommier* propping up all the pipes, holding them below the mouth. Provided the different pipe dimensions within a rank (with different fundamental signing frequency f_1 and foot volumes) and given the five different test pipes used in measurements, a non-dimensional time using the resonator's oscillation period is employed throughout the rest of this paper for comparability unless stated otherwise: $\hat{t} = tf_1$ and $\hat{\tau} = \tau_{10\rightarrow 90}f_1$, where $\tau_{10\rightarrow 90}$ expresses the rise times in p_{grv} and p_{f}. The PRT is calculated using the times when the growth first attains 10% and 90% of the target pressure. The target pressure is evaluated as the average pressure in SS over a span of 20 periods. The workflow of steps in the model is shown in Algorithm 1.

Algorithm 1: Routine for p_{grv} and p_{foot} prediction

```
Input: Pipe length, rank foot height, target pressure
Output: Init function
begin
    Input $(L_{\mathrm{p}}, L_{\mathrm{f}}, P_{\mathrm{i}}^{targ})$
    $f_1$ ← Compute bore's acoustic
            frequency: $c_{\mathrm{o}}/2(L_{\mathrm{p}} + \Delta l)$
    Reference-transform $f_1$ :
            $log_{10}(D_{\mathrm{p}})$ versus $12\,log_2(f_1/f_{\mathrm{ref}})$
    $D_{\mathrm{p}}$ ← Apply scaling rule to transformed $f_1$
    $V_{\mathrm{f}}$ ← Volume of foot with $D_{\mathrm{p}}$ and $L_{\mathrm{f}}$
    $\partial_t p_{\mathrm{i}}$ ← Bernoulli and continuity equations
    $\beta_i$ ← $p_{\mathrm{i}} = \psi(\ L_{\mathrm{p}},\ L_{\mathrm{f}},\ P_{\mathrm{i}}^{targ},\ p_{\mathrm{grv}}(0),\ p_{\mathrm{f}}(0)\ )$
    $p_{\mathrm{i}}(t) = P_{\mathrm{i}}^{(targ)}/(1 + e^{-\beta_i(t-t_{o,i})})^{1/\nu_i}$
end
```

A given foot height L_{f} is known and constant across the rank, frequently also across the entire pallet-box. With that parameter fixed, the foot volume depends on

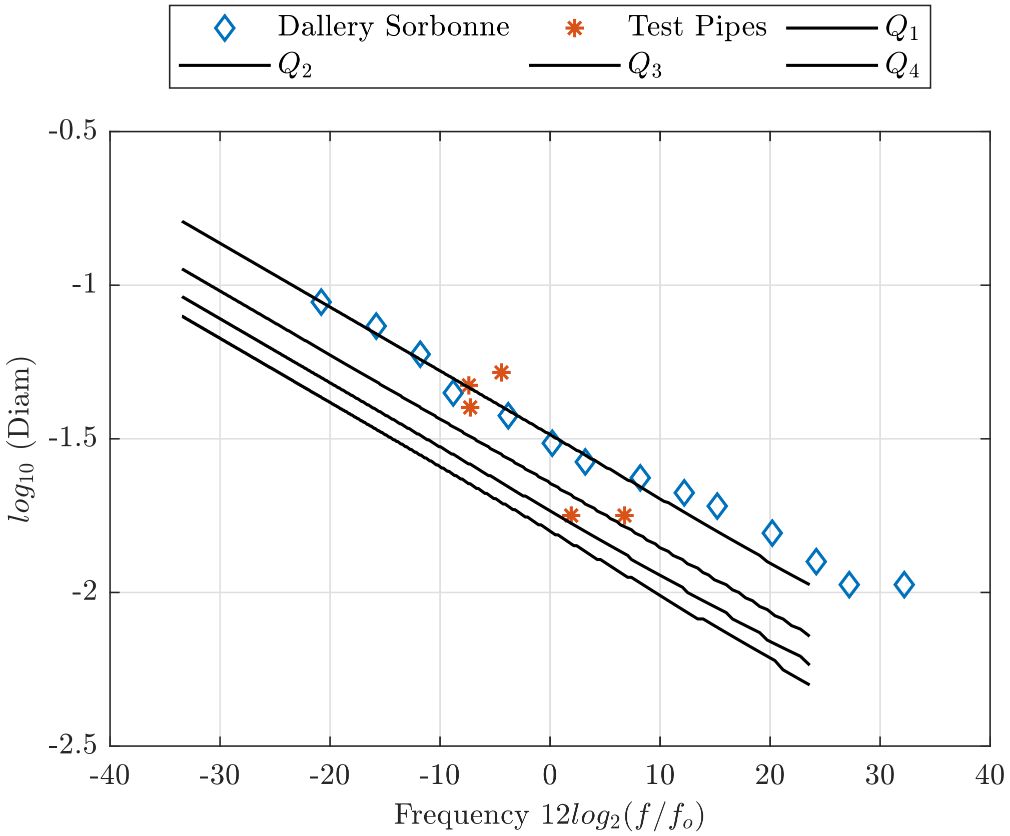

Figure 3.4: Pipe diameter (D) scaling rules as a function of the resonator's singing pitch (ref A_{440}, $f_o = 440\,\text{Hz}$) and the stop typology to which they belong. Measured diameters from Prestant 4' from Dallery organ in Chapelle Sorbonne (♦), test Pipes 1-5 (★), $Q_{\text{n,max}}$ models for $n = \{2, 3, 4\}$ (- ● -, - - -, and ——, respectively).

the diameter $2R_\text{p}$ of the pipe, matched by the foot's largest section. In a rank, the pipe sounding at 440 Hz can be taken as the reference frequency f_o. For example, follow the $Q_{n,max}$ scaling rule analysis by Blanc *et al.* [Blanc et al., 2010] to find that for an $f_1 = 16 f_o$ (48 semitones, 4 octaves), a shift in diameter of $D_\text{p} \longrightarrow D_\text{p}/10$ is seen. Another readily available rule for scaling can be found in Fletcher [Fletcher, 1977]. One strategy relies on solving $\partial Q_n / \partial R_\text{p} = 0$ for the n^{th}-mode quality-factor, and the other on a semi-empirical $D = D_0(f_o/f_1)^x$ manufacturing historical principle.[2]

In Figure 3.4, one finds examples of the scaling of bore diameters as a function of where in the tessitura the oscillating frequency of each pipe is. This is shown for computed models of the n^{th} quality-factor maximization, for the five test pipes used in the current work, and for the measured diameter of the remains of the Prestant 4' in the Chapelle Sorbonne organ (see [Dubois and Lueders, 2002]). Wider diameter

---

[2] A diagram-based principle for contemporary variations of scaling rules is found in the book on organ building by Dom Bédos de Celles [Bédos De Celles, 1766].

scalings such those of Pipes 1-3 used in these measurements are better fitted by values comprised between the optimization of the modal quality-factors $n = \{2-4\}$. Conversely, the narrower diameter scalings of Pipes 4-5 fit better the optimization of higher mode quality-factors. The rule of thumb is that narrow compasses, with smaller cut-up distances (W_m), have further harmonic development than larger pipes in the tessitura.

The following set of initial conditions can be posed for Equation (3.3). With regard to the pallet-box, the past of the time series of the Heaviside $H(t < 0)$ is not relevant as long as the pallet-box had been initialized before any key was pressed.

$$\begin{aligned} p_\mathrm{pal}(0) &\approx P_o^{(targ)} \\ p_\mathrm{grv}(0) &= 0,\ \partial_t p_\mathrm{grv}(0) = 0 \\ p_\mathrm{f}(0) &= 0,\ \partial_t p_\mathrm{f}(0) = 0 \\ p_\mathrm{m}(0) &= 0 \end{aligned} \tag{3.7}$$

For the sake of verification, we temporarily neglect the downstream coupling with the oscillations in the resonator, ${p'}_\mathrm{m} = 0$, when solving Equation (3.3) for p_grv and p_f (see the first 15 ms of p_p in Figure 3.3). Consider the state of the jet as a representation of the oscillating operation, which is informed by the reduced jet velocity (RJV) $\theta = u_\mathrm{j}/W_\mathrm{m} f_1$, following [Chaigne and Kergomard, 2016]. Equations (3.3d) to (3.3e) provide the link between the PRT steepness and the jet velocity steepness. As per Algorithm 1, the model can predict this quantity in terms of the geometry. As a first approximation, the state of the jet is proportional to the pressure series in the foot. Without loss of generality, both the groove and the foot volumes may factor in the rise-time steepness, whose causality can be tracked backward:

$$u_\mathrm{j} \propto \sqrt{p_\mathrm{f}} \propto \sqrt{p_\mathrm{grv}} \tag{3.8}$$

Let us consider the individual groove volumes of constant size across the tessitura (supported by visual inspection of the center-to-center pipe foot spacing, see Figure 3.7). In the frame of the pipe dimensions presented in Figure 3.4, we use a reference 4' rank of medium-sized diameter scaling with $L_\mathrm{p} = 1.29\,\mathrm{m}$ giving the lowest frequency of 132 Hz, and an upper frequency of 1976 Hz.

For a fixed foot height across the rank pipes, the high-pitched pipes see a very narrow foot, where one may expect a short fill-up time. For lower compasses, differences in V_f produce substantial changes in the foot's PRT. In comparison, the oscillating frequency of the resonator changes less significantly compared to higher compasses.

The crucial element under analysis is which cavity or set of cavities upstream from the flue exit limits the pressure rise. More specifically, we want to establish whether this is imposed by (1) the largest volume in the system, (2) the individual ratios of cavity volumes ($V_\mathrm{grv}/V_\mathrm{pal}$, $V_\mathrm{foot}/V_\mathrm{grv}$), or (3) the ratio between the sum of upstream volumes and the largest volume in the system. In the last case, we further question whether a cutoff point can be proposed within a given compass and pallet-

Table 3.1: Geometry parameters of the test pipes and pallet-box. Units are expressed in mm unless stated otherwise. L_p and R_p are the length and radius of the pipe's resonator, respectively. Concerning the foot, L_f is its length, and $R_\mathrm{f,in}$ the radius of its inlet. H_m and W_m refer to the mouth's depth and cut-up distance flue-to-labium, while h is the flue-way thickness. The oscillation frequency f_1 for Pipe 3[‡] is reported for both the experimental reservoir and the Pinchi organ. Values $h^\dagger$ are estimated during SS operation.

	L_p	R_p	L_f	$R_\mathrm{f,in}$	H_m	W_m	$h^\dagger$	W_m/h	f_1	V_f
Pipe 1	507	23.6	179	1.9	36.6	9.8	0.68	14.4	284.7 Hz	0.150 L
Pipe 2	415	26	144	3.4	39	9.5	0.56	16.9	324 Hz	0.120 L
Pipe 3	530	20	176	3	33.5	8.9	0.64	13.9	284.3/294 Hz[‡]	0.084 L
Pipe 4	234	8.9	205	1.6	11.7	4.2	0.55	7.6	643 Hz	0.020 L
Pipe 5	318	8.9	189	2.2	15.7	4.2	0.39	8.9	486 Hz	0.021 L

Laboratory	4 L experimental reservoir
Church	Pallet-box: 0.5 m^3, Grooves: ∼7.5 L per individual groove
Workshop	Pallet-box: 0.052 m^3, Grooves: ∼0.5 L per individual groove

box-groove volumes, where the contribution of the foot volume may be negligible in the higher compasses with respect to the pallet-box-groove. The consequence of this would establish how many of the coupled equations in Equation (3.3) factor the most in explaining the behavior of the p_f PRT.

3.4 Measurements

Measurements were carried out in an experimental laboratory reservoir and two real organs by the same Italian organ builder. The action of both Pinchi organs entails electric blowing systems, hand operation at the keyboard level, direct mechanical action to the pallet valves, and changing time intervals between note-on and note-off. In the laboratory, the flow activation was controlled by means of an electric valve. This case lacks the realism of an instrument made by an organ maker and the keyboard traction while playing. On the other hand, it yields repeatable results that serve as a reference case.

Two scenarios were considered. First, measurements were carried out in purely experimental conditions in the laboratory using Pipes 1-3, from different ranks, with foot volumes 0.150 L, 0.120 L, and 0.084 L. They are comparable in resonator's length and diameter. Their fundamental oscillation frequencies fall within the range 284 Hz to 330 Hz. The groove volume remains the same, as well as the initialization system. A readily intuitive result is that the biggest the foot volume, the longer the fill-up time.

Second, Pipes 3-5 were used to measure in two real organs. In a first time, we used the groove volume in the workshop and church organs (∼0.5 L per pipe and 7.5 L, respectively). The non-dimensionalizing of the measured pressure was expected to show different slopes not only because of the different rise times, but also because the factor f_1 was different for each of them. Lastly, Pipe 3 was used in a less invasive setup in the church organ pallet-box, with a different number of stops engaged. This results in a constant groove volume common to all open registers, but the foot volume becomes a summation of N pipes operating under the same key-down for a single *note*.

3.4.1 Setup of the laboratory measurements

For the experimental reservoir, a hermetic 4 L metallic cavity was built. Orifices were made for the supply inlet, the sensors, and the outlet to the pipes on the top (see Figure 3.5a). Organ pipes are placed vertically on the top plate in a similar fashion as they are placed on the windchest in real organs. The initialization is triggered by a solenoid valve (Bürkert, Type 0406), acting as the pallet-box pallet. A compressor (Atlas-Copco, LFx) provides 0.5 bar of air separated by 5.8 m of plastic tubing with a diameter of 13 mm upstream from the valve, and 30 cm of 3.5 mm diameter tube connects the valve with the experimental reservoir.

The 5 test pipes were a selection from a stock of 18 flue pipes available in the laboratory, showing the following ranges for resonator length, diameter, and foot length: $L_\mathrm{p} \in (120, 735\,\mathrm{mm})$, $R_\mathrm{p} \in (7, 25\,\mathrm{mm})$, and $L_\mathrm{f} \in (145, 225\,\mathrm{mm})$. They were selected with preference to best represent a variety of foot volumes, while also anticipating that these pipes needed to be perforated for measurements to be carried out.

In the first set of measurements, Pipes 1-3 are used (see Figure 3.5b and Table 3.1), comparable in compass, with similar f_1 frequency, and different foot volumes. They are driven by the system shown in Figure 3.5a. For comparability with the Pinchi organs, the driving pressure is set to match the $\sim$500 Pa in SS.

The locations for acquisition are kept comparable with those in the real organs: pressure history in the pipe foot and its upstream reservoir, the pipe interior, and the radiated field in front of the mouth at a distance of one bore diameter.

3.4.2 Setup of the measurements in Pinchi organs

Access to relevant locations of the acquisition chain was possible in two Pinchi instruments: one in the workshop and the other in Sant'Antonio da Padova church in Perugia (Italy). The single-rank organ featuring an *Ottava 4'* stop spanning 61 notes was moved to the workshop facilities of the University of Perugia in 2020. It is provided with the same windchest commonly installed in Pinchi pipe organs.

The church organ is a Pinchi Op. 375, dating from 1987, consisting of 30 stops, 5 m long, 1.75 m deep, and 3.4 m height. It has two keyboards (*Grand'Organo* and *Positivo*) of 58 keys each and a 30 keys pedal-board. Attention is brought to the fact that the dimension of real-sized instruments does not make the logistics of data acquisition an easy task. In addition, reservoirs are, by definition, closed cavities only designed for the in and out flow of air. Gaining access to synchronous pressure measurements everywhere in the system entails that our probes are both inside and outside simultaneously, a delicate and intrusive scenario for which few organs are prepared. In this experiment, Pipes 3-5 are used (see Figure 3.5b and Table 3.1), thus having Pipe 3 in common with laboratory and real instrument measurements. The

(a) Setup of the experimental reservoir, measuring Pipe 2.

(b) Test Pipes 1-5.

Figure 3.5: Measurement setup in the laboratory and sample test pipes 1-5.

(a) Pressure transducer in the interior of the workshop organ pallet-box.

(b) Pallet valve in the workshop wind-chest.

Figure 3.6: Close-up views of the interior of the measurement setup in the workshop.

Figure 3.7: Measurement setup overview in the workshop organ as seen from the back. The keyboard is at the other side.

windway cross-section of the two Pinchi windchests is a rectangular area of 20 cm × 1.5 cm. In this study, we do not account for the delay between key transmission and the pallet opening [Woolley and Campbell, 2017].

Pressure acquisitions were made in the following positions:

- Pallet-box: p_{pal}
- Groove, after the pallet and before the pipe foot: p_{grv}
- Pipe foot: p_{foot}
- Inside the mouth: $p_{\mathrm{m,in}}$ ($\propto$ $p_{\mathrm{p,end}}$)
- Radiated pressure from the mouth, frontwards and perpendicular, 55 mm away or one bore diameter: $p_{\mathrm{m,rad}}$
- Inside the resonator at the passive end: $p_{\mathrm{p,end}}$

Pressure transducers (Endevco, class 8507 C-1 and C-2) of 2 mm diameter were flush-mounted in certain pipe positions where the flow could have been perturbated with larger probes, and in narrow orifices in the reservoirs of the real organs. The other locations used acoustic pressure probes (Brüel & Kjaer, types 4938 and 4939). A reference pressure transducer (Keller, PR-41 series) was used to calibrate the other sensors. The acquisitions were made using two National Instruments 9234 cards at a sample rate of $51.2\,\mathrm{kS\,s^{-1}}$.

Data processing included segmentation and event extraction for the following regions: note-off, transients, and steady-state operation. Zero-phase filtering with 2^{nd}- and 4^{th}-order Butterworth's was used to eliminate undesired low-frequency components below $f_{\mathrm{c}} = 50\,\mathrm{Hz}$. An overview of the setup is shown in Figure 3.7, and Table 3.1 summarises the geometry of the test pipes studied. L_{p} and R_{p} express the length and radius of the pipe's resonator, while the length of the foot L_{f} helps estimate its volume. The radius of foot inlet $R_{\mathrm{f,in}}$, H_{m}, and h (depth and height of the flue exit at the end of the channel) provide the inlet and outlet cross-sections S_{in} and S_{j}. $S_{\mathrm{m}} = H_{\mathrm{m}}W_{\mathrm{m}}$ is the mouth section area.

3.4.3 Results

Ernoult *et al.* [Ernoult et al., 2016, Ernoult and Fabre, 2017a] propose the examination of the Fourier coefficients of each modal amplitude in attack transients of recorder-like instruments and relate them to the blowing conditions and jet velocity. We follow the same strategy to compare in Figures 3.9a to 3.9f the coefficients for the first three modal amplitudes over time for the transients of the Pipes 1-3 and 3-5.

Concerning attack transient characteristics and timbre, noticeable events measured comprised: slow versus steep reduced jet velocity rises (RJV, noted as θ), overall fundamental mode dominance versus second and third mode dominance, or overshoots that retract during SS, and multiple-staged overshoots. The modal amplitudes for the first three modes are noted a_1, a_2, and a_3. Common to all cases is that the fundamental mode dominates at least during the first few ms ($a_2/a_1 < 1$ and $a_2/a_1 < 1$ immediately after triggering of the pipe). Third, as exposed in §3.3.3, the higher harmonic development for narrower compasses is consistent with short cut-up heights (W_{m}).

Analysis of measured data from both Pinchi organs not only reveals variations in the steepness and the modal order (notice the distinct double slope in Figure 3.10c and the Fourier coefficient ratios for the first three modes in Figures 3.9a to 3.9f), but also stands in line with the notion introduced in §3.3.3: the transient rise depends on the ratio of foot volumes to groove volume. In the case discussed for the laboratory experimental reservoir, the system consisted only of one groove and one pipe foot. In Figure 3.10, one can see the limiting case of five stop registers pulled out. There, the ratio becomes $\sum_k V_{\mathrm{f,k}}/V_{\mathrm{grv}}$, where $V_{\mathrm{f,k}}$ is the foot volume of the k^{th} pipe.

After the work by Nolle and Finch [Finch and Nolle, 1986, Nolle and Finch, 1992], one would expect the supply system to respond dif-

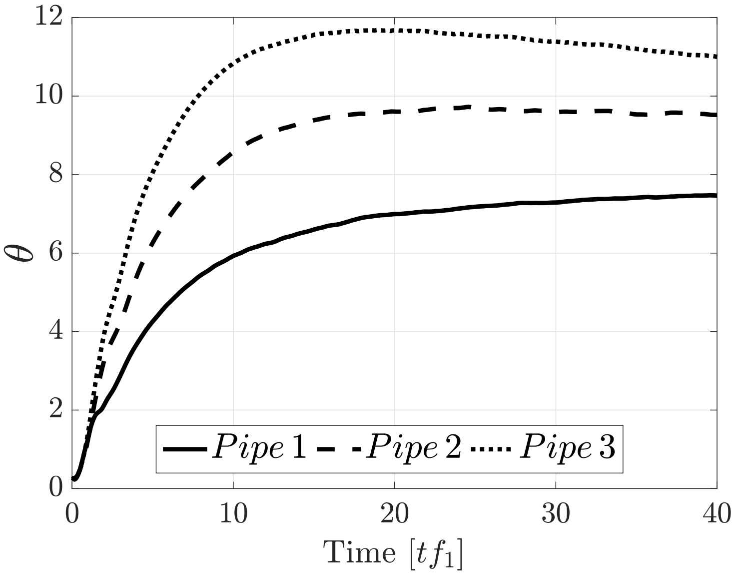

(a)

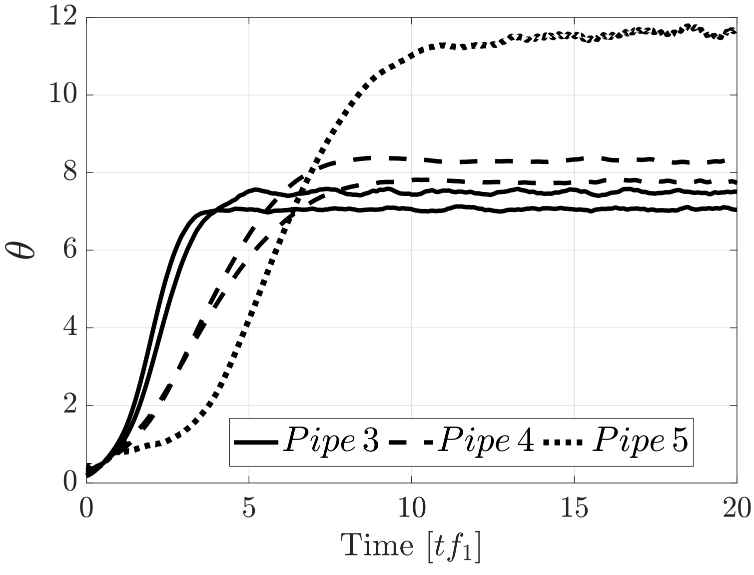

(b)

Figure 3.8: Reduced jet velocity $\theta = u_\mathrm{j}/W_\mathrm{m} f_1$ over non-dimensional time $t\,f_1$ (multiple measurements). (a) Pipes 1-3 (having foot volumes 0.150 L, 0.120 L, and 0.084 L, respectively) in the laboratory experimental reservoir driven by a fast-opening valve and reaching ∼500 Pa in SS. (b) Pipes 3-4 measured in the church organ and Pipe 5 in the workshop organ (having foot volumes 0.084 L, 0.020 L, and 0.021 L, respectively).

ferently to a changing air demand at the groove and pipe level. However, electric blowing systems have evolved since those earlier studies.

Figures 3.10a to 3.10c show that the influence of the number of registers pulled is noticeable at the groove level and the pipe foot. According to Nolle and Finch's [Finch and Nolle, 1986, Nolle and Finch, 1992], an intuitive expectation would reduce to the smaller the demand of air for p_{grv}, the smaller the pressure drop that the blowing system has to compensate for, thus satisfying a steeper ascent to the groove SS pressure.

3.4.4 Steady-state results in real organs

As per the operation illustrated in Figure 3.3, data consistency is found for the coupling upstream and downstream of the groove and foot. Zoom detail on the pallet-box reservoir, groove, and foot pressure time-series (see Figure 3.11) highlight the time-scale periods due to the blower and to the resonator. Low-amplitude high-frequency components (~500 Hz, f_1) from the resonator appear in the pallet-box, where the blower's power mitigates the upstream coupling and contributes the 13 Hz to 17 Hz (10 Pa to 20 Pa amplitude) component, appearing in the pipe foot. The latter preexists before engaging the pipe oscillation, which leads one to believe that the source for this is the sum of the blower and the regulating system (a mechanical looped control system found at the bottom of Figure 3.7). Additionally, within slight oscillation, the target pressure values found in the pallet-box and grooves match the expected values in the range of 50 mm to 120 mm H_2O [Rochas, 1997] —with 1 mm H_2O ~9.8 Pa).

Let us now consider Coltman's mouth sound radiation analysis for the organ pipe [Coltman, 1969], where the pipe's passive end and mouth flows are equivalent ($q_{\mathrm{p,end}} = q_{\mathrm{m}}$). With this in mind, and knowing that the mouth area is $S_{\mathrm{m}} = H_{\mathrm{m}}W_{\mathrm{m}}$, we can establish the flow strength of the monopole outside the labium, whose characteristic radiation can be compared with the measured radiated pressure near the mouth (at ~55 mm, one bore diameter).

After triggering p_{grv}, it took 60 ms for the pipe pressure at the passive end of Pipe 5 ($p_{\mathrm{p,end}}$) to reach its SS target level for the first time, of which 36 ms were needed to rise from 10% to 90% of said value. In addition to the relation between p_{p} and p_{m} suggested by Coltman, the following bounds were checked during transient and the SS operation:

$$\|p_{\mathrm{pal}}(t)\| > \|p_{\mathrm{grv}}(t)\| \tag{3.9}$$

$$\|p_{\mathrm{grv}}(t)\| > \|p_{\mathrm{f}}(t)\| \tag{3.10}$$

$$\|p_{\mathrm{f}}(t)\| > \|p_{\mathrm{p,end}}(t)\| \tag{3.11}$$

By means of sample correlation, a consistent delay is found between $p_{\mathrm{m,in}}$, $p_{\mathrm{p,end}}$, and $p_{\mathrm{m,rad}}$ which accounts for the distance between transducer capsules. Equations (3.9) to (3.11) are found valid as soon as the transient starts (for strictly $t > 0$).

The modal pressure amplitudes ([Verge et al., 1997a]) are estimated from the pressure measured at the passive end, $P_{\mathrm{n}} = |p_{\mathrm{n}}(x = L_{\mathrm{p}})/sin(k_{\mathrm{n}}0.6R_{\mathrm{m}})|$, which leads to the flow of the nth mode:

$$q_{\mathrm{n,p,end}} = S_{\mathrm{p}}\, v_{\mathrm{n}} = \frac{\pi R_{\mathrm{m}}^2}{\rho c} \frac{|p_{\mathrm{n,p,end}}(0)|}{sin\, k_{\mathrm{n}}\, 0.6\, R_{\mathrm{m}}} \tag{3.12}$$

and the radiated pressure by the outside monopole near the labium, neglecting the contribution of the open end

$$p_{\mathrm{n,\{m,rad\}}}(r') = \frac{\rho}{S_{\mathrm{m}}} j\omega q_{\mathrm{n}} \frac{e^{-jk_{\mathrm{n}}r'}}{4\pi r'} \tag{3.13}$$

and matching phase and magnitude of the measured pressure in the vicinity of the mouth (r' is the source-receiver distance). Using the fact that in steady-state, the flow from the large reservoir through the pallet has to be the same as that through the foot inlet and the outlet into the mouth ($q_{\mathrm{res}} = q_{\mathrm{in}} = q_{\mathrm{out}}$), an estimated correction is found for the flue exit h. These dimensions of the cross-section out from the foot $S_{\mathrm{j}} = h\, H_{\mathrm{m}}$ where the jet originates are possible but poor for precision below 1 mm.

We find, for Pipe 3 in the laboratory and Pipe 5 in the workshop, that the first regime of oscillation is practically skipped given the values of RJV attained during the PRT. With a $\theta_{1\to 2} \in [12, 16]$ it can be assumed that the state of the jet may have reached the second regime. The difference between Pipe 3 and 5 is that during the transition to SS, the Fourier coefficient ratios return to unity in about 200 ms and θ also descends monotonically, while Pipe 5 shows in 80 ms in Figure 3.9f the regime that remains for the rest of the measurement. Further examination of the state of the flow for acquisitions in Pipe 5 reveals that Reynolds numbers at the pipe foot entrance and its outlet during SS were no larger than 3300 and ∼900, respectively, and the largest Mach number found is $M < 0.07$.

Visual inspection reveals that the resonator's fundamental oscillation is found upstream in p_{pal}. Two frequency components are noticeable: the blowing system presents ∼15 Hz oscillations around the set-value P_{wind} and f_2 and f_1 downstream from the resonator's oscillation (from Pipes 1 and 2, respectively). The phase shift between groove and foot signals is also apparent. The statistical distribution of data displayed in Figure 3.3 shows a span of 13 ms. No significant changes are found if the sample space is constricted to a shorter periodicity, such as that of the resonator ($T_1 = 1$ ms).

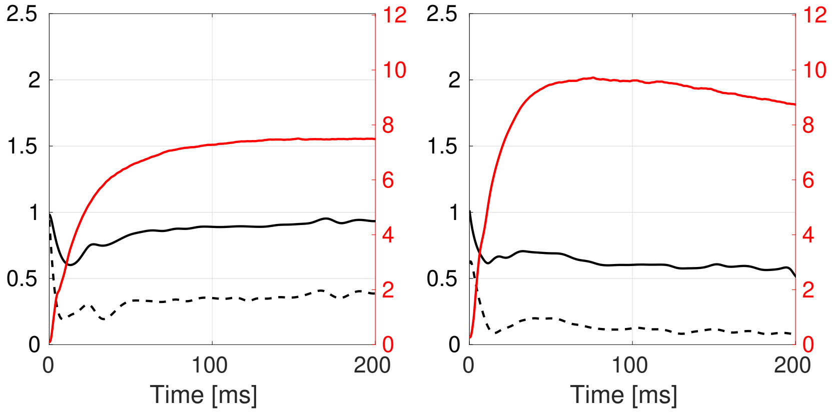

(a) Pipe 1 **(b)** Pipe 2

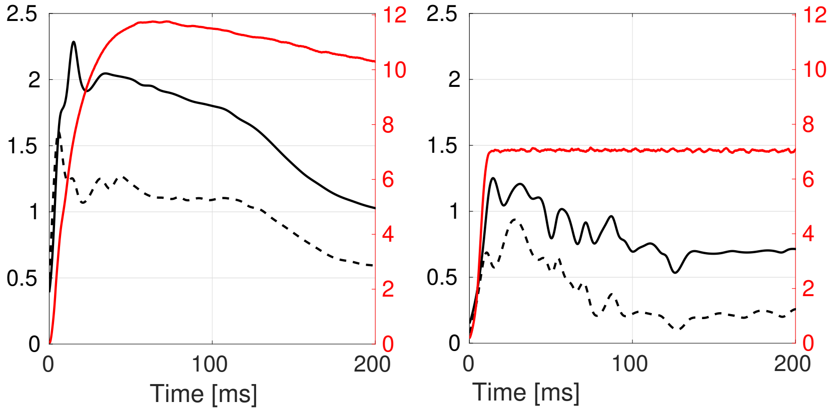

(c) Pipe 3 **(d)** Pipe 3

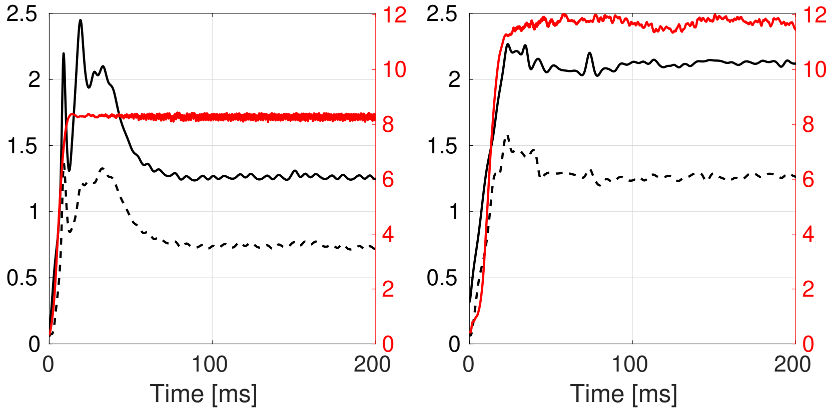

(e) Pipe 4 **(f)** Pipe 5

Figure 3.9: Ratio of second and third mode Fourier coefficients of the pipe's resonator internal pressure over the fundamental during the transient (a_2/a_1 —, a_3/a_1 - - -, LHS numerical axes), overlaid with the reduced jet velocity (θ —, RHS numerical axes). (a)-(c) Pipes 1-3 were measured in the experimental laboratory reservoir. (d)-(e) Pipes 3-4 were measured in the church organ. (f) Pipe 5 was measured in the workshop organ.

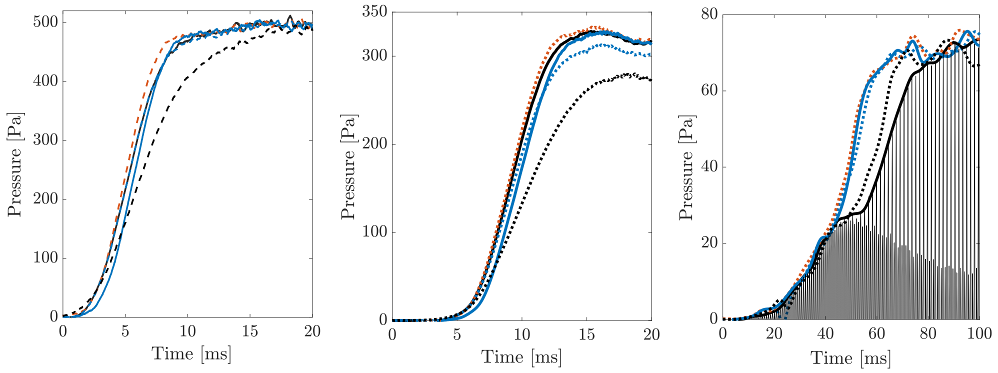

Figure 3.10: Measured pressure evolution as a function of increasing stops engaged. From left to right: p_{grv}, p_{f}, and p_{p}). The great organ windchest of the church organ in Sant'Antonio da Padova, using Pipe 4. Only Principale 8' (—), adding Ottava 4' (····), adding Decimaquinta 2' (—), adding Decimanona 1 1/3' (····), adding Vigesimaseconda 1' (····). From top to bottom: pressure at the groove, foot and pipe. Envelopes of the total acoustic pressure in the pipe. Envelopes are computed with an averaging window of length T_{s}. For the Principal 8' stop alone, the full signal in the pipe is also shown.

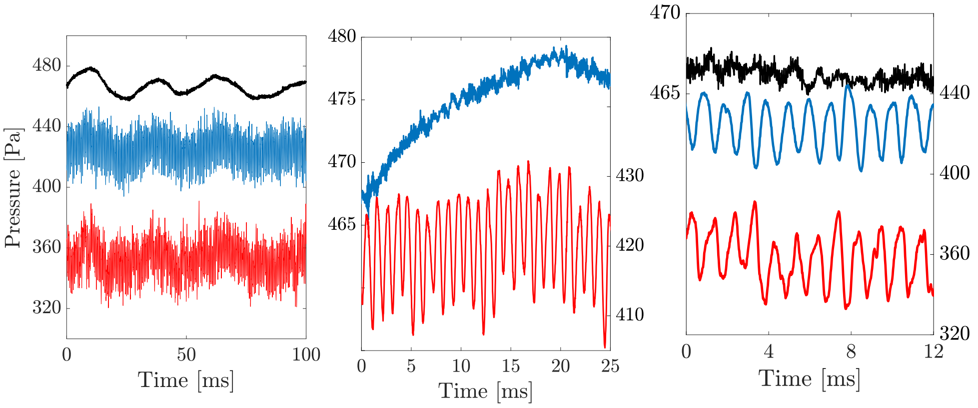

(a) **(b)** **(c)**

Figure 3.11: Measured pressure for p_{pal} (—), p_{grv} (—), and p_{f} (—) during steady-state segments with test pipe 5 in the workshop organ. (a) SS during 100 ms. (b) 12-period zoom segment from (a), where data for p_{pal} has been offset for visualization, and its axis appears at the top LHS.

3.5 Discussion

Table 3.2: Fitted results of logistic function initialization for the Pipes 1-5 in all the setups above, their resulting non-dimensional rise-time steepness $\beta_{\mathrm{p,f}}\, T_1$, and the ratios of foot volume to groove. $\beta_{\mathrm{p,f}}$ is the maximum slope of dp_{foot}/dt during the transient (without Pa units), and T_1 is the fundamental oscillating period in the resonator.

Pipe	$P_{\mathrm{foot}}^{(targ)}$ [Pa]	$\beta_{\mathrm{p,foot}}$ [s^{-1}]	$\nu_{\mathrm{p,f}}$	$\beta_{\mathrm{p,f}}\, T_1$	$V_{\mathrm{f}}/V_{\mathrm{grv}} \cdot 10^3$
1	189.2	136.8	0.753	0.4805	37.5
2	268.4	287.9	0.001789	0.8886	30
3	238.7	555.2	0.8999	1.9529	21
3	203.7	883.6	1.098	3.0054	11.2
4	302.1	401	0.9852	0.6236	2.67
5	244.1	244.1	0.004372	0.5023	42

We introduced above the idea that the limiting effect on the foot PRT we want to model may be caused by the largest reservoir's volume, by the 1-to-1 volume ratios, or by the ratio of a cumulative foot volumes sum to larger volumes upstream. When solving for the air supply equations, these yield different relations between rates of change inside the cavities, $V_{\mathrm{grv}}\, dp_{\mathrm{grv}}/dt$ to $V_{\mathrm{f}}\, dp_{\mathrm{f}}/dt$, and finally evidence different degrees of strong-weak coupling. That hypothesis was verified in the last stage of our measurements (see Figure 3.10). A single note-down was played in the church Pinchi organ for the following cumulative sequence of ranks: Principale 8', Ottava 4', Decimaquinta 2', Decimanona 1 1/3', and Vigesimaseconda 1'. Each further iteration added one more stop to the same playing *pitch* (except in compound stops, which contain the harmonic series continuation of the lowest sound). The following were fixed constants: pallet-box volume, groove volume, the driving pressure in the pallet-box, and the foot volume of Pipe 4 being measured. The only element changing was $V_{\mathrm{f}} \to V_{\Sigma}$; one then solves for an equivalent volume coupled to the groove. The same target pressure is reached in all cases for p_{grv} and p_{p} of Pipe 4; the changes appear in the transients and with that the evolution of the modal contributions during the attacks.

Solving the physical model in Equation (3.3) for p_{grv} and p_{f} is computationally more intensive than producing fitted models with four parameters per initialization function. Additionally, the fitted model is less challenging to control than the physical model. The trade-off when using the fitted model versus the physical model is that the former does not directly shape the modal behavior. Errors for the two solutions proposed are shown in Figure 3.13 for the groove and foot PRT. One distinct feature appears in the half-rise time before the maximum growth rate: integrating the physical model leads consistently to an overestimation of the beginning of the transient. Conversely, the use of the non-linear parameter ν in the fitted logistic function better implements the sharp change of slope near the lower asymptote ($p_{\mathrm{i}} = 0$).

Figures 3.9a to 3.9f show a consistent monotonic modal growth with an over-

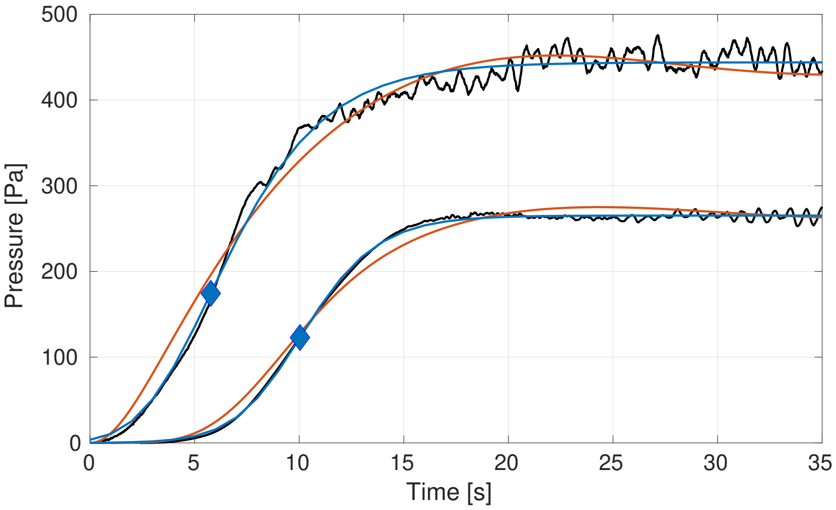

Figure 3.12: Measured pressure transient overlaid with time-stepping numerical solution of Equation (3.3) and the fitted model for p_{grv} and p_{f}. Markers indicate the maximum growth rate. Measured pressure (—), physical model (—), fitted model (—).

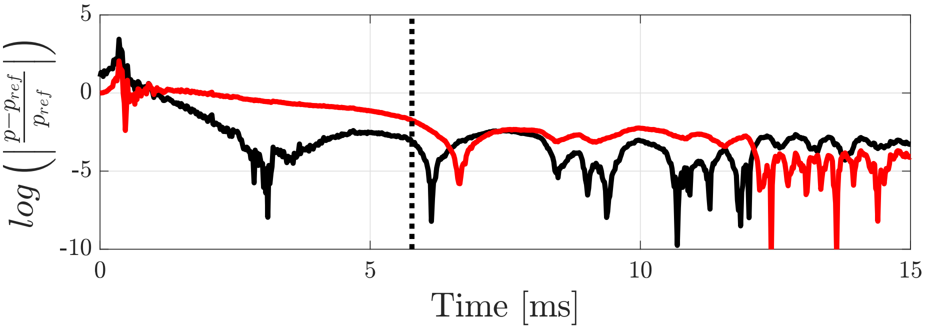

(a) Simulaton errors for p_{grv}

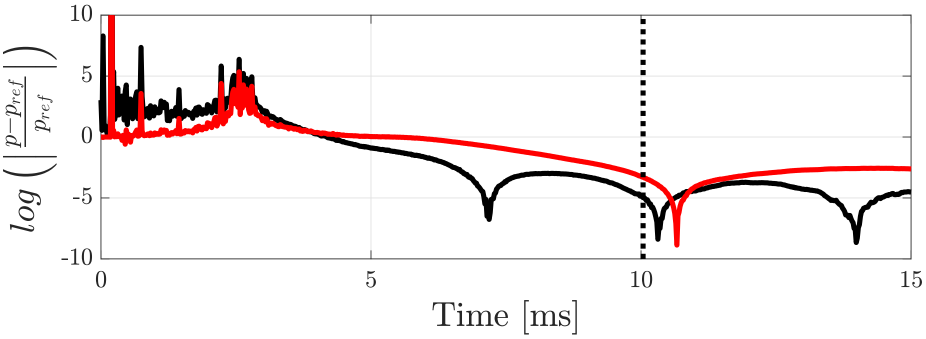

(b) Simulation errors for p_{foot}

Figure 3.13: Normalized errors with respect to measured data from Pipe 4 in the church organ. Numerical integration of Equation (3.3) (—). Fitted model as per Equation (3.5) (—). The dotted vertical line indicates the location of $max(dp_{\mathrm{i}}/dt)$, Equation (3.6).

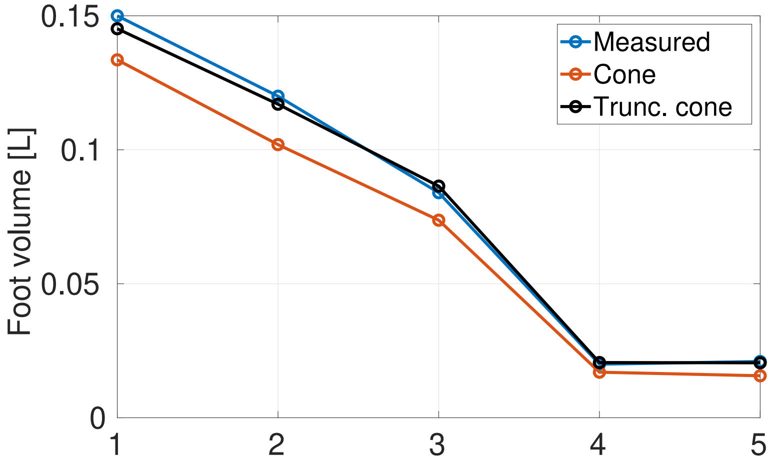

Figure 3.14: Foot volume estimation versus measured values for sample test Pipes 1-5.

shoot of the second modal pressure over the fundamental in most cases, which during the transition periods at the end of the attack, fall below the fundamental unless over-blowing conditions are present. Aside from the blowing condition, the higher harmonic development in the pipes of shorter cut-up distance is consistent with the modal amplitudes found. Notwithstanding that data is not shown in dimensionless time, it appears to be counter-intuitive that in the actual organ (with less control), the pressure rise in the groove happens more steeply than in the small, experimentally controlled 4 L reservoir without a pallet valve. Instead, the solenoid valve is placed 30 cm upstream. This result is also visible by comparing Pipe 3 in both systems: Figures 3.8a to 3.8b.

Physical differences are apparent, firstly, from the fact that upstream from the groove, the experimental reservoir is preceded by a significant length of tubing. At the same time, the real organ presents a large volume with even dimensioning of width, depth, and height, less prone to friction losses in the vicinity of walls (as opposed to the 5.8 m of narrow tubing between the valve and the compressor). Secondly, even when the numerical estimation of the pallet cross-section $S_{\mathrm{pal}} = S_{\mathrm{pal}}(t)$ had led to unrealistically small values both with quasi-steady Bernoulli time windows between measured data of p_{pal} and p_{grv} or by numerically solving Equation (3.3), the area of the pallet windway (62 mm equivalent diameter) in SS is unmistakably larger than its substitute solenoid valve (13 mm diameter). This suggests the use of the effective pallet cross-section term $S_{\mathrm{pal,eff}}$.

The foot can be simplified to a truncated cone of volume $V_{\mathrm{f}} = \pi L_{\mathrm{f}}(R_{\mathrm{p}}^2 + R_{\mathrm{f,in}}^2 + R_{\mathrm{p}}R_{\mathrm{f,in}})/3$ if information on the foot inlet radius is available. Full cone and truncated cone approximations of the the foot volume led to 15 %–30 % and 2 %–3 % errors, respectively, compared to measured values as seen in Figure 3.14.

Estimating the foot volume can be simplified to a cone as a first approximation. However, if information exists on the inlet cross-section or minimum radius of the foot, this leads to a better prediction using a truncated cone. In the test pipes used

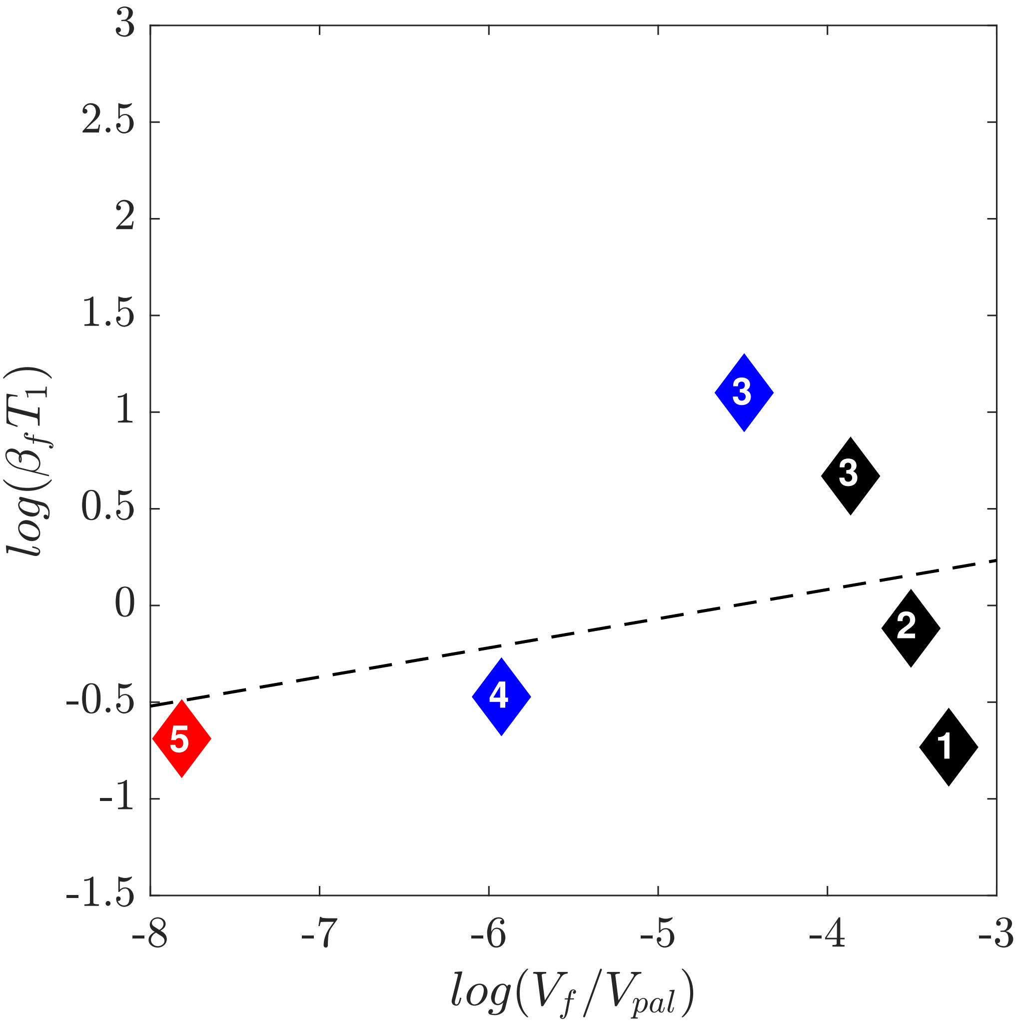

Figure 3.15: Non-dimensional pressure-rise time steepness $\beta_{p,f}\,T_1$ in the foot (from measured data) as a function of the foot volume to pallet-box volume ratio.

here, the non-truncated cone led to 65-85 % of the actual V_f.

Table 3.2 and Figure 3.15 (together with the steepness variation using changing number of ranks coupled at the groove level, Figure 3.10) would suggest that the relationship between the dimensionless pressure rise time (DRT) steepness and the cavity volumes depends on the ensemble of foot-to-palletbox ratio proposed in §3.3.3, giving a prominent role in PRT limitation to the pallet-box over the groove, since the ratio $V_\mathrm{grv}/V_\mathrm{pal}$ remains constant. The larger the $\beta\,T_1$ quantity, the quicker the a_2/a_1 and a_3/a_1 ratios drift away from unity (Figure 3.9). Second, when operating in the fundamental regime, smaller $V_\mathrm{f}/V_\mathrm{grv}$ relate to steeper RJV rises. Even though increasing the number of ranks coupled to the pallet-box for the operation of the same note has shown variation of transients, it is not evident that the groove plays a major limiting role (over the pallet box case) other than satisfying the minimal air consumption imposed by the sum of all the toe inlets of the same-note pipes.

Finding indices of an organizing principle is a promising start. However, one would need further data points in Figure 3.15 to ascertain the relevant interpolation for the DRT quantity. Should the order of interpolation be better known, the relationship $\log\left(V_{\mathrm{f}}/V_{\mathrm{grv}}\right) \sim \log\left(\beta_{\mathrm{p,b}}\, T_1\right)$ would provide information towards the question of proposing a cutoff region where the contribution of V_{f} would be negligible, or not, within the rank.

3.6 Conclusions

This study has explored the driving mechanisms of the air flow in pipe organs, which constitutes a basis for a family of initial conditions in organ pipe synthesis simulation. The formulation presented here introduces five coupled equations that govern a one-dimensional approximation of the flow from the organ's largest reservoir downstream until the coupling term with the mouth pressure that is solved for in pipe simulations, which has been neglected in order to facilitate clarity of the system.

Data from measurements carried out under controlled laboratory and real instrument conditions were used with five different test pipes to validate the predicted signal by the non-dimensional ideal model and to assess the numerical techniques used for solving the system. Under fully coupled conditions with the pipe model and the resonator's response, an energy-conserving balance is not immediately available. In future work, bounds found on signal growth rate across all positions in organ and organ-like cavities upstream from the pipe's mouth will aid in deriving such analysis.

Time stepping methods and fitted parameter models have been used to show two possible numerical strategies. During the simulation run-time, the first approach requires the use of iterative methods to solve the full unsteady Bernoulli equations at each time step, which come to a cost in addition to the computation of nonlinear losses in the mouth and neutral-delay differential equations intrinsic in the jet-drive model. One advantage of the fitted initialization function is that one can precompute its parameters before the simulation and store the time-series in an instrument file. The correlation between non-dimensional jet velocity and spectral changes was examined to show the impact that the pressure transient before the half-rise time has on the jet evolution. Another advantage we found in favor of using the second numerical strategy is that it produces more accurate computed results of the actual signal measured during the interval of interest.

The non-dimensional model revealed a relationship between the slope of the pressure growth in the foot and the scaling ratio of foot-volume to groove-volume. In the context of musical and numerical applications, it is hoped that this rule and the initialization function model will aid in refining physical models where the onset of the jet velocity and its evolution is sometimes the result of an arbitrary choice. In order to apply the proposed model to the digital reconstruction of historical organs, two pieces of information are of most importance: the dimensions of the pallet-box and the static pressure in the blowing system. Regarding the first one, if documentation is available on the number of pipes per rank or the stop list, the groove volume can be estimated. Concerning the second one, it is not uncommon to find mm H_2O level marks on the walls near the organ made by the person in charge of blowing the bellows or descriptions about the weights sitting on top of the parallel reservoir. As an example, the geometry of the Dallery blowing system is shown in Figure 3.18, where the dimensions, type, and number of bellows can be inspected. Unfortunately, it lacks any evidence of the weights installed on the parallel reservoir after the bellows.

A note of caution should be taken. At the time of measuring and writing the current work, only 18 flue pipes were available at the laboratory, a selection of which would eventually be drilled into and transported across countries. This constraint causes the interpretation of the sample data points to be highly spectulative. The unknown origin of the pipes in the laboratory makes it difficult to determine which organ and pressure they were originally voiced for. Additionally, the voicing may have deteriorated during the years they have remained in the laboratory and during their travels. The oversimplified laboratory setup missing crucial elements with respect to the supply chain in an actual organ made it difficult to relate behaviour of some transients in terms of organ operation: namely, Figure 3.9c showed a long transient for Pipe 3 whose duration in an organ is typical of $C1$ pipes (lowest note in the rank). The laboratory setup verified the condition $V_{res} > V_{foot}$, however in the link reservoir-to-foot the pallet valve, groove cavity (which may or may not be neglected), and the tone channel were overlooked. Upstream from the experimental reservoir a solenoid valve is found that violates the principle of monotonically decreasing cross-sections found by the flow (leading to the largest pressure drop being found at the foot toe inlet). Upstream from the solenoid valve a small diameter flexible tube was used together with a compressor in replacement of a wind trunk (of comparable length) of large cross-section and wooden walls, preceded by a large volume reservoir and a centrifugal blower (which can reject excess of wind consumption). Inevitably, the experimental valve-tube-compressor strategy delivers different physical behaviour than the organ system that need to be accounted for.

The information obtained reflects the result of mixing pipes with organs or experimental setups for which they were not conceived and voiced beforehand. The jet inverse Strouhal number being high in several acquisitions supports the idea that such mixtures may not lead to the standard operation intended. Further stages of this work should ensure a pre-verification stage of such aspects before ideally enlarging the corpus of results, which may require the assitsance of at least one organ maker for all the reservations presented above.

Additional precautions are required with regard to pressure overshoots during transients. In this study we have privileged the observation of transients whose maximum values were smaller or not significantly larger than the steady-state pressure in the foot of the pipe. Woolley and Campbell [Woolley and Campbell, 2017] have shown pressure overshoots at the groove level depending on the key action: they distinguish between force and velocity action on the key leading to smooth

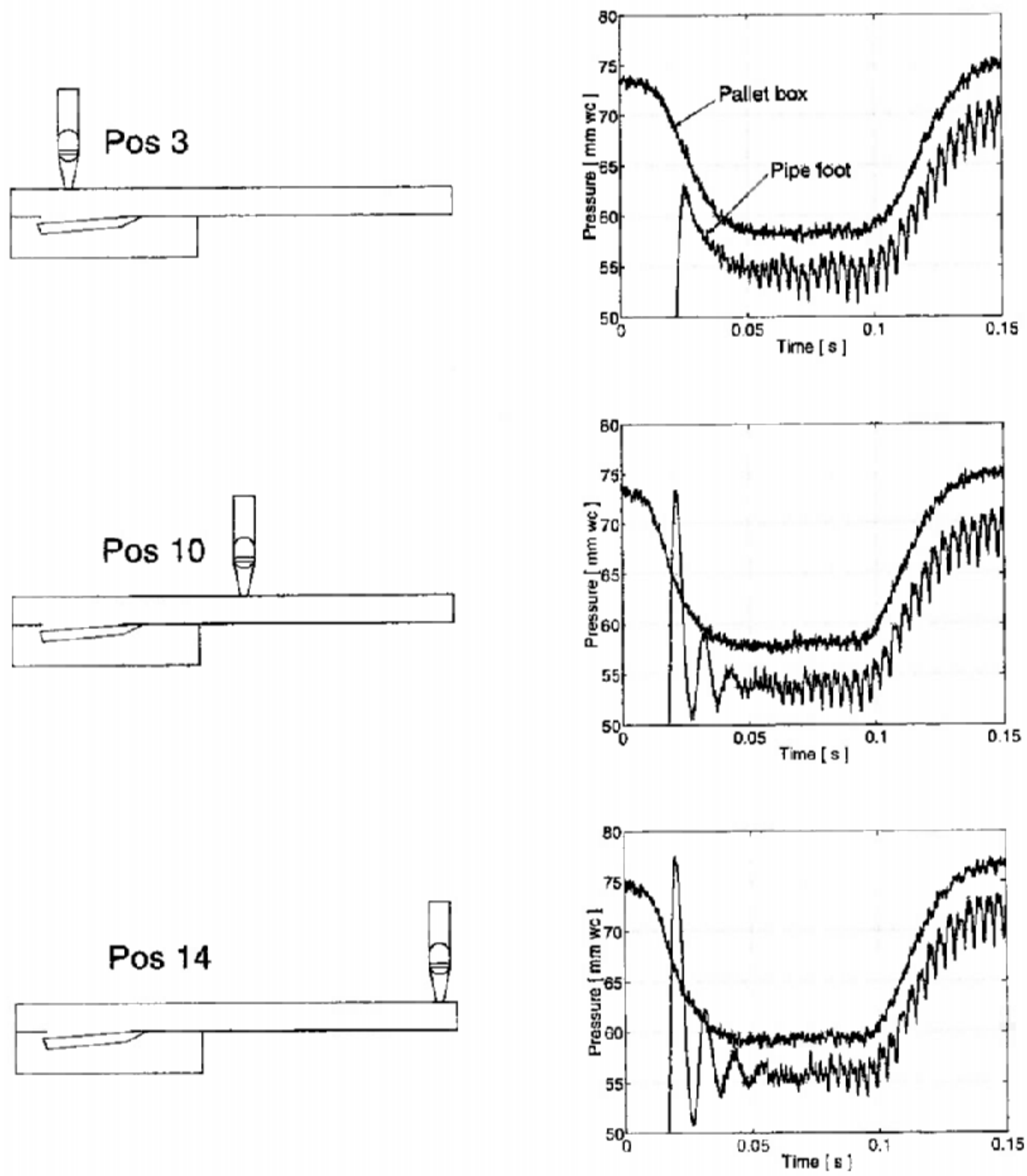

Figure 3.16: Different response amplitudes of the pipe foot pressure as a function of the distance to the opening valve. From [Carlsson, 2002]. Organ makers traditionally indicate blowing pressures in height water column. The target pressure of 75 mm water column corresponds to approximately 730 Pa.

or overshoot transients (measured at the groove). This information may be related with the study by Carlsson [Carlsson, 2002] where the position of the foot within the groove length may have a significant attenuation effect in foot pressure overshoots as shown in Figure 3.16.

3.7 Future perspectives

We found that the geometrical derivation of a scaling rule for driving pressure function at the pipe foot is promisingly yielding interesting results. Above all, it provides an inexpensive computational estimate applicable to organ pipe simulations in rooms.

Further investigations are pertinent with respect to consider the effect of these elements:

- Access the pallet box and grooves for each organ measured and report precise dimensions to consider the variability of the ratio $V_f/V_{grv}/V_{pal}$.
- Account for the mistmatch between experimental pipes placed in otherwise foreign toneholes.
- The absence of tone hole in the laboratory experimental reservoir
- Automatization of the *note-on* in actual organ measurements, after repeatability assessment and factoring out any mechanical limitations to the flow growth rate
- Take into account the distance of the foot to the valve
- Take into account the slightly different width of the grooves (see Figure 3.17)
- Check whether the diameter of the tone hole has a major effect than the inlet cross section of the pipe foot
- The coupling of different stops is still rather obscure
- 100 organ pipes for laboratory use and an actual windchest are now available (the sample space of 5 pipes makes conclusions limited)
- The reservoir and curtain effect on regulating the response of the supply system (see Figure 3.17)

Figure 3.17a and Figure 3.17b show close-up views of the Koenig chamber organ in the laboratory. The first one shows the interior of the regulation mechanism, which in common practice consists of a roll-up curtain on a heavy cylinder impeding more or less access of wind. In Figure 3.17b a few of the pallet slots are visible as the pallet valve is removed and the the system is lit from above the upper board, thus illuminating the interior of the grooves.

The blowing system can be seen as per recent photographies and diagrams in Figure 3.18. It is consistuted by three cuneiform bellows (or wedge-bellows) that feed directly into the wind trunk. With a reservoir missing in this system, the bellows act as such and their sequational operation of lifting the opposite end ensures stable wind into the trunk: the once the top board has been lifted, it is released, the outlet valve at the interior closes and the weight of the board or added on top of the board provides the target pressure. This is seen in Figure 3.18a, where the aformentioned weight is missing for all the bellows of the Dallery.

(a) Curtain regulating system between the blower and the parallel reservoir box.

(b) Interior of a pallet-box and grooves with the sliders open and pipes removed. While Figure 3.1 shows a lateral view of the wind-chest and the pallet valve open, this frontal image offers the view from below the slot to which the pallet valve gives access.

Figure 3.17: Close-up view of interior elements of the wind supply system.

(a) Modern photography of the bellows, courtesy of P. Dubois

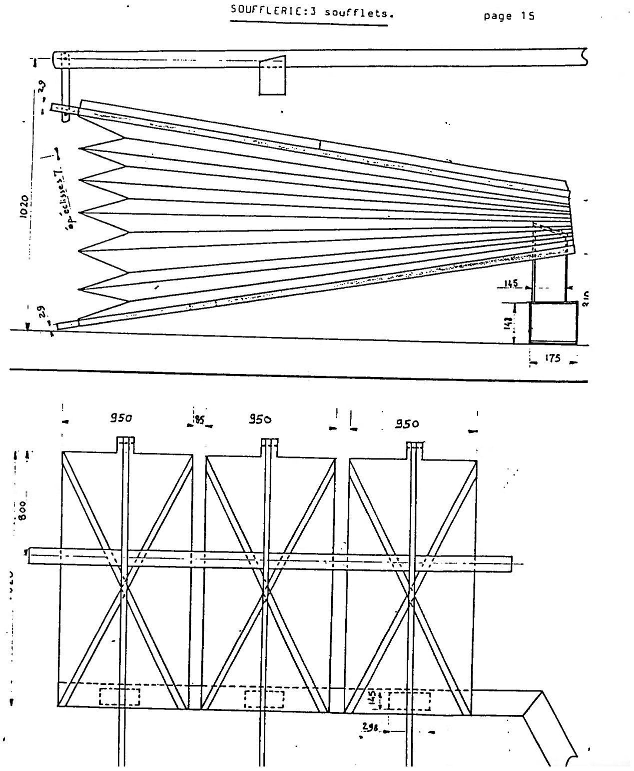

(b) Diagram of the blowing system in the Dallery organ as per [Dubois and Lueders, 2002]

Figure 3.18: *Soufflerie* of the Dallery organ found in the attic of Chapelle de la Sorbonne

3.8 Summary

A review of flue organ pipe elements and models has been compared with measurements carried out in different setups: a laboratory reservoir-like system, a workshop organ, and a church organ, where the two latter ones were build by the same manufacturer. A set of sample pipes was used and manipulated to obtain common references between them, where the focus was placed on the transient times, the shape of the pressure rise in the reservoirs and pipe foot, and the evolution of spectral content of the sound produced. The sample space being reduced in number led to weakly conclusive scaling laws, although relevant enough in character so as to point out potential approaches.

One major purpose of the work developed was to compare the performance of a physical model and a fitted initialization function that would produce realistic driving pressures for numerical simulation of organ pipe sounds. Further research directions are mentioned with respect to modeling elements of the flow through cavities and inlets/outlets and the effect of the stability delivered by wind supply and control systems.

Chapter 4

Numerical methods for organ pipe and supply system simulation

Contents

4.1 Introduction **69**
4.2 On the continuous model **70**
  4.2.1 The windchest air supply system 70
  4.2.2 The pipe system 72
  4.2.3 The coupling of air supply and pipe 74
4.3 Continuous-time system analysis **75**
  4.3.1 Stability of the open loop 76
4.4 Implementation **77**
  4.4.1 State space formulation 77
  4.4.2 Semi-discrete model 80
  4.4.3 Discrete model 82
  4.4.4 Temporal finite difference operators 83
  4.4.5 Forward Euler 83
  4.4.6 Second-order trapezoid and 1st order backwards-difference 84
  4.4.7 Störmer-Verlet scheme 84
4.5 Validation **84**
  4.5.1 Numerical stability 84
  4.5.2 Measurements 85
4.6 Summary and future perspectives **87**

4.1 Introduction

Numerical time-stepping methods are found among numerous approaches that have tackled the realization of musical instrument physical models in time-domain application. Examples of that are: digital waveguides, lumped models, finite differences, and machine learning-based (where the link with a physical model as such is less evident). In chronological order they appear in: [Coltman, 1992], [Valimaki et al., 1992], [Valimaki et al., 1996], [Verge et al., 1997b], [de la Cuadra, 2006], [Terrien et al., 2012], [Auvray et al., 2014], [Terrien, 2014], [de la Cuadra et al., 2014], [Gabrielli et al., 2017], [Tateishi et al., 2019], [Gabrielli et al., 2019], [Darabundit and Smith, 2021], and [Nagy et al., 2022].

Applications targeted by such efforts are primarily: instrument plug-ins, sound design, academic research of musical instrument dynamics, digital reconstruction of historical instruments, instrument's parameter design optimization, and bridging communication between scientific advances and actual digital or physical instrument manufacturers.

This was missing analysis of two crucial aspects. Firstly, the nature of the driving supply (with some studies on player's mouth pressure and cavity systematization and approximation and preliminary analysis in the organ case by Nolle and Finch [Finch and Nolle, 1986, Nolle and Finch, 1992]. Secondly, the feasibility of the numerical implementation of all the elements cascaded in the whole system simulation. In the current work, we refer to this in continuous and discrete time as *update.* In [Terrien et al., 2012], one such examination appeared considering a Runge-Kutta based scheme proposed by Bogacki-Shampine [Bogacki and Shampine, 1989].

In this work we examine numerical considerations of the jet-drive model driven by the supply system examined in [Villegas Curulla et al., 2023]. Far from solving a high resolution 2D or 3D DNS for the flow in the pipe, we limit the model to its one-dimensional approximation seeking computational feasibility and efficiency, targeting a realistic *enough* sound output as radiated by the mouth and passive end of the resonator. This corresponds to the frequently found case of the tin-lead flue organ pipe open at both ends.

A summary of the continuous model is presented in §4.2, followed by comments on aspects of the system analysis in §4.3. In §4.4, the semi-discrete model is presented, along with its discretization, a discrete-time open-loop gain, and the system's matrix form. Measurements for modal parameter extraction and time-domain are used in §4.5 for validation purposes. We close this study with some remarks on computational performance of one scheme and future perspectives in §4.6. As a caution note, in this section k is not to be confused with a wave number in this paper, but instead it is systematically used to express the sampling interval (with the relationship $k = 1/fs$, unless otherwise stated) in line with numerical literature of the like [Strikwerda, 2004, LeVeque, 2007]).

4.2 On the continuous model

4.2.1 The windchest air supply system

A windchest air supply flow model is proposed where an initialization function can be used instead of solving the flow equations. The significance of the driving pressure may be better understood in the model representation in Figure 4.1a. The input function is outlined together with the jet-drive model and the radiated pressure at the mouth level as the output. The parameters are calibrated with respect to the geometry of the pipe. Said initialization function is responsible for modeling the pressure rise in the foot of the pipe, therefore, leading to a realistic growth of the

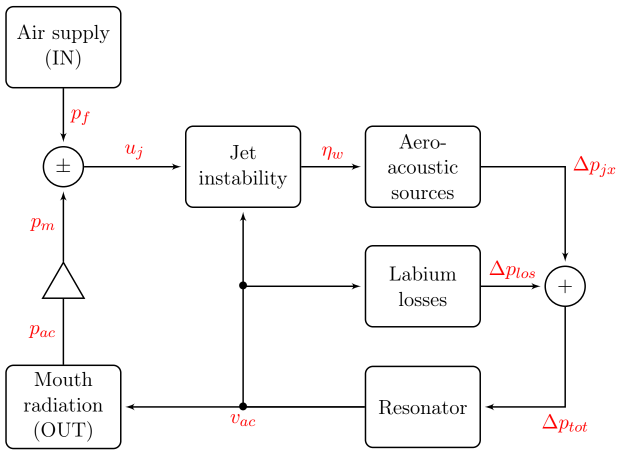

(a)

Figure 4.1: Closed loop operation in wind instruments of self-sustained oscillation type.

jet velocity time-series.

$$\rho l_{\mathrm{pal}} \frac{d}{dt} u_{\mathrm{pal}} + \frac{1}{2}\rho u_{\mathrm{pal}}^2 + p_{\mathrm{grv}} = P_{\mathrm{wind}} \tag{4.1a}$$

$$\frac{V_{\mathrm{grv}}}{\rho c^2}\frac{d}{dt} p_{\mathrm{grv}} - S_{\mathrm{pal}} u_{\mathrm{pal}} + S_{\mathrm{in}} u_{\mathrm{in}} = 0 \tag{4.1b}$$

$$\rho l_{\mathrm{in}} \frac{d}{dt} u_{\mathrm{in}} + \frac{1}{2}\rho u_{\mathrm{in}}^2 - p_{\mathrm{grv}} + p_{\mathrm{f}} = 0 \tag{4.1c}$$

$$\frac{V_{\mathrm{f}}}{\rho c^2}\frac{d}{dt} p_{\mathrm{f}} - S_{\mathrm{in}} u_{\mathrm{in}} + S_{\mathrm{j}} u_{\mathrm{j}} = 0 \tag{4.1d}$$

$$\rho l_{\mathrm{j}} \frac{d}{dt} u_{\mathrm{j}} + \frac{1}{2}\rho u_{\mathrm{j}}^2 - p_{\mathrm{f}} + p_{\mathrm{m}} = 0 \tag{4.1e}$$

which can be significantly simplified if a geometry-based initialization function [Villegas Curulla et al., 2023] is calibrated to compute the foot pressure taking the form

$$p_{\mathrm{i}}(t) = \frac{P_{\mathrm{i}}^{(targ)}}{(1 + e^{-\kappa(t-t_o)})^{1/\nu}} \tag{4.2}$$

where the tuning parameters (κ, $P_{\mathrm{i}}^{(targ)}$, t_o, and ν) adjust the set-value of foot pressure reached in SS in the foot (without accounting for acoustic oscillations from the resonator), the growth rate of dp/dt, the delay from the triggering initial time in the windchest to the maximum slope location, and the non-linear coefficient that approaches the steeper slope to the initial or final asymptotes. Instead of going ahead with solving the flow equations, we focus our attention in the use of the foot pressure fitted function (of the type Equation (4.2)), assuming the set of parameters is known ($P^{(targ)}$,κ,t_o, and ν), where the maximum pressure growth rate in the foot is given by

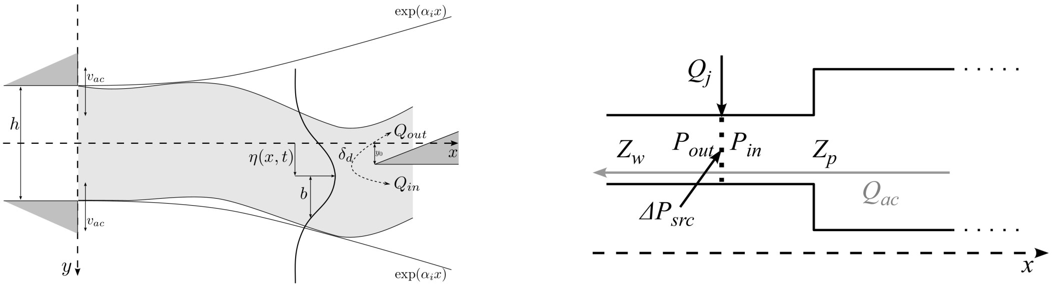

(a) **(b)**

Figure 4.2: (a) Diagram of the mouth region and the associate geometrical and jet-related parameters (adapted from [Ernoult, 2016]). (b) One-dimensional impedance analogy of the flute-like instrument.

$$\frac{d}{dt}p_{\mathrm{f}} = \frac{\kappa e^{-\kappa(t-t_o)}}{\nu}p_{\mathrm{f}} \tag{4.3}$$

at time $t_{\max} = (\kappa\, t_o - log_e(\nu))/\kappa$.

4.2.2 The pipe system

A common model to explain the aero-acoustic sources is the jet-drive. The jet originates at the flue exit of the pipe's foot windway and injects volume into the mouth region (see Q_{j} in the one-dimensional pipe approximation Figure 4.2b). Said region is considered compact and small enough to assume a laminar flow for relevant Reynolds numbers (see [Fabre and Hirschberg, 2000] for further explanation on this). However, the difference of media state between the inside and outside domains of the mouth give rise to a Kelvin-Helmholtz instability, whose governing Rayleigh equation can be expressed following [Verge et al., 1994a] as

$$\left(U(y) - \frac{\omega}{\alpha}\right)\left(\frac{\partial^2\psi}{\partial y^2} - \alpha^2\psi\right) - \frac{d^2U}{dy^2}\psi = 0 \tag{4.4}$$

which can be solved for space or frequency. $U(y)$ is the jet velocity profile (following the system of coordinates showed in Figure 4.2a) and $\psi = \psi(x, y, t)$ is a perturbation velocity field. One can find that solutions show two modes: varicose and sinuous oscillations, with the latter having a dominant effect [Ségoufin, 2000] causing the jet's center-line to oscillate with respect to inside and outside of the pipe. By fixing the temporal analysis (ω is fixed by the pulsation of the resonator) and solving for the complex spatial wavenumber ($\alpha = \alpha_{\mathrm{r}} + j\alpha_{\mathrm{i}}$), the imaginary component of α expresses an amplification equal to $h\, e^{\alpha_i x}$ on the transverse oscillation amplitude of the jet in the mouth, where h is the height of the flue exit, in the order of one or few mm (see Figure 4.2a).

The operation of the aero-acoustic sources at the labium are dominantly driven by the alternating injection of flow by the jet-drive mechanism at the labium ($x = W_{\mathrm{m}}$). The flow into the pipe is expressed by

$$Q_{\mathrm{in}}(t) = H_{\mathrm{m}} \int_{-\infty}^{y_{off}-\eta(t)} U(y)dy \tag{4.5}$$

with H_{m} the depth of the mouth in the z-dimension. The alternating wafting of the jet at the edge can be understood as injecting a total flow into the pipe which can be decomposed into mean and perturbation flow components

$$Q_{\mathrm{tot}} = Q_{\mathrm{in}} + Q_1 \tag{4.6}$$

where the oscillating part $Q_1 \propto tanh(\eta/b - y_{off}/b)$ and $Q_2 = -Q_1$ are responsible for the dipole source at the labium, at a distance δ_d from each other. Establishing the following parameters will be necessary for the formulation of the pipe system:

- $\tau = W_{\mathrm{m}}/c_{\mathrm{p}}$: convection delay of the jet travelling from $x = 0$ to $x = W_{\mathrm{m}}$
- W_{m}: cut-up distance from the flue exit to the labium interaction point
- $b = 2h/5$: jet half-width under Bickley assumption
- $\delta_d = 4/\pi\sqrt{2hW_{\mathrm{m}}}$: distance between Q_1 and Q_2 sources, by conformal mapping
- $\alpha_i = \beta/h$: imaginary part approximation [de la Cuadra, 2006] of the instability's solution wavenumber
- $c_p = \gamma u_{\mathrm{j}}$: jet convection velocity approximation [de la Cuadra, 2006]
- $\beta \sim 0.3$: jet spatial amplification
- $\gamma \sim 0.4$: relative convection velocity
- $\alpha_{vc} \sim 0.6$: vena-contracta due to the mouth cross-section constriction to the resonator's flow
- Y_r: modal pipe input admittance amplitudes
- ω_r: pulsation of each of the resonator's modes
- ε_r: the inverse of each mode's quality factor (modal damping)

Terrien et al.[Terrien et al., 2015] show a concise summary of the operation of the pipe physical model leading to the following system of equations:

$$\eta_{\mathrm{w}}(t) = he^{\alpha_i W} \frac{v_{\mathrm{ac}}(t-\tau)}{u_j(t)} \tag{4.7a}$$

$$\Delta p_{jx}(t) = \frac{\rho \delta_d b}{2W_{\mathrm{m}}} u_{\mathrm{j}} \frac{d}{dt}\left[tanh\left(\frac{\eta_{\mathrm{w}}(t) - y_{off}}{b}\right)\right] \tag{4.7b}$$

$$\Delta p_{los}(t) = -\frac{\rho}{2}\frac{(v_{\mathrm{ac}}(t))^2}{\alpha_{\mathrm{vc}}^2} sgn(v_{\mathrm{ac}}(t)) \tag{4.7c}$$

$$\Delta p_{tot}(t) = \Delta p_{jx} + \Delta p_{los} \tag{4.7d}$$

$$Y_{\mathrm{p,in}}(\omega) = \frac{V_{\mathrm{ac}}}{\Delta P_{tot}} = \frac{a_o}{j\omega b_o + c_o} + \sum_{r=1}^{\infty} \frac{Y_{\mathrm{r}} j\omega}{\omega_{\mathrm{r}}^2 + \varepsilon_{\mathrm{r}}\omega_{\mathrm{r}} j\omega + (j\omega)^2} \tag{4.7e}$$

Equation (4.7a) expresses the jet displacements from an imaginary trajectory line from the flue exit to the labium ($x \in [0, W_{\mathrm{m}}]$) due to the hydrodynamic instability in the mouth. The factor $he^{\alpha_i W}$ is the spatial amplification of the instability with an h factor corresponding to the flue exit height; v_{ac} and u_{j} are the acoustic velocity and the jet center-line velocity. The jet velocity profile ($U(y)$) is approximated by a Bickley family function.

Equation (4.7c) expresses the non-linear losses due to the vena-contracta and the energy losses due to vorticity conservation, flow separation at the labium, and interaction of jet and acoustic flows every time that the flow changes inwards/outwards direction (see [Fabre and Hirschberg, 1996] and [Verge et al., 1997b]). It acts as a limiter to the modal growth of the pressure oscillations in the pipe. The pipe's input impedance as seen by the jet at the injection point is represented by $Y_{\mathrm{p,in}}$. The poles of the frequency behavior of the pipe input admittance and the acoustic velocity can be approximated by a modal decomposition form as the one showed in Equation (4.7e). In time domain, this is equivalent to say

$$\mathcal{L}_R\{v_r(t)\} = \left[\frac{d^2}{dt^2} + \varepsilon_{\mathrm{r}}\omega_{\mathrm{r}}\frac{d}{dt} + \omega_{\mathrm{r}}^2\right] v_{\mathrm{r}}(t) = Y_r \frac{d}{dt}\Delta p_{tot}(t) \tag{4.8}$$

$\mathcal{L}_R$ denotes a second-order time-differential operator in the resonator's equation. The total acoustic velocity is the sum of the modal contributions $v_{\mathrm{ac}} = \sum_r^{\infty} v_{\mathrm{r}}$, where the sum is truncated to N_{modes} here for simulation purposes. The modal parameters Y_k, ε_k, and ω_k are extracted numerically from the frequency response of the bore

$$Y_{\mathrm{p,in}} = \frac{1}{S}\frac{1}{(Z_{\mathrm{p}} + Z_{\mathrm{m}})} \tag{4.9}$$

where radiation end-corrections are accounted for in the pipe (Z_{p}) and the mouth window impedance (Z_{m}).

4.2.3 The coupling of air supply and pipe

The last consideration to add to the system above is the coupling between the foot (Equation (4.1e)) and pipe (Equations (4.7a) to (4.7e)), which is the mouth pressure (p_{m}) whose difference with respect to the foot pressure upstream (p_{f}) causes the flow at the flue that drives the jet. Coltman [Coltman, 1976] proposed an approximation of $p_{\mathrm{m}} \sim 0.5 p_{\mathrm{ac}}$ in line with investigations by Karamcheti and Stegen [Stegen, 1967] on mapping the pressure from the resonator to the mouth; alternatively, the acoustic velocity retrieved by the resonator equations, v_{ac}, may be scaled using the approximation $q_{mouth} = q_{pipe}$ that leads to saying that $v_{ac,mouth} = v_{ac,pipe} S_p / S_m$ (if one diregards effects by the right angle bend). An alternative strategy would utilise a low frequency radiation condition at the mouth as an unflanged baffle orifice:

$$P_{\mathrm{ac}}(\omega) = Z_{\mathrm{rad}}\, V_{\mathrm{ac}}(\omega) \tag{4.10}$$

$$Z_{\mathrm{rad}} = \frac{\rho}{2c}(R_{\mathrm{m}}\omega)^2 \ + j\ 0.7\rho(R_{\mathrm{m}}\omega) \tag{4.11}$$

where the radiation impedance at this location $Z_{\mathrm{rad}} = Z_{\mathrm{m}} + Z_{\mathrm{p}}$, with $Z_{\mathrm{m}} \gg Z_{\mathrm{p}}$ at $x = 0$ (in the 1D pipe analogy). If we express this in time-domain, then it becomes:

$$p_{\mathrm{ac}}(t) = \left[\frac{\rho}{2c}(R_{\mathrm{m}}\omega)^2 + 0.7\rho R_{\mathrm{m}}\frac{d}{dt}\right]\frac{S_p}{S_m}v_{\mathrm{ac}}(t) \quad \to \quad p_{\mathrm{ac}}(t) \simeq \ 0.7\rho R_{\mathrm{m}}\frac{S_p}{S_m}\frac{d}{dt}v_{\mathrm{ac}}(t). \tag{4.12}$$

where R_{m} is the mouth equivalent radius and $v_{ac}(t)$ here refers to the acoustic flow velocity at the mouth level.

4.3 Continuous-time system analysis

For a known and well-behaved function as input in the source term, analytic solutions can be examined for the zero-forcing (homogeneous), constant input, and sinusoid. These conditions can be considered for a number N_m of resonator modes. If the uniform mode (or zero frequency) is considered, the complete expression becomes

$$\begin{aligned} b_o\frac{d}{dt}v_o + c_o v_o &= a_o\Delta p_{tot} \\ \frac{d^2}{dt^2}v_{\mathrm{r}} + \varepsilon_{\mathrm{r}}\omega_{\mathrm{r}}\frac{d}{dt}v_{\mathrm{r}} + \omega_{\mathrm{r}}^2 v_{\mathrm{r}} &= Y_r\frac{d}{dt}\Delta p_{tot} \end{aligned} \tag{4.13}$$

with the equivalent modal decomposition, in the frequency domain, as

$$Y_{in}(\omega) = \frac{a_o}{j\omega b_o + c_o} + \sum_r \frac{j\omega Y_r}{\omega_r^2 + j\omega\varepsilon_r\omega_r + (j\omega)^2} \tag{4.14}$$

If one considers the simplest case of the resonator with $N_m = 1$, a unitary excitation source, and without the uniform mode, the expected behaviour will be that of an under-damped oscillator ($\zeta_r = \varepsilon_r/2 < 1$)

$$v_r(t) = V_{r,1}e^{\lambda_r t} + \frac{1}{\omega_r^2} \tag{4.15}$$

where the amplitude V depends on the initial conditions and the propagation constant λ_r of the mode r has a real (damping) and imaginary (oscillatory) components

$$\lambda_r = -\frac{\omega_r\varepsilon_r}{2} + j\omega_r \tag{4.16}$$

and the numerical solution will be equal to $\Re\{v_r(t)\}$. If one now looks at a sinusoidal input term, the analytical solution is

$$v_r(t) = -\frac{Y_r}{\varepsilon_r\omega_r}e^{-\lambda_r t}sin(\omega_r t) + \frac{Y_r}{\varepsilon_r\omega_r}sin(\omega_r t) \tag{4.17}$$

where the transient response is represented by the first term (with $\lambda_r = \varepsilon_r\omega_r/2$) and second term is the stationary solution ($t \to \infty$). The previous analytical solutions will be helpful to assess the numerical solutions in simulations.

4.3.1 Stability of the open loop

A common method in literature [Van Valkenburg, 1974] to test the stability of the loop shown in Figure 4.1a consists on testing the validity of a set of parameters when the cycle η_b-Δp-v_{ac} is discontinued or assumed non-closed. Barkhausen criterion [Van Valkenburg, 1974] is used to investigate the gain and phase conditions of the open loop system for solutions to be static or oscillating. To show this, we assume quasi-static variations of u_j and $N_m = 1$ for simplicity, and take the loop system equation

$$\eta_b = \frac{he^{\alpha_i W_m}}{bu_j} v_{ac}(t-\tau) = \Pi v_{ac}(t-\tau) \tag{4.18}$$

$$\Delta p = \frac{\rho\delta_d bu_j}{W_m}\frac{d}{dt}[tanh(\Pi v_{ac}(t-\tau) - y_b] - \frac{\rho}{2\alpha_{vc}^2} v_{ac}^2 sgn(v_{ac}) \tag{4.19}$$

$$\begin{aligned}\frac{d^2}{dt^2}v_{ac}(t) &= -\varepsilon_1\omega_1\frac{d}{dt}v_{ac}(t) - \omega_1^2 v_{ac}(t) + Y_1\frac{d}{dt}\Delta p \\ &= -\varepsilon_1\omega_1\frac{d}{dt}v_{ac}(t) - \omega_1^2 v_{ac}(t) + \frac{Y_1\rho\delta_d bu_j}{W_m}\frac{d^2}{dt^2}[tanh(\Pi v_{ac}(t-\tau) - y_b] \\ &- \frac{Y_1\rho}{2\alpha_{vc}^2}\frac{d}{dt}(v_{ac}^2(t) sgn(v_{ac}(t)))\end{aligned} \tag{4.20}$$

to realize that the static solution $v_{ac}(t) = 0$ serves as a linearization point. Using the provisional coefficient $\Pi = he^{\alpha_i W_m}/bu_j$ for compactness, the terms $tanh()$ and $v_{ac}^2(t)$ become

$$tanh(\Pi v_{ac}(t-\tau) - y_b)|_{v_{ac}(t-\tau)=0} \rightarrow tanh(-y_b) + [1 - tanh^2(-y_b)]\Pi v_{ac}(t-\tau) \tag{4.21}$$

$$v_{ac}^2(t)|_{v_{ac}(t)=0} \rightarrow 2\cdot 0\cdot v_{ac}(t) \tag{4.22}$$

hence the linearized resonator equation becomes

$$\frac{d^2}{dt^2}v_{ac}(t) = -\varepsilon_1\omega_1\frac{d}{dt}v_{ac}(t) - \omega_1^2 v_{ac}(t) + \tag{4.23}$$

$$\begin{aligned}&+ \frac{Y_1\rho\delta_d bu_j}{W_m}\frac{d^2}{dt^2}\left\{tanh(-y_b) + [1 - tanh^2(-y_b)]\Pi v_{ac}(t-\tau)\right\} \\ &= -\varepsilon_1\omega_1\frac{d}{dt}v_{ac}(t) - \omega_1^2 v_{ac}(t) + \frac{Y_1\rho\delta_d bu_j}{W_m}[1 - tanh^2(-y_b)]\Pi\frac{d^2}{dt^2}v_{ac}(t-\tau)\end{aligned} \tag{4.24}$$

Following a similar apparoch in §4.3, we use an exponential test solution of the form $v_{ac}(t) = V_{ac,o}e^{\lambda t}$ to obtain the characteristic equation

$$\lambda^2\left(1 - \frac{Y_1\rho\delta_d he^{\alpha_i W_m}}{W_m}[1 - tanh^2(-y_b)]e^{-\lambda\tau}\right) + \varepsilon_1\omega_1\lambda + \omega_1^2 = 0 \tag{4.25}$$

where the real part of the λ-roots will yield evanescence for negative values (stable solution) and growth for positive values (unstable solution) to any small perturbation added to the static solution. If, on the other hand, the roots of the characteristic polynomial are purely imaginary, oscillatory behaviour is expected if the Barkhausen conditions on the gain of the open loop are fulfilled: for a gain amplitude equal or larger than unity and a total loop phase equal to zero or integer multiples of 2π, the solution will oscillate. The blocks involved in the loop (jet, amplification, sources, and resonator) are only concerned by phase changes in the jet delay $\tau = \frac{W_m}{\gamma}\frac{1}{u_j}$ and the resonator. Departing from resonance in the loop, if the τ delay decreases (jet velocity increases), the resonator response will shift towards positive phase, thus slightly moving the oscillating frequency away from the resonance peak. Additionally, the resonator is the only block where the response is frequency dependant. We proceed using the linearization above for the pressure

$$\Delta p = \frac{\rho \delta_d b u_j}{W_m}\beta[1 - tanh^2(-y_b)]\frac{d}{dt}v_{ac}(t-\tau) \tag{4.26}$$

Laplace transforming it yields

$$\Delta P(s) = \frac{\rho \delta_d b u_j}{W_m}\beta[1 - tanh^2(-y_b)]sV_{ac}(s)e^{-s\tau} \tag{4.27}$$

Using the frequency-domain resonator equation $V(s) = \Delta P(s)Y(s)$ and defining the gain of the loop as the ratio $G = \frac{Y(s)\Delta P(s)}{V(s)}$, one substitutes the result obtained above for the Laplace pressure to arrive at the gain of the loop:

$$G(s) = he^{\alpha_i W_m}\frac{\rho \delta_d}{W_m}[1 - tanh^2(-y_b)]e^{-s\tau}sY(s) \tag{4.28}$$

where terms are now rearranged to facilitate recognizing the different contributions from each block (amplification, delay, sources, and resonator), consistent with the non-dimensional model proposed by Terrien in [Terrien, 2014].

4.4 Implementation

4.4.1 State space formulation

One can resort to a state-space formulation to perform a stability analysis of the system consisting of pressure supply and pipe, which in continuous form is usually represented ([Smith, 2007]) as

$$\begin{bmatrix} \partial_t \mathbf{x}(t) \\ \mathbf{y}(t) \end{bmatrix} = \begin{bmatrix} A(t) & B \\ C & D \end{bmatrix} \begin{bmatrix} \mathbf{x}(t) \\ \mathbf{u}(t) \end{bmatrix} \tag{4.29}$$

Consider the windchest supply and the pipe systems above. System 4.1 (encapsulated as Equation (4.2)) leads to knowing the input p_f for $\mathbf{u}(t)$. The operation of the pipe as expressed by System Equation (4.7) is contained in the system matrix $\mathbf{A}(t)$. Analysis of the behaviour of η in the Laplace space has been examined by Nagy *et al.* [Nagy et al., 2022].

We focus the attention on $\mathbf{A}(t)\mathbf{x}(t)$ and $\mathbf{Bu}(t)$ of the pipe system, provided that $\mathbf{C}$ is time-invariant and using [Coltman, 1976] $\mathbf{C}\,\mathbf{x} = p_m = \begin{bmatrix}0 & \dots & 0 & 0.5\end{bmatrix} p_{ac}$ to produce the output and feedback term p_m. The feed-through matrix $\mathbf{D}$ is null.

The driving input in the simplest form is the foot pressure that ramps from 0 Pa up to $P_{\mathrm{f}}^{(targ)}$ plus some low-amplitude oscillation at the frequency of the resonator. The matrix of the inputs yields

$$\mathbf{Bu}(t) = \begin{bmatrix}1 & 0 & \dots & 0\end{bmatrix}^{\top} p_{\mathrm{foot}}(t) \tag{4.30}$$

The complete system of equations that constitute the pipe model are stated below

$$p_{\mathrm{f}} = p_{\mathrm{f}}(t) \tag{4.31a}$$

$$\rho l_{\mathrm{j}} \frac{d}{dt} u_{\mathrm{j}}(t) = p_{\mathrm{f}}(t) - p_{\mathrm{m}}(t) - \frac{\rho}{2} u_{\mathrm{j}}^2(t) \tag{4.31b}$$

$$\tau = \frac{W_{\mathrm{m}}}{\gamma} \frac{1}{u_{\mathrm{j}}} \tag{4.31c}$$

$$\eta_{\mathrm{b}}(t) = \frac{h e^{\alpha_i W}}{b} \frac{v_{\mathrm{ac}}(t-\tau)}{u_{\mathrm{j}}(t)} \tag{4.31d}$$

$$\Delta p_{\mathrm{jx}}(t) = \frac{\rho \delta_d b}{W_{\mathrm{m}}} u_{\mathrm{j}}(t) \frac{d}{dt} tanh \left\{ \eta_{\mathrm{b}}(t) - y_b \right\} \tag{4.31e}$$

$$\Delta p_{\mathrm{los}}(t) = -\frac{\rho}{2\alpha_{vc}^2} v_{\mathrm{ac}}(t) |v_{\mathrm{ac}}(t)| \tag{4.31f}$$

$$p(t) \triangleq \Delta p_{tot}(t) = \Delta p_{jx}(t) + \Delta p_{los}(t) \tag{4.31g}$$

$$\left(\frac{d^2}{dt^2} + \mathbf{E}\frac{d}{dt} + \mathbf{F} \right) \mathbf{v}(t) = \mathbf{G} \frac{d}{dt} p(t) \tag{4.31h}$$

$$p_{\mathrm{ac}}(t) = 0.7 \rho R_{\mathrm{m}} \frac{S_p}{S_m} \frac{d}{dt} \sum_r v_{\mathrm{r}}(t) \tag{4.31i}$$

The resonator equation, Equation (4.31h), contains N_m modal acoustic velocities v_{r}, N_{m} damping terms ($\varepsilon_{\mathrm{r}}\omega_{\mathrm{r}}$), N_{m} resonant frequencies (ω_{r}^2), and N_{m} admittances (Y_{r}). For an arbitrary number of modes, it is convenient to express the equation encapsulated in terms of a column vector $\mathbf{v}$, the forcing term p of the total input pressure difference Δp_{tot}, and the constant parameters

$$\mathbf{E} = \begin{bmatrix} \varepsilon_1 \omega_1 \\ \vdots \\ \varepsilon_{N_m} \omega_{N_m} \end{bmatrix}, \qquad \mathbf{F} = \begin{bmatrix} \omega_1^2 \\ \vdots \\ \omega_{N_m}^2 \end{bmatrix}, \qquad \mathbf{G} = \begin{bmatrix} Y_1 \\ \vdots \\ Y_{N_m} \end{bmatrix} \tag{4.32}$$

Dimensional inspection of Equation (4.31h) reveals that left-hand side and right-hand side terms of the expression must be in units of $[ms^{-3}]$, which aids selecting the relevant normalization of the modal admittances in $\mathbf{G}$ (which is computed following [Ernoult and Fabre, 2017b] and [Lefebvre, 2010]), needs to be scaled by the pipe's cross-section, the pulsation frequency, and the damping factor (dimensionless).

$$Y_r = \frac{Y_{\text{in}}}{S_p}\omega_r\varepsilon_r \tag{4.33}$$

since the values extracted at each pulsation from the modal decomposition yielded

$$\left|\frac{j\omega Y_r}{\omega_r^2 - \omega^2 + j\omega\omega_r\varepsilon_r}\right|_{\omega=\omega_r} = \frac{|Y_r|}{\omega_r\varepsilon_r} \tag{4.34}$$

In order to find the pressure at the pipe, and subsequently at the mouth (p_{m}), the total acoustic velocity ($v_{\text{ac}} = \sum_r v_{\text{r}}$) has to be mapped: $v_{\text{ac,m}} = v_{\text{ac,p}} S_{\text{p}}/S_{\text{m}}$. The state variables involved in the update are:

$$\mathbf{x}(t) = \begin{bmatrix} p_{\text{f}} & u_{\text{j}} & \tau & \eta_b & \Delta p_{src} & \Delta p_{loss} & p & \sum_r v_r & p_{\text{m}} \end{bmatrix}^\top \tag{4.35}$$

The second-order differential Equation (4.31h) may be reduced to its first-order-form

$$\frac{d}{dt}v_{\text{r}} = q_{\text{r}} \tag{4.36}$$

$$\frac{d}{dt}q_{\text{r}} + \mathbf{E}q_{\text{r}} + \mathbf{F}v_{\text{r}} = \mathbf{G}\frac{d}{dt}p \tag{4.37}$$

The steps followed in the organ pipe simulation are indicated in Algorithm 2, spanning from retrieving the current value of the foot pressure (p_{f}) to updating the acoustic and mouth pressures after the resonator's effect (p_{ac}, p_{m}). Alternatively, one can express the resonator equation in matrix form using $\mathbf{q} = [v\ \dot{v}]^\top$ as

$$\dot{\mathbf{q}} = \mathbb{M}\mathbf{q} + \mathcal{J}\dot{p} \tag{4.38}$$

where $\mathcal{J} = [0\ 1]^\top$ and

$$\mathbb{M} = \begin{bmatrix} 0 & 1 \\ -W & -E \end{bmatrix} \tag{4.39}$$

It is easy to see that the eigenvalues of the system matrix $\mathbb{M}$ are the resonator's pulsations ω_r^2.

4.4.1.1 Some refinements

Reynolds numbers in the mouth region belong to the transition between low Reynolds and critical: in that regime coexist the laminar incompressible flow and the turbulent structure of vortices in small scales. Accounting for said turbulence would entail adding a source term in Δp_{tot} with pressure units.

The initialization of simulations and triggering of non-static solutions is achieved adding small perturbations (band-limited, low-amplitude noise) to the jet transverse displacement. Additionally, during the initial time while $\tau > t$, the *noise* and other perturbations dominate over the effect of $v_{\text{ac}}(t-\tau)$. The discontinuity in $v_{ac}(t-\tau)$ when $t = \tau_{max}$ (before which the solution is not known), is magnified by the differentiation involved in computing the mouth pressure $p_m(t)$ and propagated over the

Algorithm 2: Update stages

```
Input: Rankchest or foot pressure function
Output: Pipe pressure time-series
begin
    Input $p_\mathrm{f}$ initialization function or solve windchest supply model
    $u_\mathrm{j}$              Calculate flow velocity at the end of the flue exit using
                      Bernoulli of $p_\mathrm{f}(t)$ and $p_\mathrm{m}(t)$
    $\tau$              Compute jet convection delay at time $t$
    $\eta$              Compute jet center-line displacement at time $t$ and $x = W_\mathrm{m}$
    $\Delta p_\mathrm{jx}$          Compute jet-drive aero-acoustic source term
    $\Delta p_\mathrm{los}$         Compute loss term at labium
    $\Delta p_\mathrm{tot}$         Compute total pressure jump in the mouth region (Figure 4.2b)
    $v_\mathrm{n}$              Compute each modal acoustic velocity,
                      using $\mathbf{f}(\Delta p_\mathrm{tot}, \mathbf{Y}, \mathbf{F}, \mathbf{G})$, Equation (4.8)
    $v_\mathrm{ac}$             $= \sum_r^{N_m} v_\mathrm{r}$
    $v_\mathrm{ac}(t-\tau)$       Compute delayed acoustic velocity
    $v_\mathrm{ac}$             Compute acoustic velocity at the mouth
    $p_\mathrm{m}$              Update mouth pressure
end
```

entire simulation time at spacings that depend on the delay entity [Shampine, 2008]. Another such perturbation is responsible for the intialization of oscillations is the hydrodynamic feedback: of more important propagation time compared to acoustic velocities, the flow sent downstream by the jet contributes the flow decomposition:

$$Q_\mathrm{tot} = Q_{jet} = Q_\mathrm{in} + Q_\mathrm{out} = (Q_\mathrm{in} + Q_1) + (Q_\mathrm{out} + Q_2) \tag{4.40}$$

As stated in Equation (4.6), $Q_1 = -Q_2$ are responsible for dipole-like aero-acoustic sources. The flow Q_jet injected in the mouth region encounters the rigid body of the sharp labium and an impedance mismatch, thus causing a reflected perturbation. The resulting velocity field in the mouth region is

$$\Phi = v_\mathrm{ac,m} + \frac{2}{\pi}\frac{Q_\mathrm{in}}{S_\mathrm{m}} + \sigma(t) \tag{4.41}$$

where $v_\mathrm{ac,m} = S_\mathrm{p}/S_\mathrm{m} \cdot v_\mathrm{ac,p}$ is the acoustic velocity at the mouth level, and $\sigma(t)$ is band-limited noise.

4.4.2 Semi-discrete model

We present here the air supply and pipe model without making specific assumptions on how the discrete time difference operators δ_{tt} and δ_t are constructed.

$$p_f^n = p_f[n] \tag{4.42a}$$

$$\delta_t u_j^2 = A_1 p_f^n + A_2 p_m^n + A_3 (u_j^n)^2 \tag{4.42b}$$

$$\tau^n = A_4 (u_j^n)^{-1} \tag{4.42c}$$

$$\eta_n^n = A_5 \left(\frac{\sum_r v_r^{n-\tau^n}}{u_j^n} + A_6 \right) \tag{4.42d}$$

$$p_{jx}^n = A_7 u_j^n \delta_t tanh(\eta_b^n - y_b) \tag{4.42e}$$

$$p_{los}^n = A_8 \left(\sum_r v_r^n \right)^2 sign \left(\sum_r v_r^n \right) \tag{4.42f}$$

$$\delta_{tt}\mathbf{v}^n = -\mathbf{E}\delta_t\mathbf{v}^n - \mathbf{W}\mathbf{v}^n + \mathbf{Y}\delta_t(p_{jx}^n + p_{los}^n) \tag{4.42g}$$

$$p_m^n = A_9 \delta_t \left(\sum_r v_r^n \right) \tag{4.42h}$$

with τ^n being the discrete form of the delay τ and the A coefficients being:

$$\begin{array}{lll} A_1 = \dfrac{1}{\rho l_j} & A_2 = -\dfrac{1}{\rho l_j} & A_3 = -\dfrac{\rho}{2} \\ A_4 = \dfrac{W_m}{\gamma} & A_5 = \dfrac{h e^{\alpha_i W_m}}{b} & A_6 = \dfrac{2h}{\pi W_m} \\ A_7 = \dfrac{\rho \delta_d b}{W_m} & A_8 = -\dfrac{\rho}{2\alpha_{vc}^2} & A_9 = \rho 0.7 R_m \dfrac{S_p}{S_m} \end{array} \tag{4.43}$$

Equation (4.42a) expresses the driving pressure at the foot of the pipe at discrete time nk, with a time-offset $n_o k$ centered at the maximum growth rate of the pressure-rise (see Equation (4.2) and Equation (4.3)). An unsteady Bernoulli equation follows in Equation (4.42b) to compute the jet velocity at time-step n and the jet phase-delay τ^n due to the travel time from the flue to the labium, Equation (4.42c).

The b-normalized transverse jet displacement is calculated in Equation (4.42d) as an exponential instability amplification, times the receptivity perturbation term at the flue exit ($v_{ac,o}/u_j$), using the transverse acoustic velocity delayed by the jet delay τ^n. The last term corresponds to the quasi-instantaneous hydrodynamic feedback of the flow, reflected from interacting with solid bodies and impedance mismatch. The hydrodynamic feedback can be expressed as $\frac{2}{\pi}\frac{Q_{in}}{S_m} = 2/\pi(u_j h H_m)/(W_m H_m) = 2u_j h/\pi W_m$.

The first aero-acoustic pressure source and the losses at the labium due to the vena-contracta flow constriction appear in Equation (4.42e) and Equation (4.42f).

The second-order resonator in modal approach takes the total pressure sources as an input and acts as a filter for the modal acoustic velocities in the bore (Equation (4.42g)). The total flow velocity is obtained by the modal sum of the pipe internal velocities. The transverse acoustic velocity at the mouth accounts for a pipe-to-mouth change of flow cross-section under the assumption that $q_m = q_p$.

The low-frequency first-order approximation of the mouth radiation impedance (see Equation (4.12)) yields the pressure at the mouth following in Equation (4.42h).

4.4.3 Discrete model

In a similar fashion to how we proceeded in Equation (4.28), the z-transform of the open loop has to be considered in discrete time to examine the non-growth of the amplification factor in the linearized system. No substantial change is found for the open-loop gain, as long as the jet delay here is rarely an integer multiple of of the sampling period (its analytical form is rather obscure). Here the scheme choice slightly modifies the derivative operator from what was seen in the Laplace space. For instance, a backwards Euler difference scheme would yield a gain

$$G(z) = he^{\alpha_i W_m}\frac{\rho\delta_d}{W_m}[1 - tanh^2(-y_b)]Y(z)e^{-j\omega n_\tau}\frac{1-z^{-1}}{k} \tag{4.44}$$

In order to ensure that the last parts of the update do not incur in exponential growth, also the resonator transfer function and the derivation of mouth pressure are analyzed. The resonator equation, presented above, in second order form under a centered and backward scheme would take the form

$$\left(z - 2 + z^{-1} + kE(1 - z^{-1} + k^2W)V_r(z)\right)V_r(z) = Y\frac{1-z^{-1}}{k}P(z) \tag{4.45}$$

In more familiar filter form, the response of the resonator is given by

$$Y(z) = \frac{V(z)}{\Delta P(z)} = \frac{kY(z^{-1} - z^{-2})}{1 + (-2 + kE + k^2W)z^{-1} + (1 - kE)z^{-2}} \tag{4.46}$$

Zeros of the filter are easily apparent. Finding poles at the denominator leads to the characteristic equation

$$p_{o,\pm} = 1 - k\frac{\varepsilon_r\omega_r}{2} - k^2\frac{w_r^2}{2} \pm k\frac{\omega_r}{2}\sqrt{(\varepsilon_r + k\omega_r)^2 - 4} \tag{4.47}$$

The factored radicand indicates that for any sampling frequency $f_s > \frac{w_r}{2-\varepsilon_r}$, the poles will be complex conjugate pairs. Furthermore, this limit is far below that imposed by the Nyquist sampling theorem in order to be able to resolve any resonator frequency ω_r. The pole eigenfrequencies are readily found with

$$f_{p,\pm} = \frac{tan^{-1}\left(\frac{\Im\{p_o\}}{\Re\{p_o\}}\right)}{2\pi}\cdot f_s \tag{4.48}$$

Most importantly, stability of the resonator's filter will be ensured as long as the magnitude of its poles is confined within the unit circle in the *s-plane*, $|p_{o,\pm}| = \sqrt{\Re^2 + \Im^2} < 1$, this becomes apparent, after some algebra, by the fact that

$$|p_o|^2 = \Re\{p_o\}^2 + \Im\{p_o\}^2 = 1 - k\varepsilon_r\omega_k < 1 \tag{4.49}$$

which holds true for any positive-definite real-valued sampling interval, damping, and pulsation (k, ε, and ω, respectively). Implementation options of the delayed acoustic velocity may be: linear interpolation, cubic interpolation, and Farrow structures [Välimäki et al., 1993, Valimaki and Laakso, 2000, Valimaki and Haghparast, 2007].

4.4.4 Temporal finite difference operators

In what follows, grid functions are used to approximate time variables such as $u_{\mathrm{j}}(t)$ and $p_{\mathrm{f}}(t)$. The series representation of those becomes a signal u_{j}^n (with $n \in [0, ..., N-1]$) sampled at discrete times $n \cdot k$. The grid-points of the series are separated by a temporal grid-spacing (time-step) that customarily is taken as $k = dt$, where the sampling interval dt is imposed by the use of a sampling frequency f_s. Thus the time-domain pressure signal becomes

$$p_{\mathrm{f}} = p_{\mathrm{f}}(t),\ \{t \in [0, T]\} \qquad \rightarrow \qquad p_{\mathrm{f}}^n,\ \{n \in [0, N-1]\} \tag{4.50}$$

where for a small enough sampling period $p_{\mathrm{f}}(t) \simeq p_{\mathrm{f}}^n$.

Time differentiation can be approximated by the operators described below, using dt as the sampling interval. The unit step operations e_{t+} and e_{t-} are equivalent to shifting the grid point one step forwards or backwards in its index.

$$\delta_{t+} = \frac{e_{t+} - 1}{k}, \quad \delta_{t-} = \frac{1 - e_{t-1}}{k}, \quad \delta_{t\cdot} = \frac{e_{t+} - e_{t-}}{2k}, \quad \delta_{tt} = \frac{e_{t+} - 2 + e_{t-}}{k^2} \tag{4.51}$$

where δ_{t+}, δ_{t-} and $\delta_{t\cdot}$ are forward, backward, and centered representations of the first-order time difference, and δ_{tt} approximates the second-order difference. Identity operators represent an approximation of the the identity operation, which are useful to consider in designing a balanced scheme. The following collection of identity operators is commonly used

$$\mu_{t+} = \frac{e_{t+} + 1}{2}, \quad \mu_{t-} = \frac{1 + e_{t-}}{2}, \quad \mu_{t\cdot} = \frac{e_{t+} + e_{t-}}{2}, \quad \mu_{tt} = \frac{e_{t+} + 2 + e_{t-}}{4} \tag{4.52}$$

Note that the time steps involved in the derivative-free terms in Equation (4.42) can be shifted using μ operators, with the advantage of aligning variables at times $n-1$, n, and $n+1$. For example:

$$\mu_{t+} p_{\mathrm{f}} = \frac{(e_{t+} + 1)}{2} p_{\mathrm{f}}^n = \frac{p_{\mathrm{f}}^{n+1} + p_{\mathrm{f}}^n}{2}, \quad \mu_{t\cdot} p_{\mathrm{f}}^n = \frac{(p_{\mathrm{f}}^{n+1} + p_{\mathrm{f}}^{n-1})}{2},$$
$$\mu_{tt} = \frac{(e_{t+} + 2 + e_{t-})}{4} p_{\mathrm{f}}^n = \frac{(p_{\mathrm{f}}^{n+1} + 2p_{\mathrm{f}}^n + p_{\mathrm{f}}^{n-1})}{4}$$

4.4.5 Forward Euler

An initial ground truth reference may be proposed by discretizing the system of ODEs with the forward Euler method. For that, we will make use of the first order form of the resonator (Equation (4.42g)), taking the form

$$\delta_{t+} y_r^n = -\mathbf{E} y_r^n - \mathbf{W} v_r^n + \mathbf{Y} \mu_{t-} \delta_{t+} (p_{jx}^n + p_{los}^n) \tag{4.53}$$
$$\delta_{t+} v_r^n = y_r^n \tag{4.54}$$

4.4.6 Second-order trapezoid and 1st order backwards-difference

Without reducing Equation (4.42g) to first order form and using the discretization

$$(\mu_{tt})^{-1}(\delta_{tt})\mathbf{v}^n + \mathbf{E}\delta_{t-}\mathbf{v}^n + \mathbf{F}\mathbf{v}^n = \mathbf{G}\delta_{t-}\mathbf{p}^n \tag{4.55}$$

one arrives at

$$\mathbf{W}^{n+1} = \mathbf{M}^{-1}(\mathbf{N}\mathbf{W}^n + \boldsymbol{\Omega}\mathbf{W}^{n-1} + \boldsymbol{\Pi}\mathbf{W}^{n-2}) \tag{4.56}$$

where $\mathbf{W}^{n+i} = \begin{bmatrix}\mathbf{v}^{n+i} & \mathbf{p}^{n+i}\end{bmatrix}^\top$ is used to simultaneously update the concatenation of variable vectors v_r and $J_\mathrm{r} \cdot \Delta p_\mathrm{tot}$ at the time step $n+i$, and J_r is a spread operator. The update matrices are

$$\mathbf{M} = \begin{pmatrix} \left[\mathbf{I} + \frac{k\mathbf{E}}{4} + \frac{k^2\mathbf{F}}{4}\right] & 0 \\ 0 & \left[-\frac{k\mathbf{G}}{4}\right] \end{pmatrix}, \mathbf{N} = \begin{pmatrix} \left[2\mathbf{I} - \frac{k\mathbf{E}}{4} - \frac{k^2\mathbf{F}}{2}\right] & 0 \\ 0 & \left[\frac{k\mathbf{G}}{4}\right] \end{pmatrix},$$
$$\boldsymbol{\Omega} = \begin{pmatrix} \left[-\mathbf{I} + \frac{k\mathbf{E}}{4} - \frac{k^2\mathbf{F}}{4}\right] & 0 \\ 0 & \left[-\frac{k\mathbf{G}}{4}\right] \end{pmatrix}, \boldsymbol{\Pi} = \begin{pmatrix} \left[\frac{k\mathbf{E}}{4}\right] & 0 \\ 0 & \left[-\frac{k\mathbf{G}}{4}\right] \end{pmatrix}, \tag{4.57}$$

4.4.7 Störmer-Verlet scheme

A straight forward discretization of the second-order modal equations that results in an inexpensive update can be achieved making use of the Störmer-Verlet in Equation (4.42g)

$$(\delta_{tt} + \mathbf{E}\delta_{t\cdot} + \mathbf{F})\mathbf{v}^n = \mathbf{G}\delta_{t\cdot}\mathbf{p}^n \tag{4.58}$$

can be recast in the compact matrix form as

$$\mathbf{W}^{n+1} = \mathbf{M}^{-1}(\mathbf{N}\mathbf{W}^n + \boldsymbol{\Omega}\mathbf{W}^{n-1}) \tag{4.59}$$

with

$$\mathbf{M} = \begin{pmatrix} \left[\frac{\mathbf{I}}{k^2} + \frac{\mathbf{E}}{2k}\right] & 0 \\ 0 & \left[-\frac{\mathbf{E}}{2k}\right] \end{pmatrix}, \mathbf{N} = \begin{pmatrix} \left[\frac{2\mathbf{I}}{k^2} - \mathbf{F}\right] & 0 \\ 0 & [\mathbf{0}] \end{pmatrix}, \Omega = \begin{pmatrix} \left[\frac{\mathbf{E}}{2k} - \frac{\mathbf{I}}{k^2}\right] & 0 \\ 0 & \left[-\frac{\mathbf{G}}{2k}\right] \end{pmatrix} \tag{4.60}$$

and $\mathbf{W}^n$ again contains a column vector that concatenates $\left[v_1^n, ..., v_\mathrm{Nm}^n, J_1\Delta p_\mathrm{tot}^n, ..., J_\mathrm{Nm}\Delta p_\mathrm{tot}^n\right]^\top$.

4.5 Validation

4.5.1 Numerical stability

The schemes proposed above may suffer from several sources of inaccuracy (such as numerical dispersion) and instability. In order to prove the feasibility of the scheme design, we performed convergence analysis of the numerical solutions. This is done

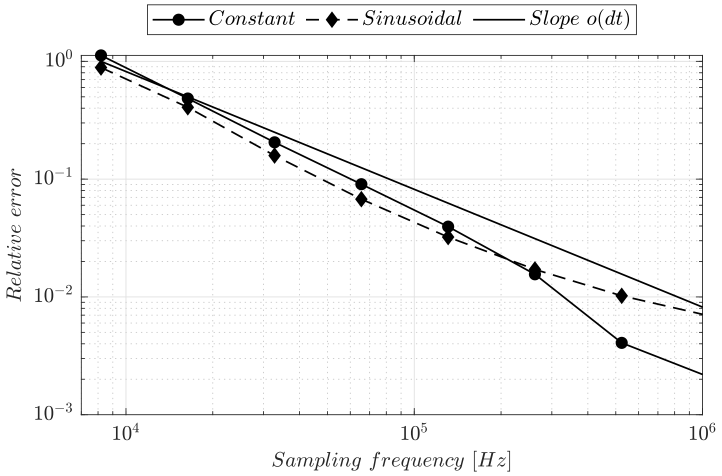

Figure 4.3: Convergence study of the resonator scheme (δ_{tt}, δ_{t-}, δ_{t-}) with constant and sinusoidal driving inputs. Numerical error is computed with respect to analytical solutions in Equation (4.15) and Equation (4.17).

for the entire system and for the individual elements of the update equations. A sample of the constants, geometry, and parameters used in simulation can be found in the instrument file in Appendix E.

The resonator is resolved without resorting to first-order reduction and numerical solutions are compared with the analytical expressions proposed (as per Equation (4.15) and Equation (4.17)). Convergence of the solution for increasing sampling frequency (diminishing sampling interval) is shown in Figure 4.3 for the resonator and for the full scheme in Figure 4.4 using δ_{tt} and δ_{t-} operators. In the case of the full update, the equations are discretized with forward Euler and the $p_f(t)$ input is replaced by the smooth, well-known forcing terms: namely, a constant input (of 500 Pa), a ramp from 200 Pa to 500 Pa, and a sinusoidal signal of amplitude 500 Pa and pulsation 0.5 Hz.

Simulations were run on MATLAB on a personal computer (Dell, Precision 7530) with an Intel i7 2.2 GHz and an Ubuntu 22.04.2 installation. Runtime for the sampling frequencies 2^{15} and 2^{21} spanned an average of 31.8 ms and 2.004 s, respectively. This means that the scheme whose convergence has been shown consistutes a feasible model for real-time implementation (47.3 ms per second of output simulated at audio rate).

4.5.2 Measurements

The numerical extraction of the resonator's modal parameters is performed over the modal decomposition approximation of the bore acoustic response, taking the form shown in Equation (4.7e) and Equation (4.9). The input impedance of a test pipe was measured with the help of the *CapteurZ* device (see [Le Roux et al., 2012] for construction and operation details) for the purpose of validating the analytical

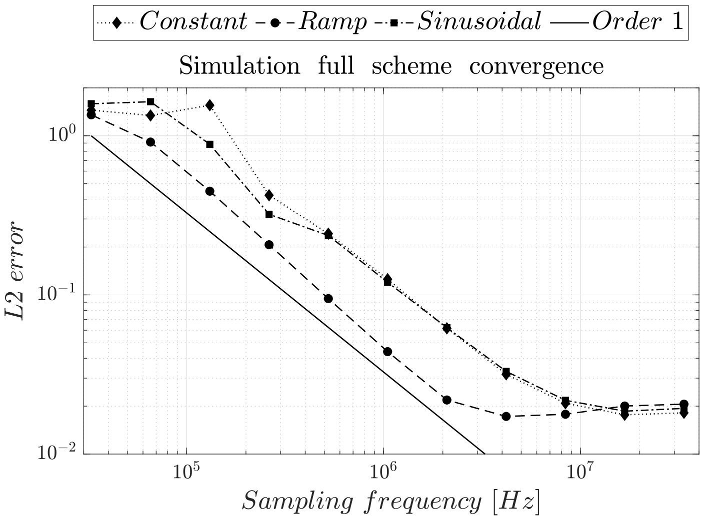

Figure 4.4: Convergence study of the full forward Euler scheme normalizing $L2$ errors by the reference numerical solution at ∼67 MHz, using 400 ms worth of steady-state mouth pressure signal. Slopes for the mid region of convergence are -0.95, -1.09, and -0.9, respectively, for constant, ramp, and sinusoidal forcing terms.

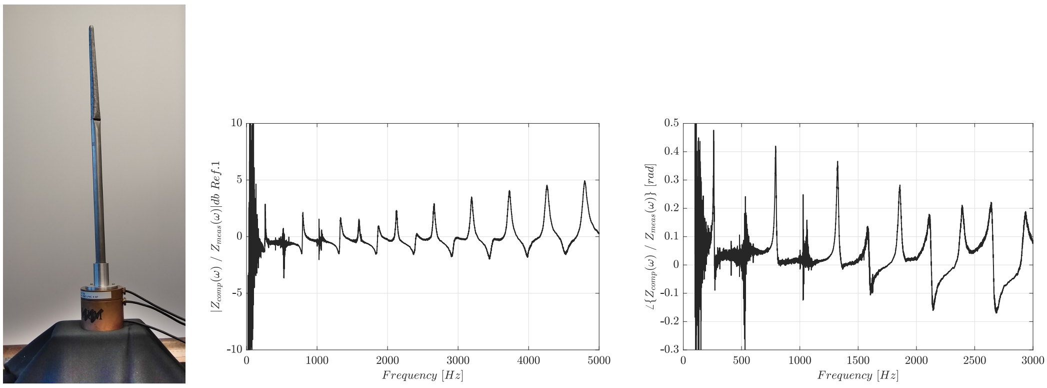

(a) Test pipe installed in the impedance measurement device

(b) Fitted magnitude error

(c) Fitted phase error

Figure 4.5: Input impedance measurement setup and fitting error of computed modal decomposition of the bore's response.

computation of the pipe's frequency response, followed by the numerical extraction technique of choice. The setup for said measurement can be seen in Figure 4.5a.

The *CapteurZ* device allows measurement of the global input impedance of the pipe (including the mouth's effect) from the passive end position of the resonator. The computed acoustic response can be assessed using measured data, if one does not account for the local radiation impedance at that boundary, which is *not-seen* by the two-microphone technique. The geometry of the test pipe is shown in Table 4.1.

Table 4.1: Geometry parameters of the test pipes and windchests. Units are expressed in mm unless stated otherwise. L_p and R_p are the length and radius of the pipe's resonator, respectively. Concerning the foot, L_f is its length, and $R_\mathrm{f,in}$ the radius of its inlet. H_m and W_m refer to the mouth's depth and cut-up distance (flue-to-labium), while h is the flue-way thickness (also called *lumière* by organ builders). The value of $h^\dagger$ is estimated during SS operation.

L_p	R_p	L_f	$R_\mathrm{f,in}$
318	8.9	189	2.2

H_m	W_m	$h^\dagger$	f_1
15.7	4.2	0.39	529 Hz

4.6 Summary and future perspectives

In this section, we have examined numerical aspects of time-domain implementation of the organ pipe simulation. We revisited the model equations and provided some criteria for oscillation and stability of solutions in continuous and discrete time.

We proposed three different numerical schemes for time integration of the pipe model as developed in previous sections: namely the forward euler, the implicit scheme by trapezoid rule, and the Störmer-Verlet. The emphasis to discuss such schemes is put in achieving low computational cost to solve the update of each scheme. Non-iterative methods are a suitable research direction to explore when algebraic equations require resolution by matrix system inversion. In the current case here, however, it is not extremely expensive to update the Jacobians for Newton-Raphson solvers, since only the scalar quadratic and delayed terms are non-constant.

A system matrix A in the form of a state-space formulation of the system was presented. Global stability of a system with non-linearities and delays is difficult, however some linearizations are possible. Examining stability of the numerial pipe model is virtually unfeasibly by traditional methods such us von Neumann analysis or energy conservation. Further work should examine growth bounds to the non-constant terms in the system matrix A in the state-space formulation: bounds to maximum pressure and oscillation amplitudes have been shown for the steady-state operation based on observation of measured data. Its physical significance needs to be linked to the role the play in justifying a well-posedness the matrix A.

By virtue of the Lax-Richtmyer theorem we have proven stability of the first scheme proposed. Showing convergence of the Störmer-Verlet and the trapezoid schemes becomes a task for further developments. Of course, solving implicitly will yield a more computationally expensive implementation. On the other hand, the stability of the Störmer-Verlet not being granted reduces the inexpensive options thus far to the forward Euler.

Assessment on whether higher order and multistep schemes, as well as the number of modes included, would be a desirable asset as to how realisitc and convincing the output of the simulations is. Not having conducted said study, we are currently working on five resonator modes. Of course again, increasing the order of the scheme and the modes will incur in more operations per second. It would be worth considering implementations such Bogacki-Shampine, RK4, and NDDE as referred in Chapter 2. However, such schemes would drift apart from attempting real-time.

Part II

Developments on buffet radiation and spaces

Chapter 5

Design of specific sources for the study of the cavities and radiation of organs

Contents

5.1 Introduction 91

5.2 Cylindrical wave propagation 93

5.3 Thiele-Small parameters 94

5.4 Application case 96

5.5 Cylindrical source 1: 1m speaker array 100

5.5.1 Directivity 100

5.6 Cylindrical source 2: for Notre-Dame de Paris, 2m speaker array 105

5.7 Summary 110

5.1 Introduction

The radiation of organ buffets will be studied in Chapter 6. Experiments have been carried that require adapted electro-acoustic sources. As a first step, 2D field approximations are considered in order to simplify the theoretical analysis of the internal acoustic field in the organ cavity as well as its radiation through the openings between the front pipes. Therefore, we developed electro-acoustic sources radiating 2D acoustic fields.

These sources are designed as vertical arrays of loudspeakers, with length adapted to the vertical dimension of the organ cavity. The vertical array of speakers is therefore positioned between two reflecting baffles, embodying an infinite vertical source radiating a perfectly 2D field. The design of a source for the work developed here responds an application-specific need to reduce the complexity of concurrent multiple phenomena. We will justify the reasons that conditioned our source design choice and models.

Problem statement Firstly, the complex internal field has to be characterized in terms of the cavity and radiation through the façade. Secondly, the ensemble of source-cavity-radiation approaches alternate in a succession of 2D-3D approximations, both in analytical and experimental cases. The global model for the 2D problem is to be extrapolated to 3D problem, extending the theorety exploited and the measurement findings.

The modeling and experimental workflow that we follow starts by the conception of a 2D source. This offers the possibility of considering a two-dimensional reduction of the cavity and slit problem. However, in the actual experimental conditions this has to match a 3D field for various reasons: we can not have infinite planes bounding the source (for certain frequencies); secondly, the radiation through the slits, again has to match a 3D space: i.e. we can reduce the complexity of the model to unblock the understanding of the radiation phenomena from façade systems, but the space where it occurs is eventually three-dimensional, therefore, model behaviour has to be extrapolated to the third vertical dimension eventually. Indeed, lastly, those conditions led to the start point of this study by characterizing the designed sources in the laboratory by matching the three-dimensional space: that is, without bounding them. The behaviour in vertical measurements will exhibit the spatial truncation effect when the source is not baffled (top and bottom), with a monopolar behaviour in low frequencies. One may also expect that the behaviour with distance, when driving the whole array of the 1 m source, will show a transition from 2D to 3D characteristics.

Thirdly, the electro-acoustic description, the pressure, and power delivered by the sources are conditioned by the dimensional scope of the problem. We will show that the pressure amplitude delivered at a given frequency by a 2D or 3D source of comparable parameters differ in such way that achieving the same level with a 3D source would incur in material and portability limitations.

The monopolar source delivering an acoustic power $\mathcal{P}$ sees a rapid decay per unit area when compared with a cylindrical source, forcing the design of the point source into significantly larger proportions affecting, first of all, proportions of membrane size and drawn current. The cylindrical source, on the other hand, allows the use of smaller speaker drivers, which in sum and bounded by reflector top and bottom cavity walls, leads to more portable design realizations. In addition, leveraging from the use of said reflectors (usually floor and ceiling of an organ internal section) allow for assumptions of vertically infinite sources.

Design, realization, and characterization. Cylindrical sources will be developed in this study, and its electro-acoustic considerations when mounted on cabinets are inspected as to their global response. We arrive at a radiated pressure field (under $kr \gg 1$ assumption) that will be used to establish linear operation regime of sources in the laboratory and in-situ. The range of operation during measurements is reported subsequently. To conclude, the behaviour of the two source realizations were tested in laboratory conditions and the results are shown.

5.2 Cylindrical wave propagation

Following [Bruneau, 2006], let us assume a coordinate system base $\vec{e} = (\vec{e}_r, \vec{e}_\varphi, \vec{e}_z)$ for the spatial variables (r, φ, z) used in the separable potential

$$\Psi = R(r)\Phi(\varphi)Z(z)T(t) \tag{5.1}$$

The wave equation in cylindrical coordinates may be factored in the following way

$$\frac{1}{R}\frac{d^2}{dr^2}R + \frac{1}{rR}\frac{d}{dr}R + \frac{1}{r^2\Phi}\frac{d^2}{d\varphi^2}\Phi + \frac{1}{Z}\frac{d^2}{dz^2}Z = \frac{1}{c^2T}\frac{d^2}{dt^2}T = -k^2 \tag{5.2}$$

$$\frac{1}{R}\frac{d^2}{dr^2}R + \frac{1}{rR}\frac{d}{dr}R + \frac{1}{r^2\Phi}\frac{d^2}{d\varphi^2}\Phi + k^2 = -\frac{1}{Z}\frac{d^2}{dz^2}Z = k_z^2 \tag{5.3}$$

$$\frac{r^2}{R}\left(\frac{d^2}{dr^2} + \frac{1}{r}\frac{d}{dr}\right)R + (k^2 - k_z^2)r^2 = -\frac{1}{\Phi}\frac{d^2}{d\varphi^2}\Phi = m^2 \tag{5.4}$$

leading to the separated variable equations having solutions expressed as

$$T = e^{j\omega t}, \qquad \text{solving} \quad \frac{d^2}{dt^2}T + \omega^2 T = 0, \qquad \text{with} \quad \omega^2 = k^2c^2 \tag{5.5}$$

$$Z = \alpha_1 e^{jk_z z} + \beta_1 e^{-jk_z z}, \qquad \text{solving} \quad \frac{d^2}{dz^2}Z + k_z^2 Z = 0 \tag{5.6}$$

$$\Phi = \alpha_2 e^{jm\varphi} + \beta_2 e^{-jm\varphi} \tag{5.7}$$

With integer m, Φ is 2π-periodic. Further letting $k_w^2 = k^2 - k_z^2$ leads to

$$\left(\frac{d^2}{dr^2} + \frac{1}{r}\frac{d}{dr}\right)R + \left(k_w^2 - \frac{m^2}{r^2}\right)R = 0 \tag{5.8}$$

which is a cylindrical Bessel equation with solutions

$$R(r) = A_1 J_m(k_w r) + A_2 N_m(k_w r) \tag{5.9}$$

$$R(r) = B_1 H_m^+(k_w r) + B_2 H_m^-(k_w r) \tag{5.10}$$

with J_m being bessel of first kind, N_m bessel of second kind, $H_m^\pm$ convergent and divergent Hankel functions of order m. The first kind of solutions are ruled out since they diverge at the origin. From the second set of solutions, we keep the divergent Hankel's and derive the approximation

$$H_m^-(x) \approx \sqrt{\frac{2}{\pi x}}e^{-j\left[x-(2m+1)\frac{\pi}{4}\right]} \tag{5.11}$$

for $x > m \geq 1$ and $x \gg 1$ if $m = 0$.

For an infinitely long cylinder with radius a and pulsation ω, the surface vibration velocity is

$$v = \left[\frac{\partial}{\partial r}\varphi\right]_{r=a} = V_o cos(k_z z)e^{j\omega t} \tag{5.12}$$

with no φ-dependency and letting $k_z = 0$ for a z-constant plane of wave propagation, making then $k_w^2 = k^2$. If the radius of the cylinder is small enough ($k_w a \ll 1$),

$$\frac{\partial}{\partial r}H_o^-(ka) = -kH_1^-(ka) \approx -\frac{2j}{\pi a} \tag{5.13}$$

$$p \sim \frac{1}{4}k\rho_o c_o Q_o H_o^-(kr) \tag{5.14}$$

using $Q_o = 2\pi a V_o$ a linear flux (per unit length). The near-field approximation ($kr \ll 1$) leads to

$$p \sim \frac{1}{4}k\rho_o c_o Q_o \left(1 + \frac{2j}{\pi} ln\frac{2}{1.78kr}\right) e^{j\omega t} \tag{5.15}$$

The far-field ($kr \gg 1$) thus writes as

$$p \sim \frac{1}{4}k\rho_o c_o Q_o \sqrt{\frac{2}{\pi kr}} e^{-j(kr-\pi/4)} e^{j\omega t} \tag{5.16}$$

and the radiation impedance

$$Z_{a,lin} = \frac{p}{L_z v} = \frac{p}{L_z V_o} = \frac{1}{4}k\rho_o c_o 2\pi a \left(1 + \frac{2j}{\pi} ln\frac{2}{1.78ka}\right) \tag{5.17}$$

5.3 Thiele-Small parameters

In order to be able to estimate the characteristics of the sources to be designed, it is necessary to establish some useful terminology, adopting for that the Thiele-Small parameters (TSP, [Leach, 2003],[Rossi, 1988]). See Figure 5.1 for reference. Let us start from the analysis of a single loudspeaker. The main elements are a voice coil attached to a conical membrane. The coil is inserted in a magnetic gap. The coil and the membrane are attached to a frame mainly by a a flexible rim around the largest diameter of the cone; the coil and the narrow base of the cone are suspended by the *spider*. The coil is topped with a dust cap to avoid debris to enter the gap and at the other end of the axis of symmetry one may usually find a vent in the magnet. The set of manufacturing parameters, some of them easily measurable, are

- S_d: effective surface of the radiating piston [m^2]
- M_{ms}: total mass of the vibrating components: diaphragm, coil, and acoutic load [kg]
- C_{ms}: compliance (stiffness inverse) of the driver's suspension [$\mathrm{N\,m^{-1}}$]
- L_e: voice coil inductance at 1 kHz [mH]

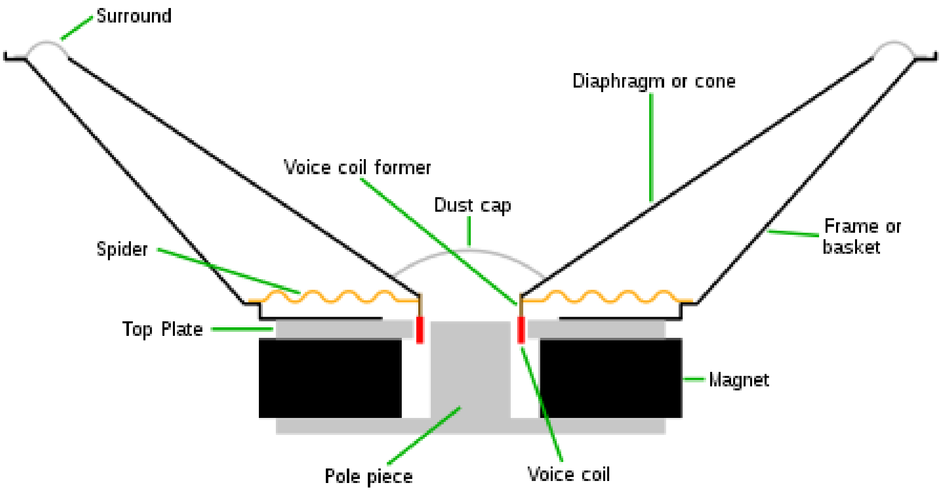

Figure 5.1: Section view of a driver. Image credit: ToutLeHautParleur online.

- R_e: DC resistance of the voice coil [Ω]
- B_l or $B \cdot l$: magnetic field force in the gap times the length of the coil [T m]
- R_{ms}: Mechanical (kinetic) resistance of the suspension [$\mathrm{N\,s\,m^{-1}}$] or [$\mathrm{kg\,s^{-1}}$]
- X_{max}: maximal cone excursion within linear regime
- X_{mech}: threshold for mechanical damage (within non-linear regime)
- $V_d = S_d \cdot X_{max}$: peak volume displacement in linear regime

The frequency of resonance of the speaker suspended in free air, at which one sees the maximal velocity of the mobile parts, is referred as f_s:

$$f_s = \frac{1}{2\sqrt{C_{ms} M_{ms}}} \tag{5.18}$$

Intuitively, f_s will decrease for increasing values of the total mass of mobile parts (M_{ms}) and for increasing values of the suspension compliance (C_{ms}). Drivers may be crudely categorized by their range of operation:

- Bass: 13 Hz to 60 Hz
- Mid range: 60 Hz to 500 Hz
- Tweeter: 500 Hz to 4000 Hz

When the speaker is excited by a current passing the coil, the damping for the mechanical elements and electric components is expressed by the following quality factors

$$Q_{es} = \frac{2\pi f_s M_{ms} R_e}{B_l^2} = \frac{R_e}{B_l^2}\sqrt{\frac{M_{ms}}{C_{ms}}} \tag{5.19}$$

$$Q_{ms} = \frac{2\pi f_s M_{ms}}{R_{ms}} = \frac{1}{R_{ms}}\sqrt{\frac{M_{ms}}{C_{ms}}} \tag{5.20}$$

$$Q_{ts} = \frac{Q_{ms} Q_{es}}{Q_{ms} + Q_{es}} = \frac{R_e}{R_{ms} + B_l^2}\sqrt{\frac{M_{ms}}{C_{ms}}} \tag{5.21}$$

Lastly, when suspended in free air, the parameter V_{as} represents the equivalent volume of air opposing the same stiffness as the driver's suspension. When a driver is mounted on a cabinet to isolate the sound radiated by the rear side of the speaker, charges apply to the performance of the speaker: most importantly, the volume of air contained by the cabinet, exerting a stiff-like compressive force that opposes the displacement of the membrane.

5.4 Application case

In our current source realisations, we systematically considered the case of driving N speakers. Such choice allows, on the one hand, to know the equal current through all of speakers, and on the other hand, the knownledge the all the components of the source array will be operating in phase and exerting the same force against the media. The force on the n^{th} speaker ($n = \{1, ..., 10\}$ and $n = \{1, ..., 18\}$ for the realisations discussed later) under a current i is

$$f_n = Bli \tag{5.22}$$

The response of the n^{th} speaker is $\dot{x} = f_n H(\omega)$, where $H(\omega)$ is

$$H(\omega) = \frac{1}{j\omega M_{ms} + R + \frac{K}{j\omega}} = H_o \frac{j\omega/\omega_o}{1 + \frac{j\omega}{Q_b \omega_o} - \frac{\omega^2}{\omega_o^2}}$$

with

$$H_o = \frac{1}{\sqrt{K M_{ms}}} \qquad Q_b = \frac{\sqrt{K M_{ms}}}{R_e}$$

K is the stiffnes (inverse of compliance, $K = 1/C_{ms}$). The total acoustic flux is $q_{tot} = N S_d H Bli$ and the forces present on one speaker are

- The radiation impedance (per unit length, and using the $kr \ll 1$ approximation): $Z_a = \frac{p}{lv} \sim \frac{1}{4} k\rho_o c_o 2\pi a \left\{1 + \frac{2j}{\pi} ln\left(\frac{2}{1.78ka}\right)\right\}$ with l the vertical length of the source of radius a.
- The suspension reaction of compliance C_{ms}.
- The internal pressure of the cabinet.

From [Rossi, 1988], the air of mass inside the cabinet has an equivalent compliance

$$C_{ab} = 1.4\frac{V_b}{\rho c^2} \tag{5.23}$$

The volume displaced by one speaker's membrane is $dV = NxS_d$, where there are N speakers, and x is the membrane displacement of each one (having $x_{tot} = Nx$). Using the law of gases $PV^\gamma = \mathcal{C}^{onst.}$, the variation of volume may be expressed as

$$\frac{dP}{P_o} = -\gamma\frac{dV}{V_o} \tag{5.24}$$

giving for the pressure

$$p = \frac{\gamma P_o}{V_o}NxS_d \tag{5.25}$$

The force *felt* behind each speaker as if there was a lumped contribution of individual volume of air behind each one is

$$p \cdot S_d = \frac{\rho c_o^2}{V_o}NxS_d^2 = \rho c_o^2\frac{N}{V_o}xS_d^2 \tag{5.26}$$

The resonance frequency of N speakers and one cabinet is equal to the resonance frequency of one speaker and one cabinet multiplied by a factor V_o/N. The cuttof frequency f_c with a cabinet relates these frequencies as

$$\frac{f_c}{f_{s,cab}} = \sqrt{1+\alpha}, \qquad \alpha = \frac{C_{as}}{C_{ab}} \tag{5.27}$$

using C_{as} as the compliance of the suspension and C_{ab} that one of the cabinet; $f_{s,cab}$ is the frequency of resonance of the speaker mounted on an infinite baffle (generally reported by the manufacturer). C_{as} is found from the equivalent volume V_{as} reported by the manufacturer as well. The effect of the cabinet increases the resonance frequency of the system, thus limiting the bandwidth available in the low frequencies.

Radiated pressure ($kr \gg 1$):

$$p \sim \frac{1}{4}k\rho_o c_o Q\sqrt{\frac{2}{\pi kr}}e^{-j(kr-\frac{\pi}{a})}e^{j\omega t} \tag{5.28}$$

with the volume flux $Q = NS_dH(\omega)Bli$. The units of the transfer function $H(\omega)$ are velocity per N. In the bandwidth, it is approximated as

$$H(\omega) \approx \frac{1}{j\omega M_{ms}} \tag{5.29}$$

therefore

$$p \sim \frac{1}{4}\frac{\rho}{M_{ms}}NS_dBli\sqrt{\frac{2}{\pi kr}}e^{-jkr}e^{j\omega t} \tag{5.30}$$

For a total sum of N sources, in the bandwidth, $i \approx U_{rms}/(NR_e)$, which after substitution results in

$$p_{rms} \approx \frac{1}{4}\frac{\rho S_d Bl U_{rms}}{M_{ms}R_e}\sqrt{\frac{2}{\pi kr}}e^{-jkr}e^{j\omega t} \tag{5.31}$$

Numerical application. Monacor 80 W has a power handling capacity of $\mathcal{P}_{nom}$ per each speaker and maximum voltage delivering that power may be derived following

$$\mathcal{P}_{nom} = \frac{1}{2}\frac{U^2}{R_e} \quad \rightarrow \quad U_n = \sqrt{2\mathcal{P}_{nom}R_e}$$
$$U_{tot} = NU_n = N\sqrt{2\mathcal{P}_{nom}R_e}$$

Case of the Monacor speaker array ($\mathcal{P}_{tot} = 10 \cdot 80\,\mathrm{W} = 800\,\mathrm{W}$):

$$U_{max} = 10\sqrt{2 \cdot 80\,\mathrm{W} \cdot 6\,\Omega} = 357\,\mathrm{V}$$

Case of the Aura Sound:

$$U_{max} = 18\sqrt{2 \cdot 15\,\mathrm{W} \cdot 6.4\,\Omega} = 249\,\mathrm{V}$$

Finally, the radiated pressure at 1 m is found for the Monacor as

$$p \sim \left[\frac{1}{4}\frac{\rho S_d BlU}{M_{ms}R_e}\sqrt{\frac{2}{\pi kr}}\right]_{r=1\,\mathrm{m}, f=1\,\mathrm{kHz}} \approx 18\,\mathrm{Pa}$$
$$\mathrm{SPL} = 120\,\mathrm{dB@1\,m}$$

Having measured an SPL level of 97 dB at 1 m ($U_{rms} = 15.28\,\mathrm{V}$, with white noise), we had ∼25 dB of head-room during which the source is behaving linearly but providing a high pressure amplitude.

The same procedure with the Aura Sound source can deliver 114 dB for 1 kHz at 1 m. Measurement applications of such source showed an SPL of 92.5 dB at 1 kHz ($U_{rms} = 3.39\,\mathrm{V}$) and a peak of 88 dB during a sine sweep. For comparison, the pressure delivered by the omnidirectional source employed in other measurements (see §6.7.1), was 78.5 dB at 1 kHz at 1 m ($U_{rms} = 3.37\,\mathrm{V}$).

The range of operation during radiation measurements was estimated calculating the delivered pressure by the sources during sine sweeps in the vicinity of 1 kHz. The 1 m speaker array delivered ∼95 dB during measurements in the anechoic chamber without walls and cylinders at a distance of 2 m from the source. The 2 m source delivered ∼100 dB at a distance of 1.7 m inside the buffet of the Notre-Dame de Paris (NDP) organ.

Relevant parameters to characterize. In our next experiments to model and assess the radiation of organ-like cavities, we will make use of a cylindrical source approximation. This was chosen so that the complexity of problems could, at least, be consired in terms of a two-dimensional radiation and scattering problem.

In order to proceed in that direction, we considered plausible measurement setups (actual organs) and laboratory idealizations of them. In order to excite such cavities, we built two vertical arrays of speakers wired in series: under the assumption of a pulsating cylinder, its entire surface displacement is expected to be the same at any point for a given frequency.

In reality, our closest implementation of a pulsating cylinder is the one-face vertical speaker array. Under low frequency approximations, we will verify that this vertical array shows a behaviour similar to a pulsating cylinder. However, for higher frequencies, the directivity of the vertical array increases in the plane normal to the array axis as predicted by theory of a plane rectangular radiator ([Junger and Feit, 1993]). Therefore, the source directed towards the region of interest under measurement. The discrete array of speakers needs some characteristics assessed before one can take them to the field:

- The radial directivity
- The efficiency or SPL delivered for a given voltage V (discussed above)
- The frequency response of the source
- The spatial deliverance due to the vertical truncation
- The decay rate at a given distance r'

The laboratory source measurements and the assembled devices is shown in Figure 5.2. Technical documentation of the drivers used is provided in Appendix A.

(a) The 1 m source measurements driving 18 speakers

(b) The 2 m source during directivity measurements at a distance of 1 m at four different vertical alignments

Figure 5.2: Setup of the measurement of the cylindrical sources.

5.5 Cylindrical source 1: 1m speaker array

5.5.1 Directivity

The differences in directivity of driving the top speaker only or the array measured at a distance of 0.2 m is shown in Figure 5.3.

Even though the speaker arrays are designed to generate a 2D field when inserted between two parallel baffles, their radiation properties are first studied in 3D free field to avoid resonances induced by reflections at the end of the baffle.

We investigate the pressure provided by the baffled piston and compare it with a set of ka frequencies for a range of distances. Given that the measurements are taken at distances larger than ten times the speaker radius, we only observe a near-field extrapolation of the far-field approximation of the plane-piston

$$p(r,\theta) = \frac{1}{2} j\rho U_o \frac{a}{r} ka \left[\frac{2J_1(kasin\theta)}{kasin\theta}\right] e^{j\omega t} e^{-jkr} \tag{5.32}$$

of the speaker as per [Kinsler et al., 2000], where the vertical measurement angle on-axis was $\theta = 0$, thus the directional term tends to unity. See measured results

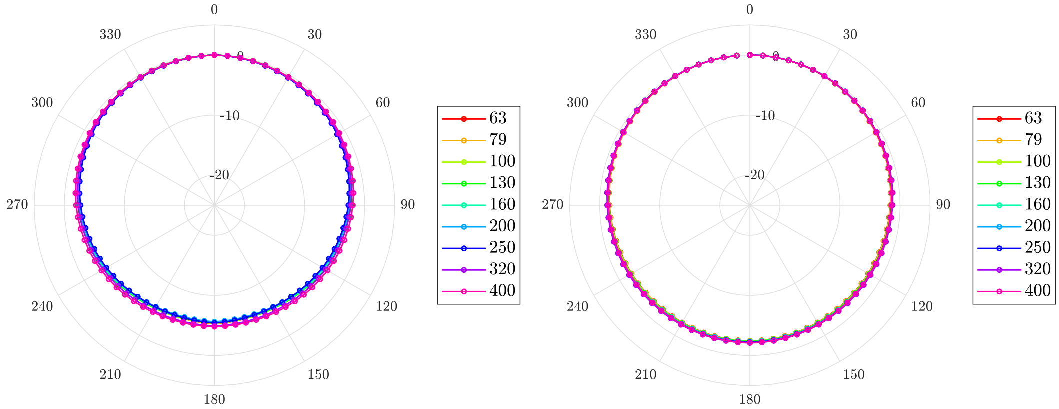

(a) Low frequencies driving one speaker. (b) Low frequencies driving full source.

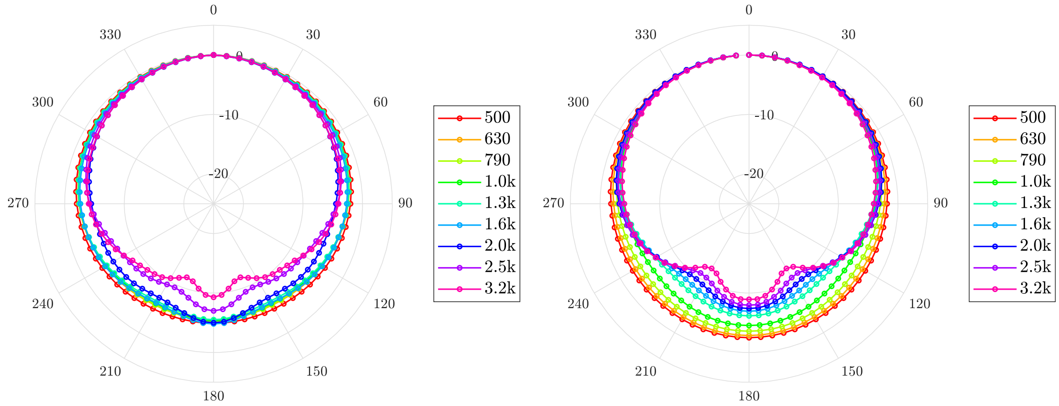

(c) Mid frequencies driving one speaker. (d) Mid frequencies driving full source.

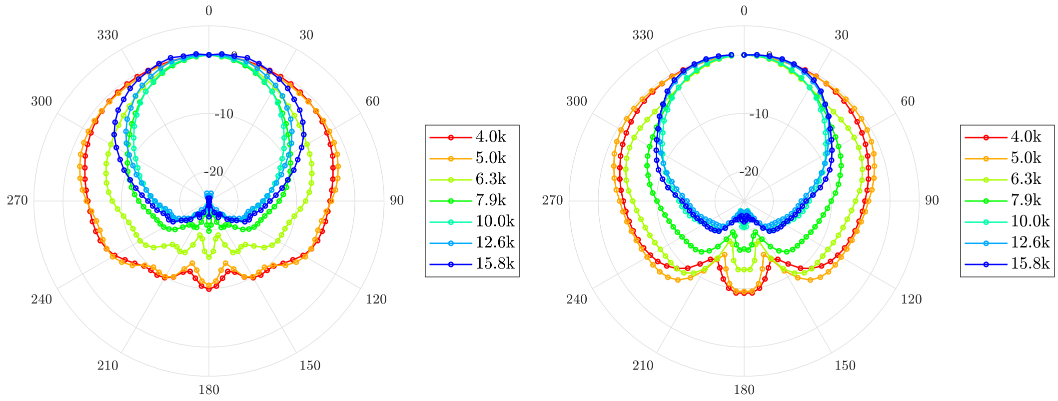

(e) High frequencies driving one speaker. (f) High frequencies driving full source.

Figure 5.3: Measured directivity of the 1 m source at 0.2 m, analyzed in thirds of octave bands. Left: single speaker. Right: full array measured at half height. Normalized data at 0° per band.

in Figure 5.7, where a unitary surface velocity was used. If we seek to provide a numerical response of the ensemble of the source, using the Rayleigh integral

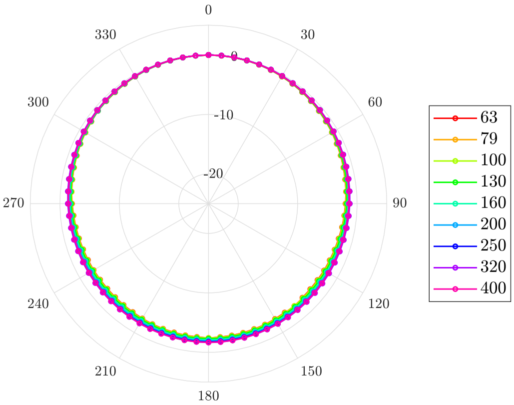

(a) Low frequencies

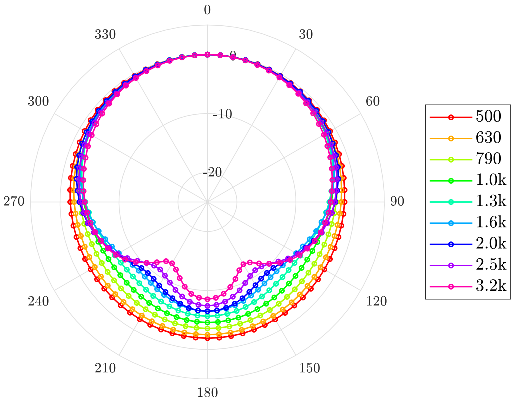

(b) Mid frequencies

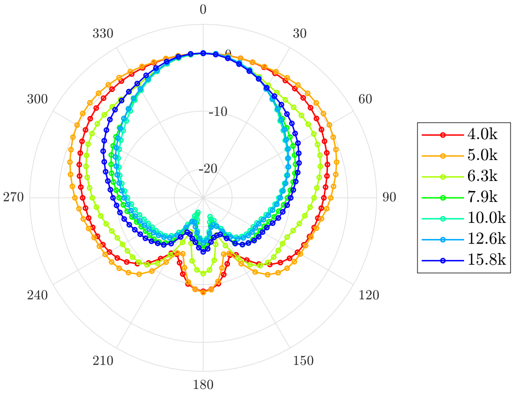

(c) High frequencies

Figure 5.4: Directivity of the 1 m source full array measured at 4 m, analyzed per thirds of octave band.

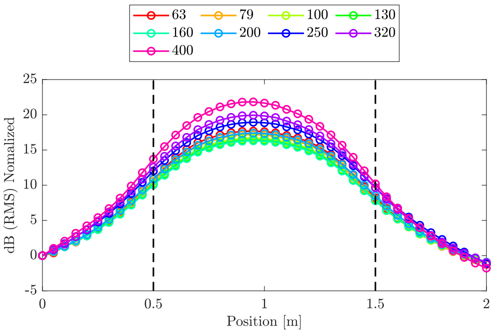

(a) Low frequencies (63 Hz to 400 Hz)

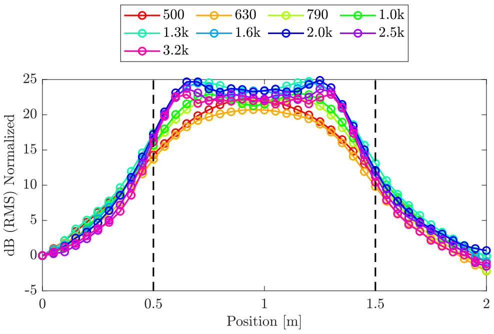

(b) Middle frequencies (0.5 kHz to 3.2 kHz)

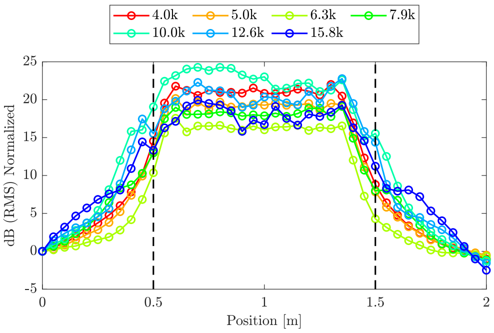

(c) High frequencies (4 kHz to 15.8 kHz)

Figure 5.5: Measured vertical response of the 1 m source due to the spatial truncation effect when measured in a 3D space instead of embeded between two parallel *infinite* planes. Data analyzed in thirds of octave bands. The dashed black line indicates the range of acquisition locations in front of the source. Normalized data at 0° per band.

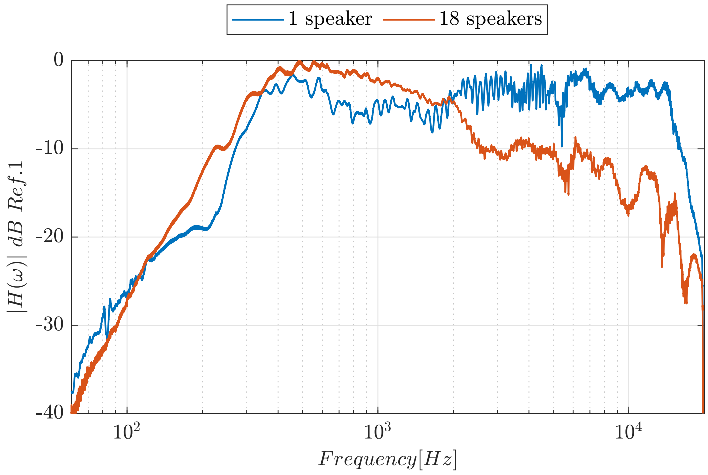

Figure 5.6: Normalized to *max* 0 dB measured pressure spectra of the 1 m source at 1 m distance driving one speaker and the full source.

and the data from one driver (from measurements and technical specifications by the manufacturer), one may preliminarily propose that the radiating surface moves uniformly with a speed

$$U_o(\omega) = \dot{X}(\omega) \tag{5.33}$$

where x is the speaker's membrane displacement. In frequency domain, the membrane's displacement can be expressed, using Thiele-Small parameters, as

$$X(\omega) = \frac{B_l}{\frac{1}{C_{ms}} + j\omega R_{ms} - \omega^2 M_{ms}} I(\omega) \tag{5.34}$$

with $I(\omega)$ being the input current. Therefore, the membrane velocity amplitude becomes

$$\dot{X}(\omega) = \frac{j\omega B_l}{\frac{1}{C_{ms}} + j\omega R_{ms} - \omega^2 M_{ms}} I(\omega) \tag{5.35}$$

The Rayleigh integral was also implemented by importing the a mesh from Gmsh of 10 drivers to MATLAB and exploiting dS as surface element.

5.5.1.1 Distance: One speaker versus full array

In one of the experimental configurations, we measured the 1 m Aurasound array driving only one of the speakers. The decay ratio with distance expected responds to the point source. The measured results are well predicted by the theoretical asymptotic approximation

$$P(r, \theta = 0) = 2\rho c_o U_o |sin\{0.5kr[\sqrt{1 + (a/r)^2} - 1]\}| \tag{5.36}$$

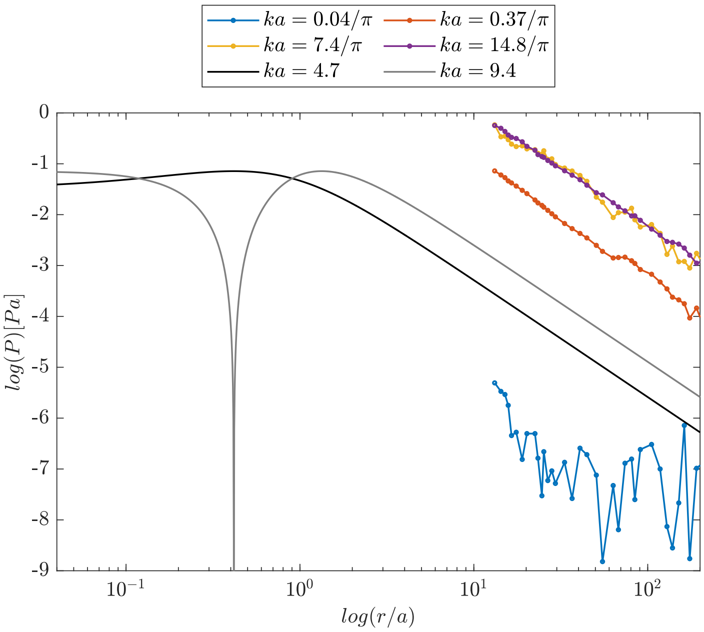

Figure 5.7: Pressure of the baffled speaker of radius $a = 25.5\,\text{mm}$ as a function of the r/a distances for $ka\pi = \{0.04, 0.37, 7.4, 14.8\}$. Far-field approximation similarity of the measured piston-like radiator. Measured pressure at 1 m driving only the top speaker of the array. The solid black and gray lines are computed from theory for $ka = 4.7$ and $ka = 9.4$.

$$p(r) = \frac{1}{2}\rho c_o U_o \frac{ka^2}{r} \qquad , for \quad r/a \gg 1 \tag{5.37}$$

as seen in Figure Figure 5.7. When the full array of 18 speakers is driven, the response with distance is no longer predicted by the point source approximation as is visible in Figure 5.8. The phase interference by multiple sources driven in-phase hardly show monotonical decrease of pressure with doubling distance in the vicinity of the source and for mid- and high frequency ranges. The constant slope for the single-drive is consistent with theory and the 18-speaker array behaves similarly for the low frequencies. The mid frequencies of the full array display, starting at the sub band of 1.6 kHz, distinct behaviours between the Fresnel region and the far-field. The highest frequency bands (10 kHz to 15.8 kHz) show a reasonably predictable behaviour, given the accuracy we are able to resolve, for distances $r' > 36R_n$ (where R_n is the nominal radius of the speaker membrane).

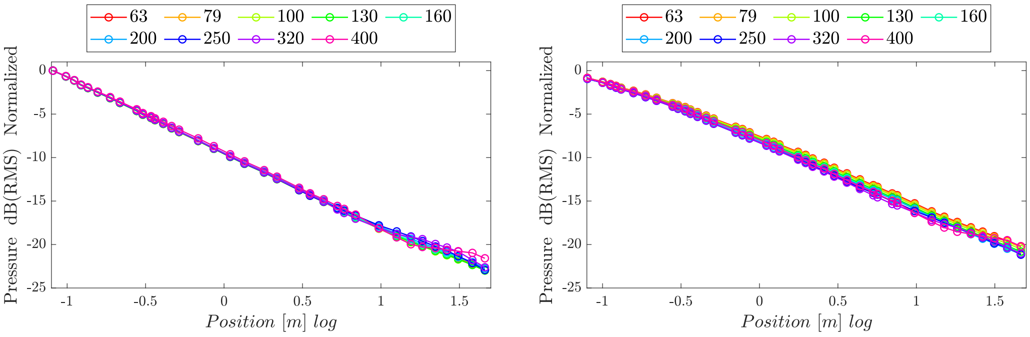

(a) Low frequencies. Top driver.

(b) Low frequencies. Full source.

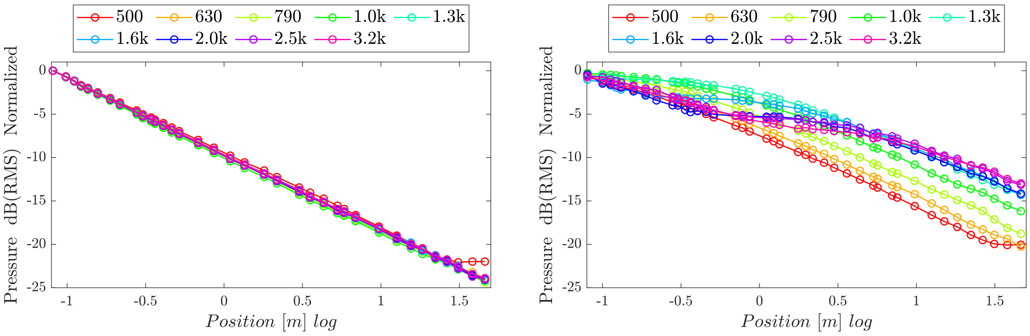

(c) Mid frequencies. Top driver.

(d) Mid frequencies. Full source.

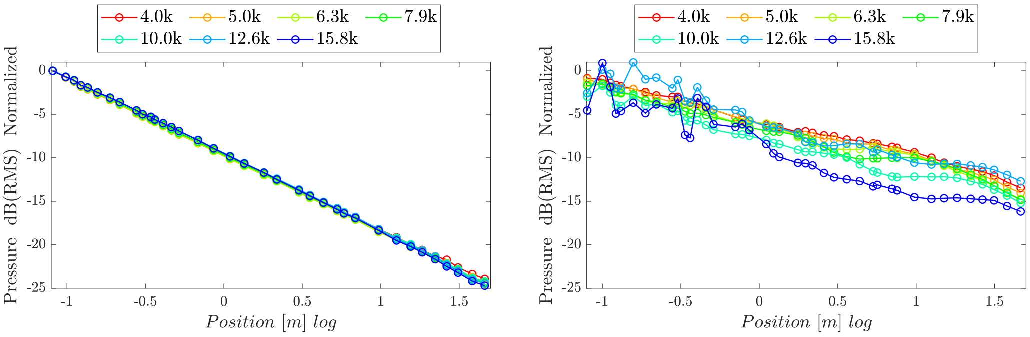

(e) High frequencies. Top driver.

(f) High frequencies. Full source.

Figure 5.8: Measured pressure decay of the 1 m source as a function of distance per sub-octave bands. Left: driving only the top speaker of the array. Right: driving the full source.

5.6 Cylindrical source 2: for Notre-Dame de Paris, 2m speaker array

The tribune organ in the cathedral of Notre-Dame de Paris (NDP) was emptied for restoration and decontamination purposes, as a result of the fire that took accident in 2019. As a consequence, all the interior pipes and windchests were removed leaving only the largest pipes of the façade in place. This proposes a façade approximation measurement. We chose the first internal floor of windchests (out of four) to carry out our measurements, provided that the top and bottom woodwork was the most regularly distributed, and thus the most similar to the two-dimensional parallel-baffle model described analytically above and used in the laboratory organ buffet idealization (to scale).

For that we conceived a 2 m tall source, configured as a vertical array of 10 165 mm diameter speakers (Monacor, SPH-165CP, see Appendix A). We characterize the behaviour of such source next. The aspects considered, after our previous smaller case investigations were:

- Directivity: Figures 5.9 and 5.10.
- Frequency response: Figure 5.11.
- Third-octave band rms-normalization of vertical response on-axis with different features: cone-center, membrane edge, and space between speakers. Figure 5.12.

The four measurement locations vertically aligned at 1 m in front of the NDP source are assessed by sub-octave bands in Figure 5.12 showing negligible variation (the largest corresponding to the alignment with a membrane edge). This may be compared with the frequencies for which the propagation front can be assumed flat in the 1 m laboratory source in Figure 5.5, where the largest variation within one band is ± 0.7 dB.

Spectral differences for driving one or two halves of the NDP source array in 5.11 may be explained by the assymetry of the microphone placement for the first case, where phase interference due to different arrival times is accentuated.

The acoustic efficiency of the source once fixed all parameters (closed cabinet and addition of an input resistance of $1\,\Omega$ for closer match of the amplifier impedance, thus avoiding modifications on the Q-factor of the speaker) was SPL of 96 dB at $15\,\mathrm{V}_{rms}$ when driving the source with a sinusoid at 1 kHz (applying zero-weight to the SPL measurement).

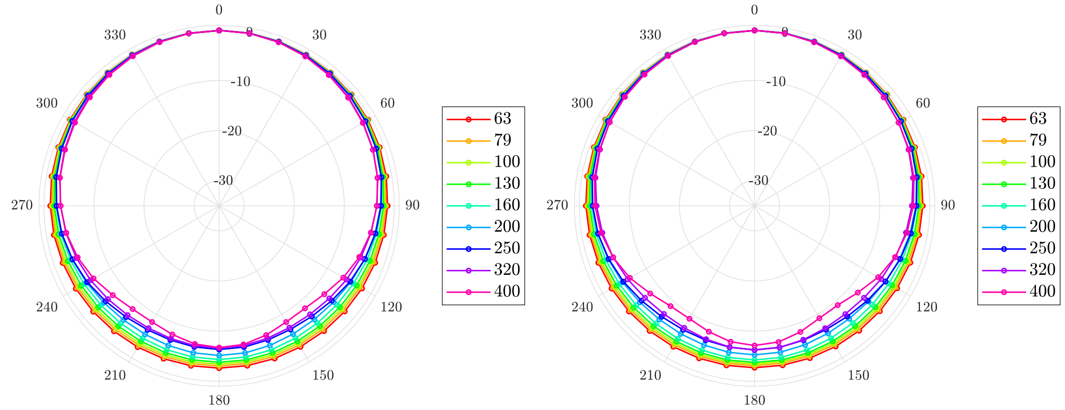

(a) Low frequencies. Position 1. **(b)** Low frequencies. Position 2.

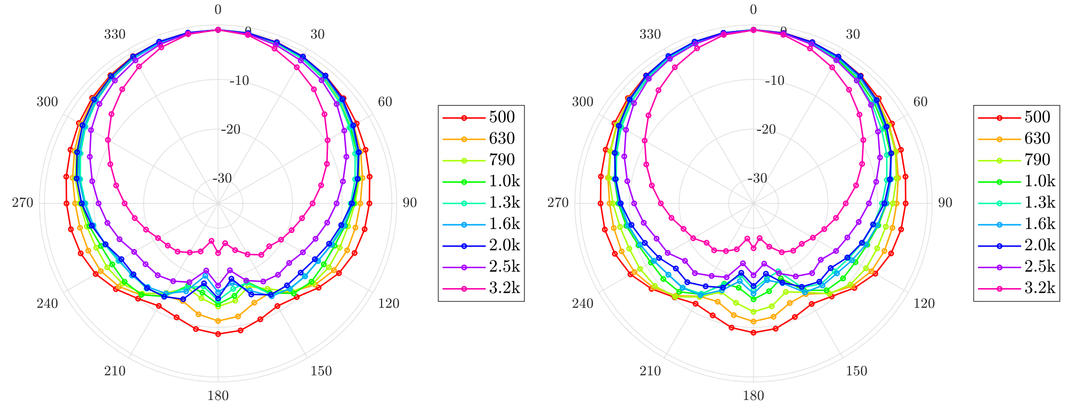

(c) Mid frequencies. Position 1. **(d)** Mid frequencies. Position 2.

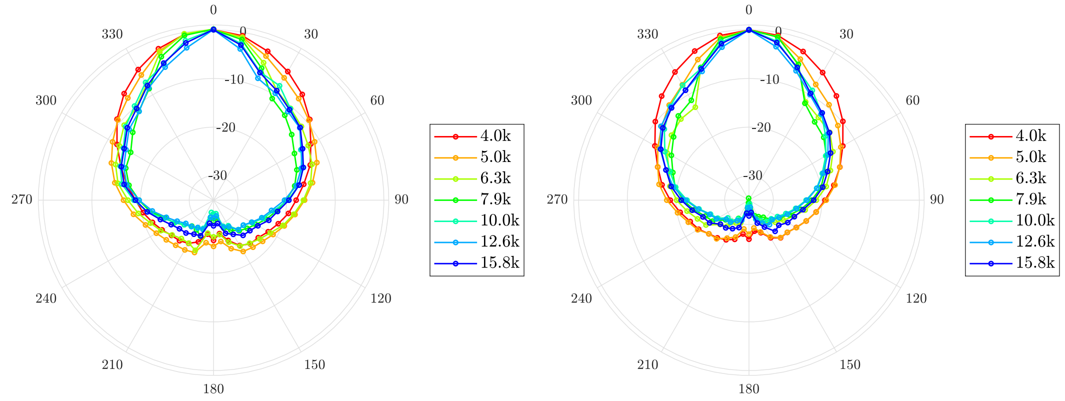

(e) High frequencies. Position 1. **(f)** High frequencies. Position 2.

Figure 5.9: Directivity of the 2 m source measured at 1 m. On the left: on axis with the membrane cone of the speaker immediately below half the height of the source. On the right: on axis with the membrane edge of the speaker immediately below half the height of the source.

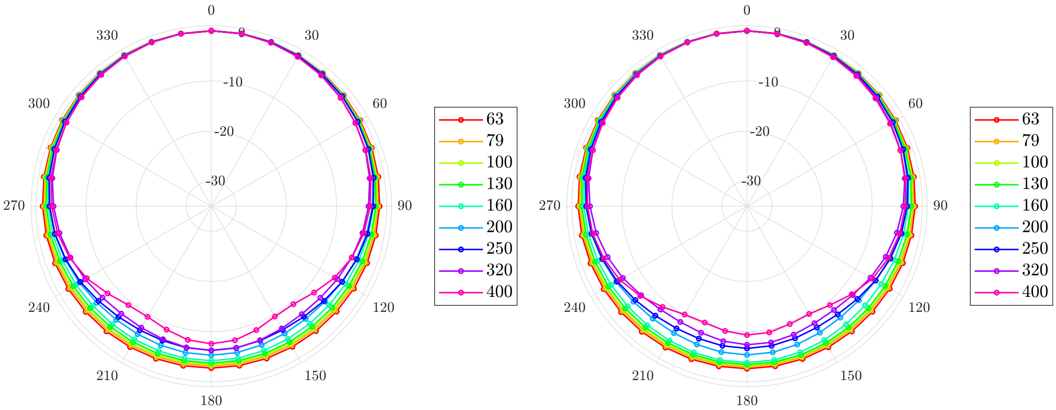

(a) Low frequencies. Position 3.
(b) Low frequencies. Position 4.

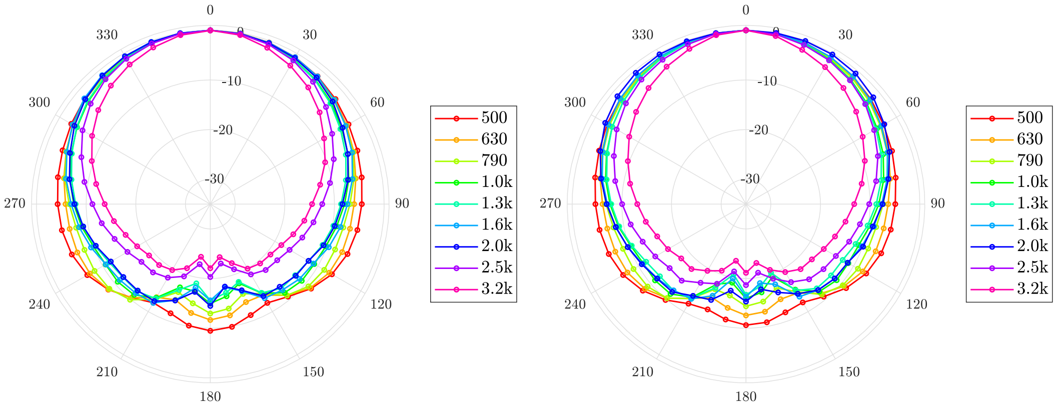

(c) Mid frequencies. Position 3.
(d) Mid frequencies. Position 4.

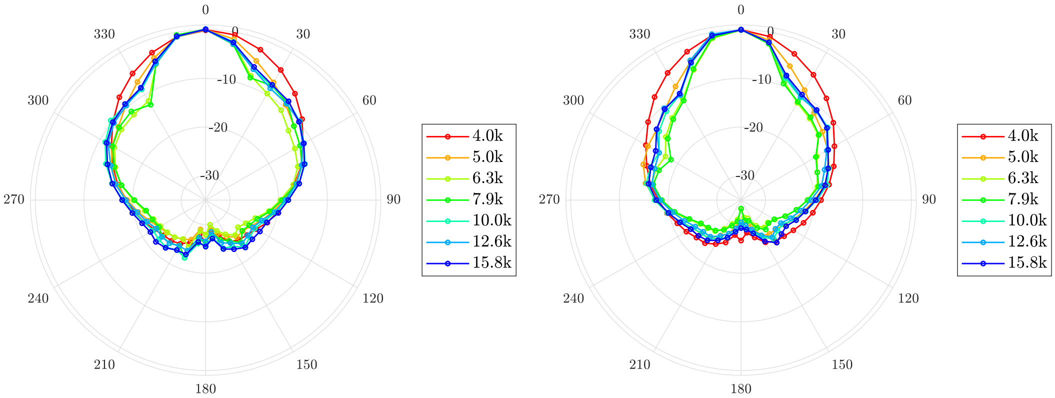

(e) High frequencies. Position 3.
(f) High frequencies. Position 4.

Figure 5.10: Directivity of the 2 m source measured at 1 m. Left: on axis with the space in between the two speakers at half the height of the source. Right: on axis with the membrane cone of the speaker immediately above half the height of the source.

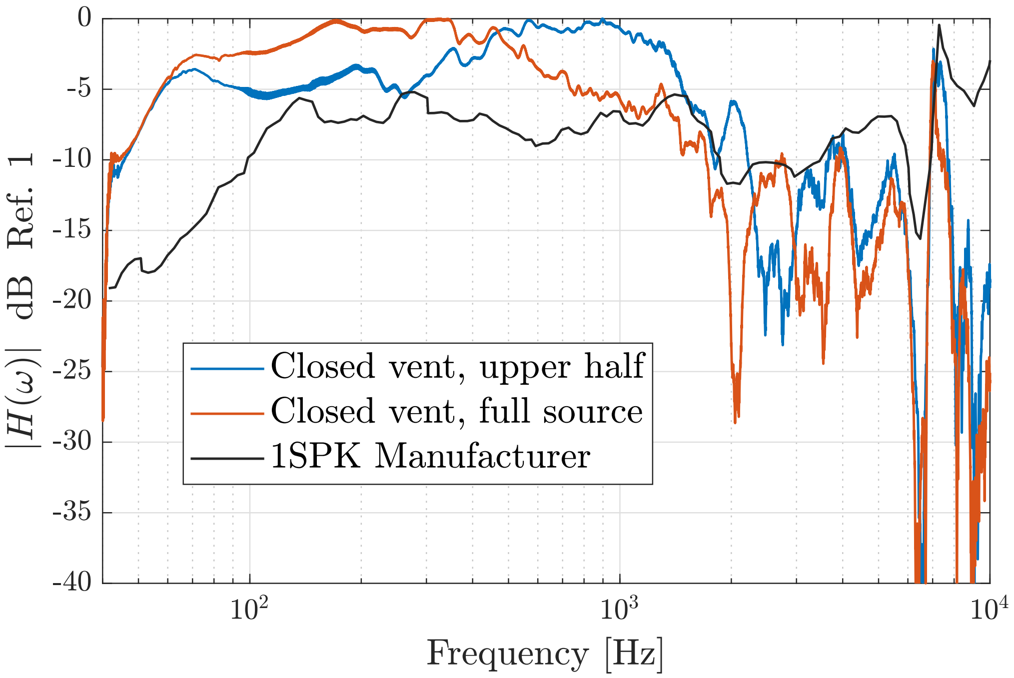

Figure 5.11: Measured spectra (normalized to max 0 dB) of the 2 m NDP source with closed cabinet (as used during in-situ measurements) for two conditions: driving only one half of the array and the entire array (as used in measurements). Data is overlaid with SPL informed by the manufacturer normalized by its peak at 7 kHz.

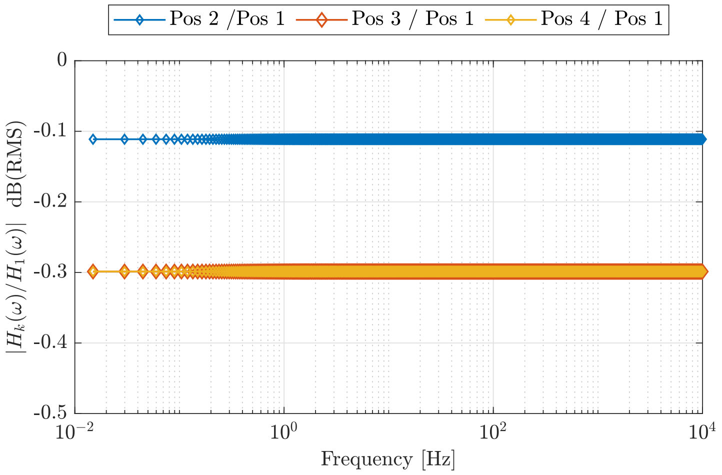

Figure 5.12: Measured pressure differences of the 2 m source across the spectrum for the vertically aligned acquisition locations using the lowest measurement point as a reference. Data is filtered per thirds of octave bands and scaled by the $db(RMS)$ of each sub-band driving the full array source.

5.7 Summary

In this section, theoretical tools were presented in order to characterize a cylindrical source and the electro-acoustic design of the actual sources built in the laboratory. The aim of such specific source design is motivated by the need to study two-dimensional radiation problems in three-dimensional spaces. Two source realisations were conceived: one for the measurements carried out in laboratory conditions in an anechoic chamber with an idealized organ-like instrument equivalent, and a second one for measurements in-situ in tribune organs of churches. Details on the organs and measurements belong to the scope of a later section of this work.

Chapter 6

Organ buffet radiation

Contents

6.1 Prelude **111**
6.2 Introduction **112**
6.2.1 Hypothesis, approximations, and methods 114
6.3 Theoretical apparatus **116**
6.3.1 [Step 1] Closed cavity, lossless, and rigid walls 117
6.3.2 [Step 2] Closed cavity, losses, non-rigid walls 120
6.3.3 [Step 3] Semi-open cavity: façade and slits 122
6.4 Measurements **130**
6.4.1 Measurement setup in ideal conditions (anechoic) 131
6.4.2 Cavity field and wall impedance estimation 133
6.4.3 Directivity measurements with the idealized organ 143
6.5 Application case: Notre-Dame de Paris **146**
6.5.1 The NDP tribune organ buffet measurements 147
6.6 Numerical experiments: finite-volume finite-difference . **151**
6.7 Future perspectives **154**
6.7.1 Sainte-Élisabeth de Hongrie 156
6.8 Conclusion and summary **158**

6.1 Prelude

In comparison to many other musical instruments, the radiation of the organ is extraordinarily imbricated. With a complex media constituted by an array of hundreds or thousands of monopolar sources (in reasonably low frequencies), the total field and its radiation need to be described by a concatenation of several models. The sources inside are located in different locations in depth, width, and height; the spectral content of the sources being very rich in harmonics causes that any given frequency at an observation point in the interior or exterior of the organ cavity sees many contributions from a distributed source field. The cavity in *closed buffet organs* is assumed semi-closed, with gaps in the front wall, the *façade*, due to the separation between pipes. The interior field interacts with the cavity walls, the apertures between pipes of the façade, and the propagation obstacles in the domain interior: mostly organ pipes, made of metal, wood, of cylindrical, conical, and square cross sections, and predominantly of different lengths. Therefore, the transmitted field through the façade apertures can be seen as the sum of normal and oblique harmonic waves and a diffuse field, whose phase state is quasi-negligible in low frequencies, relevant in middle frequencies, and statistical or randomized in high frequencies.

To the knowledge of the author, no previous studies have attempted to described the ensemble of the field created by sources inside an organ, the transmission of the field through a façade system and the radiation to the listening space in the exterior. The fundamental research aspects to address here have to be split into several smaller elements and stages (see Figure 6.1) for which one can find the best suited models: i.e., a semi-ideal resonant enclosing space, an array of multiple sources, a forest of multiple scattering bodies, an equivalent model for sound transmission, a lumped or array of equivalent sources (multiple apertures) at the interface between the interior and exterior, and the interference of sources at the exterior. A general division of frequency ranges can be posed as low frequencies, middle-to-high frequencies, and high frequencies.

There are several questions one may want to consider: can we predict the internal field at any location of the interior domain? Can we represent the enclosure interior acoustically and its many sources? Can we estimate what the field is like when impinging the internal side of the apertures? Can we approximate the effect of the appertures on the field passing through? Are there any well-posed models for each radiation regime that we can lump together at the façade of an organ? Can we predict what the listener percieves at a large distance from the instrument?

6.2 Introduction

Pipe organs are one of the musical instruments that have received less attention to modeling. Their size and the lack of portability are major reasons to cause that. Their complexity as an instrument is increased by the ubiquity of multiple sources, organized by windchest and *plans sonores* in their interior. As an instrument, they can be constituted by one or multiple wooden cases. In many occasions, the case or *buffet* might be closed on all sides, but this is not necessarily a predominant feature any more since this instrument has evolved since the middle ages [Rochas, 1997, Thistlewaite and Webber, 1998, Audsley, 1965a].

Organs are a bespoke instrument, built to adapt to each space, historically linked to church services. This causes that measurements setups for pipe organs have to tackle two issues: the large horizontal and vertical distances between elements under measurements, and the fact that the instrument can not be decoupled from the environment in which they are built: in rare cases, their size and the mechanical means for operation can be transported to controlled ideal conditions such as anechoic chambers. This causes that the measured data need to account for the presence of the response of the church.

Although the resonator of the organ pipes is the *initial* frequency selection means of the primary sources, the organ buffet acts as a intermediate resonator cavity[1].

An organ consisting of one or multiple buffets contains several *plans sonores*, distributed following the enclosure subdivisions of the organ: great organ, positive, pedal, swell box and echo are the most common. One of the walls of the cavities has evolved following aesthetic premises: this it the façade or *montre*, which is visually *shown* to the listener, the most visible one. Such embellishment does not only affect the pipes of the façade (often appearing longer than they sound), but also to the woodwork. The contribution to modifying the sound by the wood garments can be considered minor compared to the pipes placed in the façade.

The façade is formed by an array of pipes with a certain degree of spacing homogeneity. They are disposed forming flat vertical surfaces, sometimes disposed in a circle arches, forming a visually appealing tower. This disposition constitutes the interface between the organ's interior and the exterior (the coupled air medium), where the best opportunity takes place for the sound transmission out to the church. It is this pipe-to-pipe spacing interface where we focus our attention with regard to the organ radiation phenomena.

Towards relevant models. Since the geometry of each organ is different and complex, an accurate model can only be developed using numerical simulations. In order to develop our understanding of the influence of the different acoustic phenomena involed (cavity resonance, radiation, etc.), we will consider an idealized geometry that allows some analysis: flat vertical radiating surface, all pipes of same diameter, rectangular buffet cavity, etc. In fact, the Dallery organ in Chapelle Sorbonne is so far one such example except for the pipe diameters (the diameters in the facade are, however, reasonably similar –reexamine Figure 1.7). Models developed under such assumptions will help interpreting experimental data on actual organs.

We will show that the cavity resonance can be modeled by different approaches: the modal behaviour in low frequencies, the quasi-uniform dense field in high frequencies. Its response is position-dependent on the source and observation positions, changing the global Green's function resulting [Bruneau, 2006]. Once the forest matrix of cylindrical obstacles is added, its effect dominates over wall losses [Linton and Martin, 2005, Norris and Conoir, 2011].

The single slit's directivity and efficiency also changes with frequency. As pointed before, little literature addresses the matter ([Park and Eom, 1997, Mellow, 2006, Pàmies et al., 2011]). The model of the multiple slits is one of superposition and interference of multiple secondary sources, which can be addressed in the infinite-continuous mode or by a lumped array of N_{sl} sources, whose low-frequency effect is of acoustic quasi-transparency and a small transmission loss. In the mid-high frequencies, the equivalent cylindrical secondary source model will exhibit a spatial truncation effect in absence of infinite limiting planes above and below as the cylindrical source itself: see Figure 5.5.

With respect to pipe radiation, the low frequency approximation of the elemen-

---

[1] Compare this, for example, with the body and plates of a guitar, harp, or piano

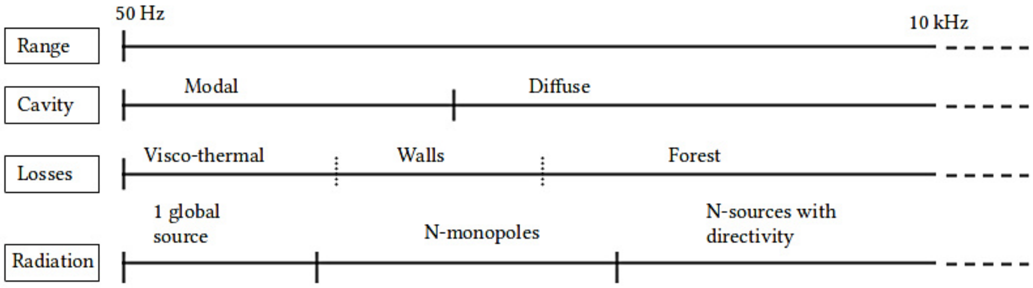

Figure 6.1: Organ radiation models per frequency ranges.

tary source is reproduced by an array of monopolar sources, however, this radiation model has a frequency limit where sources would need to be considered as per their geometry. Nonetheless, the wavelength limit to this effect is rather high in frequency.

Regarding the radiation of the ensemble model, different responses can be expected depending on the frequency range they span. Indeed, wavelengths radiated by the organ range from values larger than the instrument itself to values smaller than the pipe diameters. Therefore, there is no single description applicable to all frequencies. At low frequencies, within the modal description, all the pipes of the façade are small with respect to the wavelength. The façade may appear as a perforated plate. At mid frequencies, an indistinc diffuse field inside the cavity appears soon in frequency. The superposition and inferference between multiple sources, or by a global model of small radiation mass (inertance). At high frequencies, the interferences between the radiation of different slits and travelled-path differences exhibit an aleatory character. At this point, one sees the phenomena of directivity of individual sources appearing. Tools for high frequencies are commonly a statistical description [Bruneau, 2006].

This aleatory chararacter in the secondary source phases is only fully predicted in regularly spaced patterns of organ façades, which is only the case in the idealized laboraty organ-like cavity but not the case in the real organs. The randomization of phases depends on the dimensions of the apertures, the cylinder-to-cylinder spacing, and angle/position. There are a variety of directivity corpuses for a single given frequency.

6.2.1 Hypothesis, approximations, and methods

We propose modelling elements for the internal field of the cavity at different regimes and frequency-dependent slit models. We propose three different radiation models for the façade, with progressive increase of the frequential and spatial complexity behaviour. We assume a closed cavity with semi-rigid walls on all faces except the front. We assume an heterogeneous arbitrary location of sources in the interior domain and the superposition of the field by each of those contributions.

Using the same approach as in Chapter 5, where possible, the scattering, transmission, and radiation problems are reduced to a two-dimensional analogy. Loss terms are lumped at the boundary of the cavity domain with the exception of the forest of scatterers (organ pipes), which is resolved with a wavenumber perturbation approach. The source terms (the pipes) are assumed to be localized in space.

We use the comparably large vertical extent of the apertures of the façade to assume an infinitely long slit and the walls of the façade pipes are considered rigid and contributing a minor vibration [Kob, 2000b], or at least easy to model in the same way that the cavity walls are modeled.

We conducted pressure measurements in an organ-lime cavity idealization in an anechoic chamber and in the empty organ (except for the façade pipes) of Notre-Dame de Paris. Additionally, we reproduced some of the geometry conditions measured to run simulations of scattering problems in finite-volume finite-difference in time domain. The modeling stages followed are:

1. Consider a closed cavity with rigid walls.
2. Consider the homogeneous boundary value problem (BVP): compute lossless eigenvalues and eigenfunctions.
3. Use modal decomposition to build the Green's function for solutions.
4. Add losses: visco-thermal at boundary, vibrating walls, propagation obstacles (scatterers).
5. Add an aperture at the front wall: the slit has a different admitance than the walls, modifying the solutions.
6. Show pressure homogeneity for modes that do not span the third dimension (vertical).
7. Add N apertures at the front wall. Low frequency approximation: *blurry* sound transmission loss. Add equivalent sources at mid and high frequency (scattering problem and secondary sources)
8. Compute pressure field behind the slit.
9. Apply pressure continuity condition at the slit and use resilient slit model. A resilient slit is an infinitesimally thin membrane-like interface. assumbed to be perfectly flexible, having zero mass and free at its outer edges
10. Impose a radiation impedance at the slit: aperture's surface velocity is derived.
11. Model the radiation of one slit: flat interface slit [Mellow and Kärkkäinen, 2011], *cylindrical-source-impedance* interface slit [Bruneau, 2006].
12. Field superposition at the farfield for N apertures.

We will present and implement models in §6.3. We introduce the measurement setup under ideal conditions and show results in §6.4. §6.5 shows an application case followed by numerical simulation methods for complex geometries in §6.6. We conclude with some remarks and work perspectives in §6.7.

6.3 Theoretical apparatus

The approach followed as indicated in reference books such as [Kinsler et al., 2000] or [Junger and Feit, 1993] is: there exists at least one source, located at $\mathbf{r_o}$ with acoustic flow strength q and time harmonic dependence $e^{j\omega t}$; the domain $\mathcal{D}$ may be bounded by an enclosure to with one designates relevant boundary conditions; the system may be approximated to a two-dimensional boundary value proble (BVP); the modeling scenarios can be presented in increasing extent of complexity of the phenomena at the walls, and the domain interior. This may be proposed as per the next steps

- [Step 1] Source in a closed cavity, without losses and with perfectly rigid walls.
- [Step 2] Source in a closed cavity, with losses and moving walls.
- [Step 3] Source in a semi-closed cavity with one and N apertures.

We had provided a few general pointers on radiation in §2.4. The problem of acoustic radiation and scattering has received some attention from research and due to its complexity and variety of approaches, it deserves a closer look at specific publications. Existing solutions to the radiation through apertures finds an heterogeneous mixture of methods and limitations that involve: 2D and 3D fields, normal and [multiple] oblique incidence, diffuse fields, circular and rectangular apertures, slits, numerical and analytical techniques. We briefly state most notable contributions below.

Radiation through apertures: a specific literature review. Wilson, Sauter, and Soroka [Wilson and Soroka, 1965, Sauter and Soroka, 1970] worked on circular and rectangular apertures, given a thick wall, and normal incidence of a plane wave. Mechel added to this the consideration of the oblique impingement case of plane waves in [Mechel, 1986].

Park and Eom worked out the 3D acoustic field (still considering oblique incidence) *in* a slit of finite depth, with the understanding of a *rectangular waveguide* in [Park and Eom, 1997]. Following a similar approach but proposing numerical solutions to Rayleigh's formula, Sgard, Nelisse, and Atalla examined in [Sgard et al., 2007] multiple models from the literature and compare the diffuse field sound transmission loss to the normal incidence case for different aperture shapes and a span of $ka \in (0.001, 10)$.

Hongo and Serizawa [Hongo and Serizawa, 1999] used what is called the Kobayashi potential (KP) on an infinitely thin slit, which was a rectangular perforation on a rigid screen. In [Pierce et al., 2002], Pierce, Cleveland, and Zampolli tackled the non-diffuse solution through a rectangular opening on a rigid screen by reducing a rather cumbersome quadruple integral[2] into four other simpler, friendlier,

---

[2] We will avoid reproducing it here, but the reader may refer to Chapter 7 of [Kinsler et al., 2000], [Pàmies et al., 2011], or [Kim and Kim, 2002], amongst other publications.

and easy to implement integrals. Both Hongo *et al.* and Pierce *et al.* papers propose a solution decomposition based on sets of basis functions for a normal velocity boundary condition at the aperture.

Trompette *et al.* ([Trompette et al., 2009]) continued to work in the line started by [Sgard et al., 2007] in terms of experimental validation, and assessed rectangular apertures and slits on reverberant rooms, with reliable agreement with models confined in the region 630 Hz to 5000 Hz.

Davy ([Davy, 2009a, Davy, 2009b]) proposed and compared with theory a directivity empirical model, dependent on the angle of incidence of the field, the surface absorption coefficients of a cavity with a *thin wall aperture*, and the radiation efficiency, all within a 2D room model.

Kim and Kim offered ([Kim and Kim, 2002]) an analytical solution to a two-dimensional coupled-cavity problem exploiting the Kirchhoff-Helmholtz integral and defining a *membrane* at the interface.

Mellow and Kärkkäinen presented in [Mellow and Kärkkäinen, 2011] an analysis on radiated fields under the combination of several conditions: rigid finite baffle, rigid infite baffle, free space, rigid strip, and *resilient* strip. Their set of assumptions included infinitely long, infinitely thing, and mass-less aperture.

It is now clear that models exist for several elements of the radiation phenomena, including analytical ones. Precision limitations on analytical models appears to be an issue on low frequencies, unless one resorts to numerical methods or to reduce the model to a 2D problem. Next, we proceed with the steps above and present the models in order.

6.3.1 [Step 1] Closed cavity, lossless, and rigid walls

Omitting the trivial case of free propagation (represented by a delay and an amplitude decay linked to the observation distance $r = |\mathbf{r} - \mathbf{r}_o|$), the total internal field in absence of cylindrical scatterers can be expressed by the following contributions

$$\Psi_{tot}(\mathbf{r}_{ob}, \omega) = \Psi_{inc}(\mathbf{r}_o, \omega) + \Psi_{wall}(\mathbf{r}_{w,p}, \omega) + \Psi_{ap}(\mathbf{r}_{ap}, \omega) + \Psi_{forest}(\omega) \tag{6.1}$$

where Ψ is a velocity potential of the acoustic field ($\mathbf{u} = \nabla\Psi$, $p = -\rho\partial_t\Psi$), $\mathbf{r}_{ob}$ is the observation position, ψ_{inc} is the incident field injected by the source at position $\mathbf{r}_o$; the vibration of the passive wall surfaces contributes $\Psi_{wall,pass}$ and Ψ_{ap} is the effect of apertures in the front surface of the cavity (the *façade*, in the case of the organ).

The diagram in Figure 6.2 shows the setup of the idealized organ-like cavity built for laboratory measurements. The system of coordinates adopted in the present work is shown there.

Let us define an acoustic flux source at the injection point $\mathbf{r}_o$ equal to $q(\mathbf{r}_o, t)$ and an observation point $\mathbf{r}$ elsewhere in the the domain. We are concerned with solving the wave equation, for velocity potential or pressure, which may be expressed (see Equation (2.4)) as

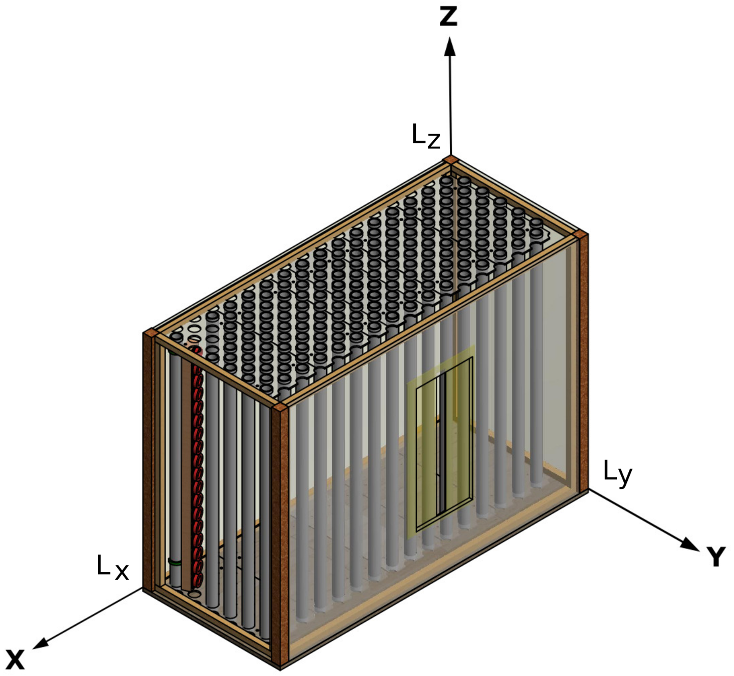

Figure 6.2: Diagram of the organ-like cavity, its internal elements, and cartesian $\mathbf{X}-\mathbf{Y}-\mathbf{Z}$ coordinate system. Figure created by L. Quartier. Further details are provided in §6.4.1.

$$\left(\frac{1}{c_o^2}\frac{\partial^2}{\partial t^2}-\nabla^2\right)\Psi = f(t) \tag{6.2}$$

For ease of manipulations, it is convenient to assume a complex potential field $\phi_{an} = \Psi + j\hat{\Psi}$ whose analytical signal can be completely defined in the frequency domain by

$$\phi_{an} = 2U(\omega)\Psi(\omega) \tag{6.3}$$

where $U(\omega)$ is a Heaviside function that vanishes the negative frequencies in the analytic signal and has the nice property that

$$U(\xi) = \int_{-\infty}^{\xi}\delta(\zeta)d\zeta \tag{6.4}$$

Lastly, in time domain, such complex field is obtained by the convolution product

$$\phi_{an}(t) = \left[\delta(t) + pv\left(\frac{j}{\pi t}\right)\right] * \Psi(t) \tag{6.5}$$

making it a very useful tool together with the Green's function solution to the BVP, in particular in cases where the forcing term of the problem is localized in space and time-harmonic:

$$\hat{f}(t) = F_o\mathcal{F}^{-1}\{\delta(\omega-\omega_o)\delta(\mathbf{r}-\mathbf{r}_o)\} \tag{6.6}$$

$$= \delta(\mathbf{r}-\mathbf{r}_o)e^{j\omega t} \tag{6.7}$$

In what follows, however, we are concerned with the real part of such potential fields, since complex fields would be used to represent a potential flow. The ideally rigid and lossless problem may be used, first, to find the eigenfrequencies and expressions for the modal shapes of the cavity under low spectral density condition. If an enclosure domain $\mathcal{D}$ is considered, with dimensions (L_x, L_y, L_z), and the boundaries are assigned a perfectly rigid condition,

$$\left(\frac{\partial}{\partial \mathbf{x}_i}p\right)_{\mathbf{x}_i=0} = \left(\frac{\partial}{\partial \mathbf{x}_i}p\right)_{\mathbf{x}_i=L_i} = 0 \tag{6.8}$$

The energy-conserving solution for standing waves in such an ideal cavity, where space variables are assumed separable

$$p(\mathbf{r},t) = X(x)Y(y)Z(z)e^{j\omega t} \tag{6.9}$$

In resonant systems, the solution to the field may well be posed in terms of modal decomposition. To that end, one may want to solve the BVP with an elementary source and arrive at the appropriate Green's function for the d'Alembert operator and pertinent boundary conditions (BC), which eventually is convolved with the source of interest. It will be convenient to define a point source such that integration and convolution do not become cumbersome, for instance:

$$f(\mathbf{r},t) = \mathcal{F}^{-1}\{F_o\delta(\mathbf{r}-\mathbf{r}_o \mid \omega-\omega_o)\} \;=\; F_o\delta(\mathbf{r}-\mathbf{r}_o)e^{j\omega_o t} \tag{6.10}$$

as per Equation (6.7). Following the different stages discussed in §6.3, we begin the analysis by the case of a closed cavity with rigid walls. Combining the Helmholtz equation (Equation (6.2)) with the boundary conditions (Equation (6.8))

$$\left[\frac{\partial}{\partial \mathbf{x}_i}\Psi\right]_{\mathbf{x}_i=0,L_i} = 0 \tag{6.11}$$

at the *walls* (in 2D) $x = \{0, L_x\}$ and $y = \{0, L_y\}$, we deduce the Neumann problem modal shapes:

$$\psi_{m,n} = A_{m,n}cos(k_x x)cos(k_y y) \tag{6.12}$$

whereby evaluating the inner product of modal shapes at the boundaries as

$$\delta_{m,n}(\mathbf{x}) = \langle\psi_{m,n}|\psi_{m',n'}\rangle_{x_i=0,L_i} \tag{6.13}$$

yields values for the amplitudes that guarantee a base of functions that are orthogonal and normed as

$$A_{m,n} = \left\{\int_0^{Lx} cos^2\left(\frac{m\pi}{Lx}x\right)dx\int_0^{Ly} cos^2\left(\frac{n\pi}{Ly}y\right)dy\right\}^{-\frac{1}{2}} = \left\{\frac{L_xL_y}{4}\right\}^{-\frac{1}{2}} \tag{6.14}$$

and the Green's functions with a wall admittance boundary condition that solve Equation (6.2) may be written as

$$\begin{cases} G(\mathbf{r}|\mathbf{r}_o) = \displaystyle\sum_{m,n} \frac{\psi_{m,n}(\mathbf{r})\psi_{m,n}(\mathbf{r}_o)}{k_{m,n}^2 - k_{eff}^2(\omega)} & (6.15) \\ \dfrac{\partial}{\partial \mathbf{n}}\Psi(\omega) = -j\dfrac{\omega}{c_o}\xi(\omega)\Psi(\omega) & (6.16) \end{cases}$$

In order to introduce losses in the model, a perturbation approach modifying the wave number allows to lump losses accounting for

- Visco-thermal losses with perfectly reflective walls
- Wall vibration not perfectly rigid walls
- Wave number perturbation in complex media, due to a forest of cylindrical scatterers (organ pipes)

where the dissipation effects are increasingly dominant as elements are added to consideration.

6.3.2 [Step 2] Closed cavity, losses, non-rigid walls

Generalizing the solution with losses as referred in [Bruneau, 2006], the types of loss mentioned may be incorporated to Equation (6.15) in the form

$$G(\mathbf{r}|\mathbf{r}_o) = \sum_{m,n}^{N_{mn}} \frac{\psi_{m,n}(\mathbf{r})\psi_{m,n}(\mathbf{r}_o)}{k_{m,n}^2 - k_o^2 + (\mathbf{I}_{wall} + \mathbf{I}_{slit} + \mathbf{I}_{scatt})} \tag{6.17}$$

where N_{mn} is the total modal sum included under truncation, $k_o = \omega/c_o$, the different scenarios mentioned above are considered as

$$I_{wall} = jk_o \int_{S_{wall}} \xi_{wall}\psi^2 dS_{wall} \tag{6.18}$$

for the vibration of walls, with ξ_{wall} being a specific acoustic wall admittance that satisfies Equation (6.15); the effect of apertures in the front wall of the cavity is resolved by

$$I_{slit} = jk_o \sum_{l=1}^{N_{sl}} \int_{S_{sl}} \xi_{sl}\psi^2 dS_{sl} \tag{6.19}$$

for the modification of eigenshapes projecting the aperture's specific admittance ξ_{ap} –see [Mellow and Kärkkäinen, 2011]) on the shapes right behind the slit, exploiting that $y = L_y$, $x_l \in]x_l - a, x_l + a[$, $dS_l = dxdz$, and N_{sl} the number of slits in the façade. In the case of the single slit, this results in

$$\mathbf{I}_{slit} = jk_o\xi_{ap}(A'_{mnl})^2[cos^2(k_{ny}y)]_{y=L_y}\int_{z_{sl,inf}}^{z_{sl,sup}}\int_{x_c-a}^{x_c+a} cos^2(k_{mx}x)cos^2(k_{lz}z)dxdz \tag{6.20}$$

where the aperture admittance $\xi_{sl} = \rho c_o/Z_{ap}H_{sl}$ per unit length (H_{sl} is the height of the slit) is taken as the radiation impedance of the flat interface equivalent to the cylindrical source of the façade (the development is shown in §5.2), A'_{mnl} are the modal amplitudes in the three-dimensional model. A representation (not to scale) of such operation is shown in Figure B.3 (Appendix B) for the case $(m, n, l) = (3, 3, 3)$.

Lastly, following the work in [Linton and Martin, 2005, Norris and Conoir, 2011, Rohfritsch et al., 2019], the dissipation due to the presence of a forest of N_{cyl} scattering cylinders is

$$\mathbf{I}_{scatt} = k_{ISA}^2 = k_o^2 - 4jn_o f(0) \tag{6.21}$$

for the wavenumber perturbation in the interior of $\mathcal{D}$ due to the presence of scatterers, with n_o being the density of scatterers, expressed as the number of cylinders per unit area, and shape function $f(\theta)$ being

$$f(\theta) = \sum_n T_n e^{jn\theta} \tag{6.22}$$

where the *diffusion coefficients* T_n, which are the eigenvalues of the transition operator $\mathcal{T}(\vec{r})$ that links the scattered field to the incident field, are expressed for an isotropic cylinder by

$$T_n = -\frac{nJ_n(k_oR_{cyl}) - (k_oR_{cyl})J_{n+1}(k_oR_{cyl})}{nH_n^{(1)}(k_oR_{cyl}) - (k_oR_{cyl})H_{n+1}^{(1)}(k_oR_{cyl})} \tag{6.23}$$

with R_{cyl} the radius of the cylindrical scatterer, $k_o = \omega/c_o$ the wave number in the air media with propagation velocity c_o, J_n are the n^{th}-order Bessel functions of the first kind, and $H_n^{(1)} = J_n + jY_n$ are the Hankel functions of the first kind, and Y_n is the Bessel function of second kind.

Following Pàmies *et al.* [Pàmies et al., 2011] one can derive a complex-valued admittances β and impedances χ as per [Bistafa and Morrissey, 2003]

$$\beta = \xi - j\sigma \tag{6.24}$$

using measured data of the closed cavity without the forest array. Knowing the *specific acoustic impedances* ζ_x, ζ_y, and ζ_z (in the notation of Bistafa *et al.*) for parallel cavity walls with matching or different impedances and present or missing aperture, Bistafa *et al.* [Bistafa and Morrissey, 2003] proposed slow variation methods to calculate $\mu = \Re(\chi)$ and $\kappa = \Im(\chi)$ for N_m modes, where μ is the wave number parameter and κ the attenuation parameter. A numerical application is shown with the measurement results in §6.4.2. Note that, unless stated otherwise, our choice of notation is ξ and Z for admittance and impedance, related as $\xi = \rho c/Z$.

6.3.3 [Step 3] Semi-open cavity: façade and slits

The effect of the façade The presence of the façade at the front wall of the organ, with its pipe-to-pipe spacings, constitutes an elaborated boundary condition between the cases of the closed rigid wall and the completely open free-propagation.

Readily intuitive hypothesis are that for low frequencies: the effect on wave transmission-attenuation and reflection will be minor; the presence of the rigid bodies of the façade pipes will have a strong scattering influence in the radiated field.

The following models can be posed

1. The single thin infinitely long slit
2. The single finite rectangular aperture
3. The slit quarter-wavelength approximation [Berry et al., 2019]
4. The trapped-space between two half cylinders
5. Multiple slits

The single slit One can consider, for now, neglecting the transient regime of the acoustic field in the interior, the slit, and in the vicinity of the façade. Under such assumption, it is plausible to assume for Equation (6.1) a normal, incident field from the cavity interior onto the façade space of

$$\Psi_{inc}(y,t) = Y(y)T(t) = e^{-jk_y y}e^{j\omega t} \tag{6.25}$$

where the y expresses the propagation longitudinally towards the church direction. This great simplification, disregarding the rest of walls and a forest matrix of cylinders momentarily, emphasizes that the admittance boundary condition at the walls Equation (6.15) may be recast for the aperture sections $\partial\mathcal{D}_{ap}$ as

$$\mathbf{u}_o(\mathbf{r}_{ap},\omega) = \frac{1}{jk\rho c}\frac{\partial}{\partial\mathbf{n}}p(\mathbf{r}_{ap},\omega) = \frac{\xi_{ap}}{\rho c}p(\mathbf{r}_{ap},\omega) \tag{6.26}$$

with $\xi_{ap} = \frac{\rho c}{Z_r}$ corresponding to a radiation admittance at the aperture.

Multiple slits Berry *et al.* [Berry et al., 2019] offered approximated expressions for the first modes of Bragg diffraction field due to an evenly-spaced array of cylinders, exploiting the organ pipe quarter-wavelength representation of the space trapped in the interface between cylinders, for a center-to-center spacing d, a pseudo pipe length $L = 2a$ corresponding to the spacing width (with a the cylinder radius). The expression is complemented with a radiation length correction in the range $(0.31d, 0.78d)$, whose average values using the geometry of our problem yield the following initial estimates for the diffraction peaks

Table 6.1: First modes of Bragg-like scattered pressure *resonances* as per [Berry et al., 2019].

696 Hz	1392 Hz	2088 Hz	2783 Hz	3479 Hz	4175 Hz

6.3.3.1 Multiple slits at low-mid frequencies

In the case of a large enough observation distance to the façade, a small source (radius a) in terms of wavelengths ($ka \ll 1$) can be replaced by a point source entailing the same volume acceleration, disregarding the geometry of the source [Junger and Feit, 1993]. Following their procedure and writing for a 2D source and field, the pressure of one pulsating cylinder is

$$p(r,t) = \frac{1}{4} k\rho c Q_{vol} \sqrt{\frac{2}{\pi kr}} e^{-j\left(kr - \frac{\pi}{4}\right)} e^{j\omega t} \tag{6.27}$$

where $Q_{vol} = a\dot{U}_o$ is the volume acceleration and the distance is $r = |\mathbf{r} - \mathbf{r}_o|$. Taking the contribution of two such sources at a distance $2e$ apart, and in phase, it is derived that the pressure at a distance r and angle θ with respect to the origin between the two sources (starting on the line that joins them) is

$$\begin{aligned} p(r,\theta) &= \frac{1}{4} k\rho c Q_{vol} \sqrt{\frac{2}{\pi kr}} e^{j\frac{\pi}{4}} e^{j\omega t} \left[\frac{e^{-jk(r+ecos\theta)}}{\sqrt{r+ecos\theta}} + \frac{e^{-jk(r-ecos\theta)}}{\sqrt{r-ecos\theta}} \right] \\ &\approx \frac{1}{4} k\rho c Q_{vol} \sqrt{\frac{2}{\pi kr}} e^{jkr} \left(e^{-jkecos\theta} + e^{+jkecos\theta} \right) \quad \text{if} \quad \frac{e}{r} \ll 1 \quad \text{and} \quad \frac{ke^2}{r} \ll 1 \\ &= \frac{1}{4} k\rho c Q_{vol} \sqrt{\frac{2}{\pi kr}} e^{j\frac{\pi}{4}} e^{-jkr} 2cos(kecos\theta) \end{aligned} \tag{6.28}$$

If we take

$$p_s(r) = \frac{1}{4} k\rho c Q_{vol} \sqrt{\frac{2}{\pi kr}} e^{j\frac{\pi}{4}} e^{-jkr} \tag{6.29}$$

then

$$p(r,\theta) = p_s(r) 2cos(kecos\theta) \tag{6.30}$$

and the directivity of the equivalent total source in the far-field ($ke \ll 1$) is given by the ratio $|p(r,\theta)/p_s(r)|$. For two sources located very close, the result becomes θ-independent and $|p(r,\theta)/p_s(r)| = 2$, thus doubling the pressure of the single point source. If the two point sources are now considered in opposite phase ($e^{-j(\omega t - \pi)}$ and $e^{-j\omega t}$, respectively), the resulting pressure becomes

$$p(R,\theta) \approx 2jp_s(R) sin(kecos\theta) \tag{6.31}$$

and directivity of the global source is found by $|p/jp_s|$, displaying a dipolar source behaviour with a vanishing pressure plane at the middle. Finally, considering a line array of $2N_{sl}$ sources and using

$$
\begin{aligned}
p(r,\theta) &= \frac{p_s(r)}{2N_{sl}} \sum_{l=-N_{sl}}^{N_{sl}-1} e^{-jke(2l+1)cos\theta} \\
&= \frac{p_s(R)}{N_{sl}} \sum_{l'=0}^{N_{sl}} cos\{ke(2l'+1)cos\theta\}
\end{aligned}
\tag{6.32}
$$

and the identity

$$
cos\sigma + cos3\sigma + \cdots + cos(2N_{sl}-1)\sigma = \frac{sin(2N_{sl}\sigma)}{2sin\sigma} \tag{6.33}
$$

where $\sigma = kecos\theta$, the generalization to $2N_{sl}$ sources in the farfield becomes

$$
p(r,\theta) = \frac{p_s(r)sin(2N_{sl}kecos\theta)}{2N_{sl}sin(kecos\theta)} \tag{6.34}
$$

with

$$
p_s(r) = \frac{1}{4}k\rho c Q\sqrt{\frac{2}{\pi kr}}e^{j\frac{\pi}{4}}e^{-jkr}, \quad \text{with} \quad r \gg 2eN_{sl} \tag{6.35}
$$

whose result is plotted for several mid-range frequencies in Figure 6.3. A different approach may be found in [Bruneau, 2006] for the case of arrays of pulsating cylinders in phase opposition, where the generalization of N_{sl} distinct phases is trivially applied to zeroth-order Hankel functions.

The system proposed thus far assumes that the incident field behind the apertures holds the same phase for all the secondary sources. Improvements of such system may be found in [Rossi, 1988] and [Bruneau, 2006]. The derivations are similar to what we have presented above and in Chapter 5, and may be found in Chapter 2 and Chapter 5, respectively.

From Rossi, where n pulsating sources are a distance d apart over a line array of length $l = (n-1)d$, the directivity factor of the uniform phase array is

$$
D_o(\theta) = \frac{\frac{sin(0.5nk_\theta d)}{0.5nk_\theta d}}{\frac{sin(0.5k_\theta d)}{0.5k_\theta d}} = \frac{sin(0.5nk_\theta d)}{nsin(0.5k_\theta d)} = \frac{sin(0.5nkdsin\theta)}{nsin(0.5kdsin\theta)} \tag{6.36}
$$

with $k_\theta = ksin\theta$ (the angle θ here is taken with respect to the normal of the line array, unlike in Junger). The expression in the last term is a scalar factor of Equation (6.34), provided that $n = 2N_{sl}$ and $l = 2L$. The first term shows that the directivity of the array appears as the ratio of two uniform arrays of length $l' = nd$, thus the two arrays relate as $l' = l + d$. When $d < \lambda/4$ (with λ as the wavelength), the directivity is accentuated and side lobes become larger, since the denominator of Equation (6.36) ($sinc(\frac{\pi d}{\lambda}sin(\theta))$) falls below unity (see the Junger uniform model exhibiting this behaviour in Figure 6.3).

If the phase-shift of the r^{th} pulsating source is considered, its acoustic flux is

$$
q_r = Q_o e^{-jr\phi} \tag{6.37}
$$

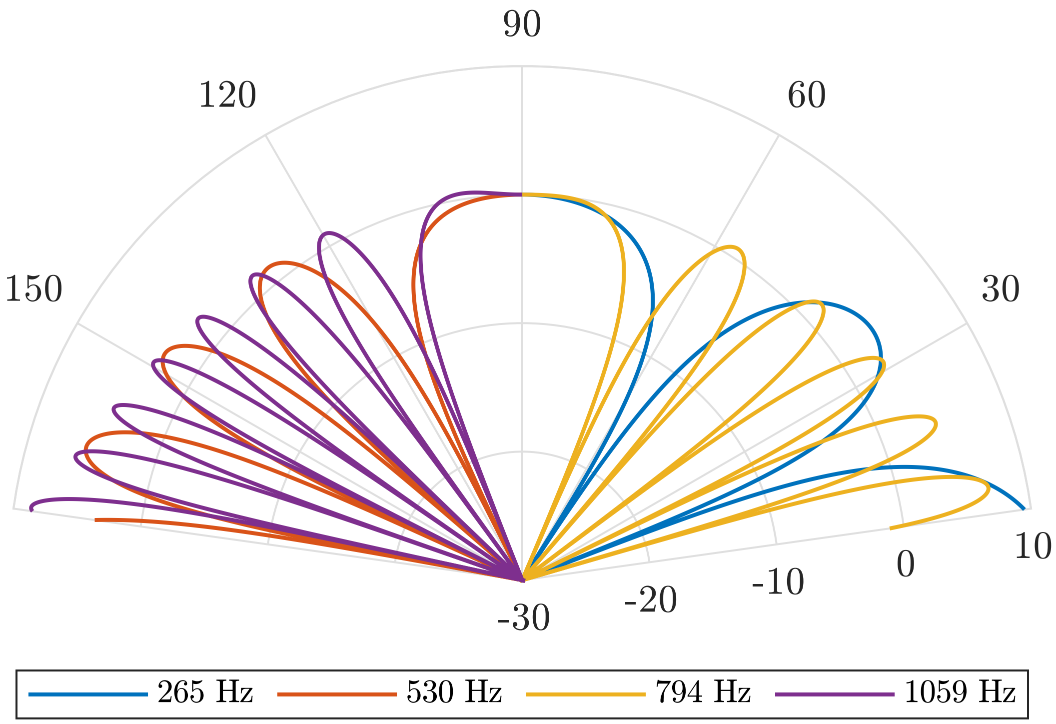

Figure 6.3: Mid-frequency range directivity of a façade equivalent array of sources as per the coordinates of [Junger and Feit, 1993]: θ and ρ (normalized by the pressure on axis with the normal of the sources array) are expressed in ° and dB, with the r origin between the centermost pair of sources of the array and the observation angle being measured with respect to the line from the origin to one end of the array. Conditions: $2N = 30$, $2e = 0.08\,\mathrm{m}$, $2L = 2.68\,\mathrm{m}$.

with $r \in [0, (n-1)]$; and the directivity factor is derived as

$$D(\theta) = \frac{sinc(0.5n(k_\theta d + \phi))}{sinc(0.5(k_\theta d + \phi))} \tag{6.38}$$

This model is shown in Figure 6.4 for $k = 2\pi 142\,\mathrm{Hz}/c_o$ at different phase shifts. Lastly, Bruneau proposes a model of two pulsating sources with the same acoustic flux strength in phase opposition, resulting in a shift of $\pi/2$ of the directivity factor. A generalization of this approach may be recast as

$$p = \frac{1}{4} k_o \rho_o c_o Q_o cos(k_z z) \sum_{l}^{N_{sl}} \phi_l H_o^-(k_w r_l) \tag{6.39}$$

with wavenumber $k_w^2 = k^2 - k_z^2$ equating k^2 when the vertical direction is omitted (vertically infinite waves of cylindrical propagation are considered), H_o^- representing a divergent Hankel function of order zero of the first type, and ϕ_l the phase of each secondary source.

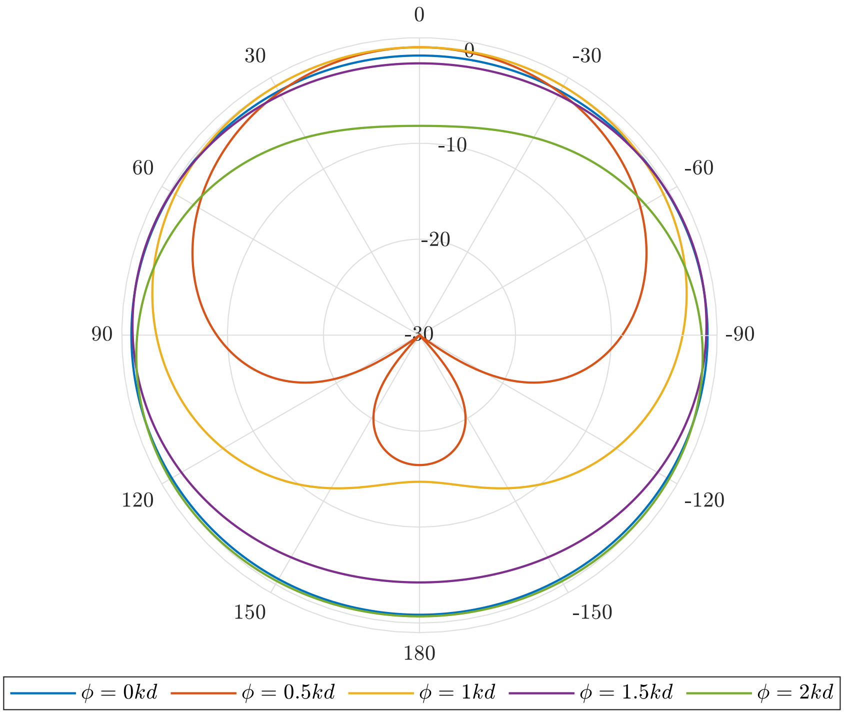

Figure 6.4: Following Rossi's model [Rossi, 1988], computation of radiated field by an array of equaly distributed pulsating sources changing the ϕ parameter for different values of kd, where d is the pipe-to-pipe separation and k the wavenumber.

6.3.3.2 High frequencies and the resilient strip in an infinite rigid baffle

For higher frequencies ($ka \gg 1$), directivity may appear and the pulsating cylinder approximation is no longer valid. Among known conditions for aperture radiation one encounters circular and rectangular pistons. They can be found in a baffle or in free space. In rectangular coordinates, they can be considered of finite or infinite extent (in the vertical dimension). The aperture can be considered to have a finite depth or infinitely thin.

The considerations that we make on the slits are: their half-width is a, the vertical extent of the aperture is infinite ($L_z = \infty$), the thickness of the slit is infinitely thin and has no mass; the walls of the pipes in the façade are considered a rigid baffle. The radiation model that matches these considerations is that of a rigid baffle and a resilient strip, where the field of the incident plane wave into the aperture and the field scattered from the complementary shape removed (the slit in free field) are equivalent.

Following [Mellow and Kärkkäinen, 2011], and using the coordinates oriented in the same directions as on Figure 6.2 but with origin of the x-coordinates in the center of the slit, the next boundary conditions are imposed at the slit

$$\frac{\partial}{\partial y} p(x,y,t)|_{y=L_{y+}} = \begin{cases} -jk\rho c u(x,y,t)|_{y=L_y}, & -a \leq x \leq a \\ 0, \quad -\infty \leq x < -a, & a < x \leq \infty \end{cases} \tag{6.40}$$

where L_{y+} is the outwards immediacy of the interface at $y = L_y$ and the expression may be expanded as

$$u(x, y, t)|_{y=L_y} = \frac{p_o(t)}{\rho c} \sum_{n=0}^{\infty} A_n \left(1 - \frac{x^2}{a^2}\right)^{n-\frac{1}{2}} \tag{6.41}$$

p_o here represents a harmonic driving pressure, and the coefficients A_n will be derived later (whose elements should not be confused with the aperture half-width a).

Following the same steps as above for the cavity, a two-dimensional Green's function can be posed for the slit, which integral form shows as

$$G(x, y|x_o, y_o) = -\frac{j}{4\pi} \int_{-\infty}^{\infty} \frac{e^{-j(k_x(x-x_o)+k_y(y-y_o))}}{k_y} dk_x \tag{6.42}$$

with the wave number in the **Y**-direction defined as

$$k_y = \begin{cases} \sqrt{k^2 - k_x^2}, & k_x^2 \leq k^2 \\ -j\sqrt{k_x^2 - k^2}, & k_x^2 > k^2 \end{cases} \tag{6.43}$$

The pressures at the front and back of the resilient *strip* are p_+ and p_- respectively, and are related by the continuity condition

$$p(x, y, t)_{y=L_{y+}} = -p(x, y, t)_{y=L_{y-}} = \frac{p_o}{2} \tag{6.44}$$

The Rayleigh integral for the monopole pressure in the near-field being

$$p(x, y, t) = 2 \int_{-a}^{+a} \frac{\partial}{\partial y_o} p(x_o, y, t)|_{y=L_{y+}} G(x, y|x_o, y_o)|_{y_o=L_y} dx_o \tag{6.45}$$

may be combined with Equation (6.40), Equation (6.41), Equation (6.42), and the Kirhhoff-Helmholtz integral to arrive at

$$p(x, y, t) = -\int_{-\xi}^{\xi} (p_+(x_o, 0, t) - p_-(x_o, 0, t)) \frac{\partial}{\partial y_o} G(x, y|x_o, y_o) dx_o \tag{6.46}$$

and integrate over x_o, to obtain

$$p(x, y, t) = -\frac{kap_o(t)}{\sqrt{\pi}} \sum_{n=0}^{\infty} A_n 2^{n-1} \Gamma\left(n + \frac{1}{2}\right) \int_{-\infty}^{\infty} \frac{J_n(k_x a)}{k_x a} \frac{e^{-i(k_x x + k_y |y|)}}{k_y} dk_x \tag{6.47}$$

Using the boundary condition of Equation (6.44) yields the coupled equation

$$\sum_{n=0}^{\infty} A_n I_n(x) = -\Phi(x) = -1 \tag{6.48}$$

where $I_n = I_{nR} + jI_{nI}$ are the integrals of Equation (6.47), and $\Phi(x)$ are pressure distributions. The full development can be found at [Mellow and Kärkkäinen, 2011], which reduces to solving the matrix system

$$\mathbf{a} = {}_n\mathbf{M}_m^{-1}\mathbf{b} \tag{6.49}$$

with $\mathbf{b}$ consisting of $N{+}1$ Kronecker deltas $-\delta_{m0}$, the matrix elements $\mathbf{a}(n{+}1) = A_n$, and the matrix indexing system as per [Mellow and Kärkkäinen, 2011] denoting

$${}_n\mathbf{M}_m ={}_n \mathbf{C}_m(ka) - j{}_n\mathbf{I}_m(ka) \tag{6.50}$$

where ${}_n\mathbf{C}_m$ and ${}_n\mathbf{I}_m$ are series expansions in bessel functions of first, second, and third kind.

The solutions A_n encapsulate the directional response, similarly to Equation (6.23) in the shape function Equation (6.22), and we will make use of them next to compute the radiated pressure of the current model. One may arrive at the far-field pressure, in spherical-rectangular coordinates, by using the far-field Green's function

$$G(x, x_o|y, y_o) = -\frac{j}{4\pi}\int_{-\infty}^{\infty}\frac{e^{-j(k_x(x-x_o)+k_y(y-y_o))}}{k_y}dk_x \tag{6.51}$$

leading to

$$p(r,\theta,t) = p_o(t)\sqrt{\frac{a}{2\pi r}}e^{-j(kr-\frac{\pi}{4})}D_{kark}(\theta) \tag{6.52}$$

where the directional term is expressed as

$$D_{kark}(\theta) = -j\sqrt{\pi ka}\sum_{n=0}^{N} A_n\Gamma\left(n+\frac{1}{2}\right)\frac{2^n J_n(kasin\theta)}{kasin\theta} \tag{6.53}$$

and truncating the series at $N = 2ka$. Refer to Figure 6.5 to find scattering models following [Mellow and Kärkkäinen, 2011] for the geometry stated in Figure 6.2. The distance considered was between the lumped sources in the façade and the receiver locations. If these results are projected onto a point source interpretation, accounting for possible 3-to-6 dB per doubling distance, its representation appears as in Figure 6.6.

The unrealistic behaviour of using [Junger and Feit, 1993] and [Mellow and Kärkkäinen, 2011] radiation models in the low frequencies is shown in Figure 6.7 for frequency ranges better described by the lower regime models.

With regard to the pertinence of the two-dimensional model introduced in §6.3.3.2, we will show in §6.4.2.1 (Figure 6.13) and Appendix B that the pressure homogeneity at the slit of the idealized organ cavity is altered by the vertical alignment of the pressure only. These corresponding to the vertical modes, omitted in our models here (except in numerical integration of the wall specific admittance), do not make the two-dimensional model invalid.

From Sgard *et al.* [Sgard et al., 2007] not only one sees the comparative analysis among 15 models of aperture radiation and impedance, but also learn that sound transmission loss of normal incidence fields compared to diffuse fields are found, at

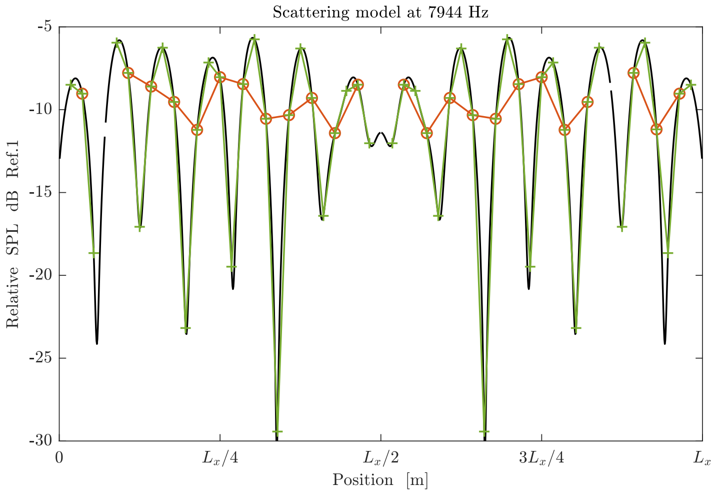

Figure 6.5: Interference models of scattering using the aperture radiation method of [Mellow and Kärkkäinen, 2011] at two different measured pressure frequencies for the laboratory organ-like cavity geometry. The field is the result of the superposition and interference of $N_{sl} = 15$ sources, with a source-to-source spacing of 0.08 m, and at a read-out distance of 1.66 m from the equivalent façade, as per anechoic measurements in §6.4. Read-out positions are spaced every 1 mm (—), 1 cm (—), and 5 cm (—). The response at a higher frequency is shown in Figure B.1 (Appendix B).

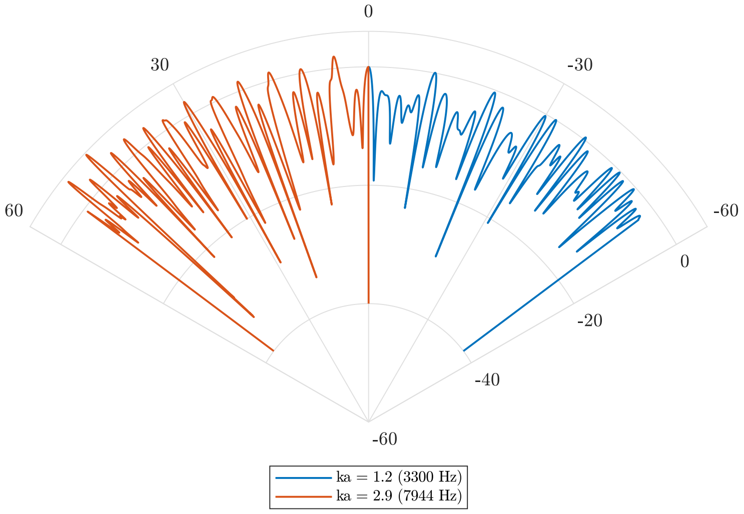

Figure 6.6: Point-source projected scattered pressure, as the result of the superposition and interference of $N_{sl} = 15$ sources modelled as [Mellow and Kärkkäinen, 2011], with a source-to-source spacing of 0.08 m, and at a read-out distance of 1.66 m from the equivalent façade, as per anechoic measurements in §6.4.

a maximum, 2.2 dB apart in the region $ka < 0.1$, and differences become smaller if approaching frequencies such as $ka = 1$ and $ka = 10$. Accounting for that difference, we remain in the case of harmonic normal incidence field for our developments.

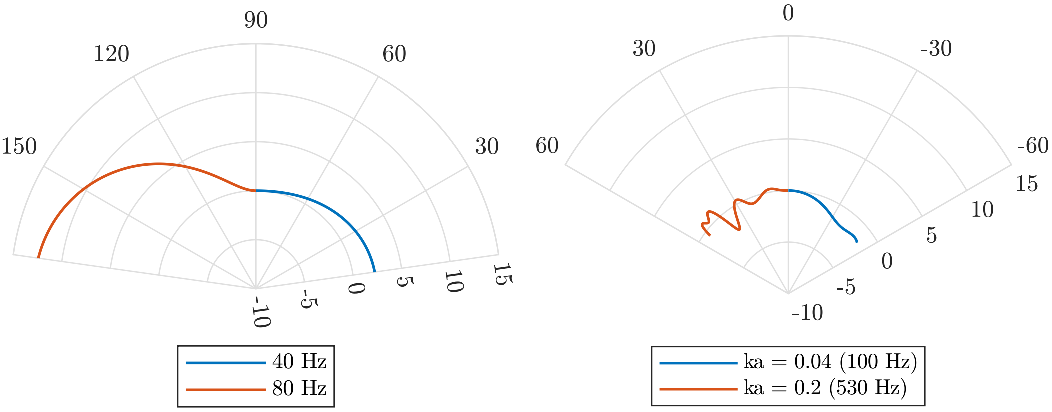

(a) [Junger and Feit, 1993] model **(b)** [Mellow and Kärkkäinen, 2011] model

Figure 6.7: Radiation models [Junger and Feit, 1993] and [Mellow and Kärkkäinen, 2011] at low frequencies using the same conditions as in Figure 6.3 and Figure 6.6.

6.4 Measurements

In this section, we aimed to gather relevant measured data that would allow for model comparison and adjustment, and eventually, support any of the simplifications assumed. The corpus of measurements was mainly focused on the two-dimensional representation of the internal pressure field and the 2D-3D coupling with the exterior radiation phenomena. As such, an initial concern was to derive the forcing term in our physical system driven by electro-acoustic sources.

One possible way to devise a force term is to use our knowledge of the sources from Chapter 5 and deduce an equivalent acoutic flow for the cylindric source. Taking the membrane displacement of the speaker (Equation (5.35)) and differentiating with respect to time one obtains the surface velocity. An acoustic flow source is obtained when we consider a surface force, such as

$$f = Pressure \cdot S_d = \dot{x} Z_r \tag{6.54}$$

where Z_r is the radiation impedance of the circular piston or driver membrane. The total mass being moved is the sum of all the moving masses and the total R_e of the speaker system is the series summation of N drivers (see model described in Chapter 5). For a frequency region above resonance the membrane acceleration is dominated by the moving mass of the speakers

$$BlI = \dot{x} M_{tot} \tag{6.55}$$

and before the inductance behaviour becomes prominent, the system's impedance is dominated by its real part related to its electrical resistance R_e, hence, having measured the voltage delivered to the source during acquisitions, one can use Ohm's law to estimate I.

One finally arrives at the source term for equation Equation (6.2) as

$$f = (\dot{x} Z_r)\delta(\vec{r} - \vec{r}_o)e^{j\omega t} \tag{6.56}$$

The conditions measured in the laboratory experimental organ-like cavity observed the following parameters:

- Different density of cylindrical scatterers
- Different number of cavity walls
- Different observation distances to the source and façade

6.4.1 Measurement setup in ideal conditions (anechoic)

In laboratory controlled conditions we made use of an idealized organ-like cavity built as per the diagram in Figure 6.2 in 15 mm thick plywood. The setup was used for the purpose of reproducing the internal field of a open, semi-closed and closed cavity, the directivity of the single and multiple slit systems, the scattering of the façade, the slit resilient state, the near and farfield comparison, and the façade transfer function.

The design and dimensioning criteria of the setup comprised: logistic assembly and transportation of the setup, relevant observable wavelengths, avoidance of modal degeneracy, comparable aspect ratio with actual organ buffets. The four lateral wall panels and the top panel where removable in order to facilitate access to the interior and to allow for different enclosure conditions.

The front wall was provided with an interchangeable plexiglass panels: a hermetically closed version and a version with an aperture of width $a = 40\,\mathrm{mm}$ (same diameter as the cylindrical scatterers used in the interior) and height $b = 550\,\mathrm{mm}$. The location of such panel was 210 mm and 215 mm away from the bottom and top. The center of the aperture was shifted $-45\,\mathrm{mm}$ from the x-axis center to avoid measuring at the **X**-nodal center line.

The internal dimensions of the cavity were $L_x = 1340\,\mathrm{mm}$, $L_y = 580\,\mathrm{mm}$, and $L_z = 980\,\mathrm{mm}$. Matrices of perforated plexiglass panels were put at the top and bottom of the cavity to accomodate a total of 173 PVC cylindrical pipes of diameter 40 mm filled with acoustic foam in order to avoid pipe resonances (three of those pipes were removed to allow space for the source), spaced 80 mm between adjacent pipes in the x-axis and y-axis, and 56.5 mm obliquely when the staggered rows were included. The distribution of pipes amounted to a total of 11 rows and 16 columns (see Figure 6.8). When the external pressure field was measured, two acquistion lines were used parallel to the front row of cylinders: one at a distance of 200 mm (from the center of the cylinder to the microphone capsule) and another one at 1665 mm. With respect to the source membrane, those distances were 535 mm and 2000 mm. The microphones were placed in 29 locations 50 mm apart along the acquisition lines, covering the width of the enclosure.

A small perforation was performed in the back wall to wire the sources and receivers (and sealed with plasticine around the cables). When façade conditions

(a) Cylinder matrix (top view)

(b) Acquisition system shown here with side walls removed during the measurement of the facade transfer function

Figure 6.8: Radiated pressure measurement setup in laboratory controlled conditions.

were measured, the front panel was removed leaving the front row of 16 cylinders interfacing between the interior and exterior of the enclosure.

The gear employed in measurements was

- An amplifier Carver PM-175
- Omnidirectional microphones (BAMT, series 1), with sensitivity ranging from $47.9\,\mathrm{mV\,Pa^{-1}}$ to $56.2\,\mathrm{mV\,Pa^{-1}}$
- A pistonphone calibrator (Brüel & Kjaer, Type 4228) delivering 123 dB SPL referenced to 20 µPa
- A turn table system (Brüel & Kjaer, Type 9640)
- The 1 m source described in Chapter 5
- A soundcard RME Fireface UFX+

6.4.2 Cavity field and wall impedance estimation

In Table 6.2, the frequencies are shown for the computed lossless rigid wall closed cavity and the relative gain with respect to the highest peak. A microphone was placed in a corner opposite to the source. The general response of the closed, empty internal field is shown in Figure 6.9 and the closer view to the low modal density in Figure 6.10 exhibits the change in shape functions in five different microphone locations along the **X**-axis, 15 cm apart without changing the position in y and z. An inverse filter was applied to account for the spectral coloration of the source (measured in free field at 1 m). It is apparent that the 2 cm and 32 cm positions are collocated shape nodes, not exhibiting the first and second **X**-eigenfrequencies. The height of the microphone capsule was $z = 44\,\mathrm{cm}$ and the half-height of the cavity 49 cm): only the microphone located in a corner allowed to see the first vertical resonance (measured at 190.4 Hz). With a y-separation of 6 cm from the closed façade, the first mode was found at 307.6 Hz.

The phase response of the wall for an incident excitation wave away from resonance of the eigenshapes will cause a wall vibration velocity shift: below resonance, the velocity response appears (in steady-state periodic regime) ahead of the excitation pressure force of the wave; in resonance, the velocity is in phase quadrature with the incident pressure; above resonance, the velocity appears to lag. As the excitation wave with frequency $\omega \neq \omega_o$ reaches the boundaries, these are seen by the incident wave as an effective distance (wavelength) smaller or larger than the actual cavity length in $\mathbf{X} - \mathbf{Y} - \mathbf{Z}$. The manifestation of such phase response, together with losses at the walls and wall vibration yield frequency shifts in the frequencies reported in Table 6.2, showing a few of them in Figure 6.12, where the cavity contains one aperture. The effect to the internal field observed there for the single aperture (and empty cavity) in low modal density appears small. However, when the density of the forest of cylinders is increased we found a progressive shift of **Z**-modes at the slit level (see Figure 6.13, Figure B.4, and Figure B.5).

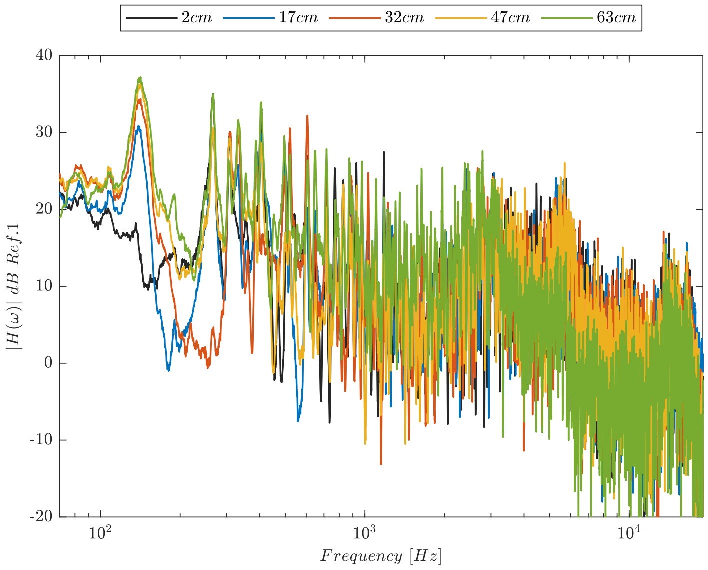

Figure 6.9: Wide span measured internal pressure spectra overview in the closed cavity: no cylinder forest in the interior and no apertures present; the source is located at $\mathbf{r}_o = (\sim L_x, 0)$ facing 45° away from its y-axis towards the center of the cavity; the receiver distances are with respect to the center of the x-axis, 6 cm away from the front wall in the y-axis and at a height of 44 cm. The values for the modal frequencies annotated may be found in Table 6.2.

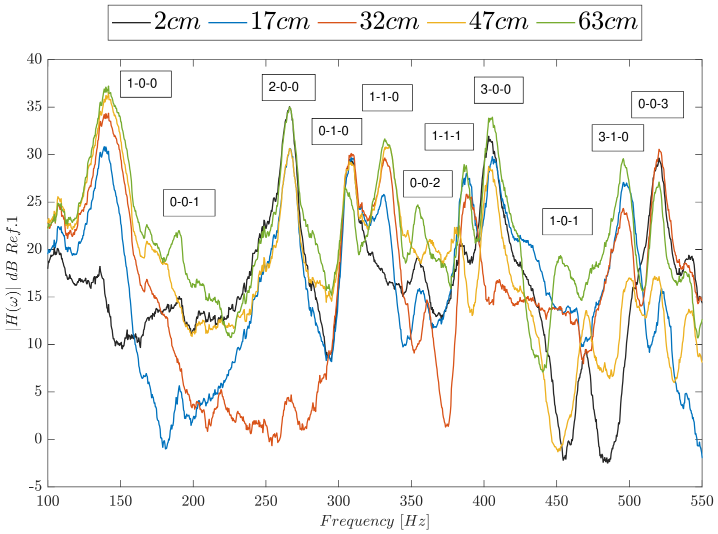

Figure 6.10: Low modal denstiy range of measured internal pressure spectra in the closed cavity: no cylinder forest in the interior and no apertures present; the source is located at $\mathbf{r}_o = (\sim L_x, 0)$ facing 45° away from its y-axis towards the center of the cavity; the receiver distances are with respect to the center of the x-axis, 6 cm away from the front wall in the y-axis and at a height of 44 cm. The values for the modal frequencies annotated may be found in Table 6.2.

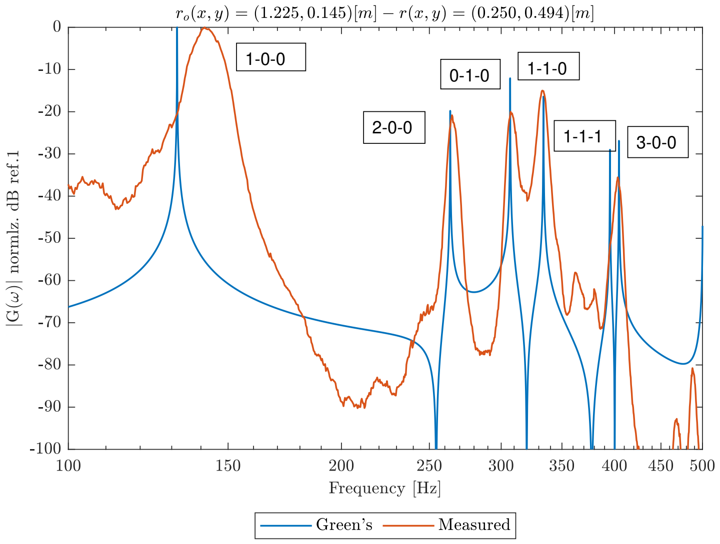

Figure 6.11: Measured spectra versus computed lossy Green's solution with wall impedance and losses of a single aperture as per Equations (6.17), (6.19) and (6.20). The source is located in a rear corner and the observation point in near the front panel, mid height (in the 3D measurement) and off the central node in the x-axis. The values for the modal frequencies annotated may be found in Table 6.2.

Table 6.2: Eigenfrequencies of the organ-like laboratory cavity comparing the computed lossless rigid walls with the measured values. The *gain* refers to the magnitude difference in dB with respect to the maximum peak (at 1-0-0).

	X	**Y**	**Z**	**XY**	**XZ**	**XYZ**
Calc. [Hz]	130.7	293.1	173.5	320.9	217.2	364.8
Meas. [Hz]	141.8	307.6	190.4	332.5	215.7	390.6
Gain [dB]	0	-9.4	-14.3	-5.7	-10.5	-9
[ΔHz]	+11.1	+14.5	+16.9	+11.6	-1.5	+25.8
Calc. [Hz]	261.5	586.2	346.9	641.9	434.5	
Meas. [Hz]	264.2	605.9	354.9	645.9	445.5	
Gain [dB]	-1.7	-8.7	-14.8	-10	-16.9	
[ΔHz]	+2.7	+19.7	+8	+4	+11	
Calc. [Hz]	392.3	879.3	520.4		651.7	
Meas. [Hz]	404.3	873.8	518.8		668.7	
Gain [dB]	-4.3	-10.3	-8.9		-23.5	
[ΔHz]	+12	-5.5	-1.6		+17	

Using mean values in the range 100 Hz to 1000 Hz, one may arrive, using [Bistafa and Morrissey, 2003], at the N_m modes of the lossy wavenumber shown in Table 6.5.

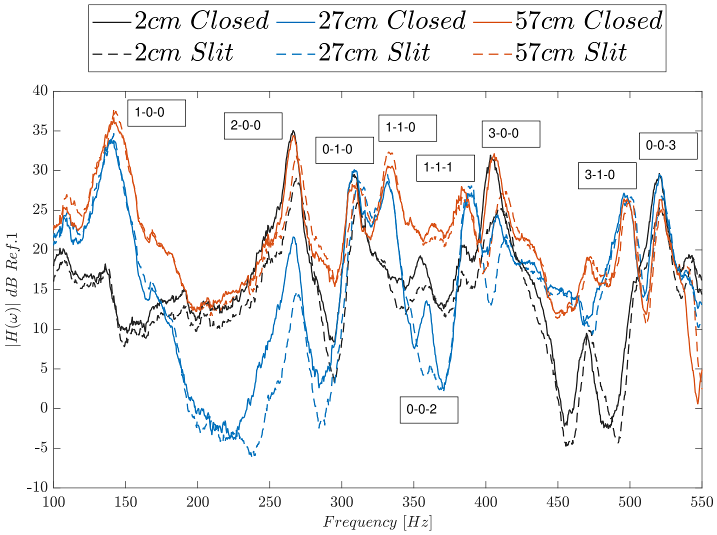

Figure 6.12: Measured internal pressure field for a cavity with no apertures and one aperture at different internal positions. Distances are referred over the **X**-axis and away from the center of the front wall. The values for the modal frequencies annotated (closed cavity) may be found in Table 6.2.

6.4.2.1 The single slit and façade transfer function

As was commented earlier, the choice of slit model was dependent on the conditions found experimentally *in* the slit. We located five microphones vertically aligned at $y = L_y$ at different heights and inspected the magnitude and phase of the pressure transfer functions with respect to one reference microphone (second to bottom one). The data evidences that alterations from unity in magnitude and equality in phase are presented with axial, tangential, or oblique **Z**-modes. This led us to conclude that the state of the slit is of homogeneous pressure distribution. We provide a selection of such data in Figure 6.13.

Table 6.3: Specific acoustic admittances of the first four resonances of the closed empty organ-like cavity. Measured frequencies from Table 6.2 (141 Hz, 307 Hz, 190 Hz, and 332 Hz). The resulting average specific acoustic impedance resulting is: $\zeta_{walls} = \mu + j\kappa = 14.419 - j46.4$.

Mode	$\beta = \xi + j\sigma$
X	$0.0064 + j0.0137$
Y	$0.0063 + j0.0242$
Z	$0.0056 + j0.0198$
XY	$0.0062 + j0.0208$
Average	$0.0061 + j0.0197$

Table 6.4: Specific acoustic admittances processing data by octave bands. The resulting average specific acoustic impedance resulting is: $\zeta_{walls} = 13.95 - j46.7$.

Mode	$\beta = \xi + j\sigma$
X	$0.0082 + j0.0137$
Y	$0.0048 + j0.0242$
Z	$0.0067 + j0.0198$
XY	$0.0038 + j0.0208$
Average	$0.0059 + j0.0197$

Table 6.5: Lossy wavenumber following impedance increments method [Bistafa and Morrissey, 2003]. The average quantity is obtained after analysis of the cavity damping response per octave bands and linear interpolation.

N_m	$\chi_x = \mu_x + j\kappa_x$	$\chi_y = \mu_y + j\kappa_y$	$\chi_z = \mu_z + j\kappa_z$	$\chi_{av} = \mu_{av} + j\kappa_{av}$
1	$0.9958 + j0.0025$	$0.9930 + j0.0014$	$0.9941 + j0.0020$	$0.9898 + j0.0031$
2	$1.9951 + j0.0029$	$1.9919 + j0.0016$	$1.9931 + j0.0024$	$1.9881 + j0.0036$
3	$2.9967 + j0.0019$	$2.9946 + j0.0011$	$2.9954 + j0.0016$	$2.9921 + j0.0024$
4	$3.9976 + j0.0015$	$3.9960 + j0.0008$	$3.9965 + j0.0012$	$3.9941 + j0.0018$
5	$4.9980 + j0.0012$	$4.9968 + j0.0006$	$4.9972 + j0.0009$	$4.9953 + j0.0014$
6	$5.9985 + j0.0010$	$5.9973 + j0.0005$	$5.9977 + j0.0008$	$5.9961 + j0.0012$
7	$6.9986 + j0.0008$	$6.9977 + j0.0005$	$6.9980 + j0.0007$	$6.9966 + j0.0010$
8	$7.9988 + j0.0007$	$7.9980 + j0.0004$	$7.9983 + j0.0006$	$7.9970 + j0.0009$
9	$8.9989 + j0.0006$	$8.9982 + j0.0004$	$8.9985 + j0.0005$	$8.9974 + j0.0008$
10	$9.9990 + j0.0006$	$9.9984 + j0.0003$	$9.9986 + j0.0005$	$9.9976 + j0.0007$

In the near field, the behaviour of the slit system in the low frequency region (much smaller than the wave lengths) exhibits an attenuation of 0 dB to 5 dB with the exception of a somewhat constant positive gain at ~200 Hz. In the range 398 Hz to 588 Hz, the seemingly same positive gain becomes angle dependent. Near ~775 Hz the angle dependence seems to be lessened or widen. The same pattern with respect to the angle appears in 1736 Hz to 2063 Hz, and is inverted in 2154 Hz to 2440 Hz, where the individualization of façade sources starts being evidenced (Figure B.6). The frequency in the center of the latter region corresponds to the half wave-length of the center-to-center spacing between cylinders. The reader is reminded that no walls are present at this stage, thus this observations are due to the front array of pipes only (see Figure B.6).

Faint evidences of plane behaviour or less angle dependent can be found around ~2770 Hz (top of Figure B.6) and ~3300 Hz (bottom of Figure B.7). The inverted angle dependency shows again in 3820 Hz to 4160 Hz. As one progresses to the higher frequencies (Figure B.8), the scattering behaviour in the directivity of the façade becomes evident (further figures concerning the near field of the façade transfer function are placed in Appendix B).

It is tempting to pose this observed behaviour in terms of some apparent properties of nonlinear dispersive wave interactions [Whitham, 2011, Drazin and Johnson, 1989], however, it is greatly explained by the linear frequency-phase interaction of wave propagation fronts after different travelled path lengths of the secondary sources rather than by dispersion phenomena. Proof of this is shown by comparison of measured and computed scattered fields in Figure B.2. Moreover, the range of amplitudes concerned here leaves little room to assume any strong nonlinearities ocurring, and the slit interface between interior and exterior of cavity may provisionally be considered in a linear form.

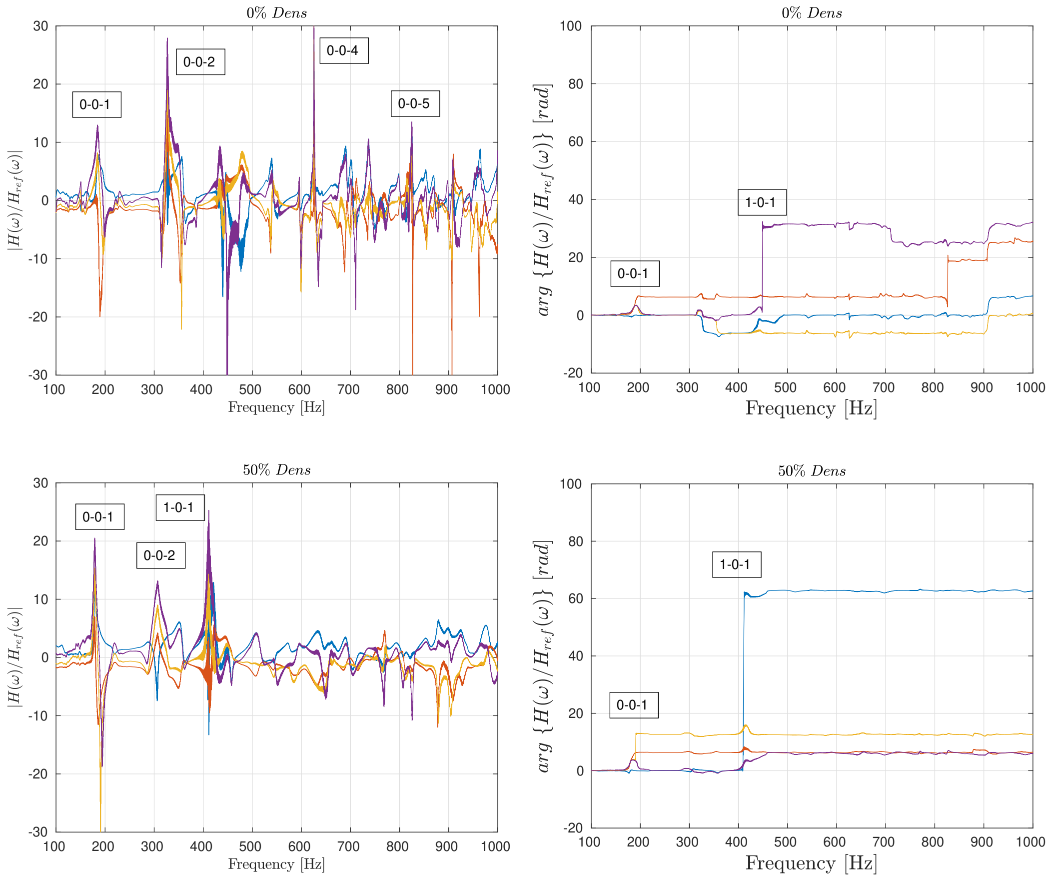

Figure 6.13: Magnitudes (left) and phases (right) of pressure at the slit for different vertical alignments. Tracing the decrease in frequency of the $\mathbf{X}-\mathbf{Z}$-mode with increasing density of scatterers, it indicates that the average effect of one cylinder diminishes the resonance by -0.378 Hz. Bottom microphone to mid-low microphone: $Mic1/Mic2$ —; mid-height to mid-low microphone: $Mic3/Mic2$ —; mid-top to mid-low: $Mic4/Mic2$ —; top microphone to mid-low: $Mic5/Mic2$ —. A complete set of measured data at different densities may be found in Figure B.4 and Figure B.5 (Appendix B).

As for the far-field (at 2 m), we observe the angular dependence with gain per frequency becomes negligible (Figure 6.14). In the mid and high frequencies, there are still traces of angular dependence but not as strong as near the organ (see Figures 6.15 and 6.16). Conversely, marked directions of positive gain and attenuation appear, a result that is consistent with the scattered pressure SPL lobes observed in Figure B.12f. With a Schroeder frequency (with closed cavity) estimated at 1715 Hz as per [Schroeder, 1996], there appears to be an end of regime at $\sim 3.2 f_{Schr}$.

Notwithstanding the different representations and observation distances, it is interesting to compare the angular-independent structure appearing right below 3 kHz in the measured pressure transfer function of the façade in Figure 6.14 (at

1.66 m) with that one appearing above 3 kHz in the simulated[3] scattered pressure of the façade system in Figure D.3 (at 1.5 m); in addition to the structure formation of spectral patterns both in the *long* window integration time (Figure D.3) and during the pseudo-transient time. See the comparison between the mid-to-high frequencies in the measured data (Figure 6.15) with the latter figure and the pseudo-transient at 4.5 m in Figure D.4.

The transfer function of the façade as computed from measured pressure with the laboratory setup in Figure 6.16 shows agreement with the numerical computation of the [Mellow and Kärkkäinen, 2011] high frequency scattered pressure for N_{sl} slits calculated at the same read-out distance for the frequency range 5 kHz to 10 kHz (Figure B.2), exhibiting both the change of regime above 5.5 kHz and the characteristic lines at $L_x/2 \pm L_x/4$. The common setup element they share is the number of façade cylinders (secondary sources in the analytic model), together with the cylinder-to-cylinder spacing and the read-out distance.

Near the interface, Figures B.6 to B.8 (Appendix B) show that the modal structure is apparent and annotated in the frequency axis of Figure B.6, as well as the beginning of evidence of individual scattering within the transition region beyond $f_{Schr} \approx 1715\,\text{Hz}$ displaying concave and convex characteristic lines of different travelled path lengths in the three figures mentioned. This effect remains visible in the high frequencies (Figure B.8) but vanishes at higher distances (1.66 m, Figure 6.16).

---

[3] We will introduce the details on simulation of scattering problems later on this chapter (§6.6).

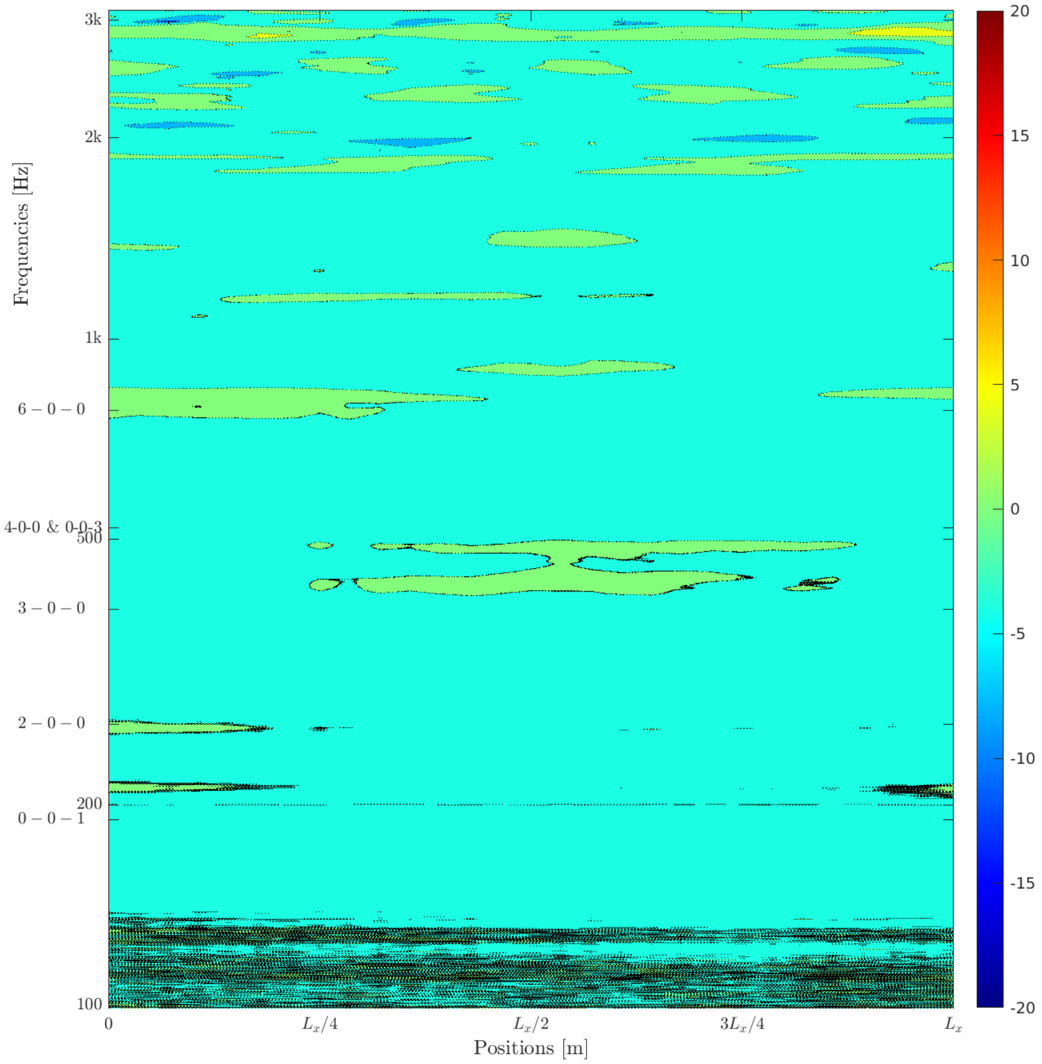

Figure 6.14: Low and mid frequencies of the façade transfer function at a distance of 1.66 m away from the façade. No lateral or rear walls present and no other cylinders than the façade array. The effect of the source reference field with no pipes and walls has been subtracted.

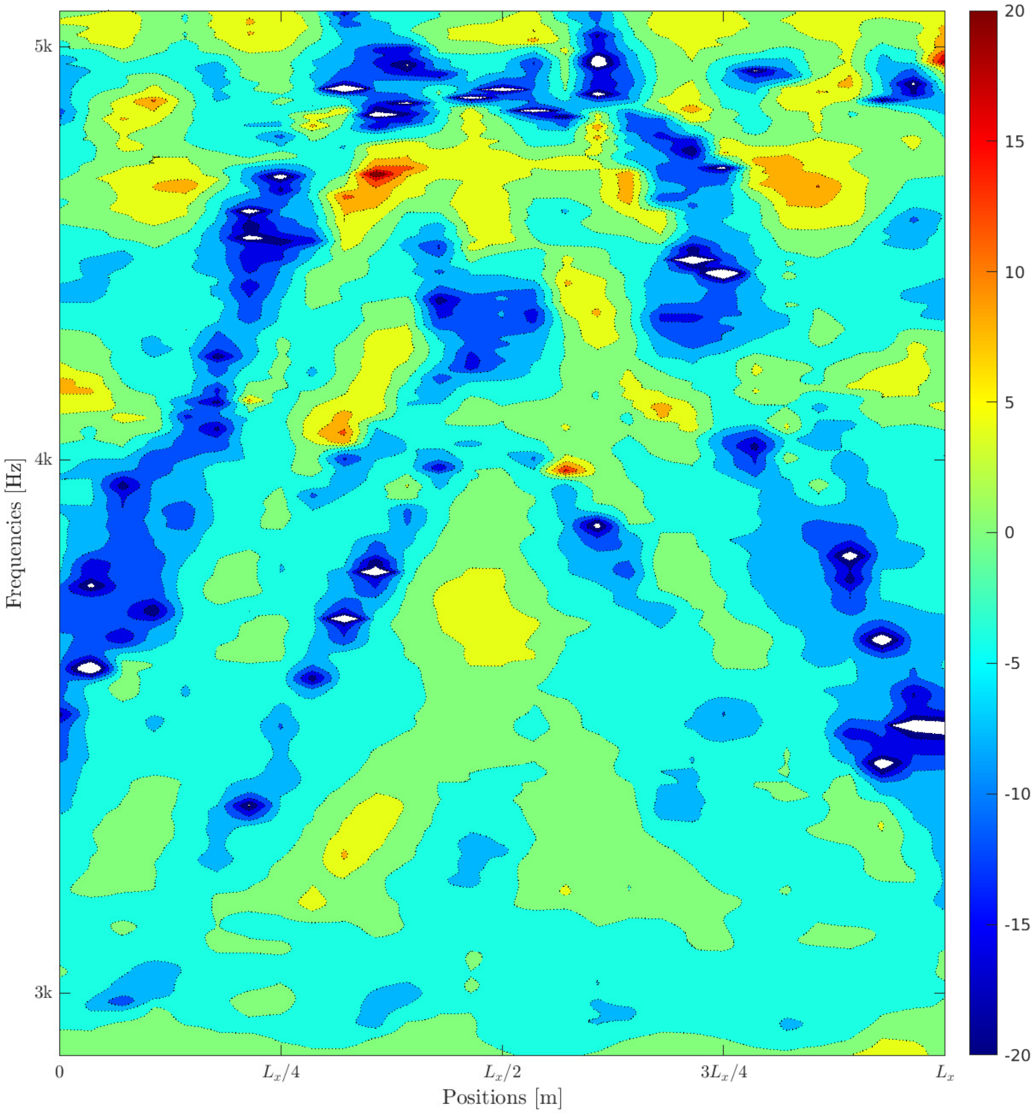

Figure 6.15: Mid-to-high frequencies of the façade response at 1.66 m away from the façade. No lateral or rear walls present and no other cylinders than the façade array. The effect of the source reference field with no pipes and walls has been subtracted.

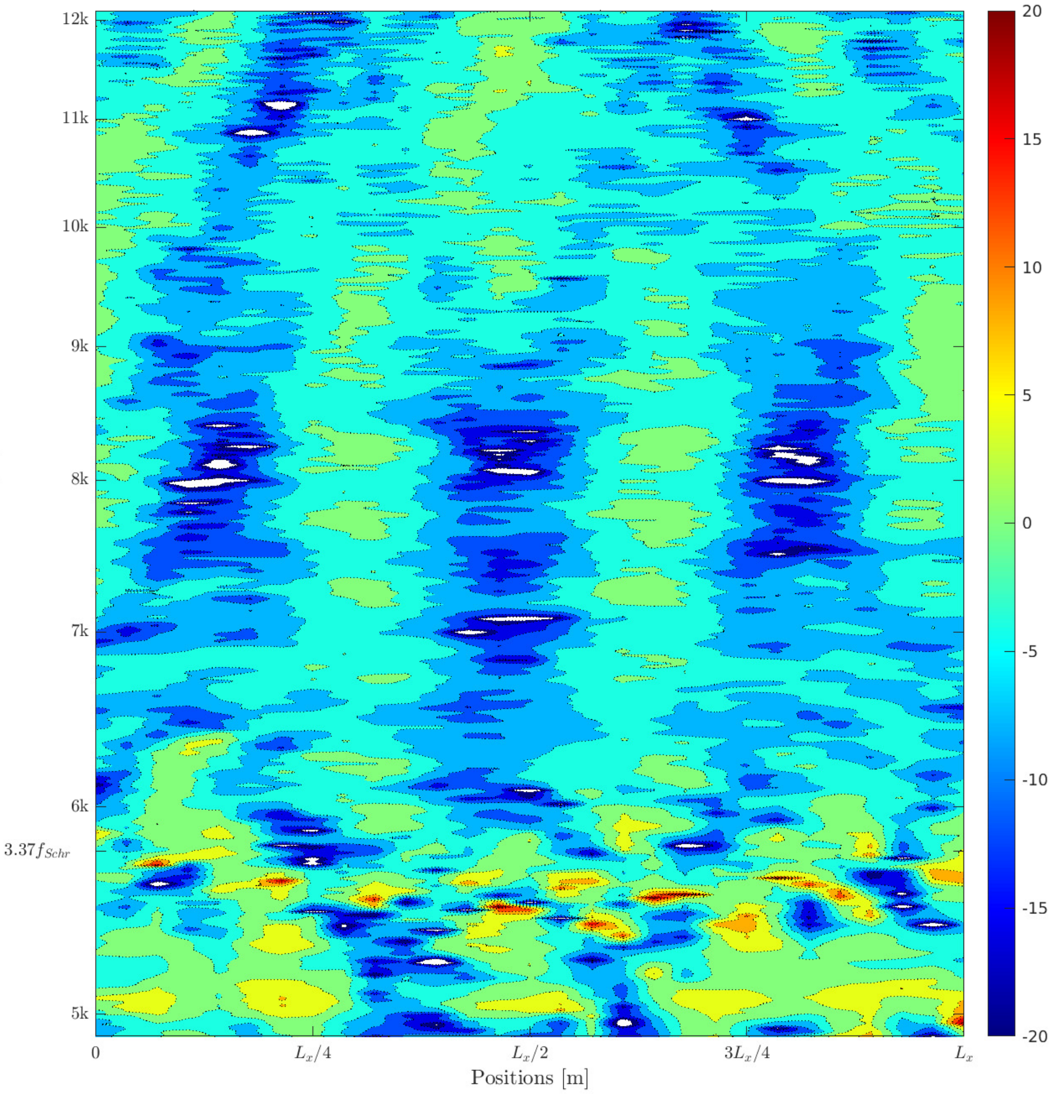

Figure 6.16: High frequencies of the façade response at 1.66 m away from the façade. No lateral or rear walls present and no other cylinders than the façade array. The effect of the source reference field with no pipes and walls has been subtracted.

6.4.3 Directivity measurements with the idealized organ

The following selection of results (a more complete version is located in Appendix B) are concerned with the relative SPL and phases of the measured pressure at two distances while modifying the system conditions

- Near-field in presence of lateral walls with no cylinders: Figure 6.18.
- Two distances for different densities of forest behind the façade array without lateral or rear walls: Figure 6.18.
- Magnitude and phase of the near-field of the semi-closed cavity (lateral and rear walls) at different cylinder densities (starting from no façade, notated as 0 %, whereas the façade is notated as 9 %): Figure 6.19 and Figure 6.20.
- Far-field pressure magnitude at different densities of cylinders presence and with the semi-closed cavity (two lateral and rear walls) : Figure 6.21.

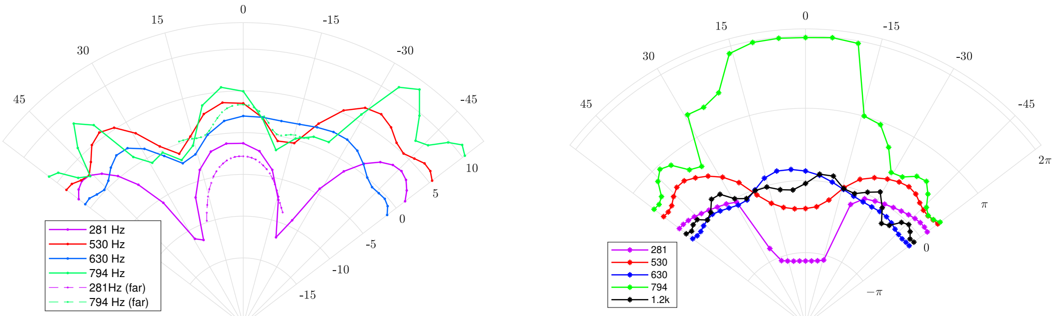

(a) Magnitude (dB) **(b)** Phase (rad)

Figure 6.17: Relative SPL and phase measured at 0.2 m from the front boundary with only two lateral walls and no pipes (no façade pipes either). Twelfth octave band analysis.

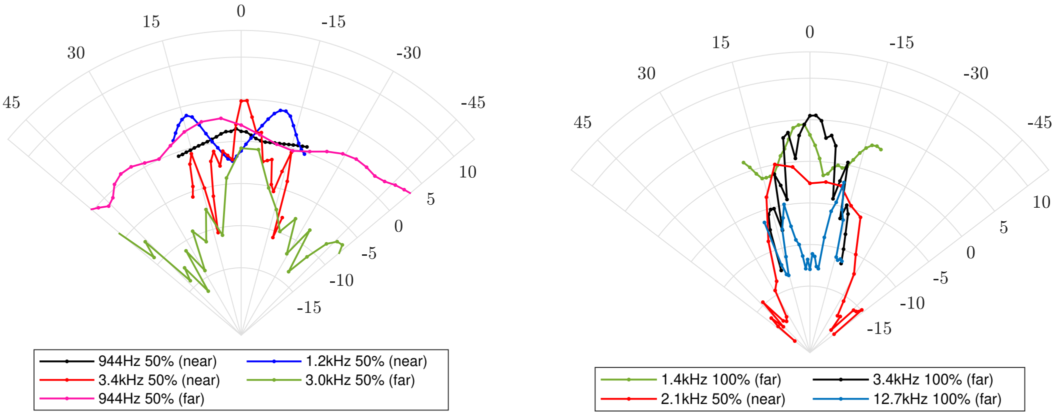

Figure 6.18: Relative SPL (dB) measured at high density of cylinders behind the façade array at different distances with no walls.

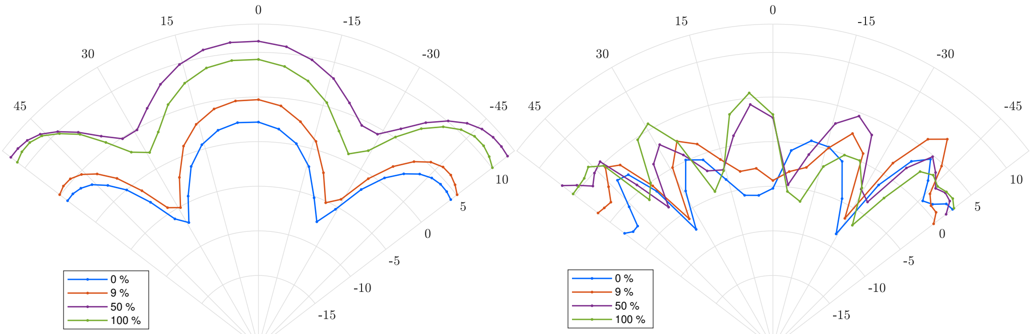

(a) Magnitude (dB) at 265 Hz **(b)** Magnitude (dB) at 1059 Hz

Figure 6.19: Relative SPL measured pressure (dB) at different densities near the semi-closed organ cavity (two lateral and one rear walls). Twelfth octave band analysis.

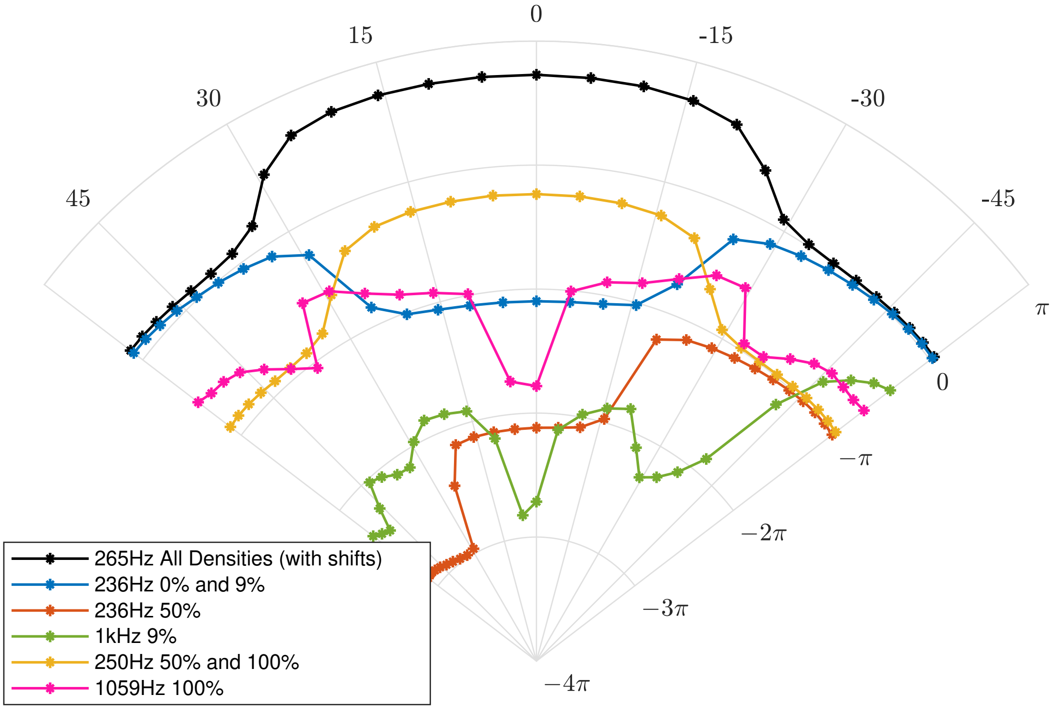

Figure 6.20: Measured pressure field phase (rad) at different densities of forest and different frequencies at 0.2 m of the semi-closed organ cavity (two lateral and one rear walls). Twelfth octave band analysis.

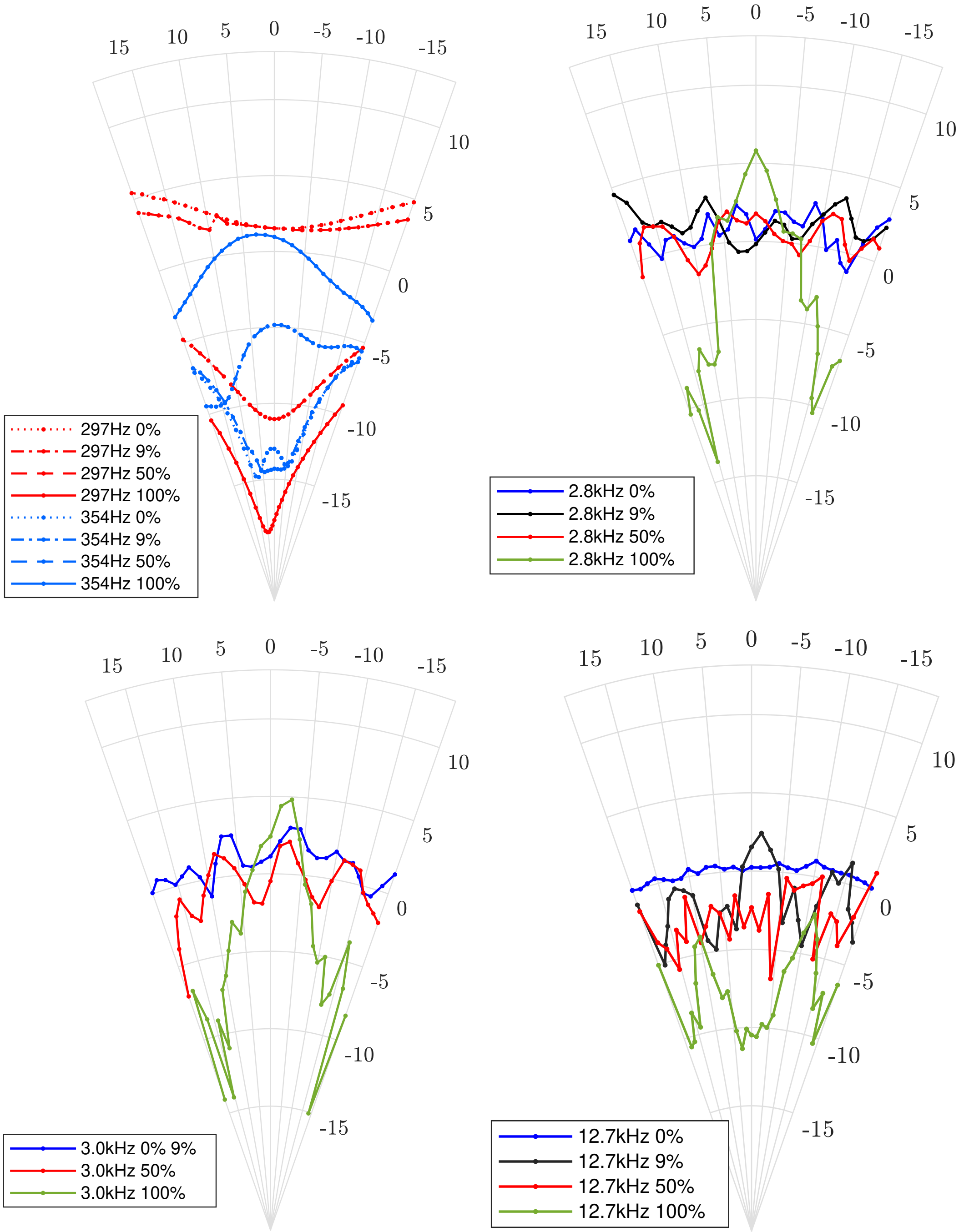

Figure 6.21: Relative SPL (dB) measured at 1.66 m from the idealized organ faced at different forest densities with all the enclosing walls included (except frontal). Twelfth octave band analysis.

Agreement with theory of low modal density was found especially in measurements carried out in the vicinity of the system (0.2 m from the facade, or 0.53 m from the source in absence of cylinders), exhibiting some of the nodal structure of the internal wall resonances in the x-axis, due to the proximity to the slits-array interface (Figure 6.17 and Figure 6.19). The phase data in Figure 6.17 not only describes cavity resonances, but also shows evidence of the spatial truncation phenomena due to the finiteness of the walls (or parallel baffles, as it was discussed already in Chapter 5), an effect that is still present at different densities of cylinders present (Figure 6.20).

Comparing results from models at frequencies where scattering is notorious (3.3 kHz in Figure 6.6) with measured data (3 kHz in Figure 6.21 with the presence of cylinders) evidences an experimental limitation: those appearing as measured observed lobes are prone to spatial aliasing due to the sampling space between microphone locations (50 mm).

The scattering problem becoming apparent as a multiple-source directivity superposition starts showing indices for frequencies above ∼2 kHz (Figure 6.14, Figure 6.15, and Figure 6.16). It was possible to observe relevant[4] directive lobe peaks at very high frequencies and even at 100 % forest densities for some cavity conditions (Figure 6.21), which is generally beyond pipe densities per unit area inside actual organs.

The third-octave band centered at 12.7 kHz exhibits notable directivity evidence despite different cylinder densities, observation distances, and wall conditions (Figure 6.21, Figure B.13, Figure B.16, and Figure B.23).

6.5 Application case: Notre-Dame de Paris

So far, the methods and models proposed[5] are good approximations with the caveat that the façade is assumed flat, thus represented by a line array of secondary pulsating sources. Such approach is a good approximation of the Dallery organ in Chapelle Sorbonne (refer to Figure 1.7 for a visual inspection). The Dallery organ is easily seen as a parallelepiped with a flat façade.

That is not the case of two other tribune organs we have carried out measurements on: the Cavaillé-Coll in Notre-Dame de Paris (NDP) and the Suret in Sainte-Élisabeth de Hongrie. Firstly, the Suret exhibits the subdivision in two main volumes: the positive and the great organ (disregarding internal *plans sonors* and other minor sub-subdivisions like the swell-box, etc.). The positive, the smaller of the two main cavities with a scaling factor in the major dimension of 1:5 with respect to the great organ, protrudes at the back of the organist and constitutes an obstacle to the field radiated by the great organ (this may be seen in Figure 2.1). Secondly, the larger conception in space of both the Cavaillé-Coll and the Suret,

---

[4] We consider relevant events if they surpass *significantly* the SPL of neibourhing and if they have prominences beyond the threshold of 2.2 dB as per [Sgard et al., 2007].

[5] The monopole with STL, the [Junger and Feit, 1993], and the [Mellow and Kärkkäinen, 2011], for low, mid, and high frequencies, respectively.

together with the greater level of embellishment, led to alternating sections of flat façade arrays of pipes and protruding towers of pipes.

Therefore, the analytical models developed thus far will fail to describe the Cavaillé-Coll (NDP) and the Suret without modifications and improvements. In this section, we show data measured in the NDP organ concerning the radiated pressure and the internal response of the cavity. We will detail in §6.7.1 more exhaustive measurements carried out in Sainte-Élisabeth de Hongrie. The increased complexity of the geometries makes the scenarios better suited for more involved numerical simulation method which we will introduce in §6.6.

6.5.1 The NDP tribune organ buffet measurements

We describe next the conditions under which measurements were carried out in NDP. The ambient temperature during the acquisitions was around 9 °C and relative humidity of 68% while we were located at the foot of the great organ, with the console level located elsewhere below us in the scaffolding. The surroundings of the organ were densely occupied by metalic, tubular scaffolding and some provisional flooring and walls, leaving a big space in front of the façade of ~8.5 m wide spanning the width of the organ and ~4.7 m from the façade to the front end of the provisional platform. Additionally, a lateral third of the platform was obstructed by large-size wooden storage cases for the maneauvering of large organ pipes, making measurements in that half of the organ impracticable. The only pipes present were those of the façade, while the interior of the organ had been completely emptied.

The setup was placed at the height of the first *floor* of the organ, containing the windchests of the actual *grand orgue* (GO) and enclosing in the back the lower half of the dismantled swell-box, behind the GO. The 2 m cylindrical source (§5.6) was placed 1.24 m behind the first flat section of façade off the central tower of pipes as shown in Figure 6.23 and the acquisition line was composed of microphones located every 1 cm over a span of 2.5 m in front of the façade at an exterior distance of 1.81 m.

In the organ buffet interior, the lateral and rear walls (with $L_x = {\sim}8.5\,\mathrm{m}$ and $L_y = {\sim}3.5\,\mathrm{m}$) were the actual limestone walls of the cathedral, while the bounding *baffles* of the source, the wooden floor and ceiling of the first floor of windchests, set a distance of $L_z = {\sim}2\,\mathrm{m}$. In some regards, the internal conditions in which we found the interior of the NDP buffet resemble some of the modeling elements we have presented earlier, with a not minor exception of the geometry of the façade: not only the presence of the towers does not meet the modeling approach, but also the dimensions of the façade pipes make equally-sized, regularly spaced cylinders a a poor assumption (see Table 6.6). The region covered in these measurements focused on inspecting the radiated field in presence of the mixture of a façade flat section and two towers.

The gear and protocol employed in our measurements was:

- The 2 m source described in §5.6.

Table 6.6: Pipe spacing in the measured section of the NDP organ. The lateral tower of said section extrude 546 mm and 472 mm. Data was extracted and processed from a high resoltion point cloud of NDP.

Measured façade flat section						
Center-2-center [mm]	174	167	160	154	145	137
Slit width [mm]	25	24	21	23	26	21
Adjancent façade flat section (towards Ut# side)						
Center-2-center [mm]	208	213	193	188	174	
Slit width [mm]	23	36	34	32	38	

- An amplifier (Carver, PM-175).
- A soundcard (RME, Fireface UFX+).
- A rack of microphone pre-amplifiers (RME, Octamic XTC).
- Ten microphones BAMT (series 1).
- A stereo bar holding (with the addition of a steel wire under tension) a horizontally sliding group of five microphones at a time in front of the façade.
- Several microphone stands placing microphones at an exterior reference position, in the slit, and three microphones dispersed in the interior of the buffet level.

We run 30 s sine sweeps from 40 Hz to 12 kHz at a sampling rate of 48 kHz with 5 s of padding. In addition to the microphone acquisitions, a loopback from the soundcard and a voltage divider of 1:200 from the amplifier output were stored as well.

Having made acquisitions in the interior of the NDP organ, also exploding big balloons, we were able to provide a preliminary comparison of the internal fields for low modal density frequencies of the idealized organ in the laboratory with the empty NDP organ. This is shown in Figure 6.22 for kL frequencies using a characteristic length scaling factor $L = \sqrt{L_x^2 + L_y^2 + L_z^2}$ that represented the dimensions and aspect ratio of both enclosures. The frequency responses are, however, as close to resemblance than dissimilar at this point if no model is developed first. Calibration of the internal response model for NDP would be required as we performed in §6.3 with measured data from §6.4. A mesh of the NDP organ geometry (Figure 6.23) was produced from a point cloud for use as bounding bodies in a numerical example discussed later in this work.

We show a selection of measured relative SPL data at the empty organ of NDP, analyzed per twelfths of octave band in Figure 6.24. Interpretation is ambiguous thus far given two main aspects: a scaling factor and the presence of lateral towers. A complete corpus of data may be found in Appendix C.

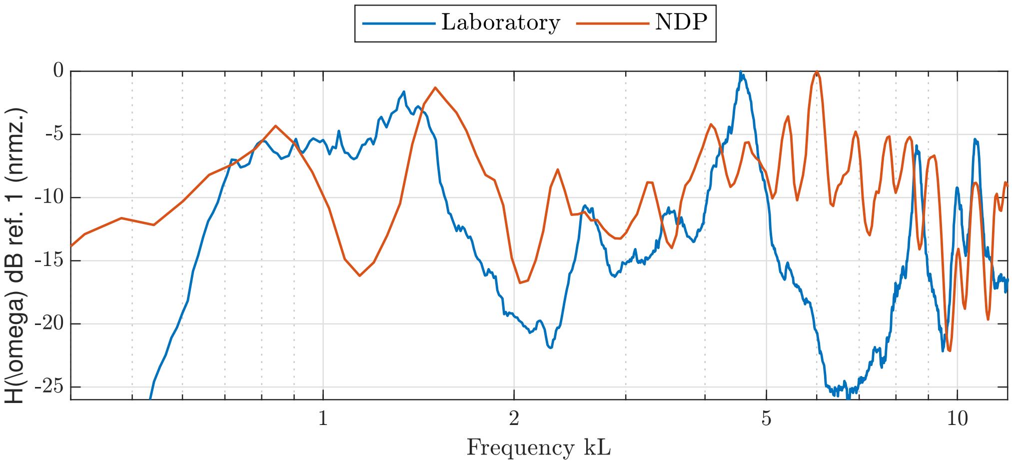

Figure 6.22: NDP buffet internal response as excited by a big balloon explosion compared with the internal response of the laboratory cavity. No pipes in the interior, and semi-open conditions (façade). The characteristic length is taken as $L = \sqrt{L_x^2 + L_y^2 + L_z^2}$, where for the NDP organ only the height of the first floor of windchests is considered ($L_{y,NDP} = \sim 2\,\mathrm{m}$).

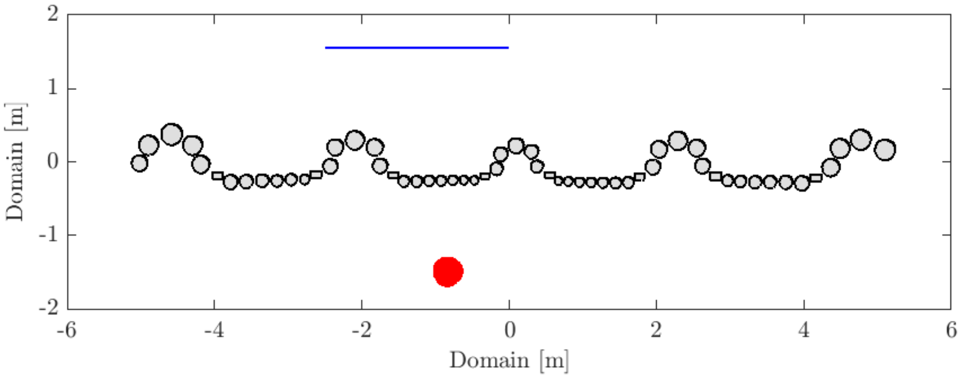

Figure 6.23: Geometry of the NDP tribune organ façade. Annotations: source position (●), acquisition line every 1 cm (—)

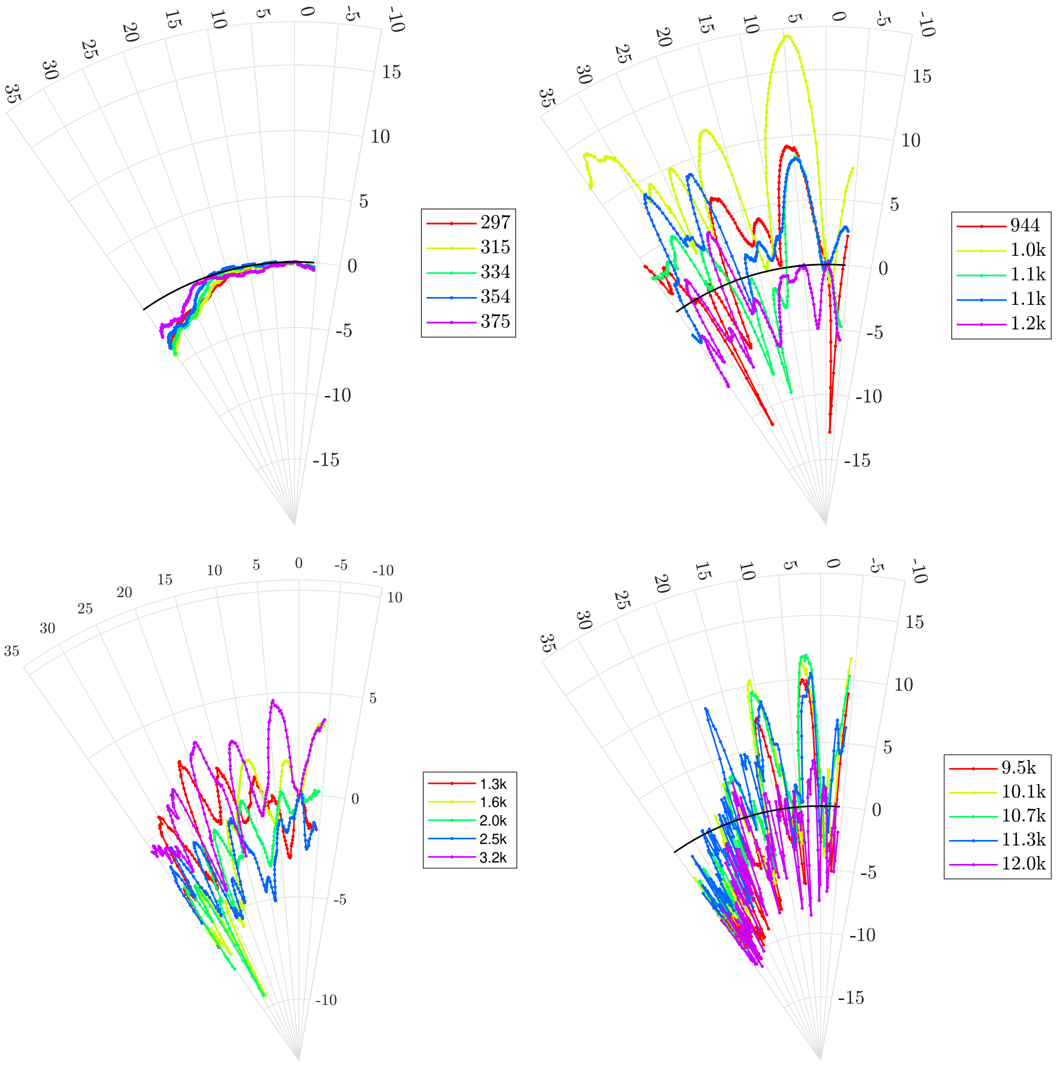

Figure 6.24: Selection of measured relative SPL data in the empty organ of Notre-Dame de Paris. Analyzed per twelfths of octave band.

Algorithm 3: FVFDTD simulation stages

```
Input: Pulse excitation: Ricker wavelet
Output: Potential and velocity fields
begin
    Import geometry mesh from Gmesh
    Create polygon objects (center / rotate apropriately)
    Set four buffer layers of FVTD cells around polygons
    Compute cell volumes and faces (2D analogy) $V_j$ and $S_{jk}$
            as per [Bilbao et al., 2016]
    Compute adjacency pointer functions $\beta_{jk}$ and $\gamma_{jk}$
    Adjust cells centroid as per Lloyd-Voronoi routine
    Generate cell coordinates
    Recompute cell adjacency for: boundary, internal FVTD layers,
            coupled layer with FDTD
    Construct hexagonal Laplacian, projection operators, velocity collocation
    Compute stability condition [Bilbao and Hamilton, 2018]
    Set initial conditions, excitation signal and coordinates for read-out
    Set PML
    Main – loop
        Update FVTD cells
        Update boundaries
        Update domain interior
        Read-out potential and velocity
    end
end
```

6.6 Numerical experiments: finite-volume finite-difference

Weber and Katz [Weber and Katz, 2022] proposed a hybrid implementation for scattering problems of the finite-volume time-domain (FVTD) scheme published by Bilbao *et al.* [Bilbao et al., 2016] and the stability condition derived by Bilbao and Hamilton in [Bilbao and Hamilton, 2018]. The solution consisted in the coupling of FVTD cells (bounding the rigid scattering bodies) with a hexagonal regular FDTD mesh. Please refer to [Weber, 2022, Hamilton, 2016, Taflove et al., 2005] for further details.

Using the same approach, we excite a potential field in an equivalent geometry of the problem at hand with a pulse-like Ricker wavelet ([Sheaffer et al., 2014]) and extract the pressure and velocity fields at the relevant acquisition locations as per the measurement setups described above. The exterior boundaries of the simulated domain (of size $2L_x$ by $2L_y$) are resolved using a perfectly-matching layer (PML) to avoid spurious signals re-entering the domain interior. The steps followed in the simulation are described in Algorithm 3.

An example of the geometry used for FVFDTD simulation as per the ane-

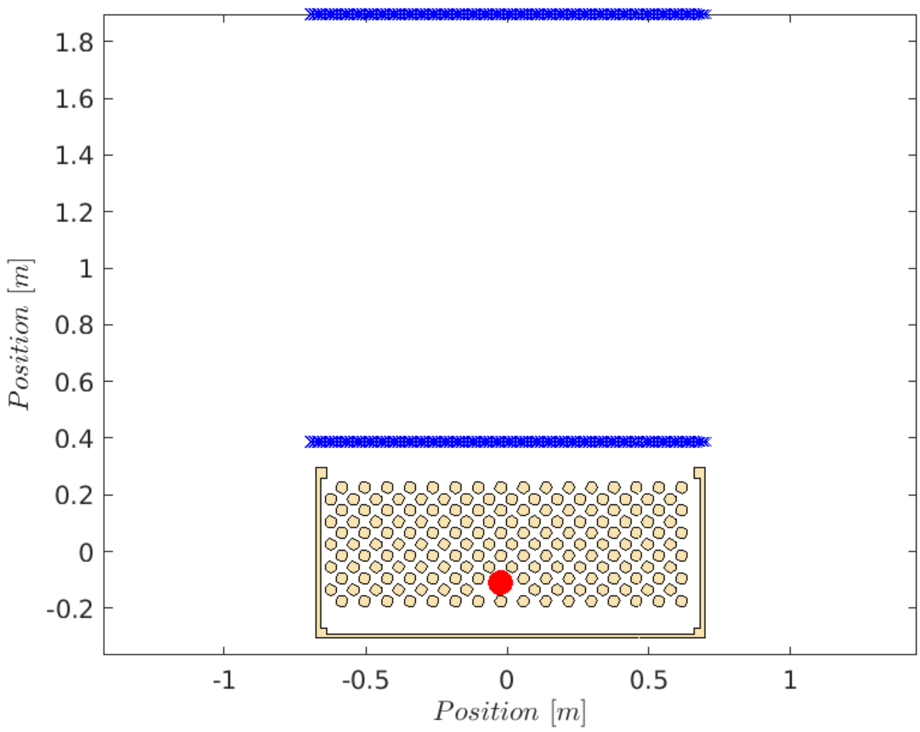

Figure 6.25: Meshed geometry for the 2D FVFDTD simulation of the scattering problem emulating the setup in laboratory condition. The red marker shows the position of excitation and the blue markers read-out locations.

choic measurements of the organ-like idealized cavity (see the measurement setup in Figure 6.8) can be found in Figure 6.25. The Acquisition lines where placed at 53.5 cm and 200 cm from the source in parallel straight lines to the façade (20 cm and 166.5 cm from the slit of the façade).

A further investigation using numerical methods allowed for finer acquisition locations around the full circumference of the cavity and made it possible also to place two closed contours around the problem: one at 1.5 m and another one at 4.5 m where both the potential and the projected velocity over the contour were stored. See the numerical experiment setup in Figure 6.26. In addition, the simulated field allows for storing the free propagation of the excitation in absence of the scattering bodies and obtain the scattered field as the difference between the total field and the free-propagation field.

Knowing the pressure and velocity fields over a closed contour around the domain would allow to perform a near-field far-field transform of the data measured in the vicinity of the problem. However, one encounters the following aspects that render the problem unwieldy

- The incident field onto the scatterers is sourced from within the scattering problem and propagates throughout

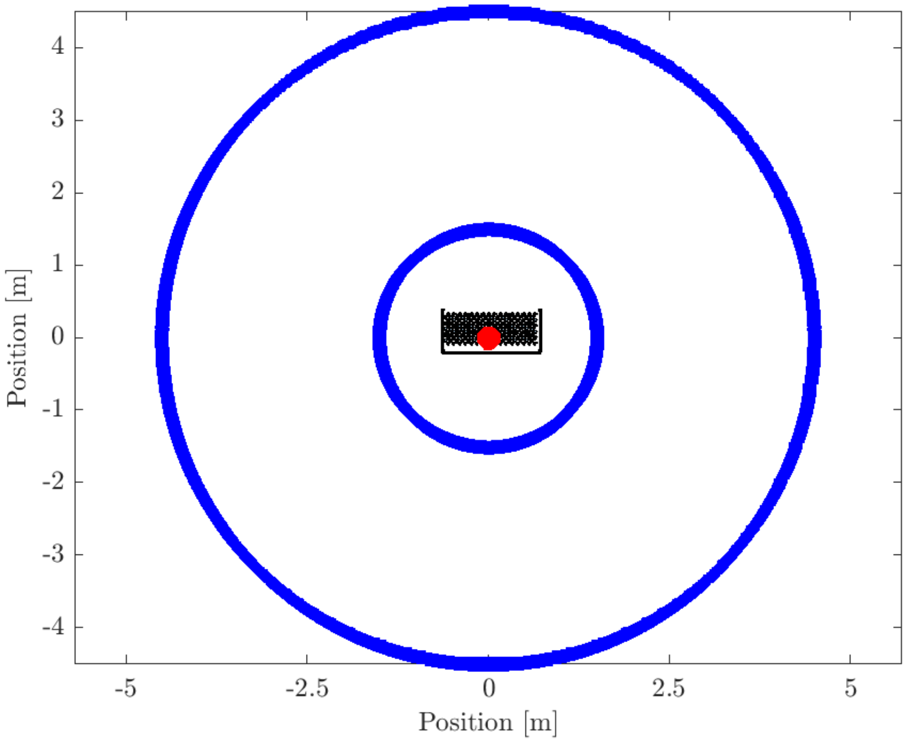

Figure 6.26: Two closed contours in the FVFDTD equivalent implementation of the anechoic measurements of the idealized organ-like cavity at 1.5 m and 4.5 m, annotated with blue markers. The red marker shows the position of the source.

- Both the source and the scatterer are found inside the contour
- The scattering problem consist of three planar finite reflectors and a complex media of regularly spaced infinite cylinders
- The Green's function can be known outside the perimeter of the scattering problem, and around a small contour around the source, but it is difficult to formulate the incident and scattered fields in any intermediate sized contour

The scattered pressure normalized by the free-propagation pressure (in absence of scattering bodies) is shown in Appendix D for an arbitrary fixed window length at the 1.5 m contour around the organ system at specific frequencies exihibing similar directivity patterns to those seen in §6.4 and §6.5, and for short sliding windows (Figure D.4) over the *pseudo-transient* at the 4.5 m contour as a transfer function for low and mid frequencies.

The Courant-Friedrichs-Levy number (CFL) used was set to values between $(0.8, 0.99)\lambda_{max}$ of the stability condition imposed by the FV part of the mesh, as per the condition published in [Bilbao and Hamilton, 2018] for the scheme at hand.

Overestimation in energy levels by the FVFDTD scheme is to be expected due to the method of loss implementation. The scheme used in FV was modified from [Bilbao et al., 2016] to

$$\psi_j^+ = \frac{\left[2\psi_j - \sigma_{jl,FV}\psi_j^- + \frac{c^2T_s^2}{V_j}\sum_{k=1}^{N}\frac{\beta_{jk}S_{jk}}{h_{jk}}(\psi_k - \psi_j)\right]}{\left[I + \frac{\rho c^2 T_s}{4V_j}\sum_{l=1}^{N_b}\sum_{m=1}^{M_l}\gamma_{jl}S_l\right]} \tag{6.57}$$

where T_s is the sampling interval or time step, V_j are the cell volumes (surfaces in 2D), S_{jk} are cell face surfaces (edges in 2D), h_{jk} is the center-to-center distance between two adjacent cells j and k, c is the propagation speed in the media, and γ_{jl} and βjk are indicator functions that map adjacency between cells and between cells and boundaries. The notation ψ_j^+, ψ_j, and ψ_j^- is shorthand for shifting the potential in the time steps $\psi^{\pm} = e_{\pm}\psi^{n+1/2}$ (where $e_{\pm}$ represents a forward or backward time-difference operator). Losses at the scatterer boundary are governed by a single value σ_{FV} in the first-order backward difference terms, while the frequency dependent losses in the FD grid are σ_{FD} and σ'_{FD}. A lossy implementation of the scatterer boundary per bands is easier to interpret as an additional update equation on the normal velocities [Bilbao and Hamilton, 2017] (using the notation there)

$$v_{\perp,l}^{n} = \sum_{m=1}^{M_l} v_{\perp,l}^{(m),n} \tag{6.58}$$

$$\rho\delta_{t\circ}\psi_j^n = R_l^{(m)}\mu_o v_{\perp,l}^{(m),n} + L_l^{(m)}\delta_{t\circ}v_{\perp,l}^{(m),n} + \frac{1}{C_l^{(m)}}\mu_\circ g_l^{(m),n} \tag{6.59}$$

$$\delta_{t\circ}g_l^{(m),n} = \mu_{t\circ}v_{\perp,l}^{(m),n} \tag{6.60}$$

where, as well as in [Bilbao et al., 2016], requires the knowledge of unphysical fitted values for $R^{(m)}$, $L^{(m)}$, and $C^{(m)}$ in the locally reactive boundary equivalent circuit. The notations $\delta_{t\circ}$ and $\mu_{t\circ}$ are used to express centered time difference and centered time average operators.

6.7 Future perspectives

Thus far, we have proposed models of the slit that assume infinite extent in the z-axis and have paid little attention to the geometry of the aperture, considering the slit mass-less and infinitely thin. Radiation impedance conditions for that case were derived in Chapter 5 for the cylindrical wave and in [Mellow and Kärkkäinen, 2011].

It is possible to formulate the impedance of the aperture between cylinders as the lumped sum corresponding to the slit admittance for the impinging wave from the interior, the air gap between the cylinders, and the outer radiation termination as inertance terms under the from

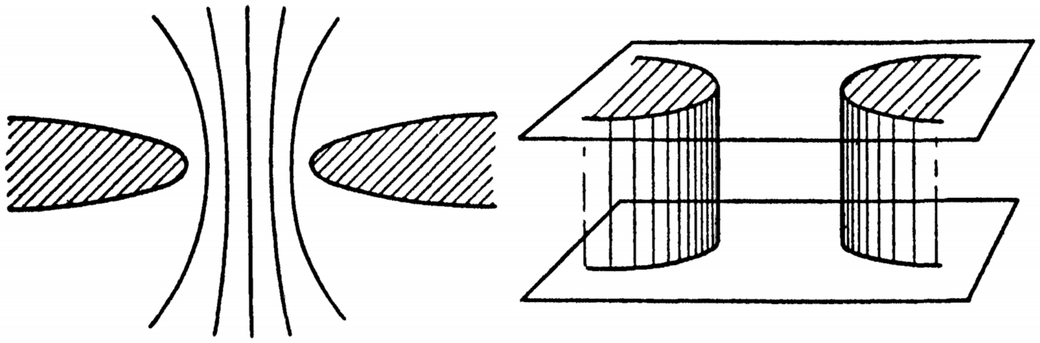

Fig. 6·10.

Figure 6.27: Conformal transform mapping of the potential through façade cylinders as per [Milne-Thomson, 1962].

$$M_{\mathrm{c2c}} = m_{\mathrm{in}} + m_{\mathrm{slit}} + m_{\mathrm{out}} \tag{6.61}$$

where m_{slit} may be approximated (and has been so in the current work) as the resilient slit admittance or by the impedance at the surface of a pulsating source, and with flanged conditions for m_{in} and m_{out}. Relevant analysis with detailed attention to the geometry is found in [Ernoult and Fabre, 2017b] with application to the impedance of the window in recorder-like instruments, making use of conformal mapping and FEM techniques. While the walls of the pipes of the façade may experience vibration when being played, the contribution by that effect was found to be significantly minor as per the investigations of [Kob, 2000b, Kob, 2000a]. Using the idea of conformal mapping ([Milne-Thomson, 1962, Verge, 1995, Ernoult and Fabre, 2017b]), a careful analysis of the impedance at the slit for the geometry seen in Figure 6.27 may be conducted to improve the impedance model of the apertures and the losses in the semi-open cavity.

Following the analysis of [Ochmann, 2004, Ochmann and Piscoya, 2021] in terms of the *complex source* would promisingly yield more involved and physically meaningul approaches for the encoding of secondary equivalent sources placed at the façade to represent the radiation problem that we have addressed here as a three-fold model depending on the frequency range.

With regard to the slit between pipes seen as the interface between the interior and exterior domains, it may be worth considered in the analysis by [Pavic and Du, 2016], in which the patch and surface harmonics technique are applied to the coupling of two rooms with a common interface, claiming that their model can span a frequency region of 0.3 kHz to 20 kHz.

Lastly, having developed tools for numerical simulation of scattering problems under complex geometry conditions, and given the current lack of a model for radiation for non-flat façade organs, it would be a source of comparison if the near-to-farfield transform were to be performed following, for example, [Taflove et al., 2005],

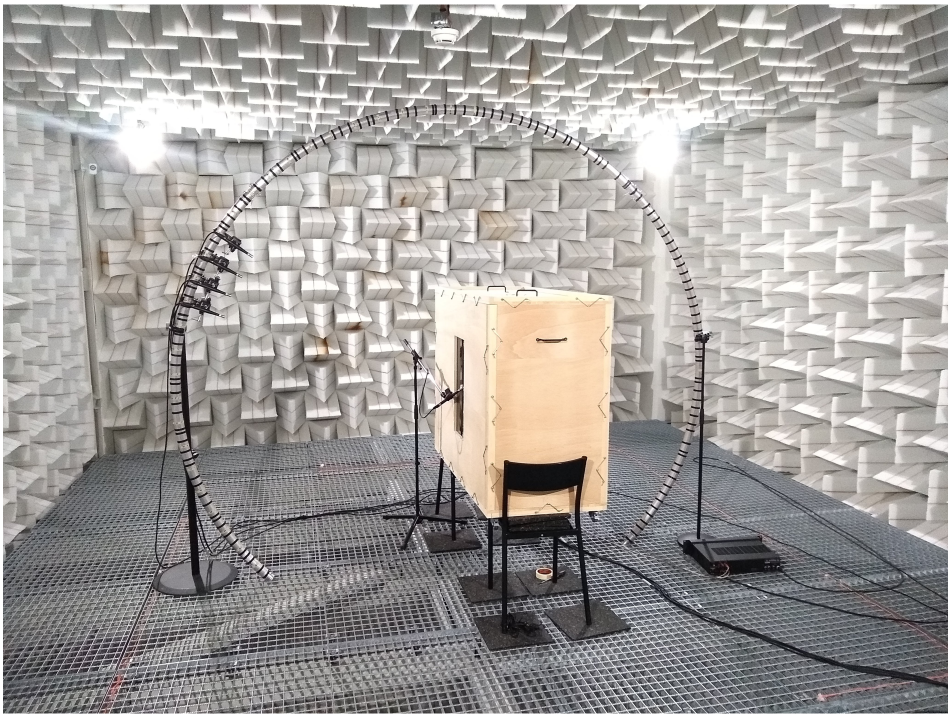

Figure 6.28: Laboratory measurement setup of the vertical directivity of the single slit at 1.3 m from the source (2D, inside) for 0% and 100% cylinder density conditions with the same protocol as in §6.4.1.

using pressure and velocity data at observation points situated on a closed contour as we evoked in Figure 6.26.

6.7.1 Sainte-Élisabeth de Hongrie

With respect to the 2D-3D coupling in models, data of the vertical directivity of the single slit was produced every 5° for the idealized cavity in the laboratory (see Figure 6.28), following the same protocol as in §6.4.1. This condition may be analyzed under comparison with 2D and 3D excitation of the positive organ in Sainte-Élisabeth de Hongrie, for which directivity measurements were carried out without any propagation obstacles (as opposed to the case of the great organ). Initial clues for the 2D and 3D behaviour of pipe radiation may be found in [Bellows and Leishman, 2022].

The gear and protocol employed in our measurements was:

- The 1 m and 2 m sources described in §5.6 and an dodecahedron omni directional speaker (Dr. Three, 3D-032).
- An amplifier (Carver, PM-175).
- A soundcard (RME, Fireface UFX+).
- A rack unit of microphone pre-amplifiers (RME, Octamic XTC).

- Ten microphones BAMT (series 1).
- Two stereo bar holding (using the addition of a steel wire under tension) a horizontally and vertically sliding group of four and five microphones at a time, in front of the façades at distances: 1.8 m and 2.1 m from the façade of the positive, for horizontal and vertical measurements, respectively; 2 m and 10 m from the façade of the GO for horizontal measurements. The extents of the measurements spanned ∼9 m in horizontal measurements and ∼8 m in vertical measurements.
- Several microphone stands placing microphones in the interior of the GO.
- Two quarter-inch microphones (Brüel & Kjaer, Type 4938, SN 2151369 and SN 2151371, with preamplifiers Type 2670) placed at the passive end of the resonator of two of the organ pipes.
- A signal conditioner stage for the the quarter-inch microphones (Brüel & Kjaer, Nexus, series 2690).

We run 6 s sine sweeps from 60 Hz to 20 kHz at a sampling rate of 48 kHz with 6 s of padding. In addition to the microphone acquisitions, a loopback from the soundcard and a voltage divider of 1:200 from the amplifier output were stored as well.

Investigations have been carried out towards quantifying scaling methods between 2D and 3D excitation strategies in a real organ (a 1853 organ by Suret in Sainte-Élisabeth d'Hongrie, Paris), as well as respective results obtained for the radiated field by the small *positive* organ and the *great organ*, with a scale factor of approximately 1 : 5. Preliminary observations have been presented in [Villegas Curulla et al., 2022c, Villegas Curulla et al., 2022b, Villegas Curulla et al., 2022a].

A corpus of experiments were carried out in the positive and great organ of the tribune organ of Sainte-Élisabeth de Hongrie (Paris) where some of the conditions exposed above were explored. In addition to façade filtering in two dimensions, the directivity of an organ cavity was investigated for small and big organs near and far from the façade, and with cylindrical and omnidirectional sources positioned inside.

Lastly, data from organ pipe excitation was acquired using notes found within a non-negligible spatial span, playing pipes from the Positive and the Great Organ every C and F over two and a half octaves. For this data set, no synchronization mechanism was devised. Therefore, one of the initial tasks to analyze the energy contained in the harmonic series of each pipe tone was to time-align the acquisitions.

The difficulty, accentuated in the low frequency tones, resides in finding a satisfactory onset criteria. To reduce the noise during measurements, the windchests where filled up manually using the bellows at the beginning of each sequence of acquisitions.

The segmentation of data that follows successfully isolated tones at 65 Hz and above, equivalent to the C 8'. One such example of this can be found in Figure 6.29

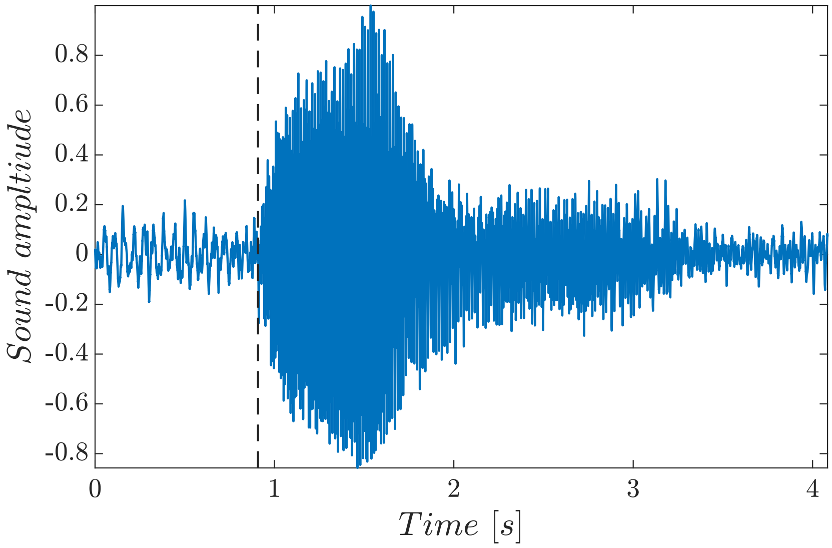

Figure 6.29: Onset detection of noisy, slow organ pipe tones at 65 Hz measured at the Sainte-Élisabeth d'Hongrie tribune organ.

1. Calculate the fundamental period of the pipe tone using the YIN algorithm [de Cheveigne and Kawahara, 2002]
2. Ball-park the central region of the tone's steady-state (acquisitions of approximately 2 s of pipe tone and 2 s of silence)
3. Extract the Fourier amplitudes of the first three pipe modes and, following [Hruška and Dlask, 2020], establish a mask for the length of the transient
4. Compute the instantaneous amplitude of the latter signal
5. Reverse integrate the instantaneous amplitude
6. Calculate the piece-wise slope of the logarithmic reverse integration curve
7. Threshold the previous signal as a ratio of the standard deviation during the transient signal (knee-detection, 2% σ)

The data acquired following the sequence described above allows for spectral analysis of the harmonic series for overlapping frequencies with different locations in space. The spectral contend of the pipe tones overlaps in second and third harmonics with narrow frequency analysis windows.

6.8 Conclusion and summary

In this section we have introduced modelling tools towards the understanding, representation, and prediction of the internal field of an organ-like cavity. These models, proposed according to different spectral and spatial regions, were followed by pressure measurements of an idealized instrument equivalent enclosure that allowed access to several modelling parameters: scatterer spacing, scatterer density, single and multiple apertures, and assessment of sources of losses.

A strong frequency dependence was found due to the acoustic response of the cavity and to the radiation properties. Both aspects were modelled independently: the cavity interior field and the radiation model for one slit, two slits, and $2N_{sl}$ slits. In the current state, a global view allows a qualitative evaluation of the observations made in ideal and actual organ measurements. The results presented consistute a step towards model validation, having pointed at analytical criteria to establish comparisons.

Furthermore, we have introduced further data and descriptions that may help future work in the fields of numerical simulation in 2D FVFDTD of scattering problems, and in-situ measured data for an actual organ with all the geometrical elements present and acquisitions for the two and three-dimensional extension of models.

CHAPTER 7

Bringing everything together: virtualizing the Dallery organ

Contents

7.1 Documentation 161
7.1.1 Reports and inventories 161
7.1.2 Interpolated pipe diameters 168
7.1.3 Modal parameter extraction 172
7.2 Chapelle de la Sorbonne 172
7.2.1 Prelude 172
7.2.2 GA model of Chapelle Sorbonne 175
7.3 The sound of the organ in the Chapelle Sorbonne 178
7.4 Summary and future perspectives 180

7.1 Documentation

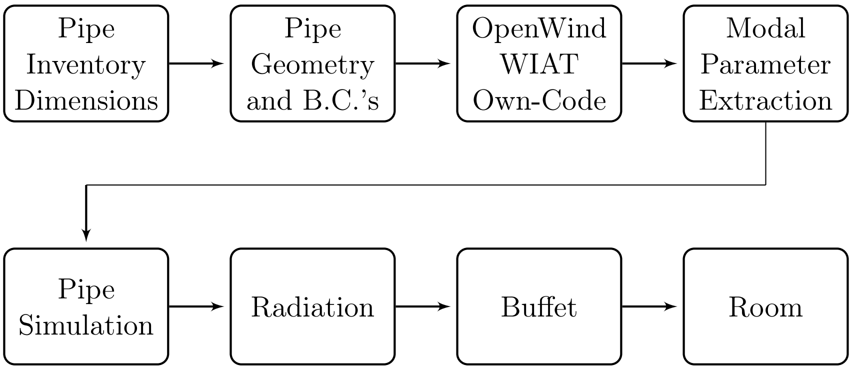

Figure 7.1: Digitalization of instrument file process workflow.

7.1.1 Reports and inventories

Similarly to the route-map presented in Figure 2.2, we propose here the stages outlined in §7.1 to conclude our work on the *organ Dallery in the Chapelle Sorbonne.* We start by one of the missing elements of the puzzle: what pipes that existed, which ones are left, what were the dimensions of them, and how can we retrieve information of those pipes missing, or geometry that is not informed. Our last point of attention, before stringing together all the elements presented is the response of the space that house the organ. We will show a geometrical acoustics model developed to simulate the response of the chapel. We start with the documentation on the organ.

A report updating the state of the organ by 2008 was produced by Galtier, which contains details on the construction, materials, conservation condition, and remarks on the pipework. [Galtier, 2008]). Technical data were found on the pipe dimensions thanks to the inventories carried out by B. Dargassies, L. Martine, P. Dumolin, R. Galtier, and P. Dubois spanning from 1881 to 2008. Valuable details were shared publicly in the International Colloquium taking place the 17th and 18th of November of the year 2000 in the Salle Louis Liard (Université de Paris-Sorbonne) and data extracted from [Dubois and Lueders, 2002] is shown in Figures 7.2 to 7.6.

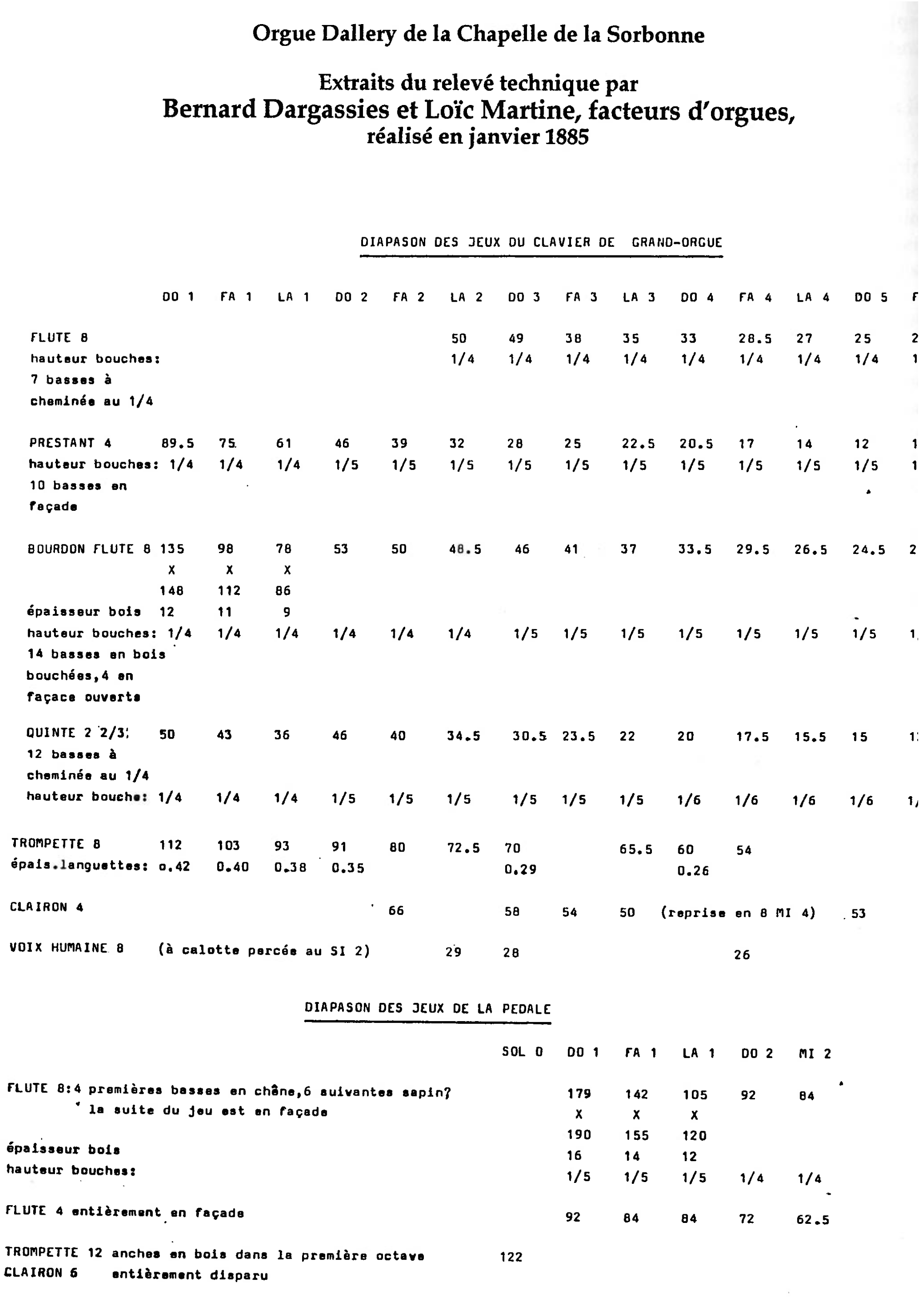

Orgue Dallery de la Chapelle de la Sorbonne

Extraits du relevé technique par
Bernard Dargassies et Loïc Martine, facteurs d'orgues,
réalisé en janvier 1885

DIAPASON DES JEUX DU CLAVIER DE GRAND-ORGUE

	DO 1	FA 1	LA 1	DO 2	FA 2	LA 2	DO 3	FA 3	LA 3	DO 4	FA 4	LA 4	DO 5	F
FLUTE 8						50	49	38	35	33	28.5	27	25	2
hauteur bouches:						1/4	1/4	1/4	1/4	1/4	1/4	1/4	1/4	1
7 basses à cheminée au 1/4														
PRESTANT 4	89.5	75	61	46	39	32	28	25	22.5	20.5	17	14	12	1
hauteur bouches:	1/4	1/4	1/4	1/5	1/5	1/5	1/5	1/5	1/5	1/5	1/5	1/5	1/5	1
10 basses en façade														
BOURDON FLUTE 8	135 X 148	98 X 112	78 X 86	53	50	48.5	46	41	37	33.5	29.5	26.5	24.5	2
épaisseur bois	12	11	9											
hauteur bouches:	1/4	1/4	1/4	1/4	1/4	1/4	1/5	1/5	1/5	1/5	1/5	1/5	1/5	1,
14 basses en bois bouchées,4 en façace ouverts														
QUINTE 2 2/3:	50	43	36	46	40	34.5	30.5	23.5	22	20	17.5	15.5	15	1:
12 basses à cheminée au 1/4														
hauteur bouche:	1/4	1/4	1/4	1/5	1/5	1/5	1/5	1/5	1/5	1/6	1/6	1/6	1/6	1,
TROMPETTE 8	112	103	93	91	80	72.5	70		65.5	60	54			
épais.languettes:	o.42	0.40	0.38	0.35			0.29			0.26				
CLAIRON 4					66		58	54	50	(reprise en 8 MI 4)			53	
VOIX HUMAINE 8	(à calotte percée au SI 2)					29	28				26			

DIAPASON DES JEUX DE LA PEDALE

	SOL 0	DO 1	FA 1	LA 1	DO 2	MI 2
FLUTE 8:4 premières basses en chêne,6 suivantes sapin?		179	142	105	92	84
la suite du jeu est en façade		X	X	X		
		190	155	120		
épaisseur bois		16	14	12		
hauteur bouches:		1/5	1/5	1/5	1/4	1/4
FLUTE 4 entièrement en façade		92	84	84	72	62.5
TROMPETTE 12 anches en bois dans la première octave	122					
CLAIRON 6 entièrement disparu						

Figure 7.2

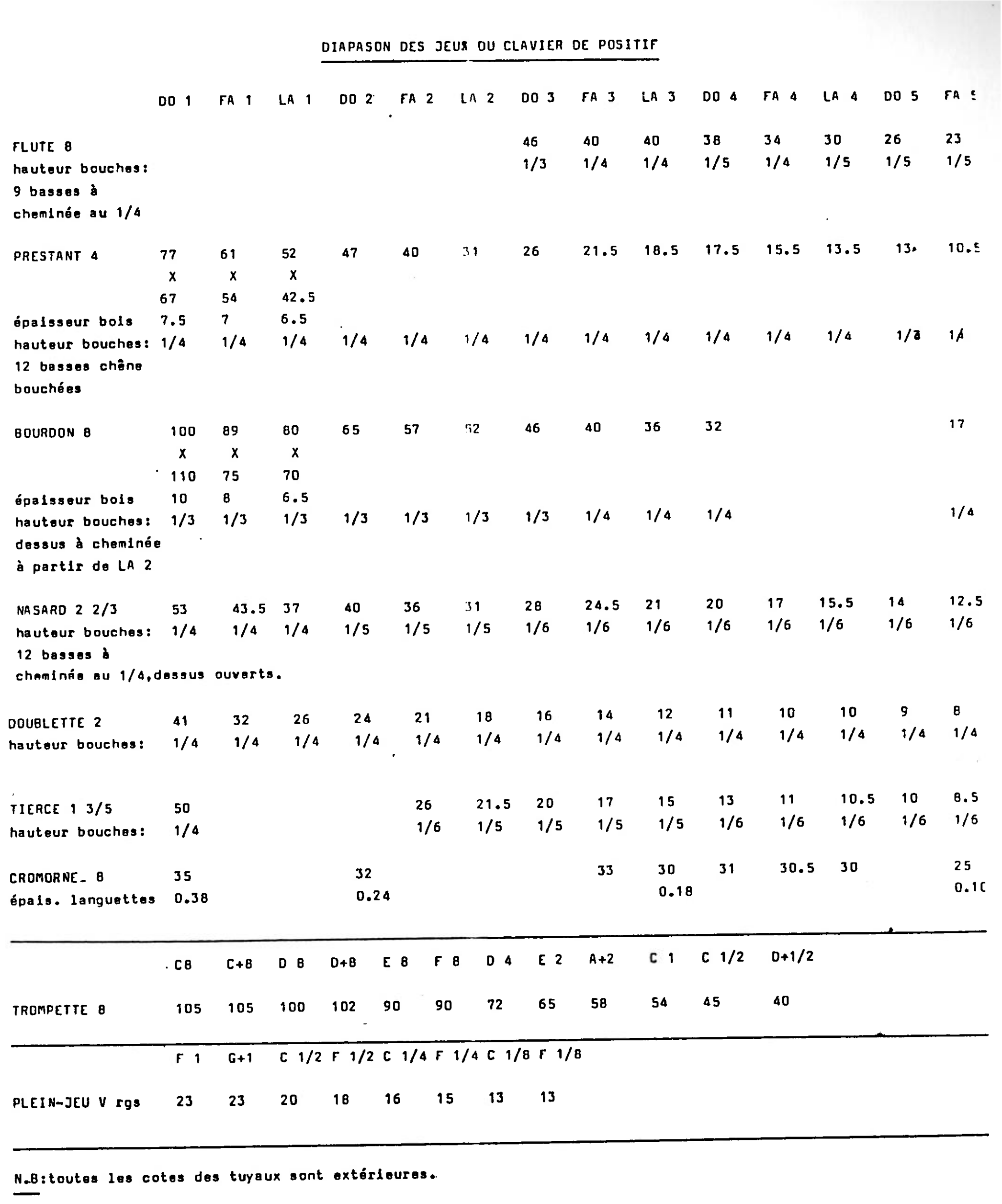

DIAPASON DES JEUX DU CLAVIER DE POSITIF

	DO 1	FA 1	LA 1	DO 2	FA 2	LA 2	DO 3	FA 3	LA 3	DO 4	FA 4	LA 4	DO 5	FA 5
FLUTE 8							46	40	40	38	34	30	26	23
hauteur bouches:							1/3	1/4	1/4	1/5	1/4	1/5	1/5	1/5
9 basses à cheminée au 1/4														
PRESTANT 4	77	61	52	47	40	31	26	21.5	18.5	17.5	15.5	13.5	13	10.5
	X	X	X											
	67	54	42.5											
épaisseur bois	7.5	7	6.5											
hauteur bouches:	1/4	1/4	1/4	1/4	1/4	1/4	1/4	1/4	1/4	1/4	1/4	1/4	1/3	1/4
12 basses chêne bouchées														
BOURDON 8	100	89	80	65	57	52	46	40	36	32				17
	X	X	X											
	110	75	70											
épaisseur bois	10	8	6.5											
hauteur bouches:	1/3	1/3	1/3	1/3	1/3	1/3	1/3	1/4	1/4	1/4				1/4
dessus à cheminée à partir de LA 2														
NASARD 2 2/3	53	43.5	37	40	36	31	28	24.5	21	20	17	15.5	14	12.5
hauteur bouches:	1/4	1/4	1/4	1/5	1/5	1/5	1/6	1/6	1/6	1/6	1/6	1/6	1/6	1/6
12 basses à cheminée au 1/4,dessus ouverts.														
DOUBLETTE 2	41	32	26	24	21	18	16	14	12	11	10	10	9	8
hauteur bouches:	1/4	1/4	1/4	1/4	1/4	1/4	1/4	1/4	1/4	1/4	1/4	1/4	1/4	1/4
TIERCE 1 3/5	50				26	21.5	20	17	15	13	11	10.5	10	8.5
hauteur bouches:	1/4				1/6	1/5	1/5	1/5	1/5	1/6	1/6	1/6	1/6	1/6
CROMORNE_ 8	35			32				33	30	31	30.5	30		25
épais. languettes	0.38			0.24					0.18					0.1

	C8	C+8	D 8	D+8	E 8	F 8	D 4	E 2	A+2	C 1	C 1/2	D+1/2
TROMPETTE 8	105	105	100	102	90	90	72	65	58	54	45	40

	F 1	G+1	C 1/2	F 1/2	C 1/4	F 1/4	C 1/8	F 1/8
PLEIN-JEU V rgs	23	23	20	18	16	15	13	13

N.B: toutes les cotes des tuyaux sont extérieures.

Figure 7.3

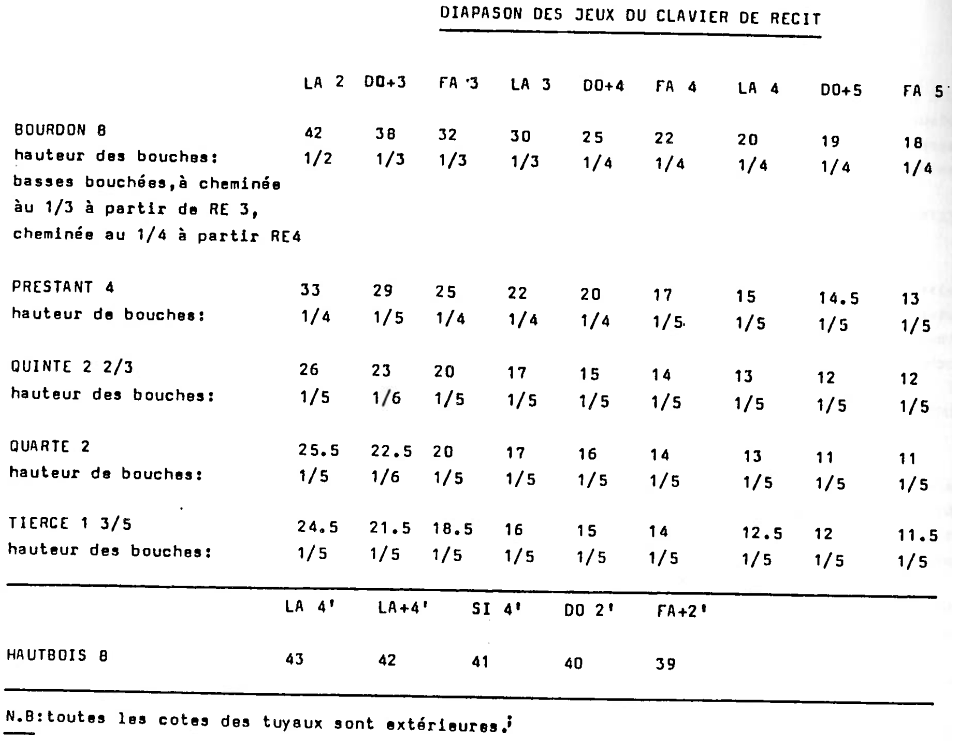

DIAPASON DES JEUX DU CLAVIER DE RECIT

	LA 2	DO+3	FA 3	LA 3	DO+4	FA 4	LA 4	DO+5	FA 5
BOURDON 8	42	38	32	30	25	22	20	19	18
hauteur des bouches: basses bouchées,à cheminée àu 1/3 à partir de RE 3, cheminée au 1/4 à partir RE4	1/2	1/3	1/3	1/3	1/4	1/4	1/4	1/4	1/4
PRESTANT 4	33	29	25	22	20	17	15	14.5	13
hauteur de bouches:	1/4	1/5	1/4	1/4	1/4	1/5	1/5	1/5	1/5
QUINTE 2 2/3	26	23	20	17	15	14	13	12	12
hauteur des bouches:	1/5	1/6	1/5	1/5	1/5	1/5	1/5	1/5	1/5
QUARTE 2	25.5	22.5	20	17	16	14	13	11	11
hauteur de bouches:	1/5	1/6	1/5	1/5	1/5	1/5	1/5	1/5	1/5
TIERCE 1 3/5	24.5	21.5	18.5	16	15	14	12.5	12	11.5
hauteur des bouches:	1/5	1/5	1/5	1/5	1/5	1/5	1/5	1/5	1/5

	LA 4'	LA+4'	SI 4'	DO 2'	FA+2'
HAUTBOIS 8	43	42	41	40	39

N.B:toutes les cotes des tuyaux sont extérieures.

DIMENSIONS DU BUFFET.

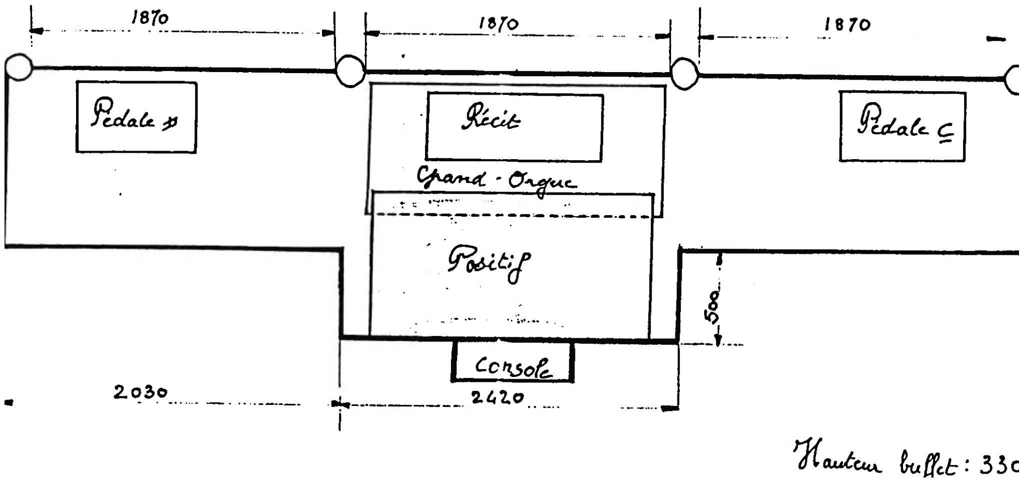

Figure 7.4

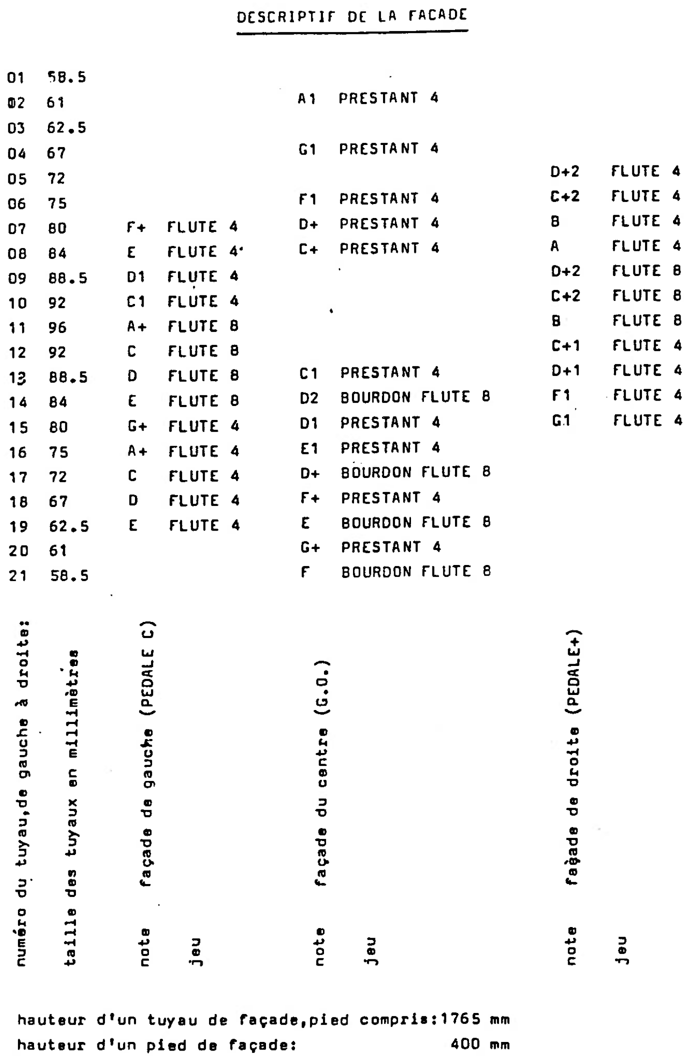

DESCRIPTIF DE LA FACADE

numéro du tuyau,de gauche à droite:	taille des tuyaux en millimètres	façade de gauche (PEDALE C)		façade du centre (G.O.)		façade de droite (PEDALE+)	
		note	jeu	note	jeu	note	jeu
01	58.5						
02	61			A1	PRESTANT 4		
03	62.5						
04	67			G1	PRESTANT 4		
05	72					D+2	FLUTE 4
06	75			F1	PRESTANT 4	C+2	FLUTE 4
07	80	F+	FLUTE 4	D+	PRESTANT 4	B	FLUTE 4
08	84	E	FLUTE 4	C+	PRESTANT 4	A	FLUTE 4
09	88.5	D1	FLUTE 4			D+2	FLUTE 8
10	92	C1	FLUTE 4			C+2	FLUTE 8
11	96	A+	FLUTE 8			B	FLUTE 8
12	92	C	FLUTE 8			C+1	FLUTE 4
13	88.5	D	FLUTE 8	C1	PRESTANT 4	D+1	FLUTE 4
14	84	E	FLUTE 8	D2	BOURDON FLUTE 8	F1	FLUTE 4
15	80	G+	FLUTE 4	D1	PRESTANT 4	G1	FLUTE 4
16	75	A+	FLUTE 4	E1	PRESTANT 4		
17	72	C	FLUTE 4	D+	BOURDON FLUTE 8		
18	67	D	FLUTE 4	F+	PRESTANT 4		
19	62.5	E	FLUTE 4	E	BOURDON FLUTE 8		
20	61			G+	PRESTANT 4		
21	58.5			F	BOURDON FLUTE 8		

hauteur d'un tuyau de façade,pied compris:1765 mm
hauteur d'un pied de façade: 400 mm

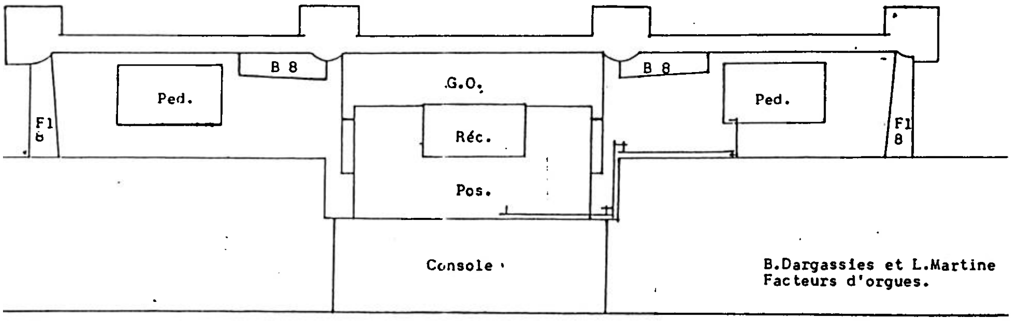

B.Dargassies et L.Martine
Facteurs d'orgues.

Figure 7.5

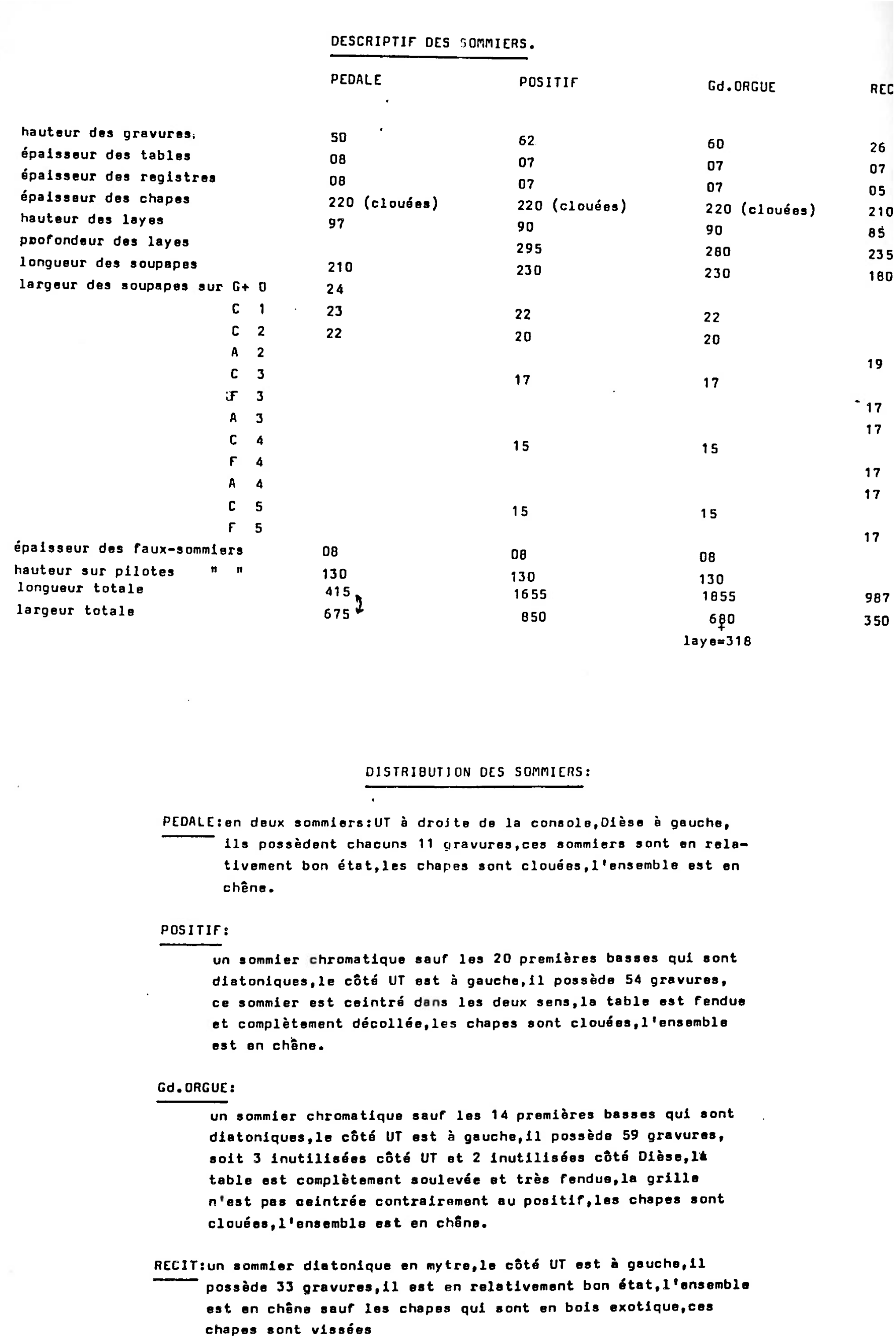

DESCRIPTIF DES SOMMIERS.

		PEDALE	POSITIF	Gd.ORGUE	REC
hauteur des gravures		50	62	60	26
épaisseur des tables		08	07	07	07
épaisseur des registres		08	07	07	05
épaisseur des chapes		220 (clouées)	220 (clouées)	220 (clouées)	210
hauteur des layes		97	90	90	85
profondeur des layes			295	280	235
longueur des soupapes		210	230	230	180
largeur des soupapes sur	G+ 0	24			
	C 1	23	22	22	
	C 2	22	20	20	
	A 2				19
	C 3		17	17	
	F 3				17
	A 3				17
	C 4		15	15	
	F 4				17
	A 4				17
	C 5		15	15	
	F 5				17
épaisseur des faux-sommiers		08	08	08	
hauteur sur pilotes " "		130	130	130	
longueur totale		415	1655	1855	987
largeur totale		675	850	680 + laye=318	350

DISTRIBUTION DES SOMMIERS:

PEDALE:en deux sommiers:UT à droite de la console,Dièse à gauche, ils possèdent chacuns 11 gravures,ces sommiers sont en relativement bon état,les chapes sont clouées,l'ensemble est en chêne.

POSITIF:

un sommier chromatique sauf les 20 premières basses qui sont diatoniques,le côté UT est à gauche,il possède 54 gravures, ce sommier est ceintré dans les deux sens,la table est fendue et complètement décollée,les chapes sont clouées,l'ensemble est en chêne.

Gd.ORGUE:

un sommier chromatique sauf les 14 premières basses qui sont diatoniques,le côté UT est à gauche,il possède 59 gravures, soit 3 inutilisées côté UT et 2 inutilisées côté Dièse,la table est complètement soulevée et très fendue,la grille n'est pas ceintrée contrairement au positif,les chapes sont clouées,l'ensemble est en chêne.

RECIT:un sommier diatonique en mytre,le côté UT est à gauche,il possède 33 gravures,il est en relativement bon état,l'ensemble est en chêne sauf les chapes qui sont en bois exotique,ces chapes sont vissées

Figure 7.6

Diameters are obtained from inventories. Cotes are external, therefore assumptions on the thickness of the tin are made to estimate the internal diameter of the bore.

Length of resonators is set such that the organ file is tuned to a temperament of choice. One readily available option is found in hydraule.org, where also the diameter scaling rules from Dom Bédos [Bédos De Celles, 1766] are explained.

Concerning dimensioning of the mouth[1]: as a rule of thumb, the mouth depth is $H_{\mathrm{m}} = 2\pi R_{\mathrm{p}}/4$ for open pipes of Principal type; the cut-up distance between flue exit and labium is $W_{\mathrm{m}} = H_{\mathrm{m}}/4$, but if more flute-like sound is desired, it may increase to $W_{\mathrm{m}} = H_{\mathrm{m}}/3$, for which a larger flue windway (h) will also be increased. As exposed in Chapter 3, the smaller the cut-up distance W_{m}, the further harmonic development; and conversely, with lower mouths, one obtains a more fundamental sound (see [Miklós and Angster, 2000] for a characterization of narrow, normal, and broad pipes).

The presence of lateral ears (which increase the inertance of the mouth window length correction) may be found in larger octaves, pipes larger than two-feet, and even in closed flutes. The larger the air pressure, the larger it is to place ears on the sides of the mouth.

The windway value h is tuned with respect to the organ air pressure. Blancafort father used to manufacture small flue windways with the resulting effect of *light and bright* but *dirty* [not clean] sound. As reported by A. Blancafort, the value of h

- May span from 1.2 mm to 1 mm in 8' pipes (progressively small for heigher *pitch* pipes), or even starting at 1.5 mm if one wills an *inflated presence* of the organ
- Would start at 0.8 mm for 4' pipes
- Would start at 0.6 mm for 2' pipes

where it would not necessarily be incorrect to linearly interpolate those values, while keeping in mind that the end result will be hand-adjusted by the builder once the pipe is installed and operated in the the destination windchest.

7.1.2 Interpolated pipe diameters

Figure 7.7a to Figure 7.9e show the data sets for pipe diameters as measured from the exterior together with linear, quadratic, and exponential interpolation. Some data sets exhibit unlikely progression of diameters, which is assessed by the lack of monotonical decrease in diameter. Provided that the measurements were taken from the exterior of the pipes, a correction has to account for the thickness of the lead-tin sheet (∼1 mm) in the flue pipes, while the equivalent diameter of the *bourdon* wooden pipes with square cross-section requires a different treatment. The use of the information in these charts is discussed in §3.3.3.

---

[1] Private correspondence with Albert Blancafort, organ builder in Sagrada Familia basilica and Palau Güell.

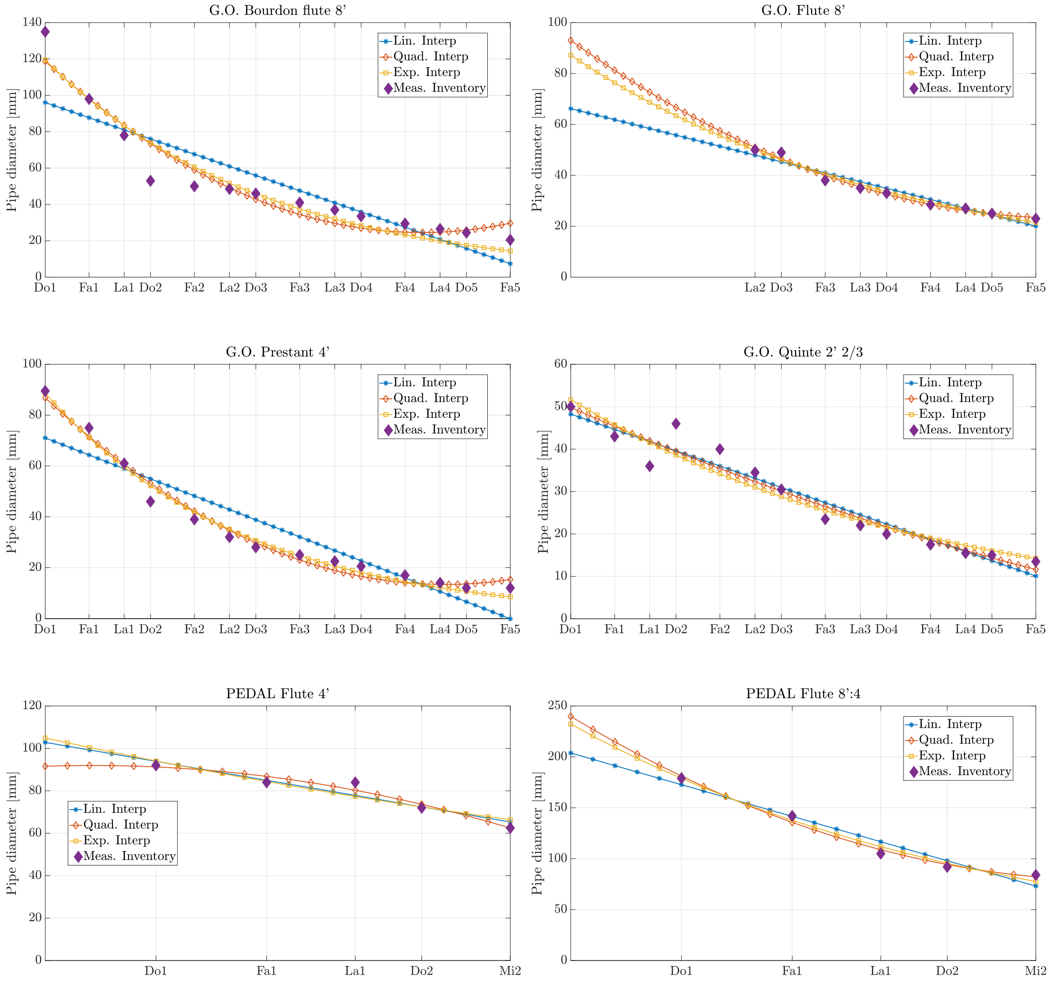

Figure 7.7: Measured diameters from Dallery pipework of the great organ and pedal.

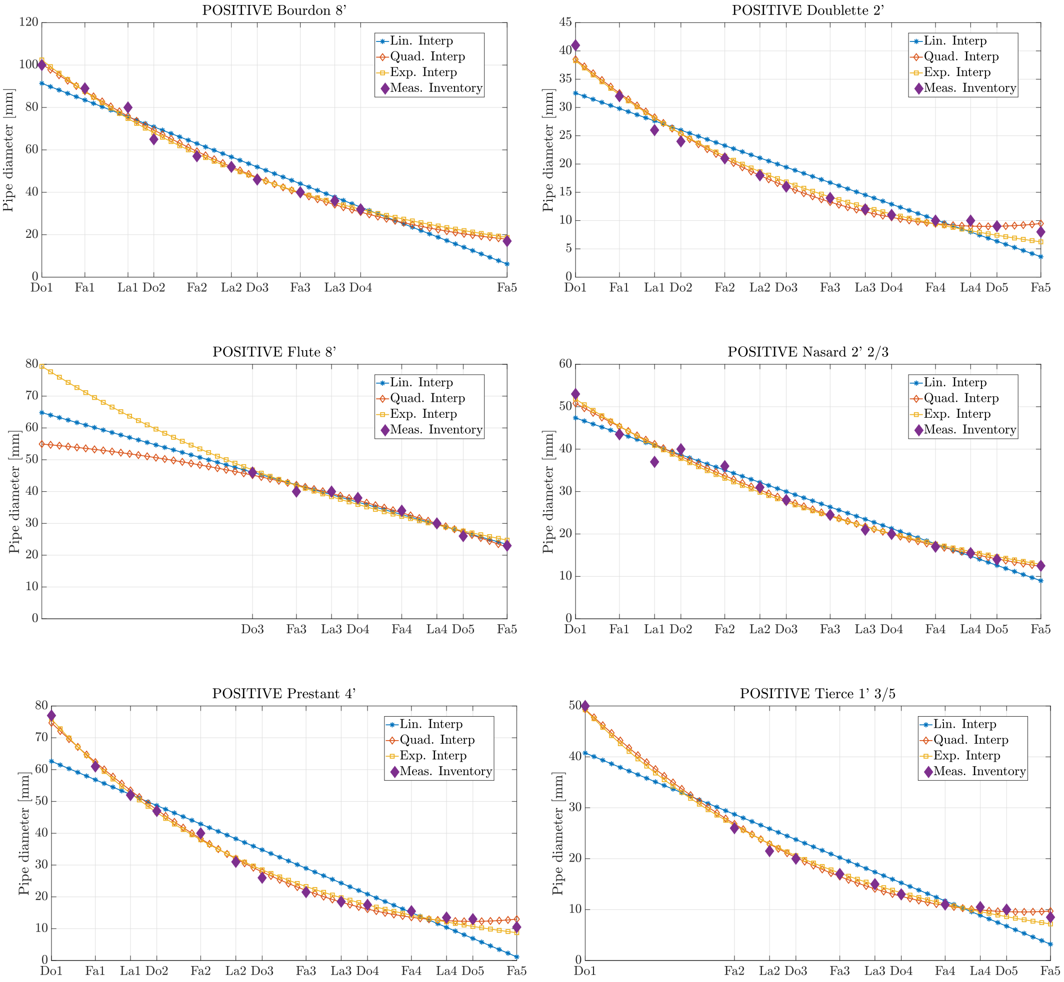

Figure 7.8: Measured diameters from Dallery pipework of the positive.

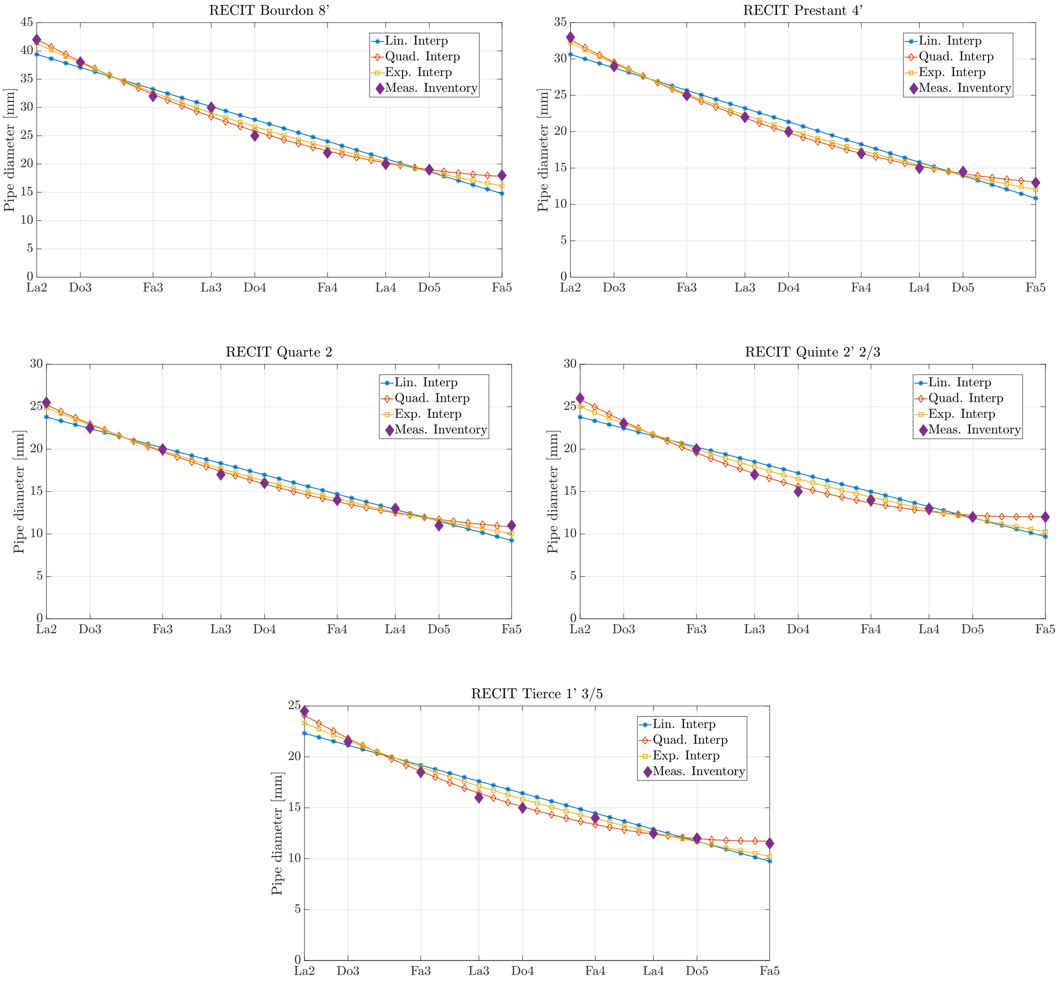

Figure 7.9: Measured diameters from Dallery pipework of the recit.

7.1.3 Modal parameter extraction

Values for the Dallery diameters are fitted two second order and missing data is interpolated (see Figures 7.2 to 7.6).

Once one has the complete set of geometry parameters for the desired ranks, it is necessary to perform modal decomposition value extraction for each pole up to an imposed limit N_{modes}. For trivial bores such as constant cross-section cylinders, one can compute without much difficulty the pipe impedance and the end corrections due to the radiating passive end (in open pipes), the mouth window, and the lateral ears. When more sofisticated bores are considered, the `OpenWind` utility can perform frequency response calculations of the bore in an automated fahsion.

The values to extract from each bore, respond to the fitting problem $J = \|Y_{\text{targ}}(\omega) - Y_{\text{modal}}(\omega)\|^2$, where the modal expansion is of the form

$$Y_{\text{modal}}(\omega) = \frac{a_o}{j\omega b_o + c_o} + \sum_{k=1}^{Nmod} \frac{Y_{\text{k}} j\omega}{(j\omega)^2 + \varepsilon_k \omega_k j\omega + \omega_k^2} \tag{7.1}$$

as per [Terrien, 2014]: the *zeroth*-mode with coefficients a_o, b_o, and c_o corresponds to the uniform mode with zero frequency, whose existence is linked to the resonators open at both ends, accepting a mean flow through the bore. The Y_{k} correspond to the admittance amplitudes, ω_{k} and ε_{k} are the mode's pulsation and damping, being related to the quality factors by $\varepsilon_{\text{k}} = 1/Q_{\text{k}}$).

7.2 Chapelle de la Sorbonne

7.2.1 Prelude

In this section, we present here a preliminary calibration of the GA model of Chapelle Sorbonne using CATT-Acoustics. Along with the analysis of relevant metrics from the synthesized responses by simulation, we also report the values for some metrics obtained with measurements in-situ.

The Chapelle Sorbonne, despite the deterioration and structural damage referred in Chapter 1, has undergone cleaning and structural repair (2004-2010, *Ville de Paris*). An exploratory recent visit allowed the assessment of the space concerning actual dimensions, materials, and changes since last evidence found.

The chapel consists of a main nave and chancel allowing for 30 m to 40 m free path for source-receiver direct sound involving a total volume of $\sim$14 250 m^3. A dome elevates over the transept, approximately found mid-length from East to West. It will be informed in Table 7.1 that the predominant material present is by far the limestone, with the presence of some decorative walls, wood in doors and pews, and stained glass in windows. The coat of arms of Richelieu appears in most of the windows with direct access, the top of the organ's façade, above the arches of the nave, and the façade of the chapel to place Sorbonne. Sections of the flooring appear finished in checked marble pattern: this concerns the chancel and the South end of the transept.

Figure 7.10: Chapelle Sorbonne chancel, nave and side chapels as seen from the altar on the East end.

In the external perimeter of the chapel, one finds Tuscan, Doric, Ionic, and Corinthian columns. The interior, however, only exhibits flat, squared-section columns toppped by Corithian capitals (with the exception of four circular, marble columns at the alter). The current state may be seen in Figure 7.10. However, we found photographic evidence of previous states of the chapell (shown in Figure 7.11) which would potentially have an effect on the acoustic response of the space, namely:

- The arches at the sides of the chancel close the East chapels are closed by stained glass and wood panels over the pews, slightly reducing the total volume.
- A wooden pulpit was placed in one of the corners under the dome.
- Current presence of wooden choir stalls but no pulpit.
- An audience worth of chairs in the nave, transept, and chapels made of wood and wicker.
- Presence of two wooden confessionals on the sides of the entrance by the *Cour d'Honneur*.
- Past presence of mays hanging at mid-height of columns.
- The marble tumb of Cardinal Richelieu has moved from the transept (opposite to the Choeur d'honnour entrance) to the front of the altar, and there was another sculpture of Richelieu by the North entrance.
- Past presence of small-to-medium size sculptures in the transept.

In contrast, and allowing for the multiple changes of use that the space underwent as we refer in Chapter 1, the chapel appears at present as a big empty volume of limestone with minimal elements of movable decoration left. Indeed, this would be not the first study where a GA model of a religious space proposes the auralization of a source such as the organ ([Boren et al., 2019, Boren, 2021]); but additionally,

Figure 7.11: Known previous states of the chapelle around the 1940s. Procedence and authors of the photographs are unkown. Further iconographic and photographic documentation may be found in Pop-Culture-MPP, credited to the Médiathèque du Patrimoine de la Photographie.

Boren investigated the change in acoustic response of the Thomaskirche at three different time instances finding subtantial differences for $T30$ metric under the empty space condition. The study spans Lutheran times, the time of Bach while being *Kapellmeister*, and the present day.

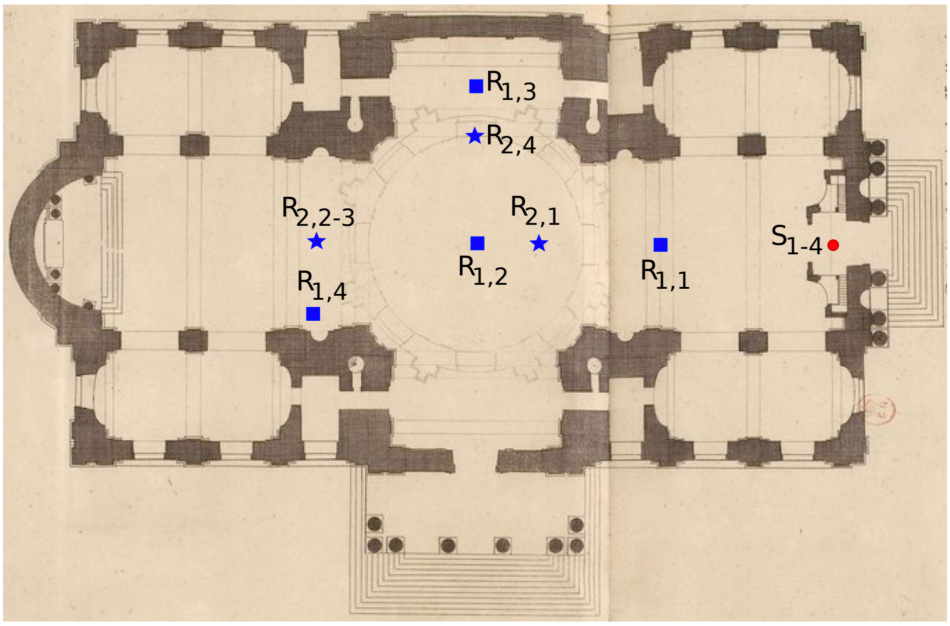

Figure 7.12: Source receiver locations annotated over a floor plan of the Chapelle from [Marot and Marot, 1727].

7.2.2 GA model of Chapelle Sorbonne

The use of CATT-Acoustics here, or any ray tracing-based method may yield debatable responses in the low and very low frequencies, which for the instrument at hand (the Dallery organ) poses the questions on applications such as auralization of organ music. In the octave band of 63 Hz, one will find numerous pipes sounding of this instrument.

The GA model is developed using CATT-Acoustic [Dalenbäck, 2016a] and simulations are performed in TUCT2 [Dalenbäck, 2016b]. The calibration stage makes use of measurements using speakers and balloons.This work presents a very modern, but current, stage of the Chapelle. Thus we show, at least, the validity of a preliminary calibration of a geometryical model as of the present state. The source-receiver position combinations investigated were

The source and receiver positions for measurement are annotated in Figure 7.12. The locations for sources and receivers for auralization of the organ appear annotated on the floorplan in Figure 7.13.

The sequence of calibration steps of the GA model is based on the methodology proposed by Postma *et al.* in [Postma et al., 2015], where the general workflow consists of

- With a reasonable initial material absorption guess, fix a low value of the scattering coefficients and assess the run-to-run variation among simulated responses
- Vary the scattering coefficients from negligible to maximum and assess the

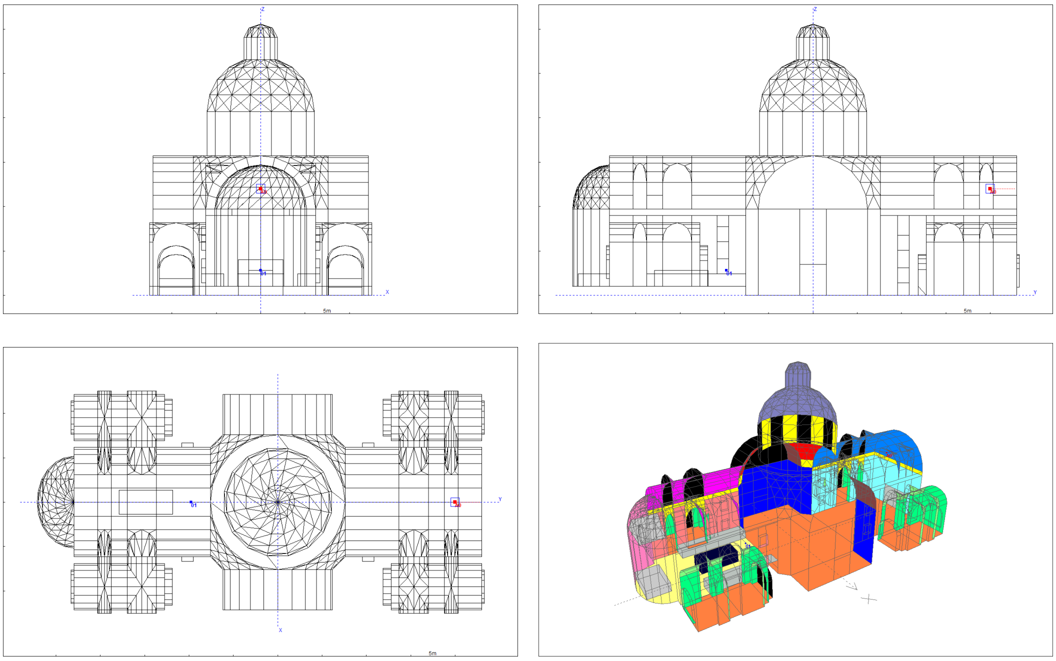

Figure 7.13: View of the GA model of Chapelle Sorbonne in CATT-Acoustic/TUCT.

changes in metrics

- Adjust absorption coefficients of major surfaces
- Adjust absorption and scattering coefficients for individual SxR combinations

during which, the results obtained by simulations may be analyzed with respect to measured data, including: numerical parameter results by Polack appeared in [Dubois and Lueders, 2002], processed with the MIDAS system [Polack et al., 1992], and a sequence of large balloon explosions in the locations specified above.

The metrics we are most concerned here, given the uses known of the space, are clarity and reverberation time, with respect to an audience located in the nave and the source considered being the organ, located at the west end of the nave over the main entrance from Place de la Sorbonne, longitudinally opposed to the altar. Sparse documentation [Dubois and Lueders, 2002] suggests interrupted and *short* periods during which the use of the space was closest to clerical, but location of sound sources as singers in the choir as we know of different eras of Eucharist and similar religious *manifestations* is a difficult hypothesis to support. Results of reverberation (EDT, $T20$ and $T30$) and clarity ($C80$) metrics can be found in Figures 7.14.

Reverberation parameters are measured over the integrated curve of the absolute amplitudes of the impulse responses in dB. Thus, the EDT [s] is the time for the energy to decrease 10 dB from the initial decrease onset, while $T20$ and $T30$ correspond to the time taken for energy drops of 20 dB and 30 dB in the fitted

Table 7.1: Absorption coefficients (in %) for GA simulation found in Chapelle Sorbonne surfaces given by octave bands. The category limestone is attritubed to floors, walls, and ceilings.

Material	125 Hz	250 Hz	500 Hz	1 kHz	2 kHz	4 kHz	Ch.Len.	Area [m^2]
Limestone	5.5	5.5	5.5	6	6	6		4061.6
Decor. walls	5.5	5.5	5.5	6	6	6	0.2	250.2
Marb. Floors	2	2	2	2	2	2		275.5
S. Glass	30	20	15	11	6	6	0.10	444.5
Stairs	5.5	5.5	5.5	6	6	6	0.2	12.3
Wood	14	10	6	8	10	10	0.05	20.0
Pews	14	10	6	8	10	10	1	96.5
Statue	2	2	2	2	2	2	1	47.6
Altar	2	2	2	2	2	2	0.05	98.5

logarithmic amplitude curve. $C80$ is an indicator of music clarity, where the ration expresses the ratio (in dB) between energy contained in the early portion of the impulse response and the energy contained in the late response. For $C80$, the initial segment of the impulse response accounts for the first 80 ms, while the late response is computed from time $t = 80\,\mathrm{ms}$ until the end of the impulse response. Note that the clarity index selected here is longer thatn that used for speech (commonly $C50$, where the early portion is set to the initial 50 ms). If the impulse response is represented by $h(t)$, the $C80$ index is computed as

$$C_{80} = 10log_{10}\frac{\int_0^T h^2(t)dt}{\int_T^\infty h^2(t)dt} \tag{7.2}$$

where $T = 80\,\mathrm{ms}$. Results indicate that further calibration is required to adjust the 2 kHz band, even when we have allowed for the case of non-expert listeners: 2 JND (5% and 1 dB). We also noticed that the clarity results as per measurements in 2000 and processing using MIDAS yield smaller values than an empty space of this characteristics would intuitively yield. Further work would inspect a one-by-one source-receiver combination of obtained results. We have shown here, both in measurements and GA simulation, the results of averaging all the location combinations.

The absorption and scattering parameters at the last stage of the calibration are reported in Table 7.1.

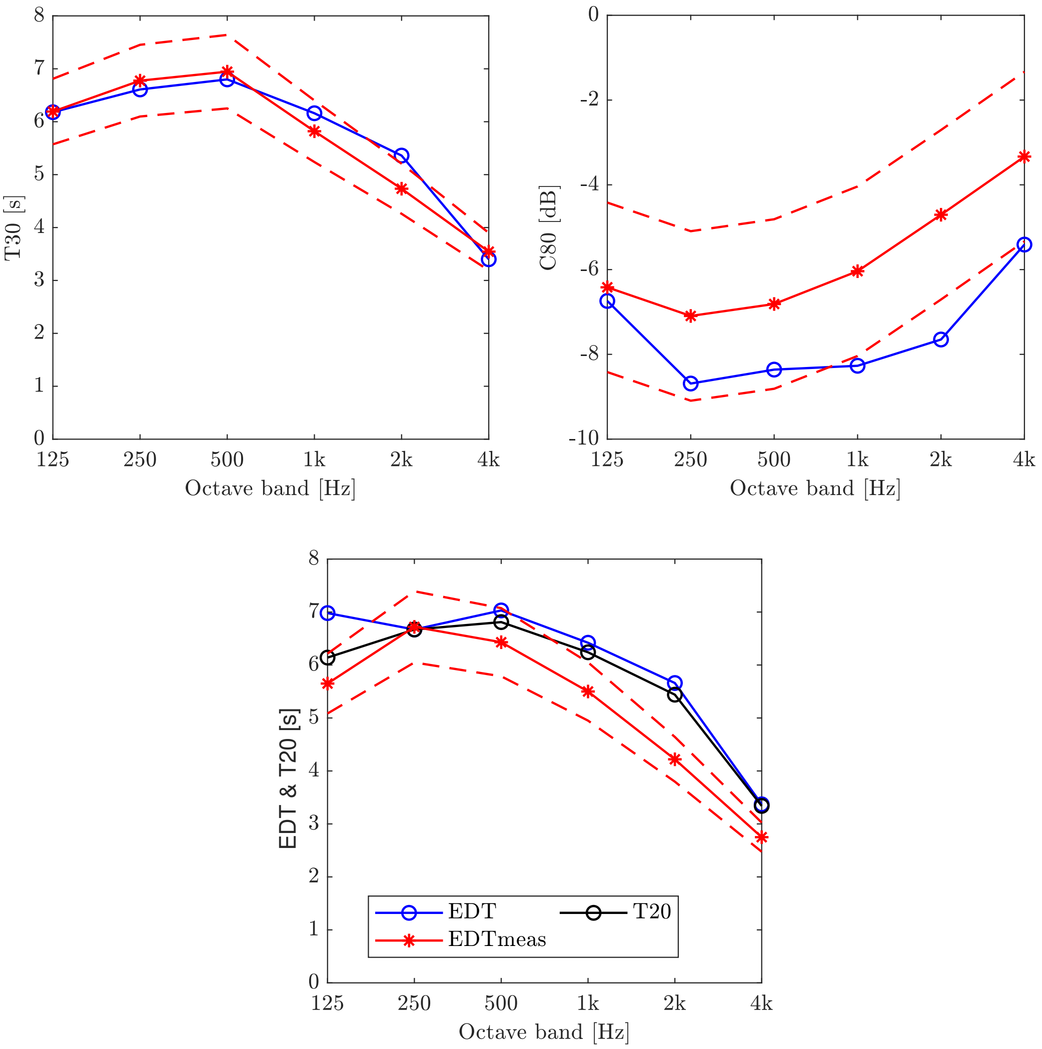

Figure 7.14: Clarity and reverberation metrics of Chapelle Sorbonne GA model, compared with measurements where data is available, and analyzed by octave bands. The dashed lines indicate 2 JND (just noticeable difference, for a non-expert audience), which has been taken as 5% for reverberation metrics and 1 dB for clarity per each 1 JND.

7.3 The sound of the organ in the Chapelle Sorbonne

- The radiated sound of the organ
- The sound of the organ in the Chapelle

The instrument directivity used for GA response simulation of Chapelle Sorbonne was an omnidirectional source. An improvement of such approach would include the octave band analysis of the far-field most complete data set, at the current state obtainable by FVFDTD simulation as per Figure D.2 and after application to the vertical axis too; this is to be entered per 10 degrees in the source directivity

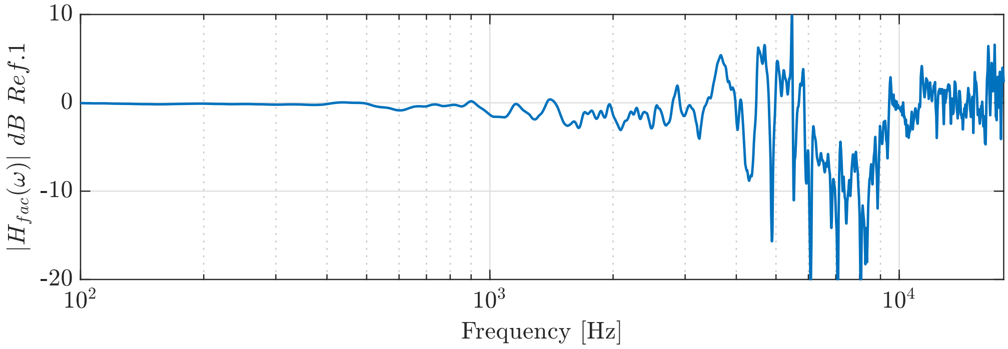

Figure 7.15: Frequency domain transfer function of the façade element in its 0° response.

application of CATT-Acoustic. The source is placed in the organ location region and an omnidirection receiver was placed at 1.5 m from the Richelieu sculpture, as per source location utilized in measurements in the year 2000.

The elements evoked in Figure 7.16 have been presented in previous sections of this work. References to their discussion are provided below.

- Driving pressure $p_{foot}(t)$ for initialization of pipe simulation: §3.3.2
- Radiated pressure from the pipe mouth $p_m(t)$: Equation (3.13) and Equation (4.12)
- Pressure at a given observation point in the interior of the buffet $p_{buff}(t) = p_m(t) * h_{buff}(t)$: §6.3.2
- Organ signal at the radiating interface (slits) in presence of façade apertures $p_{org}(t) = p_{buff}(t) * h_{fac}(t)$: §6.3.3
- Sound of the organ at the given location of the chapel space $p_{list}(t) = p_{org}(t) * h_{chap}(t)$

The façade filter, as discussed in §6.4.2.1, with an angular dependency even in its far-field form, was simplified to its on-axis case for the sake of the example, whose frequency domain representation is shown in Figure 7.15.

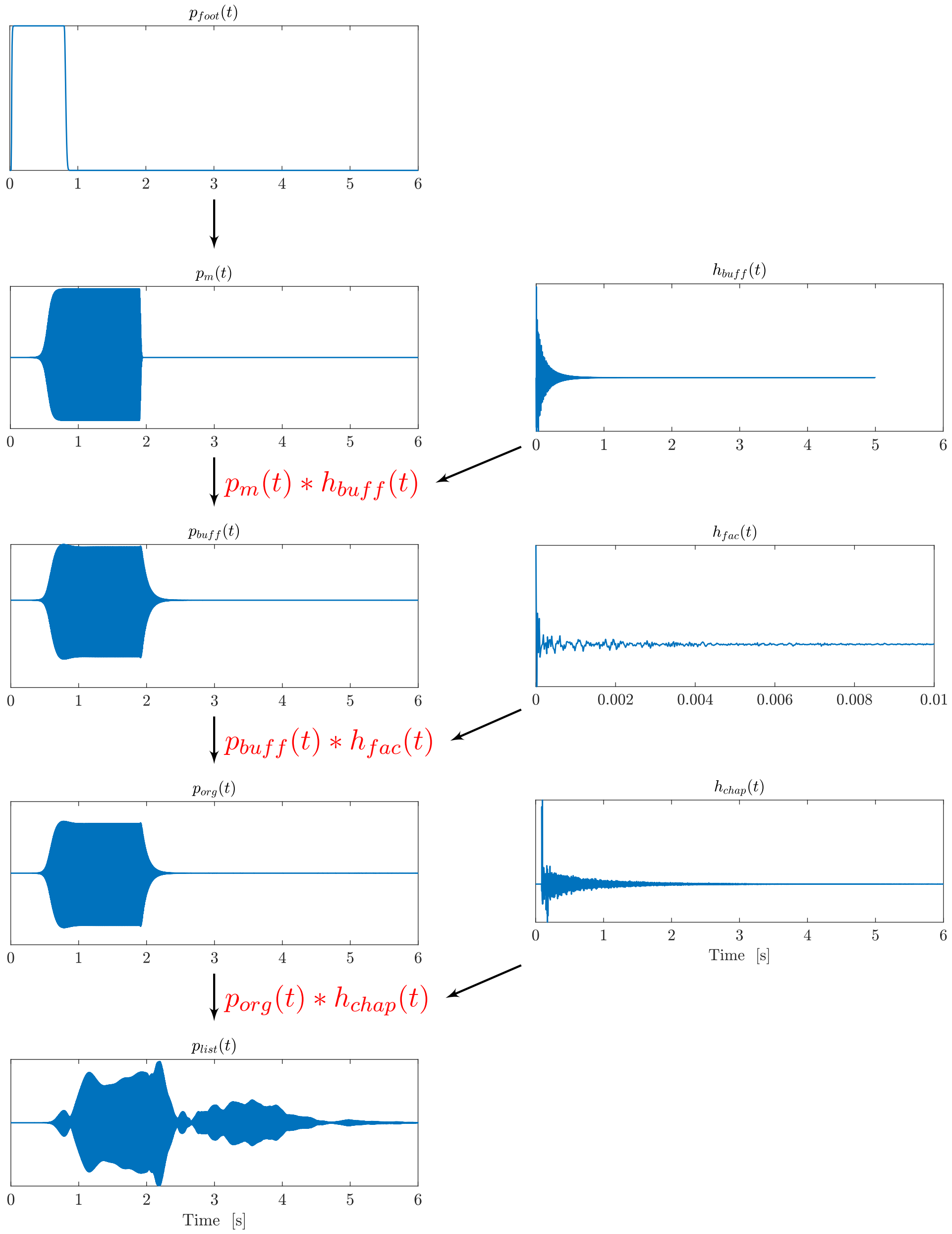

Figure 7.16: Sound production chain of the organ sound in Chapelle Sorbonne. The notation $*$ represents convolution product.

7.4 Summary and future perspectives

An approach was presented to gather old geometry documentation of the Dallery organ pipework and enclosure, together with knowledge from organ makers on to empirical scaling of other parameters such as the flueways of the pipes.

Protocols are presented to deal with missing and inaccurate data from documentation. Modal parameter extraction was commented as several approaches and tools had been presented in Chapter 2.

Following a visit to Chapelle Sorbonne and accessing room impulse response measured data, we produced a geometrical acoustics model of the chapel and offered the results of a preliminary calibration that allowed for computation of responses at relevant locations of the space, according both to measurement locations and *normal* use of the space.

Lastly, we have proposed a route-map as to how all the elements of previous studies in this work articulate in an end-to-end chain from the driving flow of the organ, to the sound production, radiation, and colvolution with the listening space.

Appendices

Appendix A

Speaker technical specifications

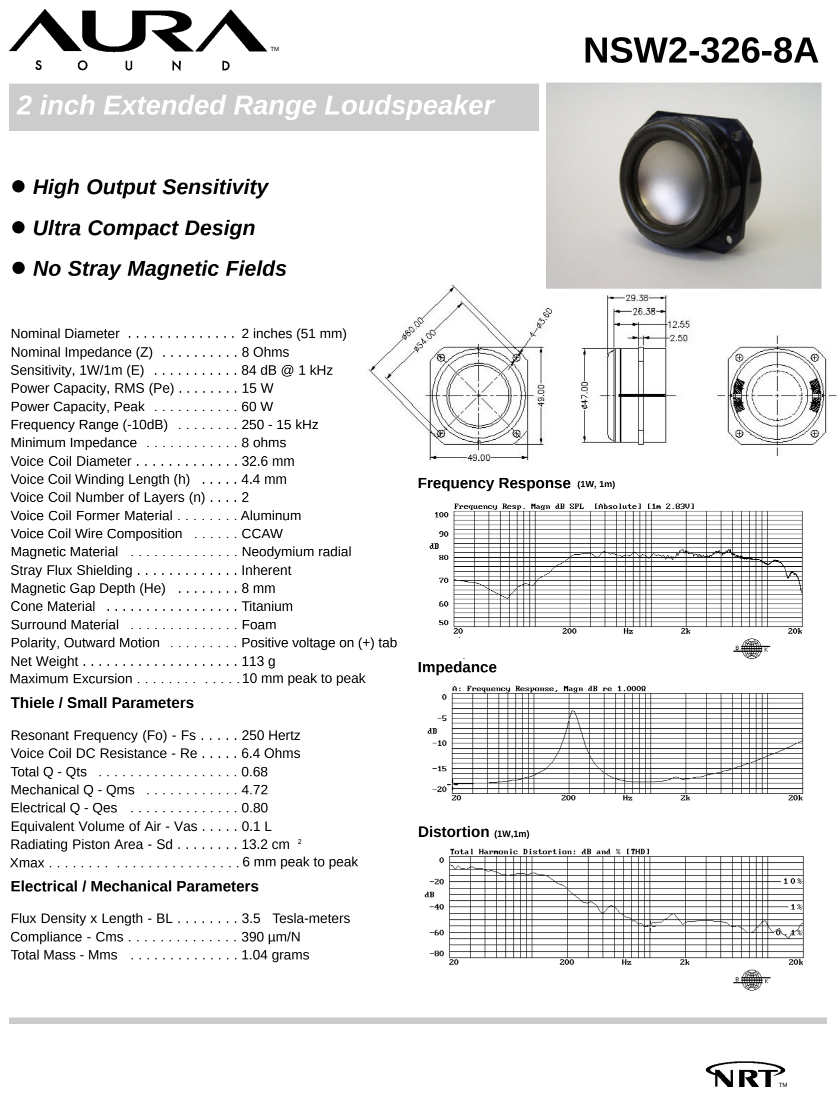

NSW2-326-8A

2 inch Extended Range Loudspeaker

- ***High Output Sensitivity***
- ***Ultra Compact Design***
- ***No Stray Magnetic Fields***

Nominal Diameter	2 inches (51 mm)
Nominal Impedance (Z)	8 Ohms
Sensitivity, 1W/1m (E)	84 dB @ 1 kHz
Power Capacity, RMS (Pe)	15 W
Power Capacity, Peak	60 W
Frequency Range (-10dB)	250 - 15 kHz
Minimum Impedance	8 ohms
Voice Coil Diameter	32.6 mm
Voice Coil Winding Length (h)	4.4 mm
Voice Coil Number of Layers (n)	2
Voice Coil Former Material	Aluminum
Voice Coil Wire Composition	CCAW
Magnetic Material	Neodymium radial
Stray Flux Shielding	Inherent
Magnetic Gap Depth (He)	8 mm
Cone Material	Titanium
Surround Material	Foam
Polarity, Outward Motion	Positive voltage on (+) tab
Net Weight	113 g
Maximum Excursion	10 mm peak to peak

Thiele / Small Parameters

Resonant Frequency (Fo) - Fs	250 Hertz
Voice Coil DC Resistance - Re	6.4 Ohms
Total Q - Qts	0.68
Mechanical Q - Qms	4.72
Electrical Q - Qes	0.80
Equivalent Volume of Air - Vas	0.1 L
Radiating Piston Area - Sd	13.2 cm ^{2}
Xmax	6 mm peak to peak

Electrical / Mechanical Parameters

Flux Density x Length - BL	3.5 Tesla-meters
Compliance - Cms	390 µm/N
Total Mass - Mms	1.04 grams

Frequency Response (1W, 1m)

Impedance

Distortion (1W,1m)

6½ 120W

SPH-165CP

Order No.: 0102330

PRODUCTINFOS

High-performance hi-fi bass-midrange speaker, 80 W, 8 Ω

- Extra large voice coil (Ø 50 mm)
- Parameters for a deep bass reproduction
- Extra long excursion
- Bass speaker for interesting dual arrangements in very slim 3-way high-performance speaker systems and for 2-way bookshelf speakers of high power capability

HOBBY HiFi 04/2017

“Requires 13 to 18 litres only. However, still provides an incredibly deep bass reproduction down to almost 30 Hz.”

TECHNICAL SPECIFICATIONS

SPH-165CP	
Impedance (Z)	8 Ω

SPH-165CP

Frequency range	f3-6,000 Hz
Resonant frequency (fs)	30 Hz
Power rating (RMS)	80 W
Peak music power output (MAX)	120 W
SPL	89 dB/W/m
Suspension compl. (Cms)	1.71 mm/N
Moving mass (Mms)	17 g
Mech. Q factor (Qms)	4.85
Electr. Q factor (Qes)	0.33
Total Q factor (Qts)	0.31
Equivalent volume (Vas)	38 l
DC resistance (Re)	6 Ω
Force factor (BxL)	7.60 Tm
Voice coil induct. (Le)	0.7 mH
Voice coil diameter	Ø 50 mm
Voice coil former	glass fibre
Linear excursion (X_{MAX})	± 4.75 mm
Eff. cone area (Sd)	127 cm^2
Magnet weight	840 g + 50 g
Magnet diameter	Ø 120 mm
Mounting cutout	Ø 142 mm
Mounting depth	86 mm
Dimensions	165 x 165 x 90 mm
Width	165 mm
Height	165 mm
Depth	90 mm
Colour	black
Admiss. ambient temp.	0-40 °C
Weight	2.57 kg
Packing unit	1
Type of speaker	6.5"
Packing dimensions (W x H x L)	0.17 x 0.11 x 0.17 m
Gross weight	2.68 kg
Net weight	2.57 kg

Appendix B

Organ radiation

The two-dimensional approach on radiation was tested on an idealized organ-like cavity under controlled conditions in an anechoic chamber. The pressure field was acquired at two different distances from the experimental setup along parallel straight lines of acquisition points with respect to the cavity's façade as detailed in Chapter 6. The wall conditions were modified as well as the density of cylinders while the cavity was excited with a cylindrical source.

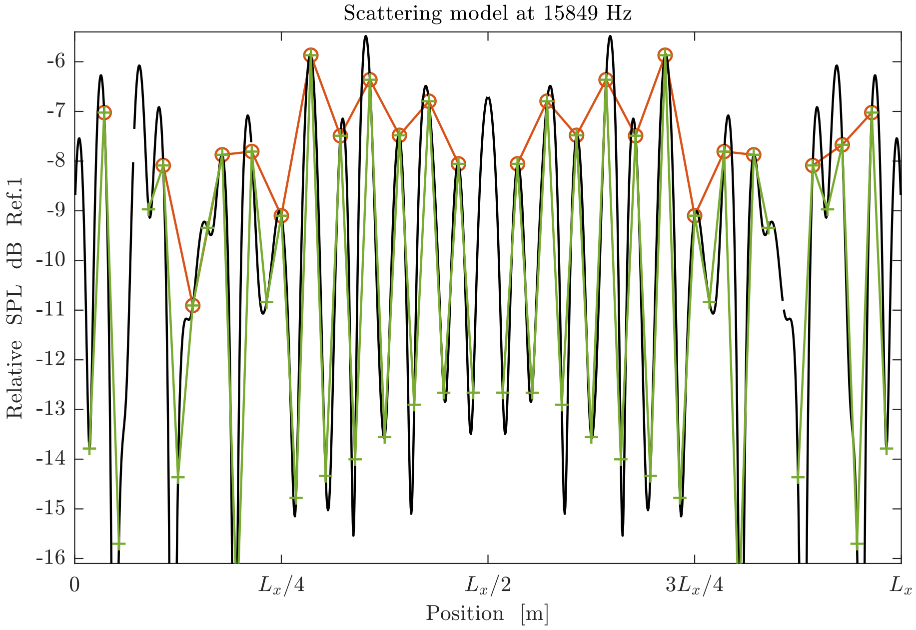

Figure B.1: Interference models of scattering using the aperture radiation method of [Mellow and Kärkkäinen, 2011] at two different measured pressure frequencies for the laboratory organ-like cavity geometry. The field is the result of the superposition and interference of $N_{sl} = 15$ sources, with a source-to-source spacing of 0.08 m, and at a read-out distance of 1.66 m from the equivalent façade, as per anechoic measurements in §6.4. Read-out positions are spaced every 1 mm (—), 1 cm (—), and 5 cm (—).

Figure B.1 shows yet a higher frequency result of the [Mellow and Kärkkäinen, 2011] model for $N_{sl} = 16$ secondary sources. This is followed by a computation of the model for the frequency range 5.5 kHz to 10 kHz, whose comparable measured equivalent appears in Chapter 6, Figure 6.16, measured at the same read-out distance. A visualization of the integral equation Equation (6.20) computing the losses due to the presence of the apertures in the case of the single slit is shown in Figure B.2a.

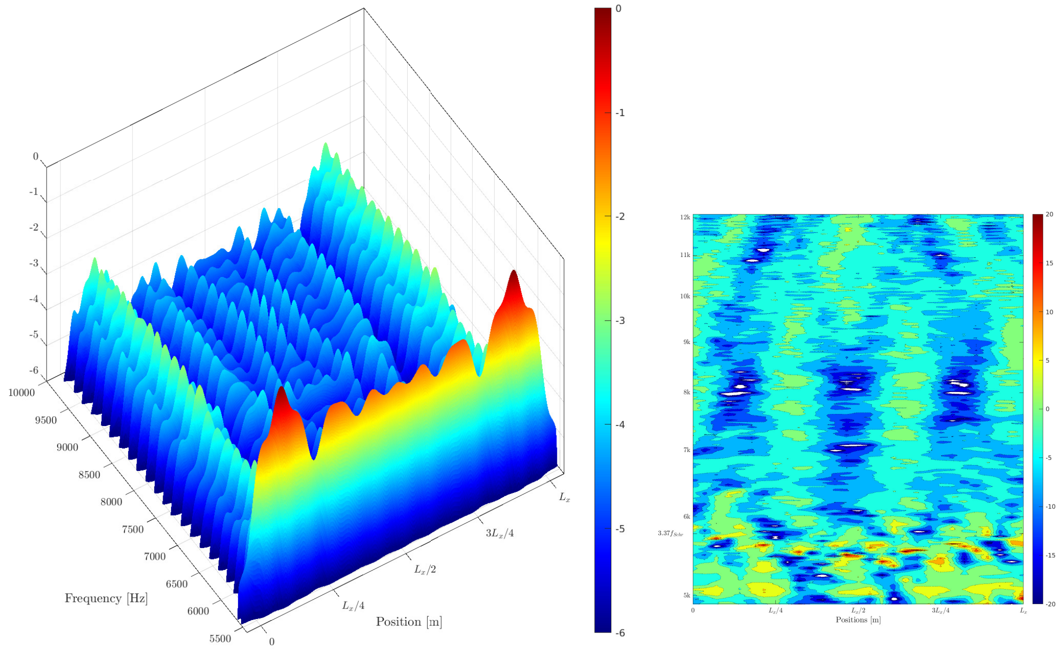

(a) Computed pressure

(b) Measured pressure (Reproduction of Figure 6.16, for comparison)

Figure B.2: Computed scattered pressure (normalized dB) in the range 5.5 kHz to 10 kHz as per [Mellow and Kärkkäinen, 2011] model, spanning the width the laboratory setup, with a grid spacing of 2 mm and a frequency bin of 2 Hz.

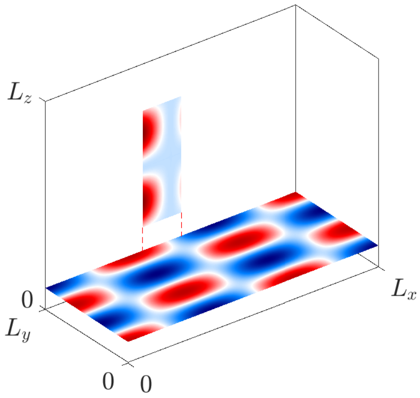

Figure B.3: Representation not to scale of the modal shape projections on the wall aperture losses as per Equation (6.20) for the case $(m, n, l) = (3, 3, 3)$.

Figure B.4 and Figure B.5 show the complete data set of measure pressure transfer functions *in* a single slit for five different vertical alignments, demonstrating that the pressure is uniformly distributed over the aperture except for the vertical modes of the cavity due to the adjacency of the interface to those.

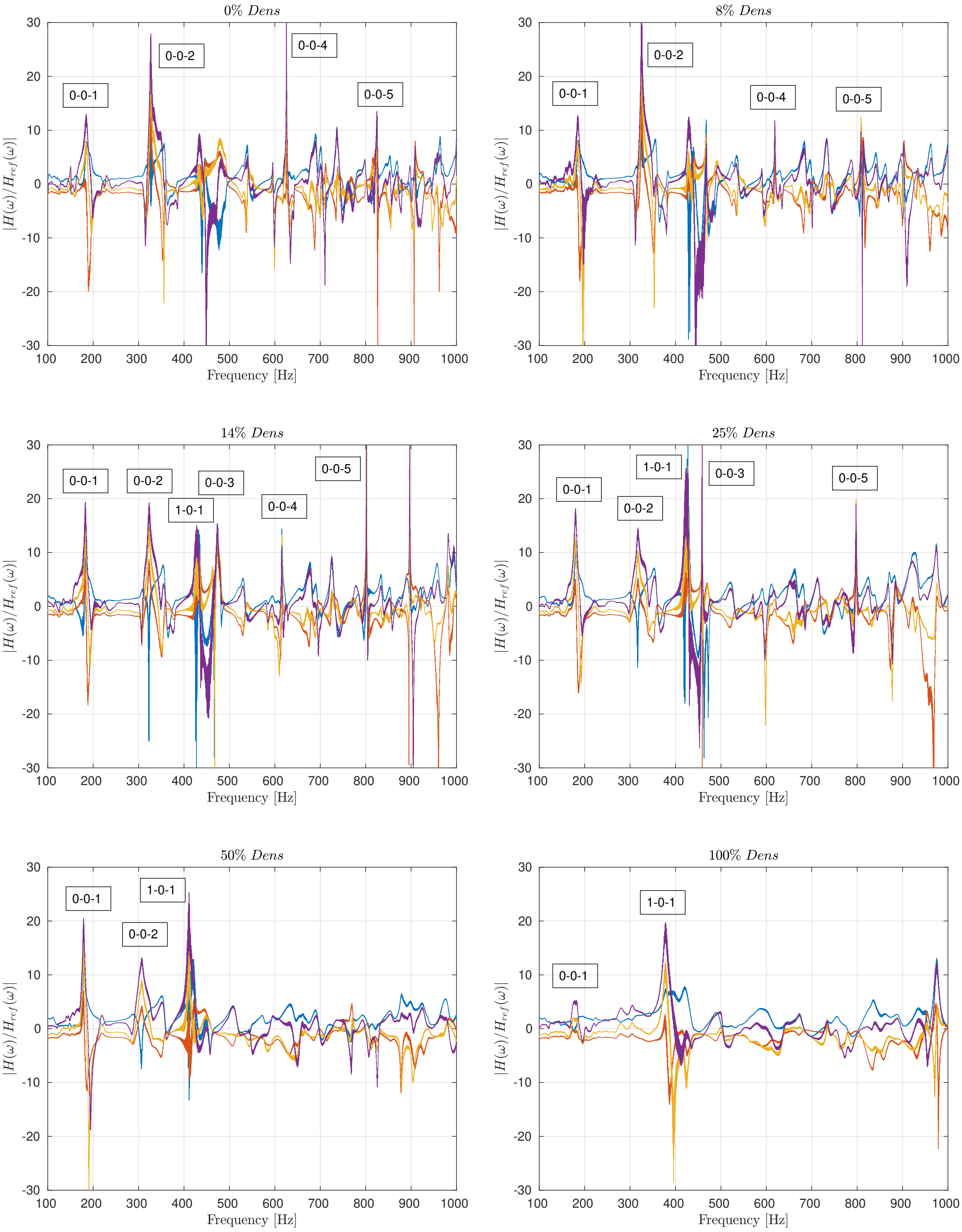

Figure B.4: Magnitudes of pressure at the slit for different vertical alignments. Bottom microphone to mid-low microphone: $Mic1/Mic2$ —; mid-height to mid-low microphone: $Mic3/Mic2$ —; mid-top to mid-low: $Mic4/Mic2$ —; top microphone to mid-low: $Mic5/Mic2$ —.

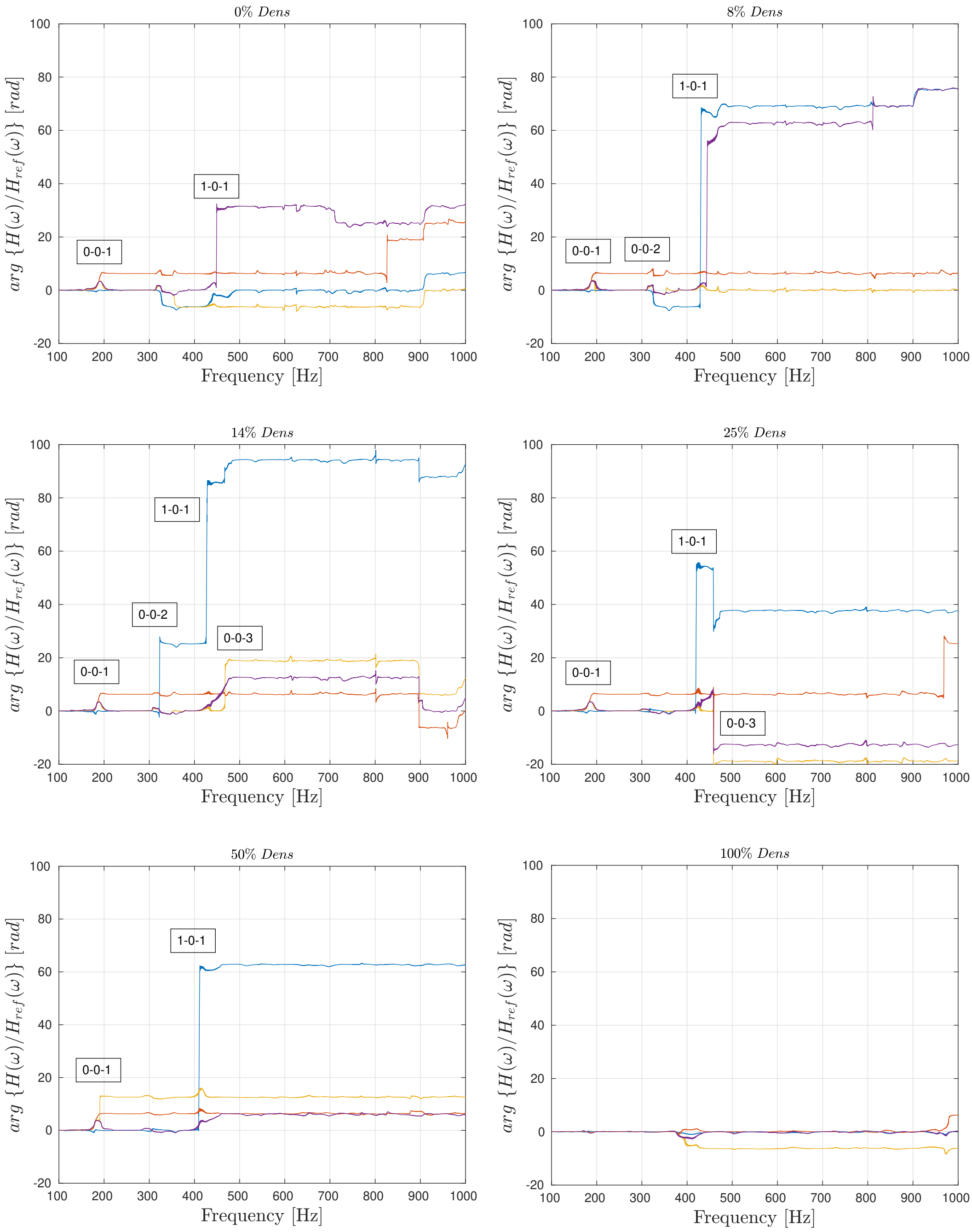

Figure B.5: Phases of pressure at the slit for different vertical alignments. Tracing the decrease in frequency of the $\mathbf{X}-\mathbf{Z}$-mode with increasing density of scatterers, it indicates that the average effect of one cylinder diminishes the resonance by $-0.378\,\mathrm{Hz}$. Bottom microphone to mid-low microphone: $Mic1/Mic2$ —; mid-height to mid-low microphone: $Mic3/Mic2$ —; mid-top to mid-low: $Mic4/Mic2$ —; top microphone to mid-low: $Mic5/Mic2$ —.

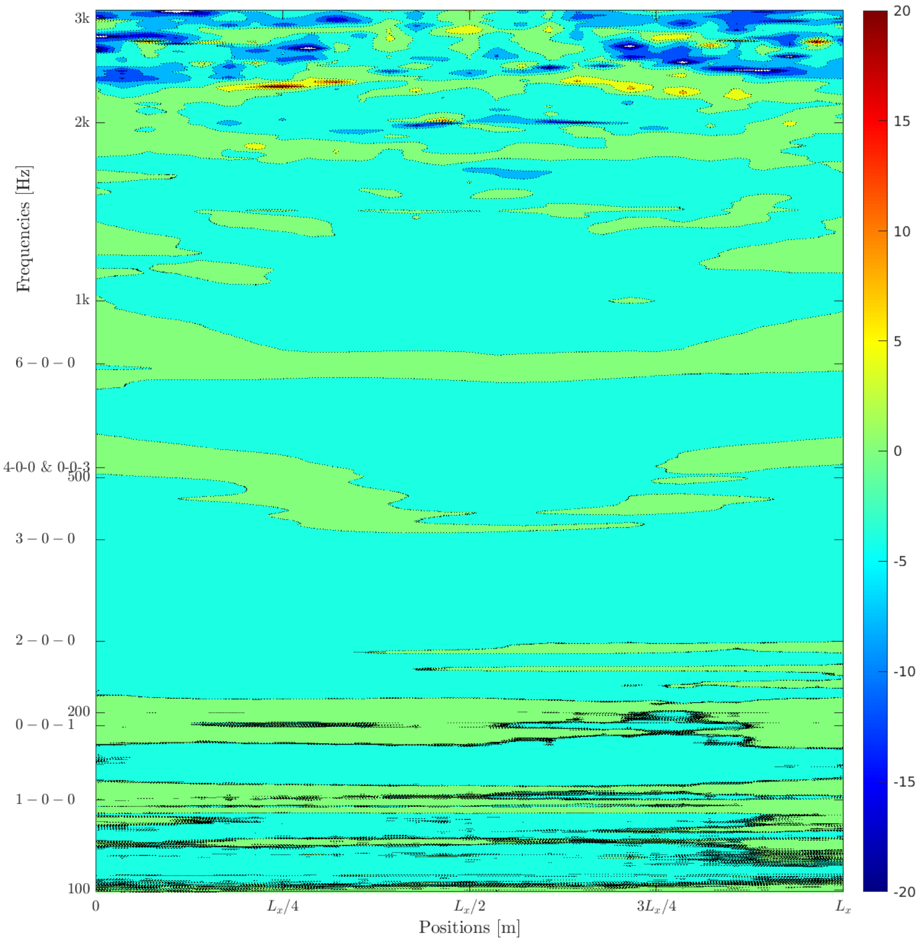

Figure B.6: Low frequencies of the measured facade pressure transfer function. Walls removed, only 16 cylinders at the front array. Measurement distance: 0.2 m from the front array. The effect of the reference field with no pipes and walls has been subtracted.

Figure B.6 to Figure B.8 show the measured pressure façade transfer function near the interface (at 0.2 m) for the low, mid, and high frequencies, with no forest present behind the façade system or any lateral wall panels. The data was normalized by the free-field propagation condition of the source alone with the common top and bottom panel reflectors included. The modal structure is apparent and annotated in the frequency axis of Figure B.6, as well as the beginning of evidence of individual scattering within the transition region beyond $f_{Schr} \approx 1715$ Hz displaying concave and convex characteristic lines of different travelled path lengths in the three figures mentioned. This effect remains visible in the high frequencies (Figure B.8) but vanishes at higher distances (1.66 m, Figure 6.16, Chapter 6) for frequencies above $\sim 3.37 f_{Schr}$.

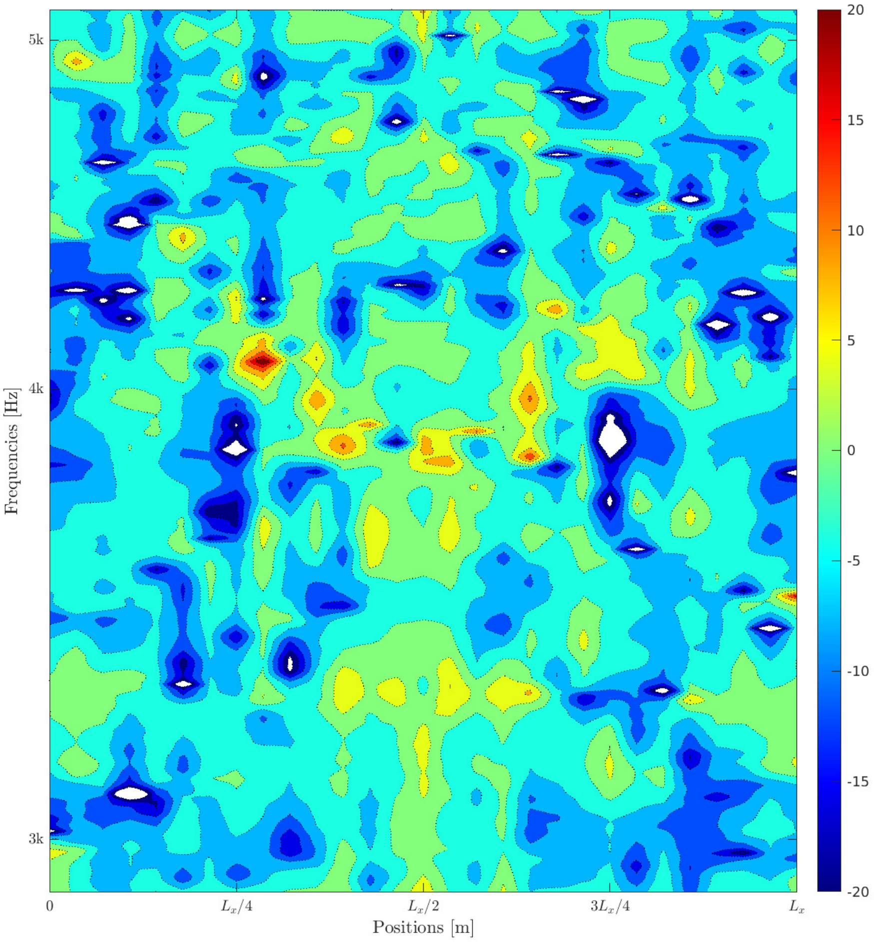

Figure B.7: Mid frequencies of the measured facade pressure transfer function. Walls removed, only 16 cylinders at the front array. Measurement distance: 0.2 m from the front array. The effect of the reference field with no pipes and walls has been subtracted.

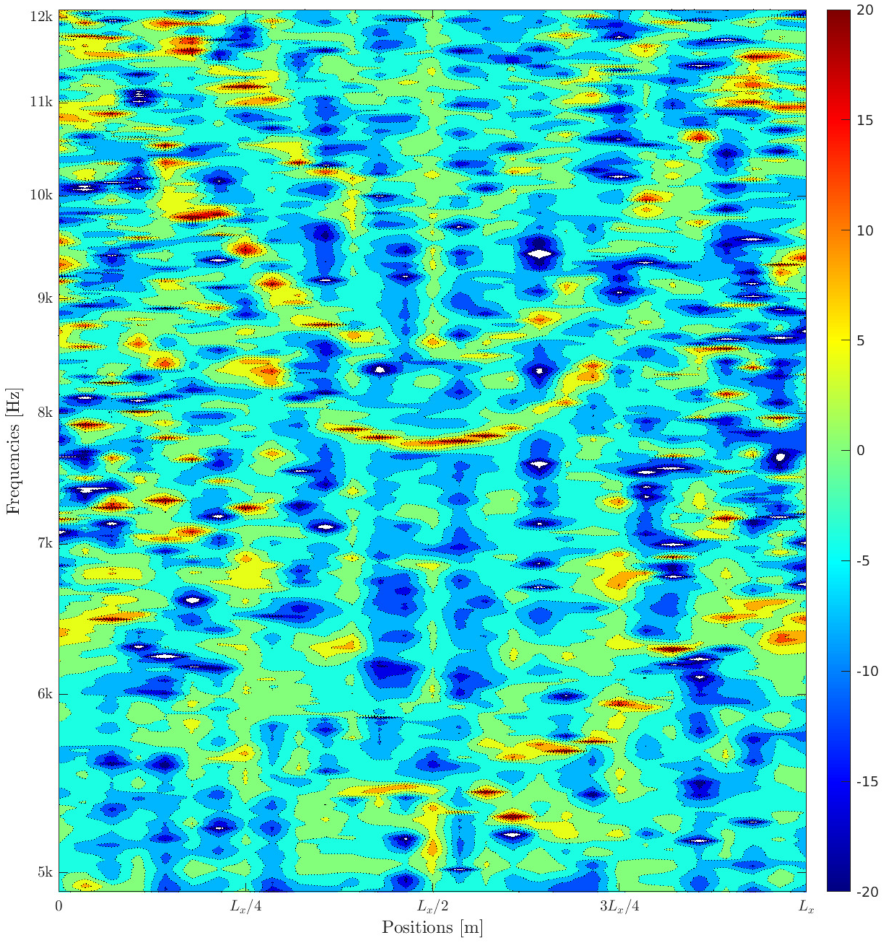

Figure B.8: High frequencies of the measured facade pressure transfer function. Walls removed, only 16 cylinders at the front array. Measurement distance: 0.2 m from the front array. The effect of the reference field with no pipes and walls has been subtracted.

Lastly, Figures B.9 to B.23 show the changes on the measured field, analyzed in twelfths of octave band and subtracting the free-propagation reference condition of the source alone at the relevenat distances, after the progressive addition of elements

- Lateral walls of the cavity, with no cylinder forest and no façade at two distances from the source (0.53 m and 2 m): Figures B.9 to B.11
- The façade array in absence of any lateral reflector walls at two distances with no forest matrix other thatn the 16 cylinders of the façade: Figure B.12 and Figure B.13
- The façade array with 50% of the total 170 PVC cylinders available behind the façade array (no walls): Figure B.14
- The façade array with 100% of the forest matrix behind the façade (no walls): Figure B.15 and Figure B.16
- Combined densities of cylinders with both lateral and rear walls present (no front panel): no cylinders at all, façade system (16 pipes), 50%, and 100% pipes, at two different distances. Figures B.17 to B.23

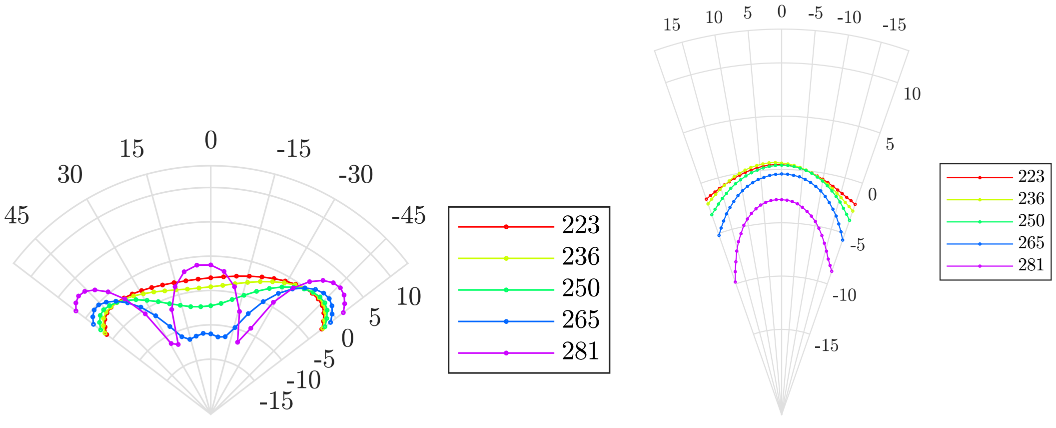

(a) 0.5 m **(b)** 2 m

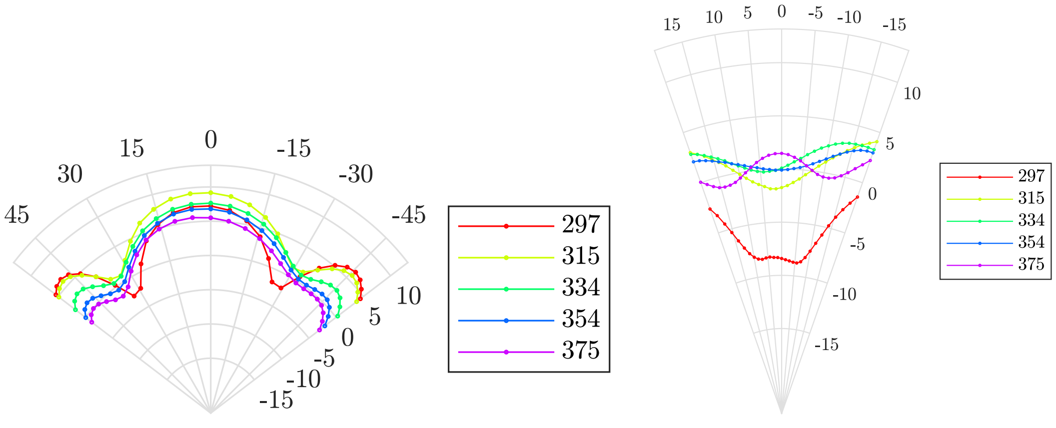

(c) 0.5 m **(d)** 2 m

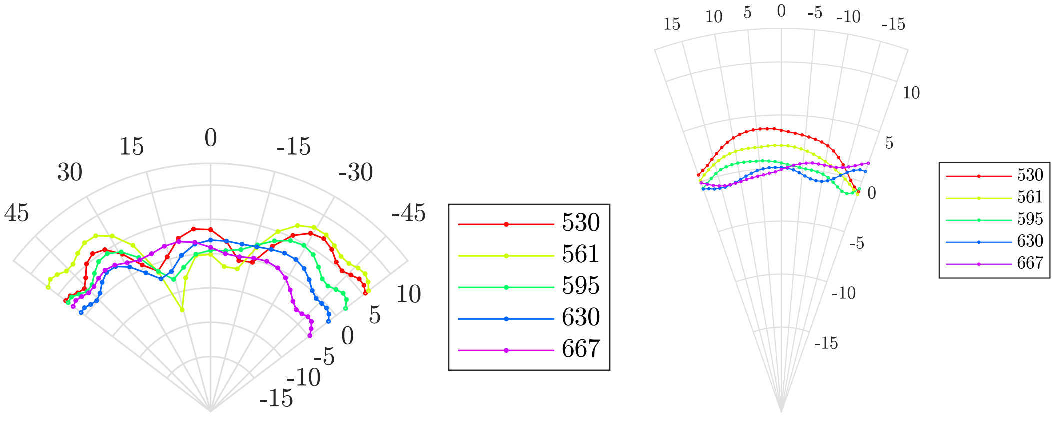

(e) 0.5 m **(f)** 2 m

Figure B.9: Lateral organ rigid walls only. Measured pressure, relative SPL dB rms normalized by free propagation reference.

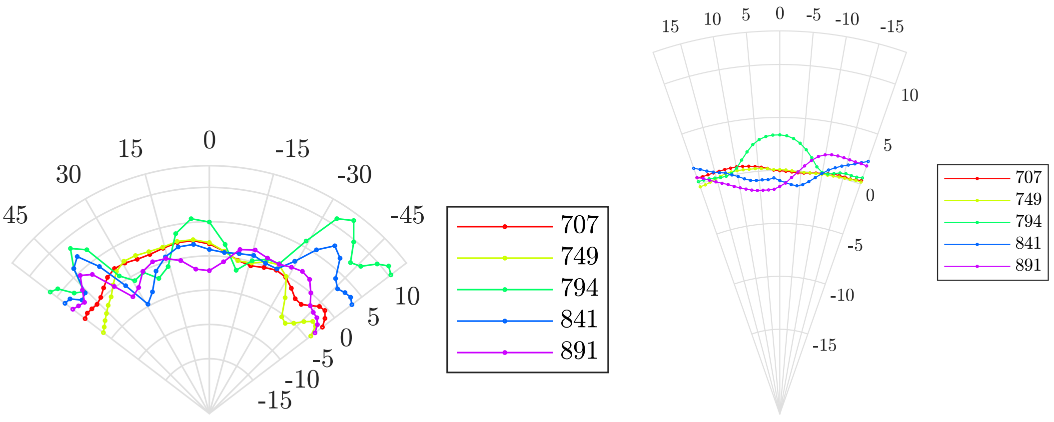

(a) 0.5 m **(b)** 2 m

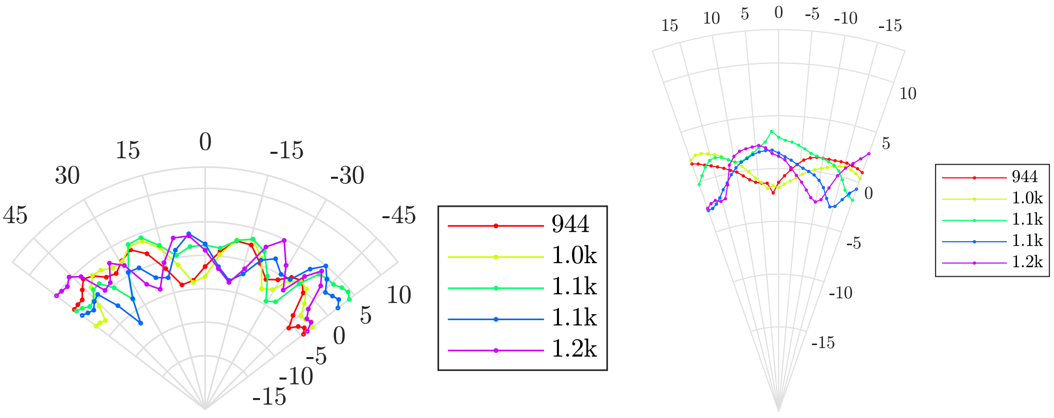

(c) 0.5 m **(d)** 2 m

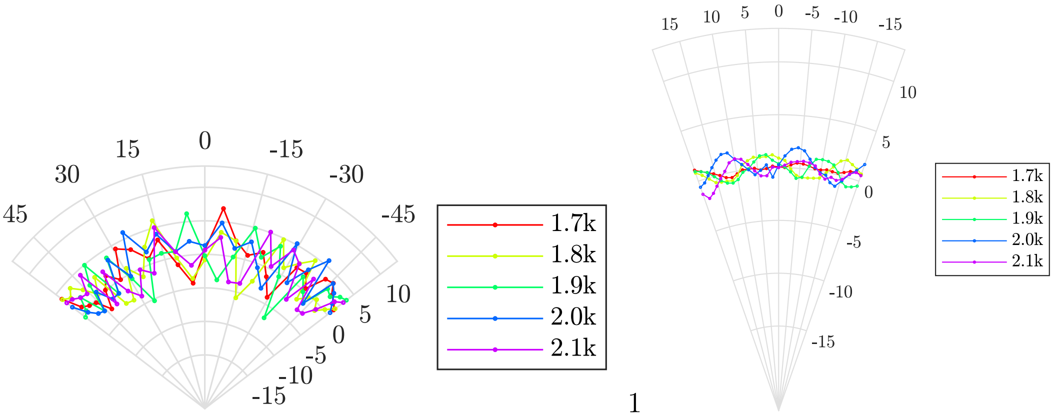

(e) 0.5 m **(f)** 2 m

Figure B.10: Lateral organ rigid walls only. Measured pressure, relative SPL dB rms normalized by free propagation reference.

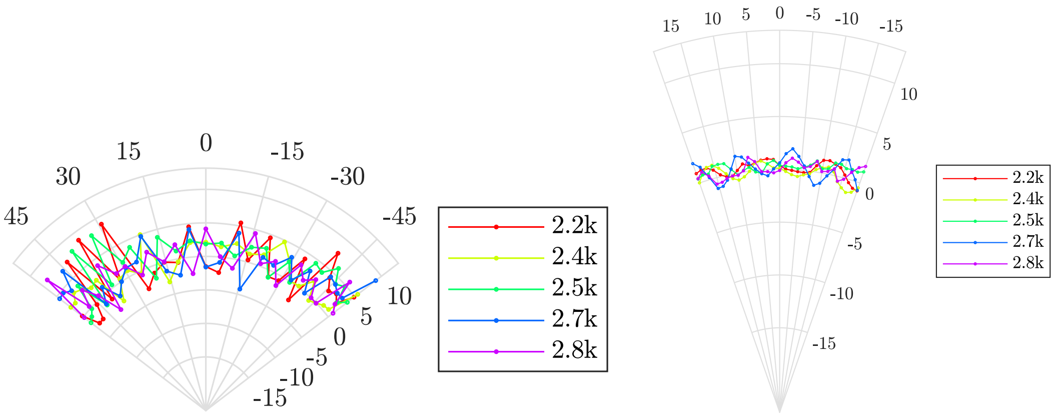

(a) 0.5 m **(b)** 2 m

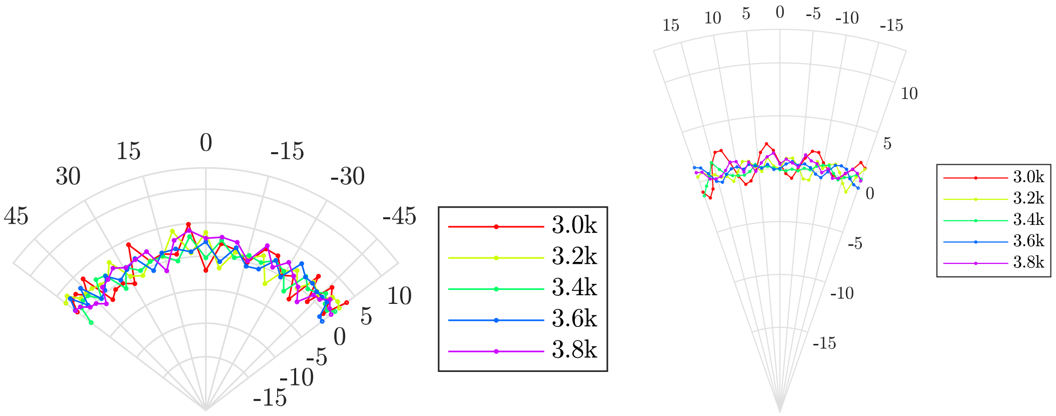

(c) 0.5 m **(d)** 2 m

Figure B.11: Lateral organ rigid walls only. Measured pressure, relative SPL dB rms normalized by free propagation reference.

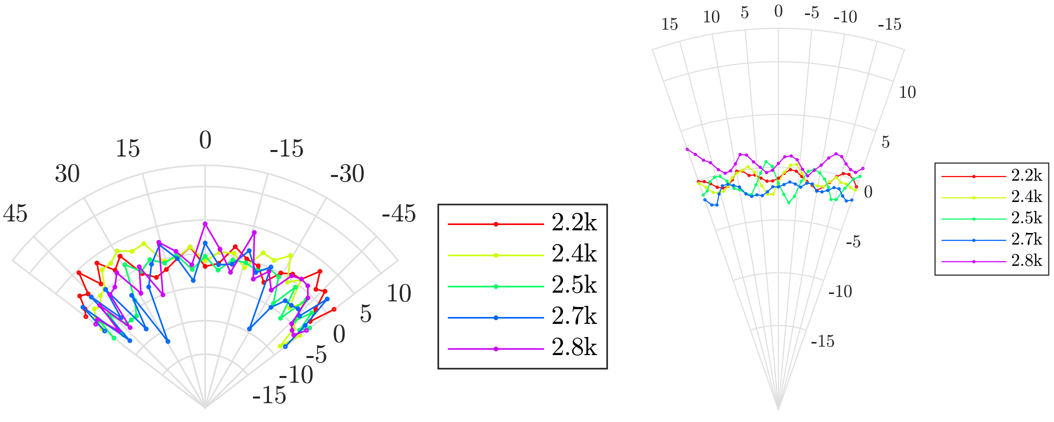

(a) 0.5 m **(b)** 2 m

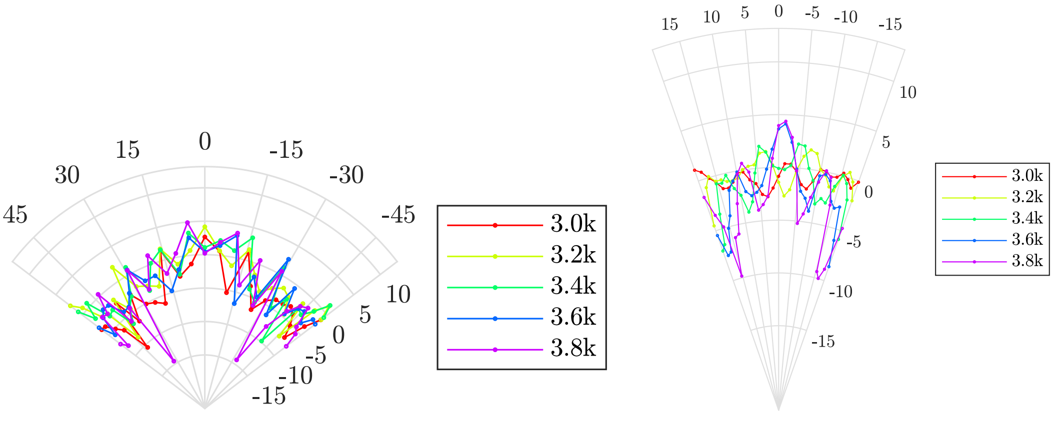

(c) 0.5 m **(d)** 2 m

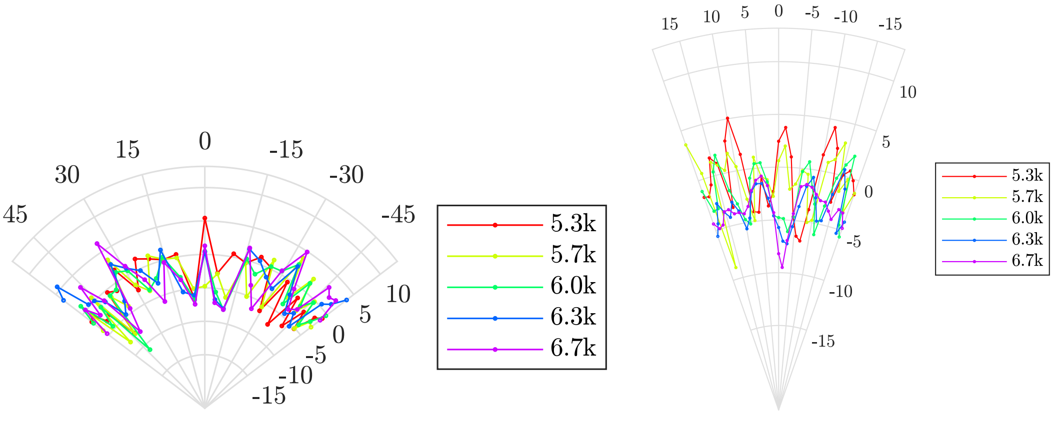

(e) 0.5 m **(f)** 2 m

Figure B.12: Façade array of 16 equally distributed cylinders only, no walls of any sort. Measured pressure, relative SPL dB rms normalized by free propagation reference.

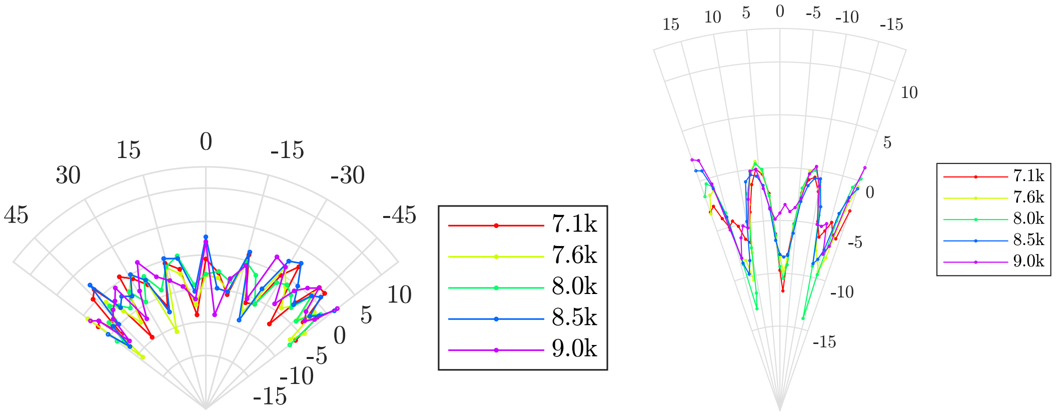

(a) 0.5 m **(b)** 2 m

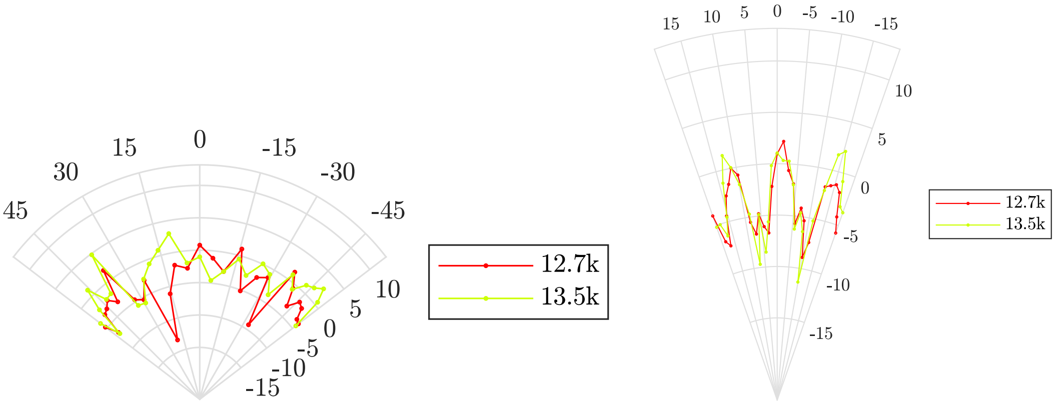

(c) 0.5 m **(d)** 2 m

Figure B.13: Façade array of 16 equally distributed cylinders only, no walls of any sort. Measured pressure, relative SPL dB rms normalized by free propagation reference.

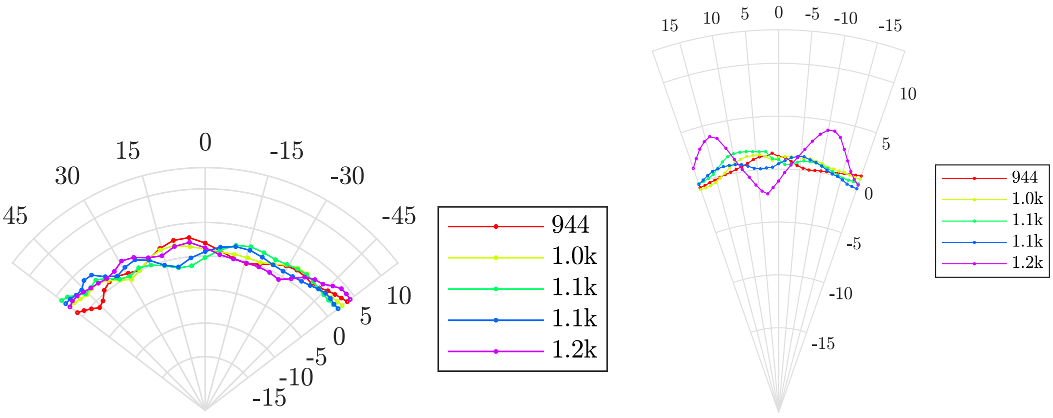

(a) 0.5 m **(b)** 2 m

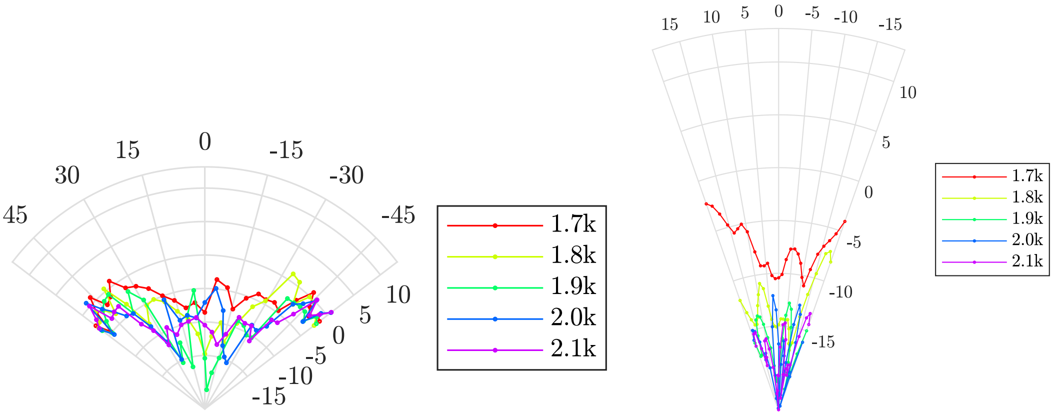

(c) 0.5 m **(d)** 2 m

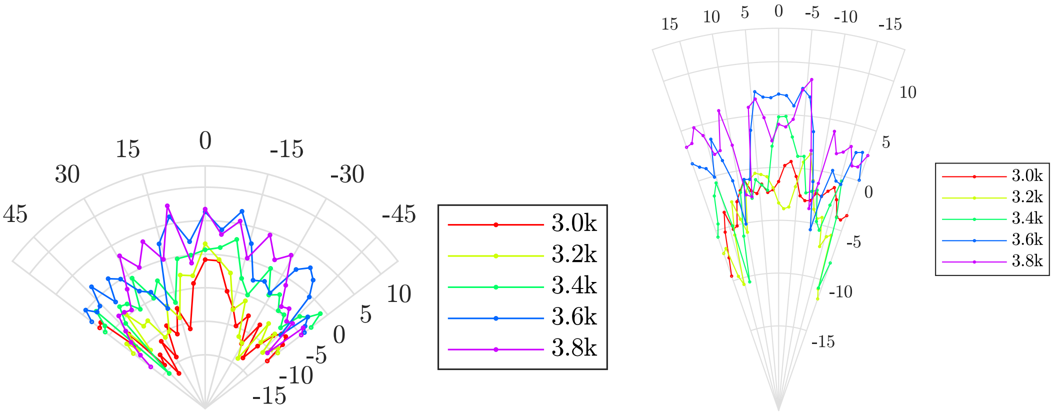

(e) 0.5 m **(f)** 2 m

Figure B.14: Façade array of 16 equally distributed cylinders and 50% of the total forest cylinders in the cavity space ($n_o = 134$), no walls of any sort. Measured pressure, relative SPL dB rms normalized by free propagation reference.

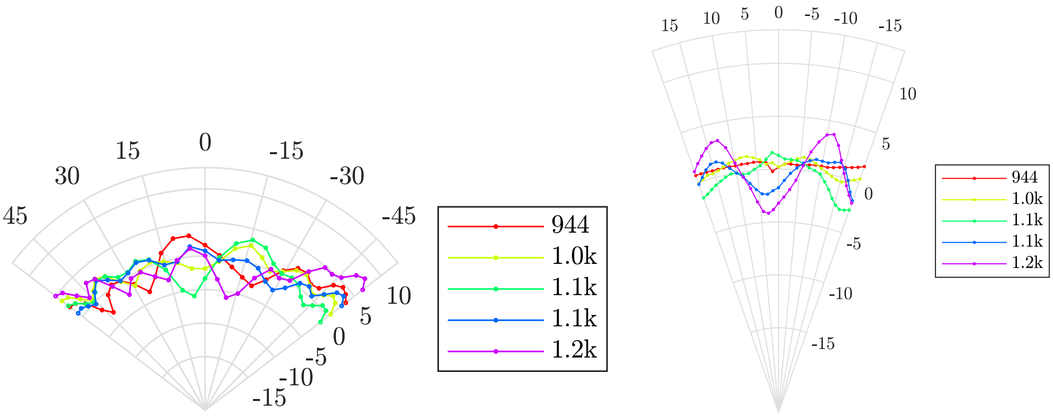

(a) 0.5 m **(b)** 2 m

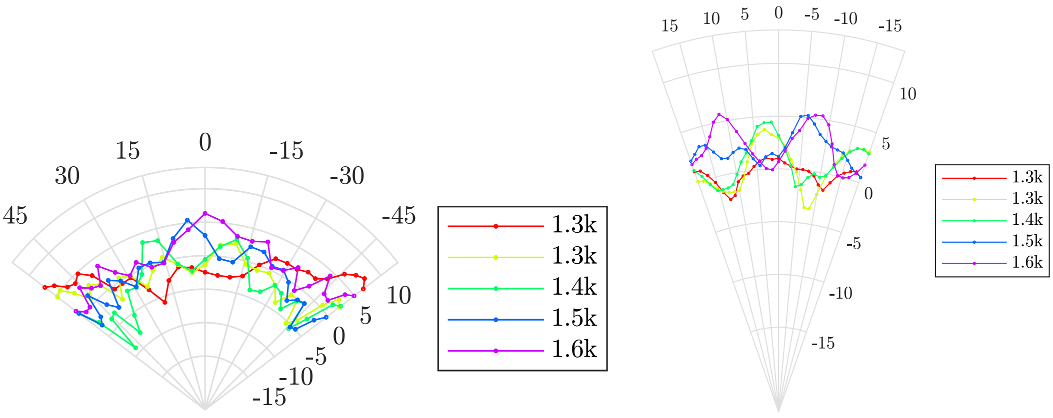

(c) 0.5 m **(d)** 2 m

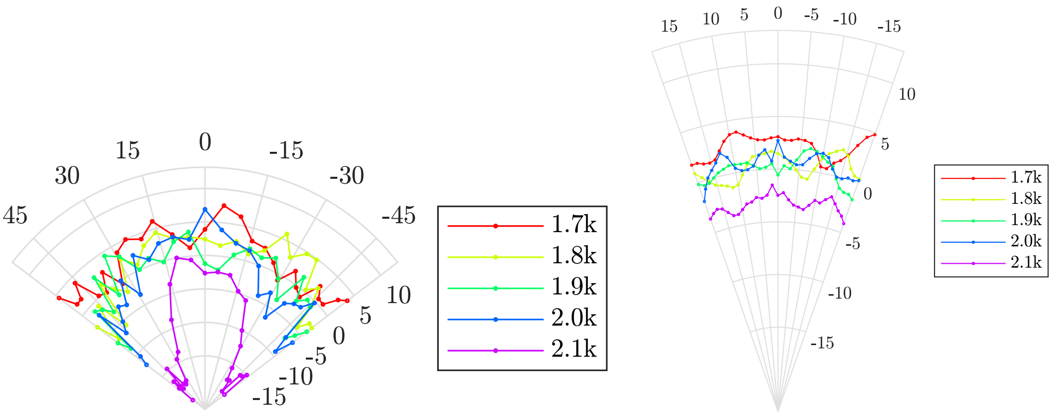

(e) 0.5 m **(f)** 2 m

Figure B.15: Façade array of 16 equally distributed cylinders and 100% of the total forest cylinders in the cavity space ($n_o = 134$), no walls of any sort. Measured pressure, relative SPL dB rms normalized by free propagation reference.

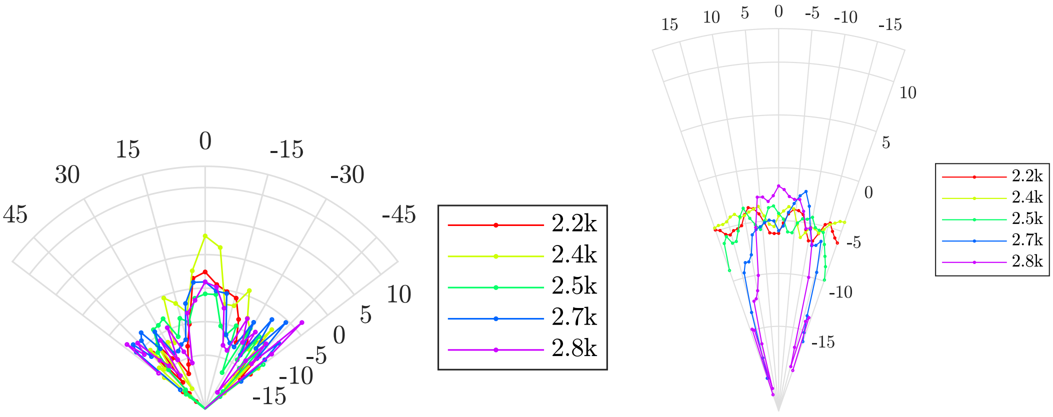

(a) 0.5 m **(b)** 2 m

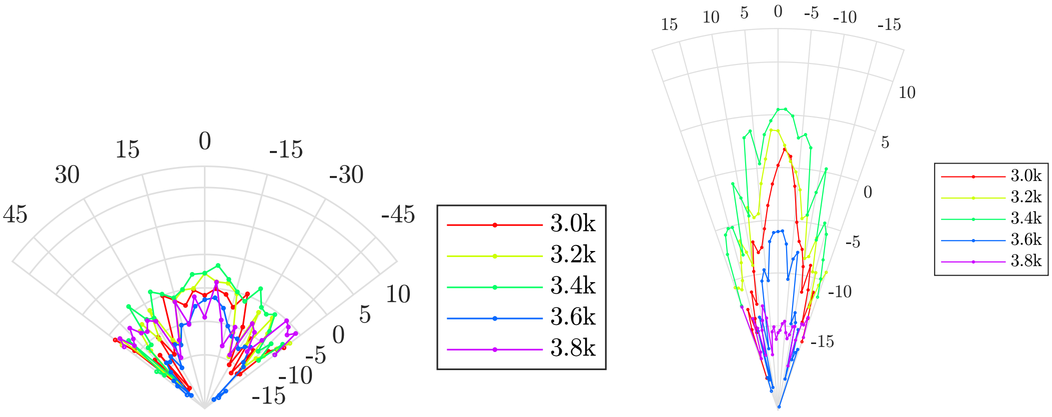

(c) 0.5 m **(d)** 2 m

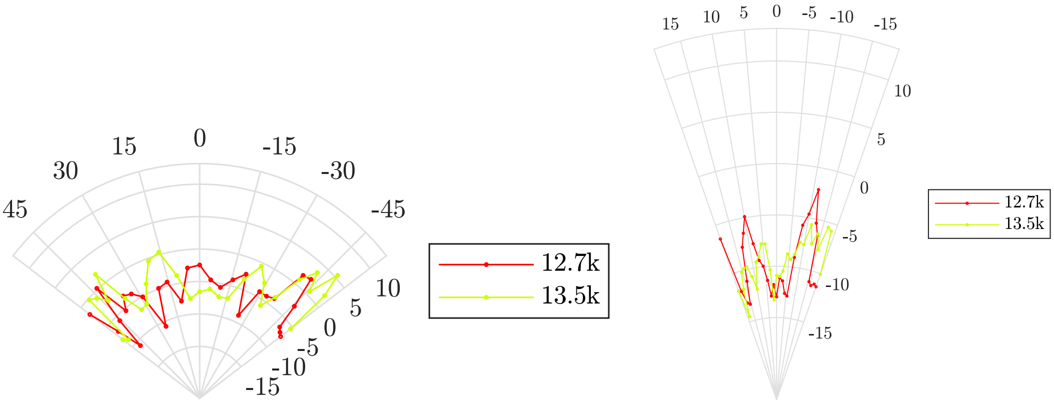

(e) 0.5 m **(f)** 2 m

Figure B.16: Façade array of 16 equally distributed cylinders and 100% of the total forest cylinders in the cavity space ($n_o = 244$), no walls of any sort. Measured pressure, relative SPL dB rms normalized by free propagation reference.

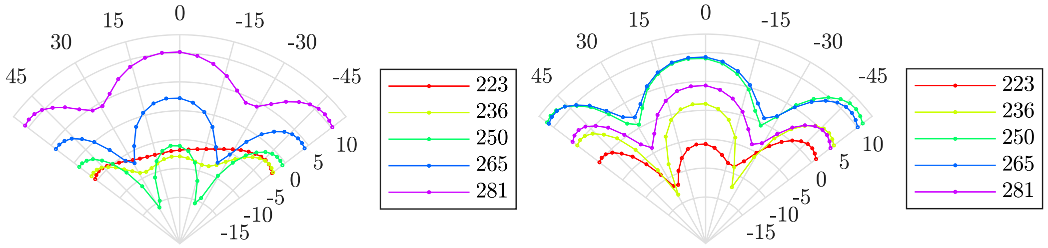

(a) no pipes **(b)** Pipes façade

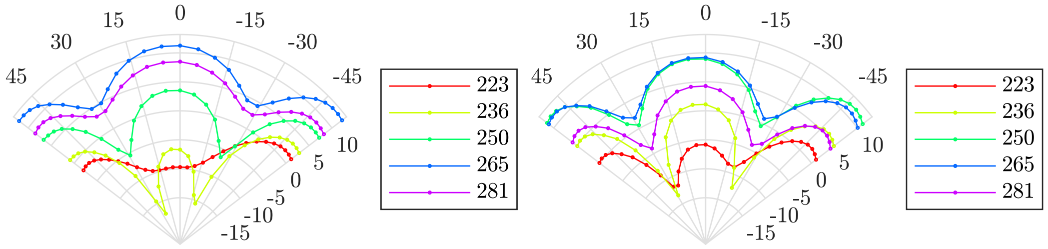

(c) 50% forest **(d)** 100% forest

Figure B.17: 3-walled organ cavity at different densities of cylinders. Measured pressure, relative SPL dB rms normalized by free propagation reference at 0.5 m.

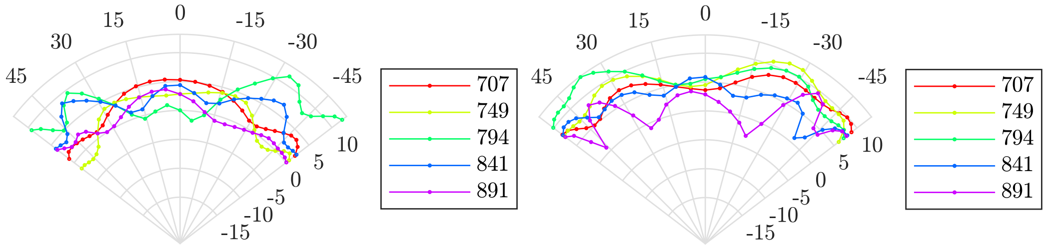

(a) no pipes **(b)** façade pipes

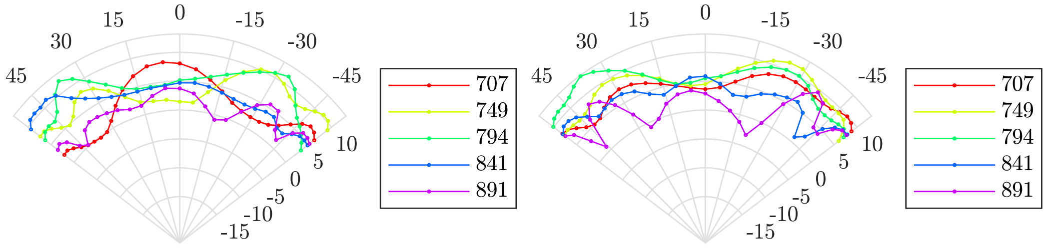

(c) 50% forest **(d)** 100% forest

Figure B.18: 3-walled organ cavity at different densities of cylinders. Measured pressure, relative SPL dB rms normalized by free propagation reference at 0.5 m.

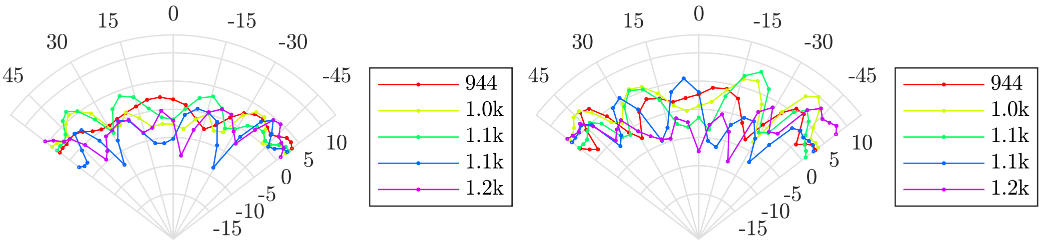

(a) no pipes **(b)** façade pipes

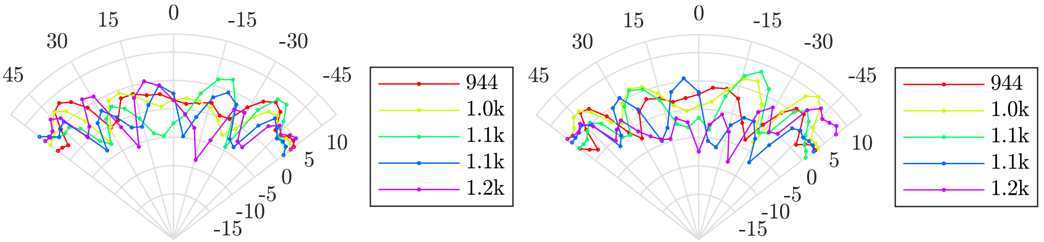

(c) 50% forest **(d)** 100% forest

Figure B.19: 3-walled organ cavity at different densities of cylinders. Measured pressure, relative SPL dB rms normalized by free propagation reference at 0.5 m.

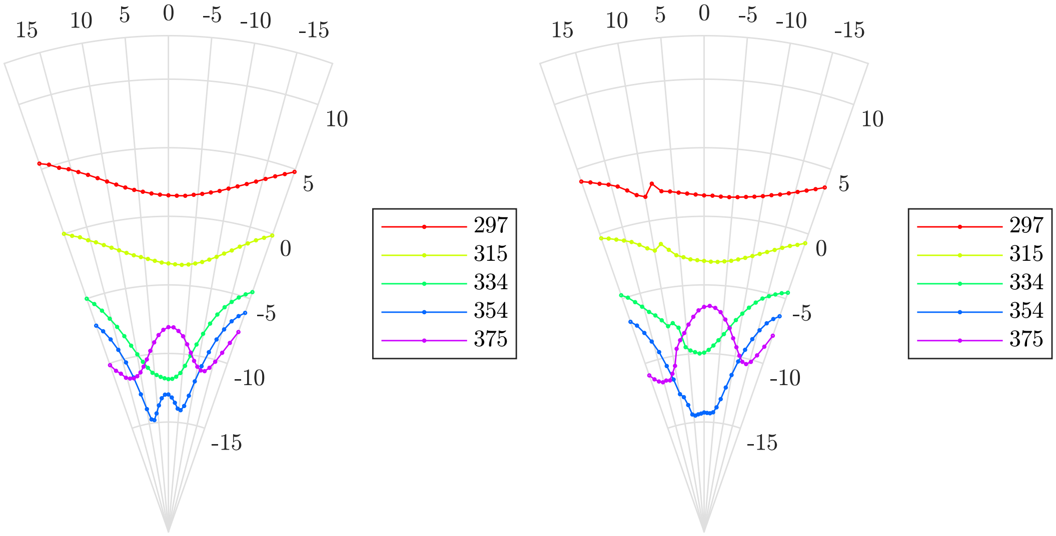

(a) no pipes **(b)** façade pipes

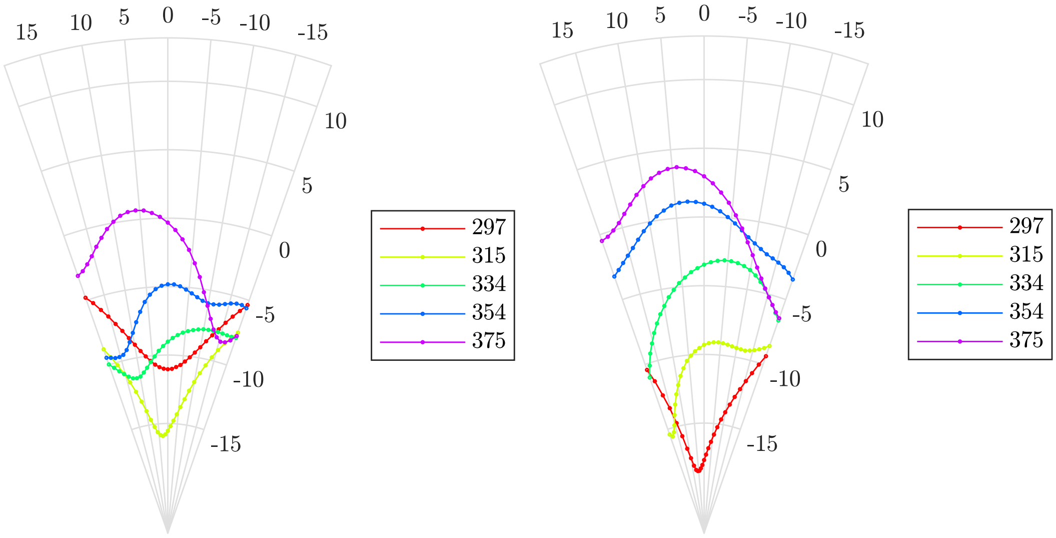

(c) 50% forest **(d)** 100% forest

Figure B.20: 3-walled organ cavity at different densities of cylinders. Measured pressure, relative SPL dB rms normalized by free propagation reference at 2 m.

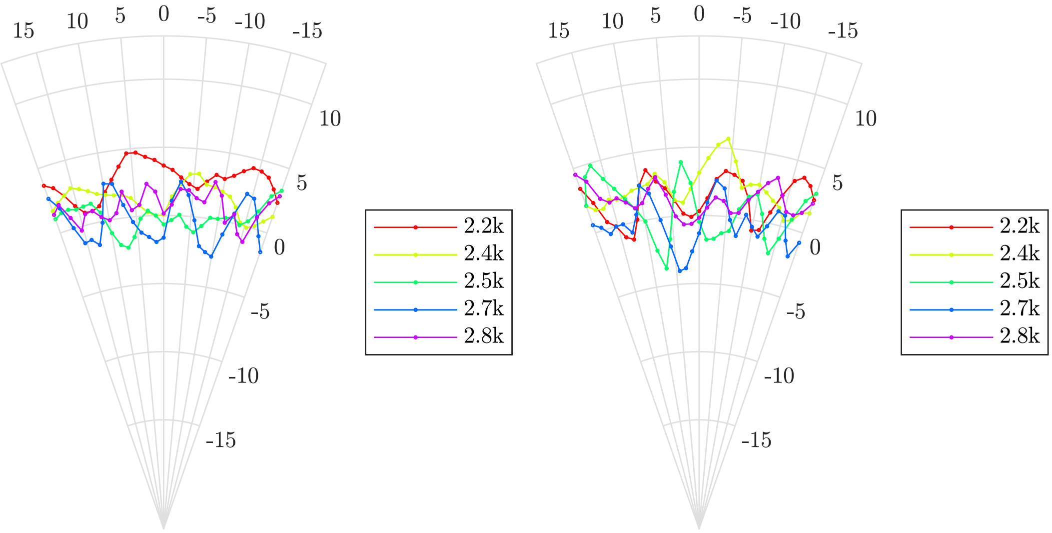

(a) no pipes

(b) façade pipes

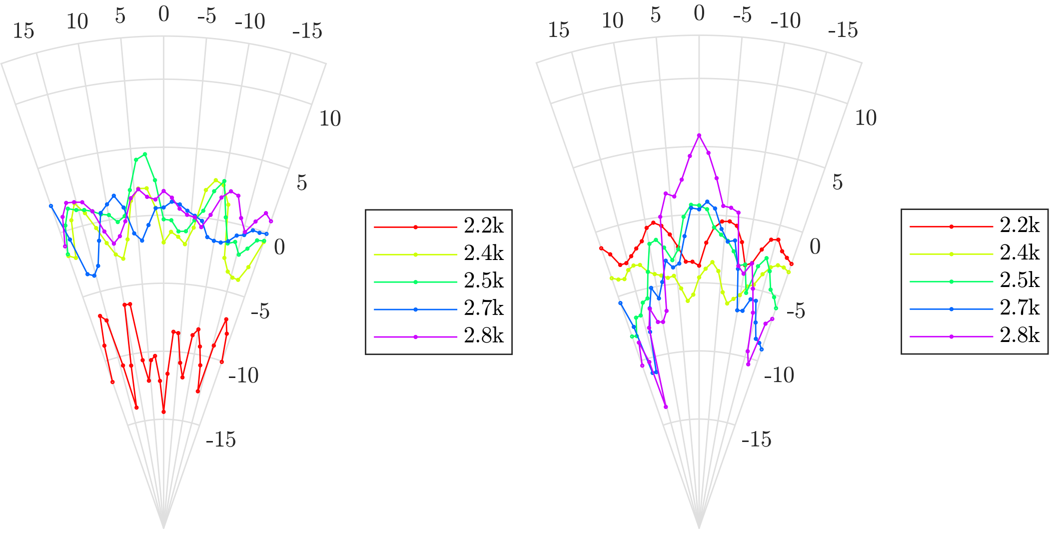

(c) 50% forest

(d) 100% forest

Figure B.21: 3-walled organ cavity at different densities of cylinders. Measured pressure, relative SPL dB rms normalized by free propagation reference at 2 m.

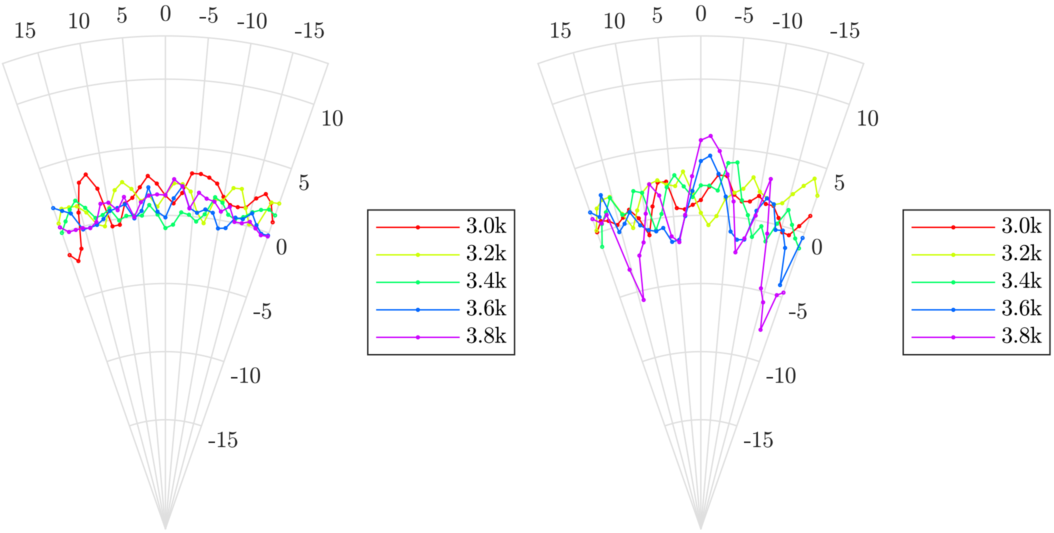

(a) no pipes **(b)** façade pipes

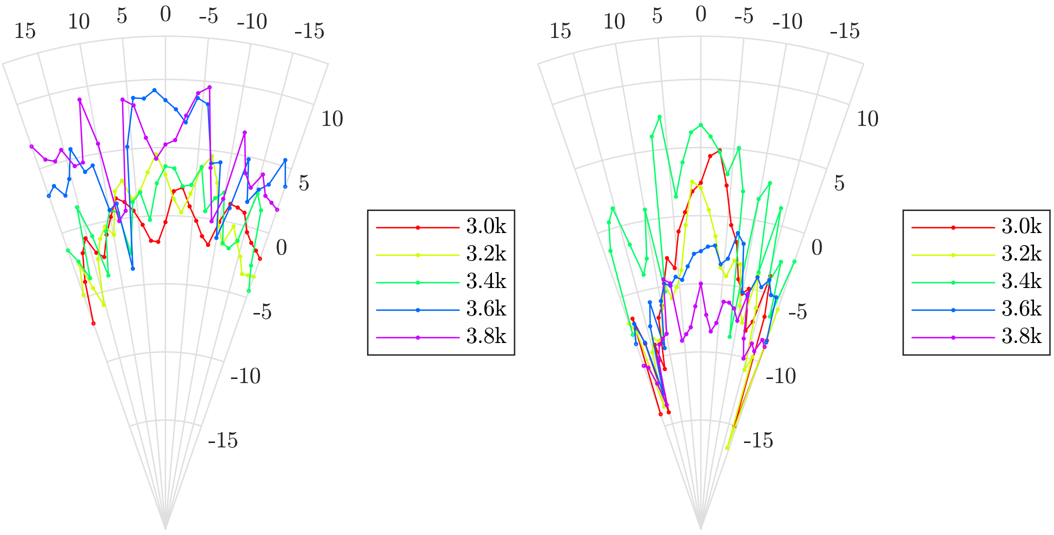

(c) 50% forest **(d)** 100% forest

Figure B.22: 3-walled organ cavity at different densities of cylinders. Measured pressure, relative SPL dB rms normalized by free propagation reference at 2 m.

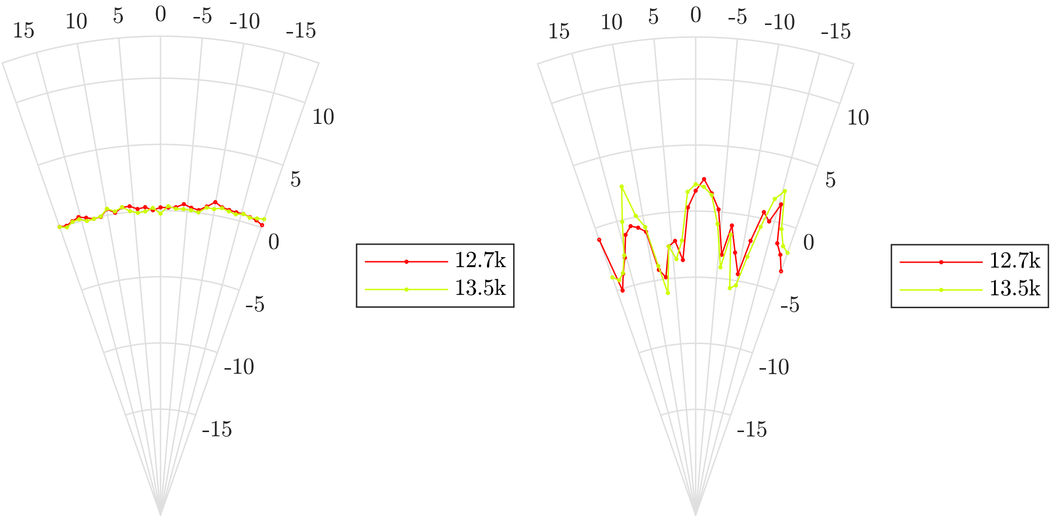

(a) no pipes

(b) façade pipes

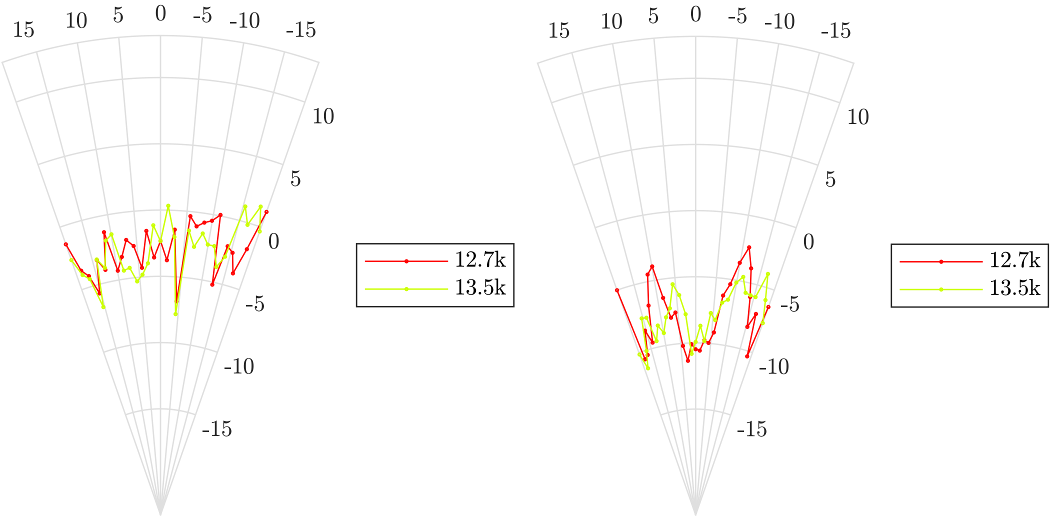

(c) 50% forest

(d) 100% forest

Figure B.23: 3-walled organ cavity at different densities of cylinders. Measured pressure, relative SPL dB rms normalized by free propagation reference at 2 m.

Appendix C

Radiated pressure in the empty organ of NDP

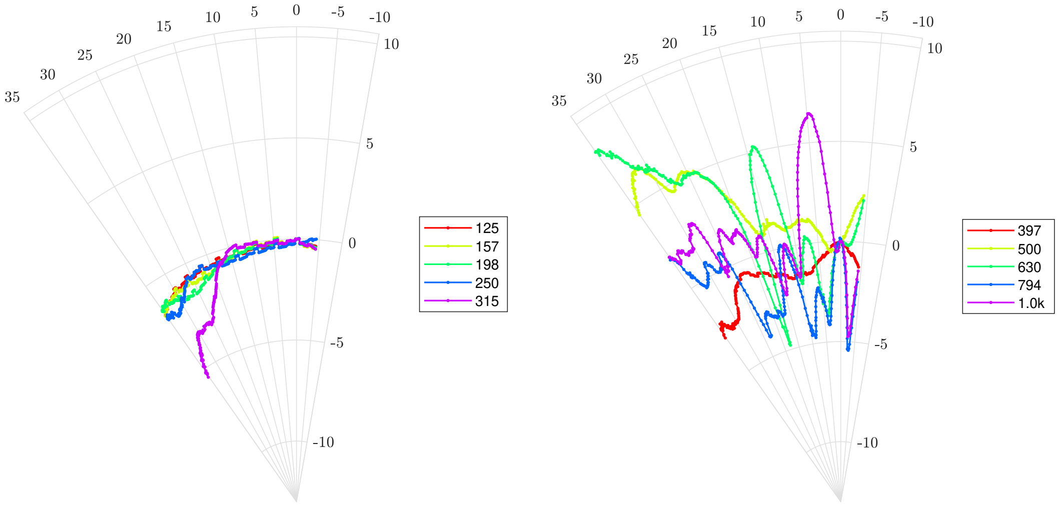

(a) Low frequencies **(b)** Low-mid frequencies

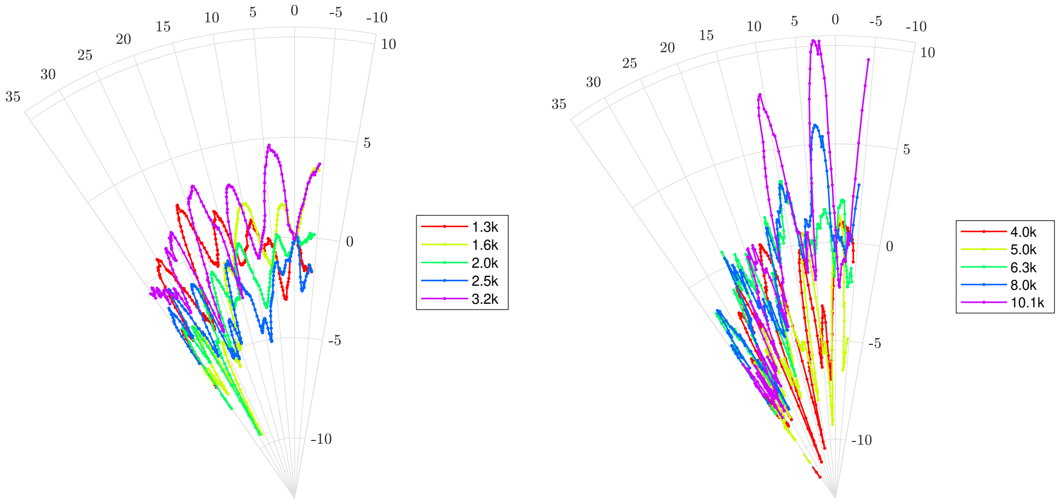

(c) High-mid frequencies **(d)** High frequencies

Figure C.1: Measured relative SPL (dB) by thirds of octave bands at the empty tribune organ of Notre-Dame de Paris. Center frequencies of each sub-band are expressed in Hz.

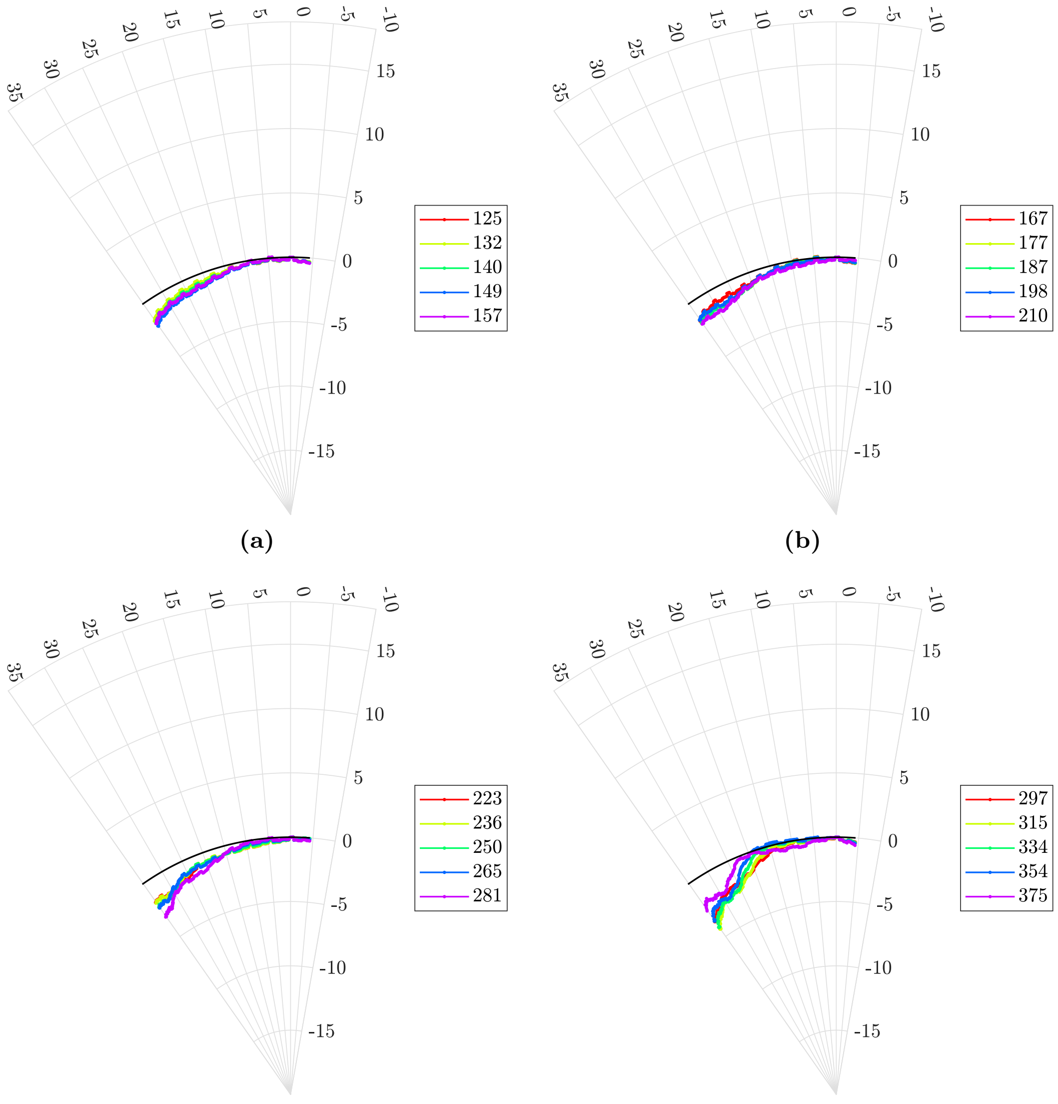

(a)

(b)

(c)

(d)

Figure C.2: Twelfth octave bands of relative SPL (dB) measured in the empty tribune organ of NDP.

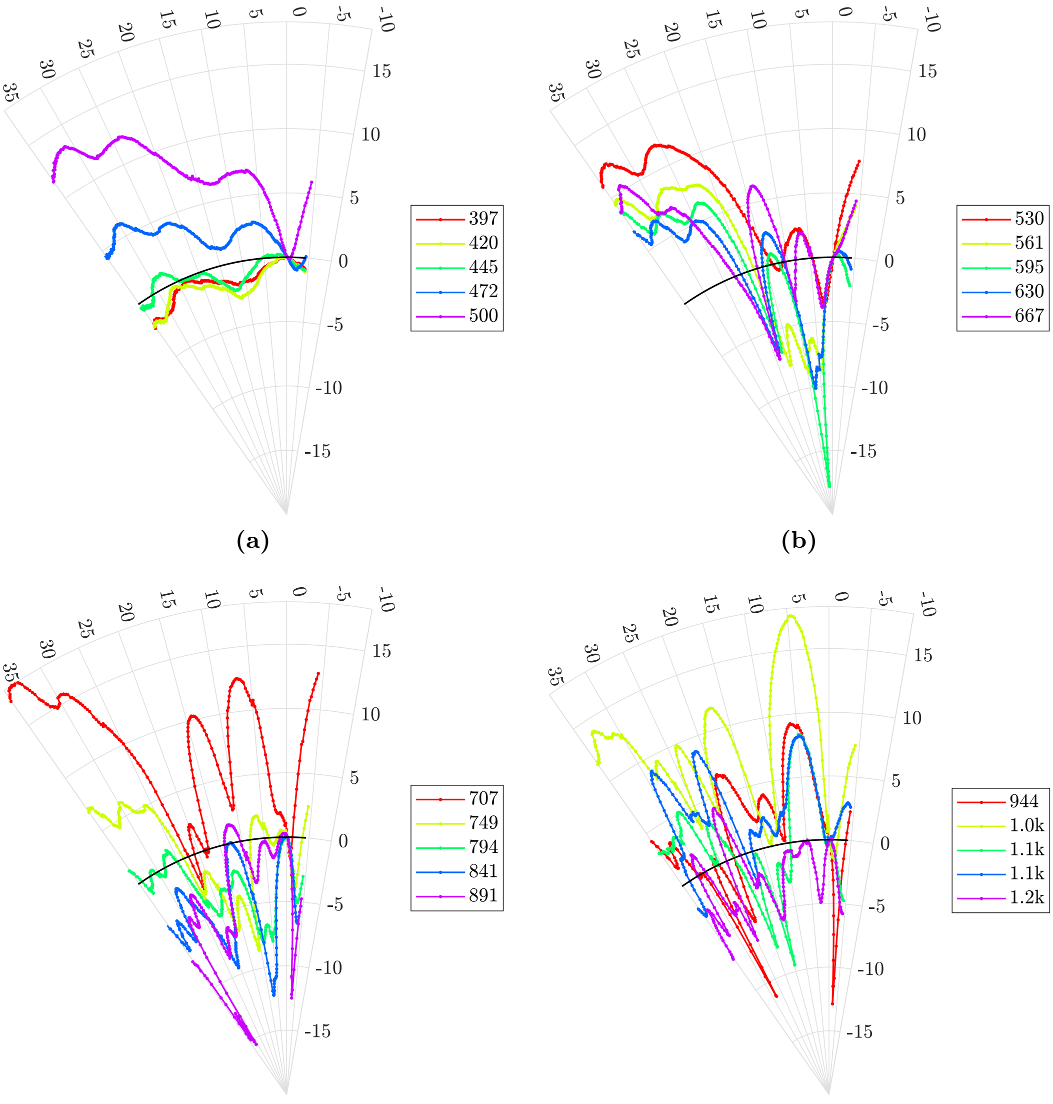

(a) **(b)** **(c)** **(d)**

Figure C.3: Twelfth octave bands of relative SPL (dB) measured in empty tribune organ of NDP.

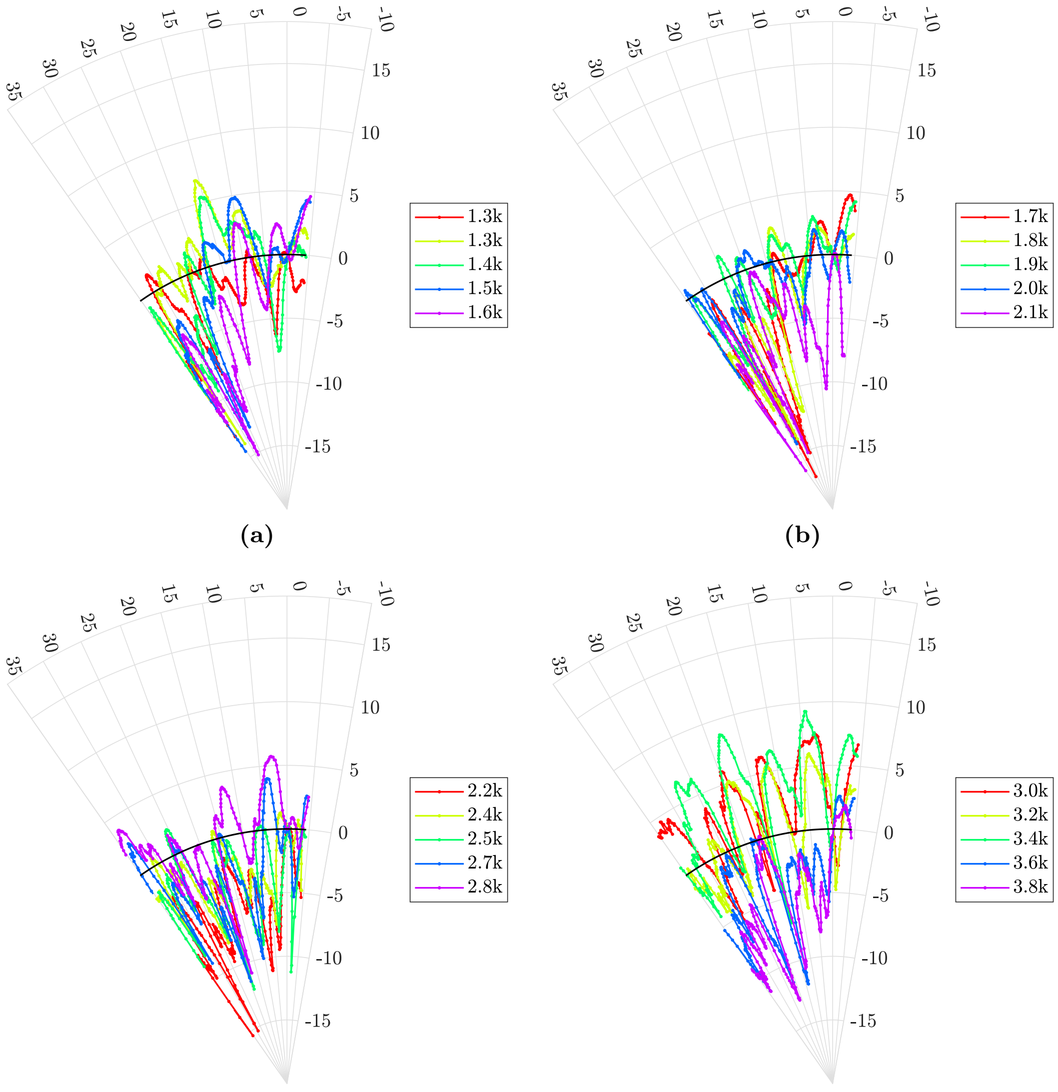

(a) **(b)**

(c) **(d)**

Figure C.4: Twelfth octave bands of relative SPL (dB) measured in the empty tribune organ of NDP.

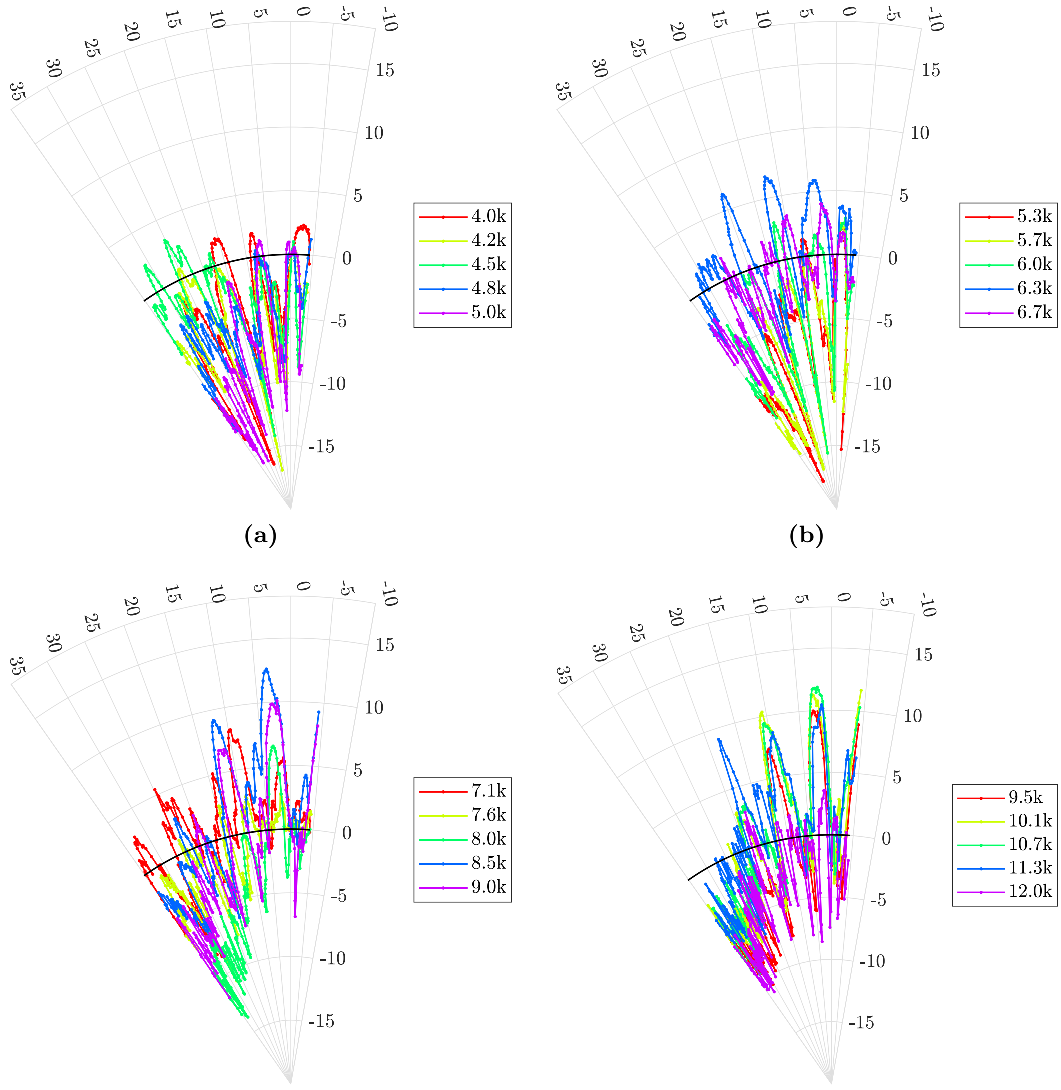

(a) **(b)**

(c) **(d)**

Figure C.5: Twelfth octave bands of relative SPL (dB) measured in the empty tribune organ of NDP.

Appendix D

Numerical directivity of an organ-like cavity geometry

A more extended collection of radiation patterns is provided here (Figure D.1 and Figure D.2) at two distances of the organ-like geometry system as per descriptions provided in §6.6, first in octave bands and secondly in twelfths of octave.

The notion of direct sound traversing a complex media is fragile, especially at mid and high frequencies where a high order of reflections is to expected. For such scenario, we propose the inspection of the scattered field during a pseudo-transient time span. We have selected a window of 800 samples, at a time sampling frequency of 123.3 kHz[1] and an FFT size of 2^{15} samples. The initial time step of windowing is shifted by amounts of 0.8 ms to observe the evolution of the scattered pressure during a span of 10.5 ms. A few of such sample times are shown in Figure D.4.

The angular-independent gain observed at 3.3 kHz to 3.5 kHz that faintly appeared in presence of a façade array of evenly distributed cylinders (Figure B.7) at a distance of 0.2 m and in the long window integration (3000 time steps, Figure D.3), does not become apparent in the sliding window at 4.5 m of simulated data until the window center time of 17.8 ms (after ∼6 m of total travelled path at $c_o = 340\,\mathrm{m\,s^{-1}}$) and remains recognizable until no spatial patterns are apparent in the spectra. In other words, it is a distinctive trait of the cylinder spacing scattering not prominent until a pseudo-transient state is over. As a reminder, the first-order expression from [Berry et al., 2019] for which we computed the first values in Table 6.1 predicted a value of 3479 Hz, which seems to be in good agreement with this behaviour observed.

---

[1] Computations took an average of 4 h on machines with Linux Mint 20.3, 64 cores, and 128 GB memory; using a maximum frequency of 11.3 kHz, 6 points per wavelength, a domain of 12 m side before hexagonal projection, with a PML starting radially at 5 m from the origin (source injection grid-point), and CFL ranging within $[0.8, 0.99]\lambda_{max}$ as per [Bilbao and Hamilton, 2018].

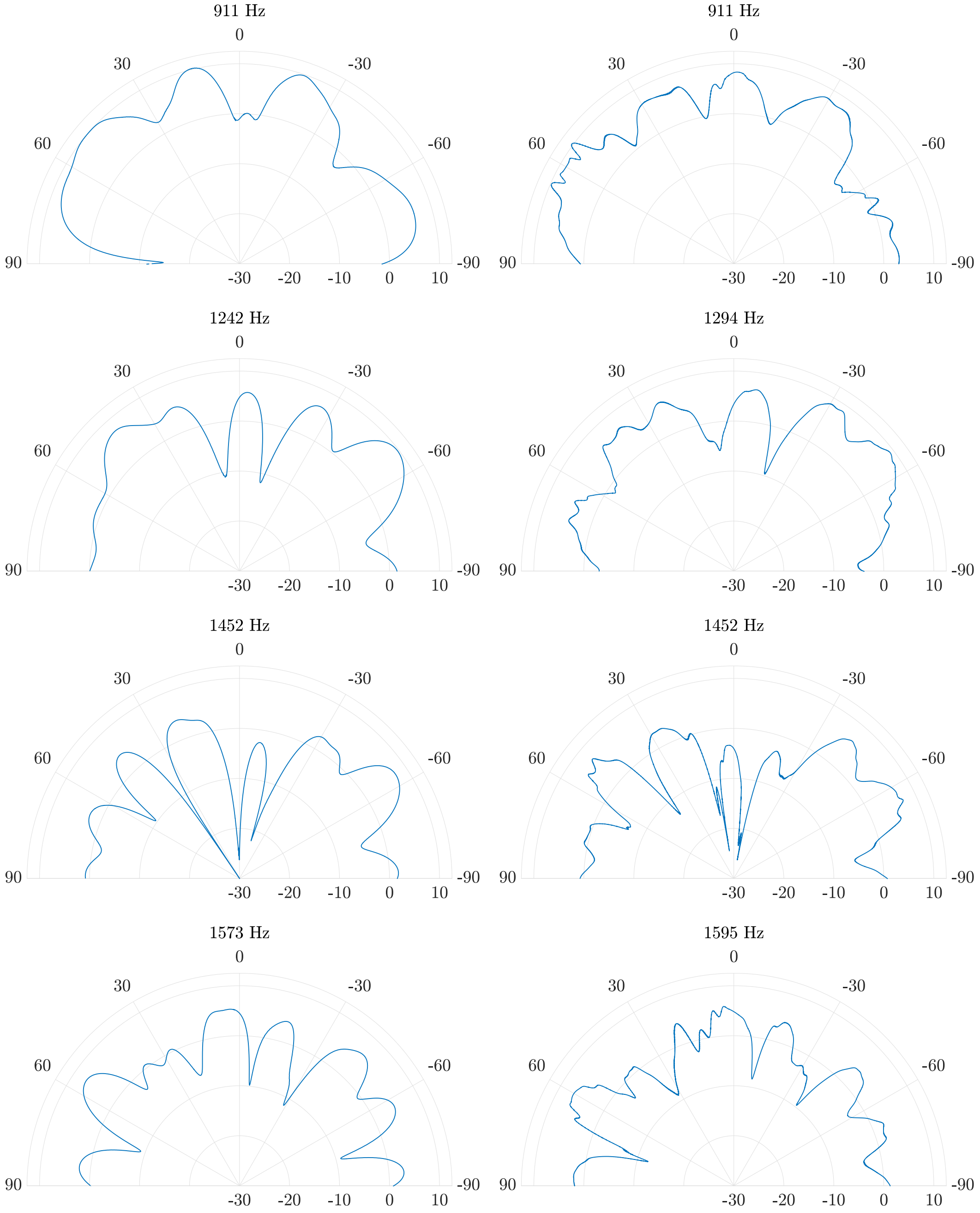

Figure D.1: Numerical simulation of organ façade's scattered field. Left: at 1.5 m contour. Right: at 4.5 m contour.

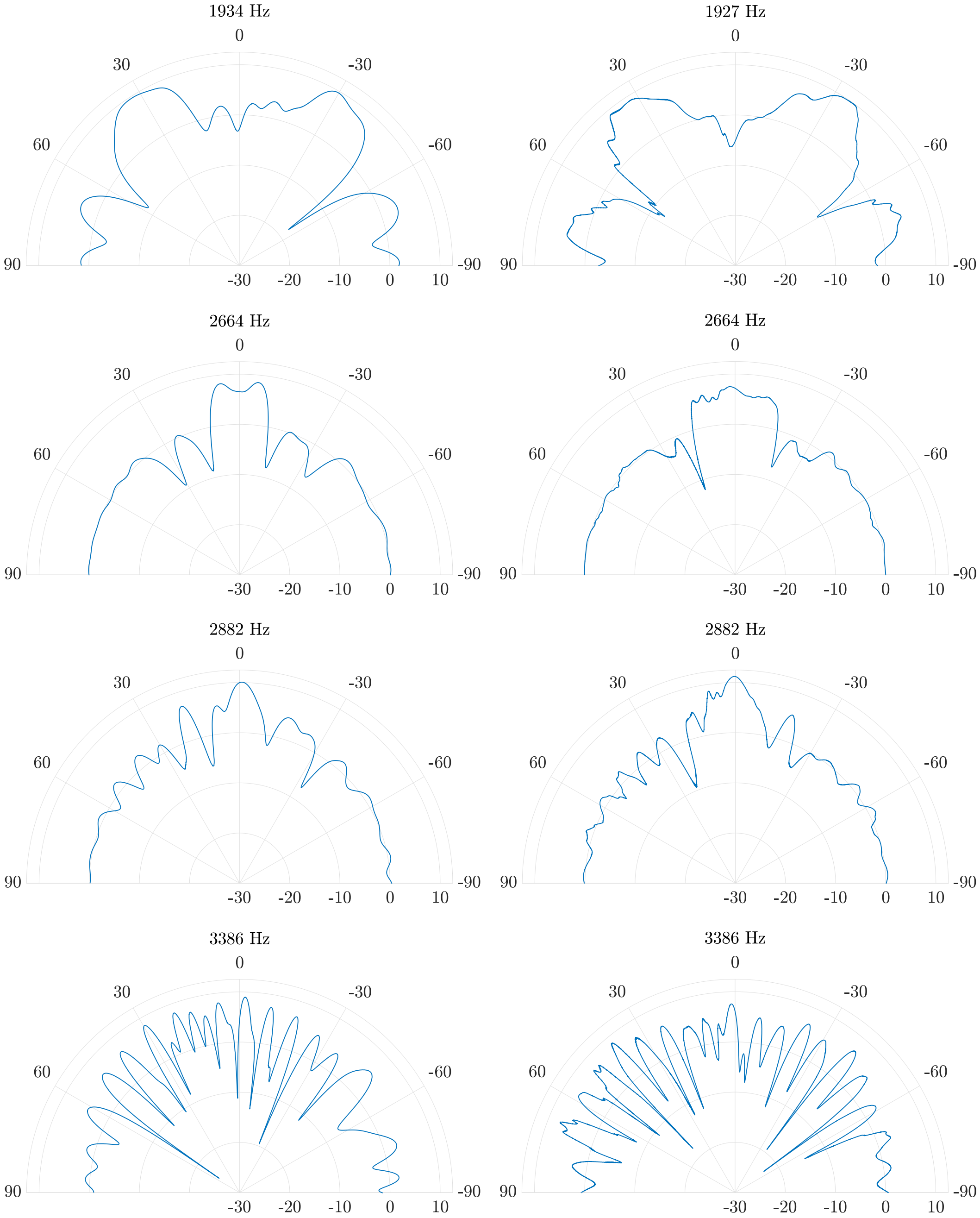

Figure D.2: Numerical simulation of organ façade's scattered field. Left: at 1.5 m contour. Right: at 4.5 m contour.

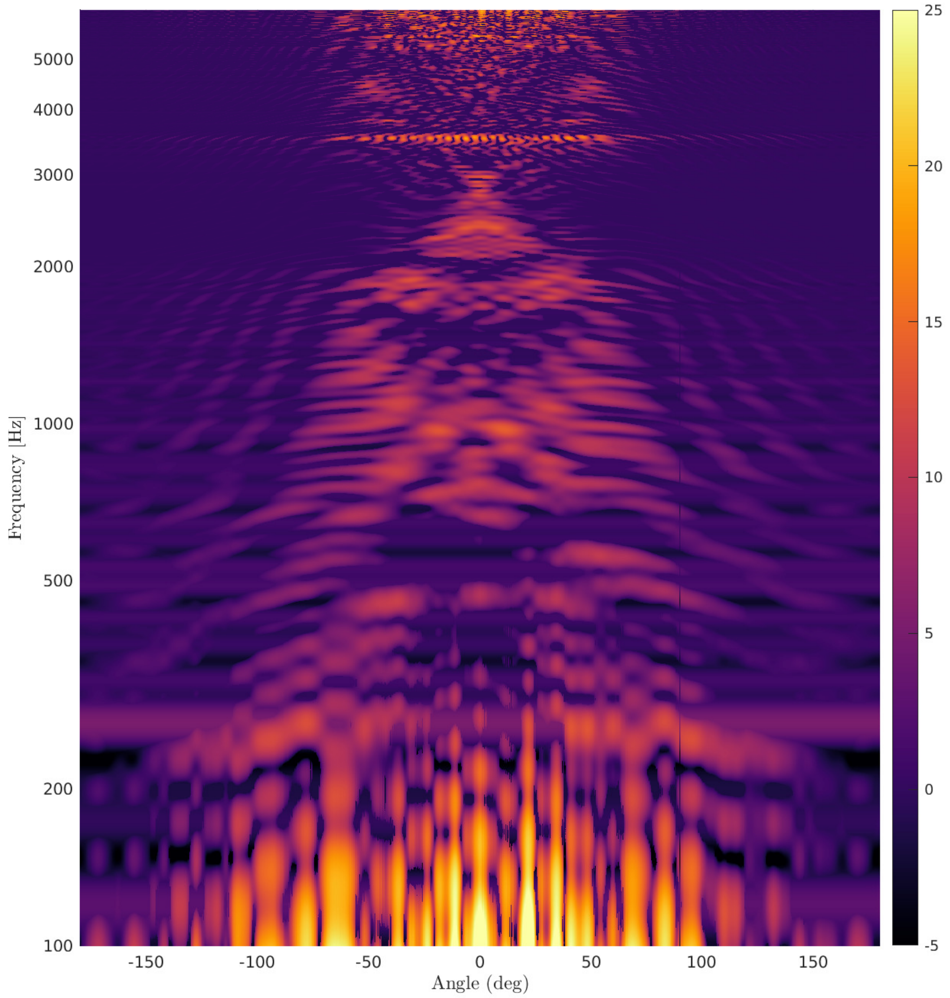

Figure D.3: Scattered pressure spectrum (dB) at the contour of 1.5 m around the organ-like system geometry. Sampling frequency 123.3 kHz, FFT size of 2^{17} samples, window time 3000 time steps. The horizontal axis expresses the angle span around the coordinate center of the excitation injection point.

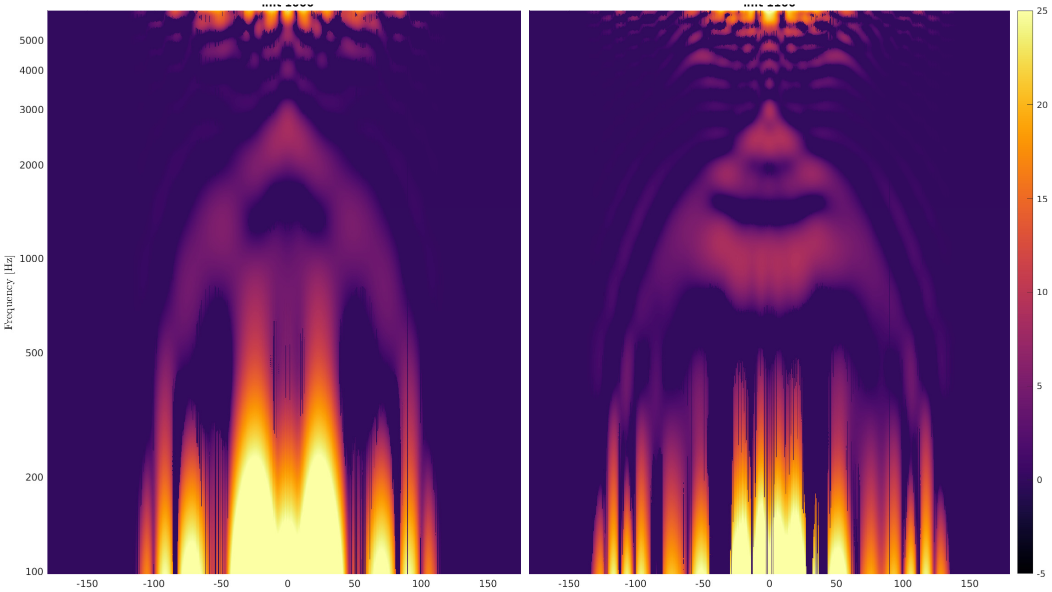

(a) Window starting at sample 1000 **(b)** At sample 1100

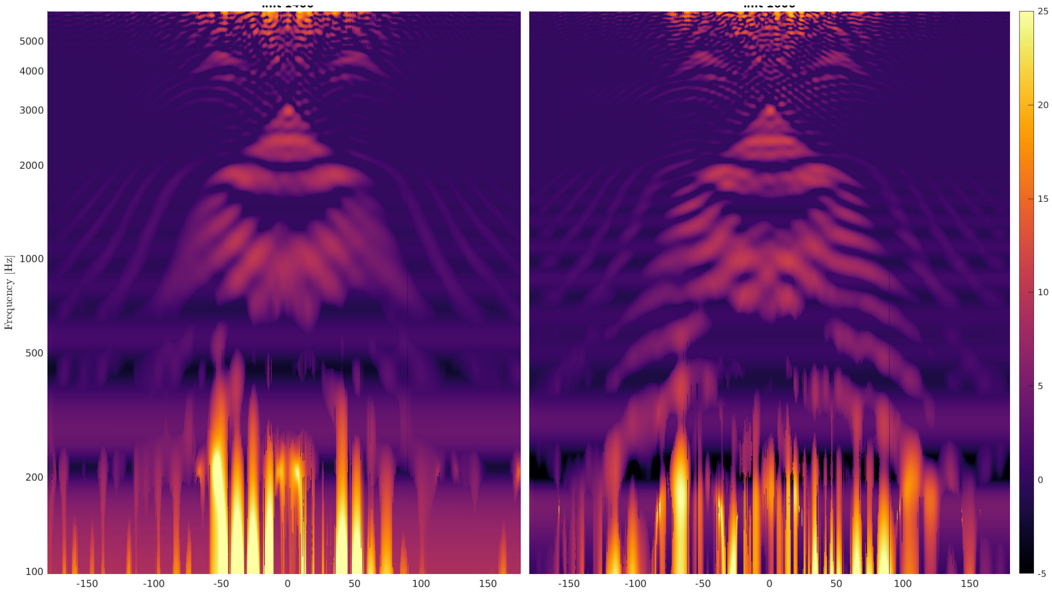

(c) At sample 1400 **(d)** At sample 1600

Figure D.4: Simulated scattered pressure read at the 4.5 m contour from the origin at different initial window times using a window lenght of 800 samples, an FFT size of 2^{15}, and a time sampling frequency of 123.3 kHz. The axes span the same angle and frequency domain as in Figure D.3.

APPENDIX E

A sample instrument file

In this section, we detail the form of an instrument file corresponding to one pipe set of geometry and extracted fitted modal data.

Where all geometry parameters were successfully accessed via direct measurement, steady-state correction or interpolation from documentation. The parameters of interest related to geometry include:

- L_p: The physical length of the resonator
- R_p: Radius of the resonator
- R_{in}: Radius of the foot inlet
- W_m: Mouth width (or cut-up height, depending on orientation); this is the distance from the flue exit to the labium
- H_m: Depth of the mouth (as a rule of thumb, $H_m \sim 4W_m$)
- h: Jet flueway thickness (generally in the order of 1 mm)

whereupon one can derive the following geometrical variables: $S_{in} = \pi R_{in}^2$, the inlet cross-section for the windchest and rankchest flow to enter the pipe foot; $S_j = hH_m$, the jet's area at the flue exit as the aperture between the foot and the mouth; $S_m = H_m W_m$, the mouth area, from which one can derive an equivalent of wetted area mouth radius; and S_p, the cross-section of the pipe's bore. In the example here we consider the case where $S(x) = S_o$, constant radius for $x \in [0, Lp]$.

The fitting of the pipe input admittance modal parameters yields and amplitude, a pulsation, and a damping for each pole of its transfer function, as discussed in Chapter 3 and Chapter 4. A zero-subindex indicates the zeroth mode or uniform mode without a frequency, thus the roles of amplitude, pulsation, and damping no longer are significant to them and Terrien's notation [Terrien, 2014] can be used for those, resulting in the set of parameters

$$\{Y_r, \omega_r, \varepsilon_r\}, \ r \in [1, \ldots, N_m] \tag{E.1}$$

The next set of parameters are well-accepted approximations (frequency dependant) of the jet spatial amplification, the relative convection velocity, and he vena-contracta effect of the flow constriction in the passage from bore's cross-section to mouth cross-section. The aforementiond are commonly labelled as $\alpha_i \cdot h = \Re\{\alpha\} \cdot h$

(where α is the solution's wavenumber to the instability's Rayleigh equation, as discussed in Chapter 3), γ, and α_{vc}, respectively.

There is a last set of parameters worth mentioning due to their high sensitivity, both to instrument manufacturing or the numerical implementation of the instrument-model:

- b: Jet half-width
- δ_d: Distance between aero-acoustic sources Q_1 and Q_2, estimated by conformal mapping of potential field around the labium [Verge, 1994]
- α_i: The imaginary part of the instability wavenumber, responsible for the oscillatory behaviour
- Str_{jet}: Non-dimensional cutoff frequency for low-pass filtering the operation state using the Strouhal number $Str_{jet} = \omega_c \cdot b/u_j$. As shown by [Ségoufin et al., 2000] and [Mattingly and Criminale, 1971], the valid region is below $Str_{jet} = 1.4$.
- l_j: The length of the jet formation channel, analogously to the flow channels for the windchest-to-rankchest and rankchest-to-foot windways. In tin-lead flue instruments, the jet channel lenght is of comparable order to the material thickness (∼1 mm).
- y_{off}: The *vertical* offset of he labium with respect to the center-line of the jet outing of the flueway. This alignment has a crucial effect on (1) the initial outwards/inwards tendency of the jet initial direction ([Verge et al., 1994b]) and the balanace between modal gain amplitudes (see open loop gain in §4.3.1). For comparability with the normalized jet transverse displacement η_b before the saturation mapping $tanh(\cdot)$, the computation version of the offset is also hardcoded as its b-normalized version.

The code architecture follows:

```
# ~~~~~~~~ GEOMETRY ~~~~~~~~

inst.Lp  = 318e-3;   # Length bore resonator [m]
inst.Rp  = 8.9e-3;   # Radius bore [m]
inst.Rin = 2.2e-3;   # Foot inlet radius [m]
inst.Hm  = 15.7e-3;  # Mouth depth [m]
inst.Wm  = 4.2e-3;   # Mouth length [m]
inst.h   = 0.39e-3;  # Flue-way height [m]

inst.Sin = pi*(inst.Rin)^2;
inst.Sp  = pi*(inst.Rp)^2;
inst.Sj  = inst.Hm*inst.h;
inst.Sm  = inst.Wm*inst.Hm;

# ~~~~~~~~ FOOT PRESSURE RISE TIME ~~~~~~~~
inst.Bf     = 244.1; # Fitted Vf/Vrankchest PRT
```

```
inst.Pftarg = 500;   # [Pa] Target pressure of foot in steady-state (SS)clear
inst.nu     = 0.001789;
inst.to     = 0.050; # [s] (Overwrite in simulation) Foot pressure max-growth
    time


# ~~~~~~~~ RESONATOR 0th MODE ~~~~~~~~
# Zeroth mode (a_o, b_o, c_o)
inst.Ro = [100, 0.1, 1.0];
# inst.Ro = [33, 0.1, 1.07];
# inst.Ro = [607.520141412284,0.782832092478694,1.02521779054998e-06];
# inst.Ro = [987.000967926814,1.25899107195802,1.07864524801561e-06];



# ~~~~~~~~ RESONATOR ~~~~~~~~
# [Y_r , omega_r , epsilon_r] k-th mode
inst.R = [36.3233757687474,3325.74212223404,0.0150211728102290;
    20.8506689431940,6667.04240282153,0.0110453848348442;
    13.5817606013882,10010.8587113370,0.00970405962658105;
    9.43272478190244,13355.9117077950,0.00907886792107337;
    6.84875572300838,16701.4927317175,0.00876021952108252;
    5.14420731929791,20046.9102873762,0.00863041139636313;
    3.96828726873086,23391.3148709656,0.00866805200933253;
    3.12412012220603,26733.5810991157,0.00890897928543882;
    2.48841592310473,30071.9886450221,0.00946849246230683;
    1.95118302382382,33406.7786874816,0.0113912372640407];

# ~~~~~~~~ PIPE'S FUNDAMENTAL FREQUENCY AND PERIOD ~~~~~~~~
inst.f1  = inst.R(1,2)/2/pi;
inst.T1  = 1./(inst.f1);


# ~~~~~~~~ JET PARAMETERS ~~~~~~~~
inst.JSA   = 0.3 ; # Jet Spatial Amplification (Def. 0.3)
inst.gamma = 0.4;  # Relative Convection velocity (Approx. Def 0.4)
inst.vc    = 0.6;  # Vena-contracta for acoustic flow through mouth constriction

# ~~~~~~~~ OTHER SENSITIVE PARAMETERS ~~~~~~~~
inst.b       = 2*inst.h/5;       # Jet half-width
inst.delta_d = 4/pi*sqrt(2*inst.h*inst.Wm); # Distance Q1-Q2
inst.alpha_i = inst.JSA/inst.h;  # (approx) Imaginary wavenumber Kelvin-
    Helmholtz instability
inst.Str_jet = 1.4;              # Low-pass jet frequency content to avoid
    injecting energy to higher modes
inst.Sm      = inst.Wm*inst.Hm;  # Mouth cross-section [m]
inst.Rm      = sqrt(inst.Sm/pi); # Mouth equivalent radius [m]
inst.lj      = 0.001;            # Jet flueway channel length
inst.yoffb   = 0.1e-3/inst.b;    # Labium vertical offset
```

Bibliography

[Ablitzer, 2021] Ablitzer, F. (2021). Peak-picking identification technique for modal expansion of input impedance of brass instruments. *Acta Acustica*, 5(53):1–13. doi:10.1051/aacus/2021046. (Cited on page 25.)

[Angster et al., 2019] Angster, J., Miklos, A., and Rucz, P. (2019). 25 years applied pipe organ research at Fraunhofer IBP in Stuttgart. In *International Symposium on Musical Acoustics*, pages 1–14, Detmold, Germany. (Cited on pages 26 and 38.)

[Angster et al., 2004a] Angster, J., Pitsch, S., and Miklós, A. (2004a). The influence of different types of wind chests on the sound formation of flue organ pipes. In *Conférence Français d'Acoustique DAGA*, pages 1–2, Strasbourg, France. (Cited on page 19.)

[Angster et al., 2007] Angster, J., Pitsch, S., and Miklós, A. (2007). Design of new wind systems for pipe organs. In *International Symposium of Musical Acoustics*, pages 1–6. (Cited on pages 19 and 37.)

[Angster et al., 2004b] Angster, J. M., Wik, T., Taesch, C., Sakamoto, Y., and Miklos, A. (2004b). The influence of pipe scaling parameters on the sound of flue organ pipes. *The Journal of the Acoustical Society of America*, 116(4):2513–2513, ISSN: `0001-4966`. doi:10.1121/1.4785024. (Cited on page 37.)

[Arasan et al., 2021] Arasan, U., Marchetti, F., Chevillote, F., Jaouen, L., and Chronopoulos, D. (2021). A simple equivalent plate model for dynamic bending stiffness of three-layer sandwich panels with shearing core. *Journal of Sound and Vibration*, 500:1–13. doi:10.1016/j.jsv.2021.116025. (Cited on page 31.)

[Arasan et al., 2022] Arasan, U., Sreekumar, A., Chevillote, F., Triantafyllou, S. P., Chronopoulos, D., and Gourdon, E. (2022). Condensed finite element scheme for symmetric multi-layer structures including dilatational motion. *Journal of Sound and Vibration*, 536:1–18. doi:10.1016/j.jsv.2022.117105. (Cited on page 31.)

[Audsley, 1965a] Audsley, G. A. (1965a). *The art of organ building*, volume 1. Dover Publications Inc., New York, USA, ISBN: `0-486-21314-5`. (Cited on pages 18 and 112.)

[Audsley, 1965b] Audsley, G. A. (1965b). *The art of organ building*, volume 2. Dover Publications Inc., New York, USA, ISBN: `0-486-21315-3`. (Cited on page 18.)

[Auvray, 2013] Auvray, R. (2013). *Hydrodynamique et acoustique des instruments de la famille des flûtes: influence du système d'alimentation sur la production du son*. PhD thesis, Paris VI, Paris, France. (Cited on page 25.)

[Auvray et al., 2014] Auvray, R., Ernoult, A., Fabre, B., and Lagrée, P.-Y. (2014). Time-domain simulation of flute-like instruments: Comparison of jet-drive and discrete-vortex models. *The Journal of the Acoustical Society of America*, 136(1):389–400, ISSN: `0001-4966`. doi:10.1121/1.4875716. (Cited on page 69.)

[Auvray et al., 2015] Auvray, R., Ernoult, A., Terrien, S., Lagrée, P. Y., Fabre, B., and Vergez, C. (2015). Effect of Changing the Vocal Tract Shape on the Sound Production of the Recorder: An Experimental and Theoretical Study. *Acta Acustica united with Acustica*, 101(2):317–330, ISSN: `16101928`. doi:10.3813/AAA.918829. (Cited on page 26.)

[Auvray et al., 2012a] Auvray, R., Fabre, B., and Lagrée, P.-Y. (2012a). Regime change and oscillation thresholds in recorder-like instruments. *The Journal of the Acoustical Society of America*, 131(2):1574–1585, ISSN: `0001-4966`. doi:10.1121/1.3672815. (Cited on page 38.)

[Auvray et al., 2012b] Auvray, R., Fabre, B., Lagrée, P.-Y., Terrien, S., and Vergez, C. (2012b). Influence of the fluctuations of the control pressure on the sound production in flute-like instruments. In *Proc. Acoustics 2012*, pages 1–7, Le Mans, France. (url). (Cited on page 19.)

[Außerlechner et al., 2008] Außerlechner, H., Angster, J., and Miklos, A. (2008). Development of an adjustable pipe-foot model of a labial organ pipe. *The Journal of the Acoustical Society of America*, 123(5):3018–3018, ISSN: `0001-4966`. doi:10.1121/1.2932630. (Cited on page 37.)

[Bellows and Leishman, 2022] Bellows, S. D. and Leishman, T. W. (2022). Modeling and measurements of organ pipe sound radiation. In *Proc. 24th International Congress on Acoustics*, pages 1–7, Gyeongju, Korea. (Cited on page 156.)

[Beranek, 1960] Beranek, L. L. (1960). Audience and seat absorption in large halls. *Journal of the Acoustical Society of America*, 32(6):661–670. (Cited on page 30.)

[Beranek, 1996] Beranek, L. L. (1996). *Acoustics*. Acoustical Society of Americal, Cambridge, MA, USA, fifth edition. (Cited on page 30.)

[Beranek, 2004] Beranek, L. L. (2004). *Concert halls and opera houes: music, acoustics, and architecture*. Springer New York, New York, USA. (Cited on page 30.)

[Berry et al., 2019] Berry, D. L., Taherzadeh, S., and Attenborough, K. (2019). Acoustic surface wave generation over rigid cylinder arrays on a rigid plane. *The Journal of the Acoustical Society of America*, 146(4):2137–2144, ISSN: `0001-4966`. doi:10.1121/1.5126856. (Cited on pages 30, 122, 123 and 215.)

[Bilbao, 2004] Bilbao, S. (2004). *Wave and scattering methods for numerical simulation*. John Wiley & Sons. (Cited on page 25.)

[Bilbao, 2009] Bilbao, S. (2009). *Numerical sound synthesis*. John Wiley & Sons, ISBN: `978-0-470-74902-9`. (Cited on page 25.)

[Bilbao and Hamilton, 2016] Bilbao, S. and Hamilton, B. (2016). Finite volume modeling of viscothermal losses and frequency-dependent boundaries in room acoustics simulations. In *60th International Conference: DREAMS*, pages 1–8. Audio Engineering Society Conference. (Cited on page 30.)

[Bilbao and Hamilton, 2017] Bilbao, S. and Hamilton, B. (2017). Wave-based room acoustics simulation: Explicit/implicit finite volume modeling of viscothermal losses and frequency-dependent boundaries. *Journal of the Audio Engineering Society*, 65(1/2):78–89. doi:10.17743/jaes.2016.0057. (Cited on page 154.)

[Bilbao and Hamilton, 2018] Bilbao, S. and Hamilton, B. (2018). Passive volumetric time domain simulation for room acoustics applications. *The Journal of the Acoustical Society of America*, 145(4):2613–2624, ISSN: `0001-4966`. doi:10.1121/1.5095876. (Cited on pages 30, 151, 154 and 215.)

[Bilbao et al., 2016] Bilbao, S., Hamilton, B., Botts, J., and Savioja, L. (2016). Finite Volume Time Domain Room Acoustics Simulation under General Impedance Boundary Conditions. *IEEE/ACM Transactions on Audio, Speech, and Language Processing*, 24(1):161–173, ISSN: `2329-9290, 2329-9304`. doi:10.1109/TASLP.2015.2500018. (Cited on pages 151 and 154.)

[Bistafa and Morrissey, 2003] Bistafa, S. R. and Morrissey, J. W. (2003). Numerical solutions of the acoustic eigenvalue equation in the rectangular room with arbitrary (uniform) wall impedances. *Journal of Sound and Vibration*, 263(1):205–18. doi:10.1016/S0022-460X(02)01123-9. (Cited on pages 121, 135 and 137.)

[Blanc, 2009] Blanc, F. (2009). *Production de son par couplage écoulement-résonanteur: étude des paramètres de facture des flûtes par expérimentations et simulations numériques d'écoulements.* PhD thesis, Université Pierre et Marie Curie - Paris VI, Paris, France. (Cited on page 25.)

[Blanc et al., 2010] Blanc, F., Fabre, B., Montgermont, N., de la Cuadra, P., and Almeida, A. (2010). Scaling of flute-like instruments: An analysis from the point of view of the hydrodynamic instability of the jet. *Acta Acustica united with Acustica*, 96(4):642–653, ISSN: `1610-1928`. doi:10.3813/AAA.918319. (Cited on pages 25 and 46.)

[Blondel, 1752] Blondel, J.-F. (1752). *Architecture françoise, ou Recueil des plans, élevations, coupes et profiles des églises, maisons royales, palais, hôtels & édicifes les plus considérables de Paris*, volume 1. C.-A. Jombert, Paris, France. (Cited on page 6.)

[Bogacki and Shampine, 1989] Bogacki, P. and Shampine, L. F. (1989). A 3 (2) pair of Runge-Kutta formulas. *Applied Mathematics Letters*, 2(4):321–325. (Cited on page 70.)

[Boren et al., 2019] Boren, B., Abraham, D., Naressi, R., Grzyb, E., Lane, B., and Mercurio, D. (2019). Acoustic simulation of Bach's performing forces in the Thomaskirche. In *Proceedings of the EAA Spatial Audio Signal Processing Symposium*, pages 1–6, Paris, France. doi:10.25836/SASP.2019.39. (Cited on page 173.)

[Boren, 2021] Boren, B. B. (2021). Acoustic simulation of J.S. Bach's Thomaskirche in 1723 and 1539. *Acta Acustica*, 5:14, ISSN: `2681-4617`. doi:10.1051/aacus/2021006. (Cited on page 173.)

[Briere de la Hosseraye, 2023] Briere de la Hosseraye, B. (2023). *In situ PU-based characterization of sound absorbing materials for room acoustic modeling purposes*. PhD thesis, Eindhoven University of Technology, Eindhoven, Netherlands. (Cited on page 31.)

[Bruneau, 2006] Bruneau, M. (2006). *Fundamentals of acoustics*. ISTE, UK, USA. (Cited on pages 30, 93, 113, 114, 115, 120 and 124.)

[Bédos De Celles, 1766] Bédos De Celles, F. (1766). *L'art du facteur d'orgues*, volume 1. Académie Royale des Sciences. (url). (Cited on pages 10, 17, 18, 46 and 168.)

[Carlsson, 2002] Carlsson, T. (2002). *On dynamic behaviour of wind systems for pipe organs*. PhD thesis, Chalmers University of Technology, Göteborg, Sweden. (Cited on pages 19, 20, 36 and 64.)

[Cavaillé-Coll, 1979] Cavaillé-Coll, A. (1979). *Complete theoretical works of A. Cavaillé-Coll*. Number 41 in Biblioteca organologica. F. Knuf. (Cited on page 18.)

[Chaigne and Kergomard, 2016] Chaigne, A. and Kergomard, J. (2016). *Acoustics of musical instruments*. Springer New York, New York. (Cited on pages 38 and 47.)

[Coltman, 1966] Coltman, J. W. (1966). Resonance and sounding frequencies of the flute. *The Journal of the Acoustical Society of America*, 40(1):99–107, ISSN: `0001-4966`. doi:10.1121/1.1910070. (Cited on pages 24 and 38.)

[Coltman, 1968a] Coltman, J. W. (1968a). Acoustics of the flute. *Physics Today*, 21(11):25–32, ISSN: `0031-9228, 1945-0699`. doi:10.1063/1.3034586. (Cited on page 24.)

[Coltman, 1968b] Coltman, J. W. (1968b). Sounding mechanism of the flute and organ pipe. *The Journal of the Acoustical Society of America*, 44(4):983–992, ISSN: `0001-4966`. doi:10.1121/1.1911240. (Cited on pages 24 and 38.)

[Coltman, 1969] Coltman, J. W. (1969). Sound radiation from the mouth of an organ pipe. *The Journal of the Acoustical Society of America*, 46(2B):477–477, ISSN: `0001-4966`. doi:10.1121/1.1911717. (Cited on pages 23, 24, 38 and 54.)

[Coltman, 1971] Coltman, J. W. (1971). Effect of material on flute tone quality. *The Journal of the Acoustical Society of America*, 49(2B):520–523, ISSN: `0001-4966`. doi:10.1121/1.1912381. (Cited on page 38.)

[Coltman, 1973] Coltman, J. W. (1973). Mouth resonance effects in the flute. *The Journal of the Acoustical Society of America*, 54(2):417–420, ISSN: `0001-4966`. doi:10.1121/1.1913593. (Cited on page 38.)

[Coltman, 1976] Coltman, J. W. (1976). Jet drive mechanisms in edge tones and organ pipes. *The Journal of the Acoustical Society of America*, 60(3):725–733, ISSN: `0001-4966`. doi:10.1121/1.381120. (Cited on pages 23, 38, 41, 74 and 78.)

[Coltman, 1979] Coltman, J. W. (1979). Acoustical analysis of the Boehm flute. *The Journal of the Acoustical Society of America*, 65(2):499–506, ISSN: `0001-4966`. doi:10.1121/1.382350. (Cited on page 38.)

[Coltman, 1981] Coltman, J. W. (1981). Momentum transfer in jet excitation of flute-like instruments. *The Journal of the Acoustical Society of America*, 69(4):1164–1168, ISSN: `0001-4966`. doi:10.1121/1.385696. (Cited on page 38.)

[Coltman, 1984] Coltman, J. W. (1984). Enhanced sound power from a recurved flute. *The Journal of the Acoustical Society of America*, 75(5):1642–1643, ISSN: `0001-4966`. doi:10.1121/1.390878. (Cited on page 38.)

[Coltman, 1992] Coltman, J. W. (1992). Time-domain simulation of the flute. *The Journal of the Acoustical Society of America*, 92(1):69–73, ISSN: `0001-4966`. doi:10.1121/1.404078. (Cited on pages 38 and 69.)

[Coltman, 2006] Coltman, J. W. (2006). Acoustic properties of miter bends. (Cited on page 24.)

[Cremer and Ising, 1968] Cremer, L. and Ising, H. (1968). Die selbsterregten Schwingungen von Orgelpfifen. *Acustica*, 19:143–153. (Cited on pages 22 and 24.)

[da Silva et al., 2007] da Silva, R., van Walstijn, M., and Scavone, G. P. (2007). Numerical simulations of fluid-structure interactions in single-reed mouthpieces. *Journal of the Acoustical Society of America*, 122(3):1798–1809. doi:10.1121/1.2759166. (Cited on page 25.)

[Dalenbäck, 2011] Dalenbäck, B.-I. (2011). Modeling 1D-diffusers-the missing link. In *Proc. Ecophone International Acoustic Symposium*, pages 1–27, Bastad, Sweden. doi:eng. (Cited on page 31.)

[Dalenbäck, 2016a] Dalenbäck, B.-I. (2016a). CATT-Acoustic v9.1 user's manual. (Cited on page 175.)

[Dalenbäck, 2016b] Dalenbäck, B.-I. (2016b). TUCT v2.0a user's manual. (Cited on page 175.)

[Dalenbäck, 2016c] Dalenbäck, B.-I. (2016c). Whitepaper: regarding diffraction for prediction using CATT-Acoustic v9.0c and higher. Technical report. (Cited on page 31.)

[Dalenbäck, 2018] Dalenbäck, B.-I. (2018). What is Geometrical Acoustics? Technical report. (Cited on page 30.)

[Darabundit and Smith, 2021] Darabundit, C. and Smith, J. O. (2021). Efficient digital waveguide synthesis of a pipe organ. *Journal of the Acoustical Society of America*, 150(4):A174. (Cited on pages 28 and 70.)

[Davy, 2009a] Davy, J. L. (2009a). The directivity of the sound radiation from panels and openings. *Journal of the Acoustical Society of America*, 125(6):3795–805. doi:10.1121/1.3117687. (Cited on page 117.)

[Davy, 2009b] Davy, J. L. (2009b). The forced radiation efficiency of finite size flat panels that are excited by incident sound. *Journal of the Acoustical Society of America*, 126(2):694–702. doi:10.1121/1.3158820. (Cited on page 117.)

[de Cheveigne and Kawahara, 2002] de Cheveigne, A. and Kawahara, H. (2002). YIN, a fundamental frequency estimator for speech and musica). *J. Acoust. Soc. Am.*, 111(4):14. (Cited on page 158.)

[de la Cuadra, 2006] de la Cuadra, P. (2006). *The sound of oscillating air jets - physics, modeling and simulation in flute-like instruments*. PhD thesis, Stanford University, San Francisco, CA, USA. (Cited on pages 69 and 73.)

[de la Cuadra et al., 2004] de la Cuadra, P., Fabre, B., Bernardoni, N. H., and Robin, T. (2004). Analysis of jet instability in flute-like instruments by means of image processing: effect of the channel geometry on the jet instability. In *International Congress on Acoustics*, pages 1–4, Kyoto, Japan. (url). (Cited on page 38.)

[de la Cuadra et al., 2014] de la Cuadra, P., Magron, P., Auvray, R., Meneses, F., and Fabre, B. (2014). Sound synthesis of Siku and closed pipe flutes. In *Proc. International Symposium on Musical Acoustics*, pages 1–5, Le Mans, France. (url). (Cited on page 70.)

[De La Cuadra et al., 2008] De La Cuadra, P., Vergez, C., and Fabre, B. (2008). Visualization and analysis of jet oscillation under transverse acoustic perturbation. (url), arXiv:0811.0333 [physics]. (Cited on page 25.)

[Dequand, 2000] Dequand, S. (2000). *Duct aeroacoustics: from technological applications to the flute*. PhD thesis, Technische Universiteit Eindhoven, Eindhoven, Netherlands. (Cited on page 25.)

[Dequand et al., 2003] Dequand, S., Willems, J. F. H., Leroux, M., Vullings, R., van Weert, M., Thieulot, C., and Hirschberg, A. (2003). Simplified models of flue instruments: Influence of mouth geometry on the sound source. *The Journal of the Acoustical Society of America*, 113(3):1724–1735, ISSN: `0001-4966`. doi:10.1121/1.1543929. (Cited on page 25.)

[Drazin and Johnson, 1989] Drazin, P. G. and Johnson, R. S. (1989). *Solitons: an introduction.* Cambridge University Press, New York, USA, fifth edition, ISBN: `0-521-33655-4`. (Cited on page 137.)

[Dubois, 2016] Dubois, P. (2016). Naufrage d'un projet patrimonial et culturel - l'orgue historique de la Sorbonne face a linertie institutionnelle. *Sauvegarde de l'Orgue de la Sorbonne*, pages 1–38. (Cited on pages 3, 7 and 14.)

[Dubois and Lueders, 2002] Dubois, P. and Lueders, K., editors (2002). *La Chapelle de la Sorbonne et son orgue Dallery: actes du colloque international.* Number 81-82 in La Flûte Harmonique. Association Aristide Cavaillé-Coll, Paris, la flûte harmonique edition, ISBN: `0398 9038`. (Cited on pages 3, 9, 13, 46, 67, 162 and 176.)

[Elder, 1973] Elder, S. A. (1973). On the mechanism of sound production in organ pipes. *The Journal of the Acoustical Society of America*, 54(6):1554–1564, ISSN: `0001-4966`. doi:10.1121/1.1914453. (Cited on pages 22 and 23.)

[Elder, 1978] Elder, S. A. (1978). Edgetones versus pipetones. *The Journal of the Acoustical Society of America*, 64(6):1721–1723, ISSN: `0001-4966`. doi:10.1121/1.382152. (Cited on page 22.)

[Ernoult, 2016] Ernoult, A. (2016). *Régimes non-stationnaires dans les instruments à embouchure de type flûte.* PhD thesis, Université Pierre et Marie Curie - Paris VI, Paris, France. (Cited on pages 19, 25 and 72.)

[Ernoult et al., 2018] Ernoult, A., de la Cuadra, P., and Fabre, B. (2018). An Inclined Plane: A Simple Model for the Acoustic Influence of the Flutist's Face. *Acta Acustica united with Acustica*, 104(3):496–508, ISSN: `1610-1928`. doi:10.3813/AAA.919192. (Cited on page 27.)

[Ernoult and Fabre, 2017a] Ernoult, A. and Fabre, B. (2017a). Temporal characterization of experimental recorder attack transients. *The Journal of the Acoustical Society of America*, 141(1):383–394. doi:10.1121/1.4973861. (Cited on pages 36, 39 and 52.)

[Ernoult and Fabre, 2017b] Ernoult, A. and Fabre, B. (2017b). Window impedance of recorder-like instruments. *Acta Acustica united with Acustica*, 103(1):106–116, ISSN: `1610-1928`. doi:10.3813/AAA.919037. (Cited on pages 38, 78 and 155.)

[Ernoult et al., 2016] Ernoult, A., Hajczak, A., and Fabre, B. (2016). Évolution du contenu spectral du son au cours d'un transitoire d'attaque d'instrument de type flûte. In *Congrès Français d'Acoustique*, pages 751–757, Le Mans, France. (Cited on page 52.)

[Fabre et al., 2012] Fabre, B., Gilbert, J., Hirschberg, A., and Pelorson, X. (2012). Aeroacosutics of musical instruments. *Annual Review of Fluid Mechanics*, 44:1–25. doi:10.1146/annurev-fluid-120710-101031. (Cited on page 38.)

[Fabre and Hirschberg, 1996] Fabre, B. and Hirschberg, A. (1996). Vortex shedding in steady oscillation of a flue organ pipe. *Acta Acustica united with Acustica*, 82(6):863–977. (Cited on pages 23, 38, 40 and 74.)

[Fabre and Hirschberg, 2000] Fabre, B. and Hirschberg, A. (2000). Physical modeling of flue instruments: A review of lumped models. *Acta Acustica united with Acustica*, 86(4):599–610, ISSN: `1436-7947`. (Cited on pages 22, 38 and 72.)

[Finch and Nolle, 1986] Finch, T. L. and Nolle, A. W. (1986). Pressure wave reflections in an organ note channel. *The Journal of the Acoustical Society of America*, 79(5):1584–1591, ISSN: `0001-4966`. doi:10.1121/1.393293. (Cited on pages 19, 36, 52, 54 and 70.)

[Fletcher, 1976] Fletcher, N. H. (1976). Jet-drive mechanism in organ pipes. *The Journal of the Acoustical Society of America*, 60(2):481–483, ISSN: `0001-4966`. doi:10.1121/1.381105. (Cited on page 22.)

[Fletcher, 1977] Fletcher, N. H. (1977). Scaling rules organ pipes. *Acta Acustica united with Acustica*, 37(3):131–138. (Cited on page 46.)

[Gabrielli et al., 2017] Gabrielli, L., Tomassetti, S., Squartini, S., and Zinato, C. (2017). Introducing deep machine learning for parameter estimation in physical modelling. In *Proc. International Conference on Digital Audio Effects*, pages 1–6, Edinburgh, United Kingdom. (url). (Cited on page 70.)

[Gabrielli et al., 2019] Gabrielli, L., Tomassetti, S., Squartini, S., Zinato, C., and Guaiana, S. (2019). A multi-stage algorithm for acoustic physical model parameters estimation. *IEEE/ACM Transaction on Audio, Speech, and Language Processing*, 27(8):1229–40. doi:10.1109/TASLP.2019.2914530. (Cited on page 70.)

[Galtier, 2008] Galtier, R. (2008). Étude préalable sur l'orgue de la Chapelle de la Sorbonne. Technical report, Ville de Paris, Paris. (Cited on page 162.)

[Glorieux, 1965] Glorieux, P. (1965). *Aux origines de la Sorbonne, II: le cartulaire de la Sorbonne*, volume 100. Vrin. (Cited on page 3.)

[Glorieux, 1966] Glorieux, P. (1966). *Aux origines de la Sorbonne, I: Robert de Sorbon. L'homme, le Collège, les Documents*, volume 100. Vrin. (Cited on page 3.)

[Hamilton, 2016] Hamilton, B. (2016). *Finite Difference and Finite Volume Methods for Wave-based Modelling of Room Acoustics*. PhD thesis, University of Edinburgh, Edinburgh, United Kingdom. (Cited on pages 31 and 151.)

[Hamilton, 2021a] Hamilton, B. (2021a). Adding air attenuation to simulated room impulse responses: A modal approach. In *Immersive and 3D Audio: from architecture to automotive*, pages 1–10. IEEE. doi:10.1109/I3DA48870.2021.9610871. (Cited on page 31.)

[Hamilton, 2021b] Hamilton, B. (2021b). Air Absorption Filtering Method Based on Approximate Green's Function for Stokes' Equation. In *24th International Conference on Digital Audio Effects*, pages 160–167. IEEE. (Cited on page 31.)

[Hamilton, 2021c] Hamilton, B. (2021c). PFFDTD Software. (url). (Cited on page 31.)

[Hamilton and Webb, 2013] Hamilton, B. and Webb, C. J. (2013). Room acoustics modelling using GPU-accelerated finite difference and finite volume methods on a face-centered cubic grid. In *Proc. Digital Audio Effects*, pages 336–43, Maynooth, Ireland. (Cited on page 31.)

[Hamilton and Webb, 2014] Hamilton, B. and Webb, C. J. (2014). Improved finite difference schemes for a 3-D viscothermal wave equation on a GPU. In *Forum Acusticum*, pages 1–9, Krakow, Poland. (Cited on page 31.)

[Hardouin, 1980] Hardouin, P. (1980). L'orgue Dallery de la Chapelle de la Sorbonne. *Connaissance de l'orgue*, 34. (Cited on pages 3, 12 and 13.)

[Harrison-Harsley, 2018] Harrison-Harsley, R. L. (2018). *Physical Modelling of Brass Instruments using Finite-Difference Time-Domain Methods.* PhD thesis, University of Edinburgh, Edinburgh, United Kingdom. (Cited on page 27.)

[Helmholtz, 1885] Helmholtz, H. (1885). *On the sensation of tone.* Dover, New York, USA, second edition. (Cited on page 22.)

[Hiller and Ruiz, 1971a] Hiller, L. and Ruiz, P. M. (1971a). Synthesizing musical sounds by solving the wave equation for vibrating objects: Part I. *Journal of the Audio Engineering Society*, 19(6):462–70. (url). (Cited on page 24.)

[Hiller and Ruiz, 1971b] Hiller, L. and Ruiz, P. M. (1971b). Synthesizing musical sounds by solving the wave equation for vibrating objects: Part II. *Journal of the Audio Engineering Society*, 19(7):542–51. (url). (Cited on page 24.)

[Hirschberg et al., 1992] Hirschberg, A., Wijnands, A. P. J., and Fabre, B. (1992). Transient behavior of flue organ pipes. *The Journal of the Acoustical Society of America*, 91(4):2411–2412, ISSN: `0001-4966`. doi:10.1121/1.403214. (Cited on page 38.)

[Holger et al., 1977] Holger, D. K., Wilson, T. A., and Beavers, G. S. (1977). Fluid mechanics of the edgetone. *The Journal of the Acoustical Society of America*, 62(5):1116–1128, ISSN: `0001-4966`. doi:10.1121/1.381645. (Cited on page 38.)

[Holger et al., 1980] Holger, D. K., Wilson, T. A., and Beavers, G. S. (1980). The amplitude of edgetone sound. *The Journal of the Acoustical Society of America*, 67(5):1507–1511, ISSN: `0001-4966`. doi:10.1121/1.384313. (Cited on page 22.)

[Hongo and Serizawa, 1999] Hongo, K. and Serizawa, H. (1999). Diffraction of an acoustic plane wave by a rectangular hole in an infinitely large rigid screen. *Journal of the Acoustical Society of America*, 106(1):29–35. doi:https://doi.org/10.1121/1.427033. (Cited on page 116.)

[Hottin, 1999] Hottin, C. (1999). La Sorbonne : Lieu de mémoires, mémoires du lieu. In *Universités et grandes écoles à Paris. Les palais de la science*, Paris et son patrimoine, pages 125–133. Action artistique de la Ville de Paris. (url). (Cited on page 3.)

[Howe, 1975] Howe, M. S. (1975). Contributions to the theory of aerodynamic sound, with application to excess jet noise and the theory of the flute. *Journal of Fluid Mechanics*, 41(4):625–73. doi:10.1017/S0022112075002777. (Cited on pages 22 and 23.)

[Howe, 1981] Howe, M. S. (1981). The role of displacement thickness fluctuations in hydroacoustics, and the jet-drive mechanism of the flug organ pipe. *Proceedings of the Royal Society of London*, 374(1):543–68. doi:10.1098/rspa.1981.0036. (Cited on page 22.)

[Howe, 1984] Howe, M. S. (1984). On the absorption of sound by turbulence and other hydrodynamic flows. *IMA Journal of Applied Mathematics*, 32:187–209. doi:10.1093/imamat/32.1-3.187. (Cited on page 23.)

[Howe, 1998] Howe, M. S. (1998). *Acoustics of fluid-structure interactions*. Cambridge University Press. (Cited on pages 22 and 23.)

[Hruška and Dlask, 2020] Hruška, V. and Dlask, P. (2020). On a robust descriptor of the flue organ pipe transient. *Archives of Acoustics*, 45(3):377–384. doi:10.24425/AOA.2020.134054. (Cited on pages 36, 39 and 158.)

[Jaffe and Smith, 1983] Jaffe, D. A. and Smith, J. O. (1983). Extensions of the Karplus-Strong plucked-string algorithm. *Computer Music Journal*, 7(2):56–69. doi:10.2307/3680063. (Cited on page 24.)

[Junger and Feit, 1993] Junger, M. C. and Feit, D. (1993). *Sound, structures, and their interaction*. Acoustical Society of Americal, ISBN: `0-262-10034-7`. (Cited on pages 99, 116, 123, 125, 128, 130, 146 and 250.)

[Karjalainen et al., 1998] Karjalainen, M., Välimäki, V., and Tolonen, T. (1998). Plucked-string models. from the Karplus-Strong algorithm to digital waveguides and beyond. *Computer Music Journal*, 22(3):17–32. doi:10.2307/3681155. (Cited on page 24.)

[Karplus and Strong, 1983] Karplus, K. and Strong, A. (1983). Digital synthesis of plucked-string and drum timbres. *Computer Music Journal*, 7(2):43–55. doi:10.2307/3680062. (Cited on page 24.)

[Kim and Kim, 2002] Kim, Y. H. and Kim, S. M. (2002). Solution of coupled acoustic problems: a partially opened cavity coupled with a membrane and a semi-infinite exterior field. *Journal of Sound and Vibration*, 254(2):231–44. doi:10.1006/jsvi.2001.3938. (Cited on pages 116 and 117.)

[Kinsler et al., 2000] Kinsler, L. E., Frey, A. R., Coppens, A. B., and Sanders, J. V. (2000). *Fundamentals of acoustics.* John Wiley & Sons. (Cited on pages 100 and 116.)

[Kob, 2000a] Kob, M. (2000a). Eigenmodes of a Flue Organ Pipe. *Acta Acustica united with Acustica*, 86(4):755–757, ISSN: `1436-7047`. (Cited on page 155.)

[Kob, 2000b] Kob, M. (2000b). Influence of Wall Vibrations on the Transient Sound of a Flue Organ Pipe. *Acta Acustica united with Acustica*, 86(4):642–648, ISSN: `1436-7047`. (Cited on pages 115 and 155.)

[Kob et al., 2022] Kob, M., Grothe, T., Thilakan, J., and Baskind, A. (2022). Analysis and modelling of bassoon directivity. In *Proc. Vienna Talks*, Vienna, Austria. (Cited on page 30.)

[Kuttruff, 1991] Kuttruff, H. (1991). *Room acoustics.* Elsevier Applied Science. Elsevier Science, New York, USA, third edition. (Cited on page 30.)

[Le Roux et al., 2012] Le Roux, J.-C., Pachebat, M., and Dalmont, J.-P. (2012). Un capteur de nouvelle génération pour la mesure d'impédance acoustique en contexte industriel. *Acoustique et Techniques: trimestriel d'information des professionnels de l'acoustique*, 68:1–6. (url). (Cited on pages 25 and 85.)

[Leach, 2003] Leach, W. M. (2003). *Introduction to eletroacoustics and audio amplifier design.* Kendall/Hunt Publishing Company, Dubuque, IA, USA. (Cited on page 94.)

[Lefebvre, 2010] Lefebvre, A. (2010). *Computational acoustic methods for the design of woodwind instruments.* PhD thesis, McGill University, Montreal, Canada. (Cited on pages 25 and 78.)

[Lehmann and Johansson, 2010] Lehmann, E. A. and Johansson, A. M. (2010). Diffuse reverberation model for efficient image-source simulation of room impulse responses. *IEEE Transactions on Audio, Speech, and Language Processing*, 18(6):1429–1439, ISSN: `1558-7916`. doi:10.1109/TASL.2009.2035038. (Cited on page 30.)

[LeVeque, 2007] LeVeque, R. J. (2007). *Finite difference methods for ordinary and partial differential equations: steady-state and time-dependent problems.* Society for Industrial and Applied Mathematics. (Cited on page 70.)

[Levine, 1983] Levine, H. (1983). On the radiation impedance of a rectangular piston. *Journal of Sound and Vibration*, 89(4):447–55. doi:10.1016/0022-460X(83)90346-2. (Cited on page 29.)

[Levine and Schwinger, 1948] Levine, H. and Schwinger, J. (1948). On the radiation of sound from an unflanged circular pipe. *Physical Review*, 73(4):24. doi:10.1103/PhysRev.73.383. (Cited on page 29.)

[Lighthill, 1952] Lighthill, M. J. (1952). On sound generated aerodynamically I. General theory. *Proceedings of the Royal Society of London. Series A. Mathematical and Physical Sciences*, 211(1107):564–587, ISSN: `0080-4630`. doi:10.1098/rspa.1952.0060. (Cited on pages 22, 23, 38 and 40.)

[Lighthill, 1954] Lighthill, M. J. (1954). On sound generated aerodynamically II. Turbulence as a source of sound. *Proceedings of the Royal Society of London. Series A. Mathematical and Physical Sciences*, 222(1148):1–32, ISSN: `0080-4630, 2053-9169`. doi:10.1098/rspa.1954.0049. (Cited on pages 23, 38 and 40.)

[Linton and Martin, 2005] Linton, C. M. and Martin, P. A. (2005). Multiple scattering by random configurations of circular cylinders: Second-order corrections for the effective wavenumber. *The Journal of the Acoustical Society of America*, 117(6):3413–3423, ISSN: `0001-4966`. doi:10.1121/1.1904270. (Cited on pages 30, 113 and 121.)

[Mahu et al., 1993] Mahu, W. E. A., Peters, M. C. A. M., Verge, M.-P., Wijnands, A. P. J., Fabre, B., and Hirschberg, A. (1993). Attack transient of a flue organ pipe. In Nieuwstadt, F. T. M. and Dijksman, J. F., editors, *Topics in Applied Mechanics: Integration of Theory and Applications in Applied Mechanics*, pages 163–171. Springer Netherlands, Dordrecht, Nederlands, ISBN: `978-94-011-2090-6`. (url). (Cited on page 36.)

[Marot and Marot, 1727] Marot, J. and Marot, D. (1727). *Architecture française*. N/A. (url). (Cited on pages 6 and 175.)

[Mattingly and Criminale, 1971] Mattingly, G. E. and Criminale, W. O. (1971). Disturbance characteristics in a plane jet. *The physics of fluids*, 14(11):2258–64. doi:10.1063/1.1693326. (Cited on pages 24 and 222.)

[Mechel, 1986] Mechel, F. P. (1986). The acoustic sealing of holes and slits in walls. *Journal of Sound and Vibration*, 111(2):297–335. doi:10.1016/S0022-460X(86)80163-8. (Cited on page 116.)

[Meek, 2012] Meek, C. (2012). *Computational impedance generation and bore optimisation for Matlab*. MSc. dissertation, University of Edinburgh, Edinburgh, United Kingdom. (Cited on page 25.)

[Mellow, 2006] Mellow, T. (2006). On the sound field of a resilient disk in an infinite baffle. *Journal of the Acoustical Society of America*, 120(1):90–101. doi:10.1121/1.2206513. (Cited on pages 30 and 113.)

[Mellow and Kärkkäinen, 2011] Mellow, T. and Kärkkäinen, L. (2011). On the sound fields of infinitely long strips. *The Journal of the Acoustical Society of America*, 130(1):153–167, ISSN: `0001-4966`. doi:10.1121/1.3596474. (Cited on pages xii, 115, 117, 120, 126, 127, 128, 129, 130, 139, 146, 154, 187 and 188.)

[Miklós and Angster, 2000] Miklós, A. and Angster, J. (2000). Properties of the sound of flue organ pipes. *Acta Acustica united with Acustica*, 86(4):611–622, ISSN: `1436-7047`. (Cited on pages 22 and 168.)

[Milne-Thomson, 1962] Milne-Thomson, L. M. (1962). *Theoretical hydrodynamics*. MacMillan & Co Ltd, London, UK, fourth edition. (Cited on page 155.)

[Nagy et al., 2022] Nagy, P. T., Rucz, P., and Szabó, A. (2022). Examination of jet growth and jet-drive in the recorder by means of linearized numerical and lumped models. *Journal of Sound and Vibration*, 527:1–21, ISSN: `0022460X`. doi:10.1016/j.jsv.2022.116857. (Cited on pages 70 and 77.)

[Ngu, 1995] Ngu, J. T. A. (1995). *The effects of turbulence on organ sound quality and its minimisation in blowing systems*. PhD thesis, University of Huddersfield, Huddersfield, United Kingdom. (Cited on page 19.)

[Nolle and Finch, 1992] Nolle, A. W. and Finch, T. L. (1992). Starting transients of flue organ pipes in relation to pressure rise time. *The Journal of the Acoustical Society of America*, 91(4):2190–2202, ISSN: `0001-4966`. doi:10.1121/1.403653. (Cited on pages 19, 36, 52, 54 and 70.)

[Norris and Conoir, 2011] Norris, A. N. and Conoir, J.-M. (2011). Multiple scattering by cylinders immersed in fluid: High order approximations for the effective wavenumbers. *The Journal of the Acoustical Society of America*, 129(1):104–113, ISSN: `0001-4966`. doi:10.1121/1.3504711. (Cited on pages 113 and 121.)

[Ochmann, 2004] Ochmann, M. (2004). The complex equivalent source method for sound propagation over an impedance plane. *The Journal of the Acoustical Society of America*, 116(6):3304–3311, ISSN: `0001-4966`. doi:10.1121/1.1819504. (Cited on page 155.)

[Ochmann and Piscoya, 2021] Ochmann, M. and Piscoya, R. (2021). *Theory and Application of Acoustic Sources Using Complex Analysis: Complex Acoustic Sources, Green's Functions and Half-Space Problems, Acoustic Radiation and Scattering Using Equivalent Source and Boundary Element Methods*. Springer Singapore, Singapore, ISBN: `978-981-336-039-6 978-981-336-040-2`. doi:10.1007/978-981-33-6040-2. (Cited on page 155.)

[Odya et al., 2017] Odya, P., Kotus, J., Szczodrak, M., and Kostek, B. (2017). Sound Intensity Distribution Around Organ Pipe. *Archives of Acoustics*, 42(1):13–22, ISSN: `2300-262X`. doi:10.1515/aoa-2017-0002. (Cited on page 30.)

[Park and Eom, 1997] Park, H. H. and Eom, H. J. (1997). Acoustic scattering from a rectangular aperture in a thick hard screen. *The Journal of the Acoustical Society of America*, 101(1):595–598, ISSN: `0001-4966`. doi:10.1121/1.417971. (Cited on pages 113 and 116.)

[Pavic and Du, 2016] Pavic, G. and Du, L. (2016). Modelling of multi-connected acoustical spaces by the surface impedance approach. In *INTER-NOISE*, volume 253, pages 4278–4287, Hamburg, Germany. Institute of Noise Control Engineering. (Cited on page 155.)

[Perraut, 2007] Perraut, A. (2007). *Recherches sur le monde universitaire parisien au XIVe siècle: l'architecture des collèges*. PhD thesis, Université Paris 4, Paris, France. (Cited on page 3.)

[Pierce et al., 2002] Pierce, A. D., Cleveland, R. O., and Zampolli, M. (2002). Radiation impedance matrices for rectangular interfaces within rigid baffles: Calculation methodology and applications. *The Journal of the Acoustical Society of America*, 111(2):672–684, ISSN: `0001-4966`. doi:10.1121/1.1430684. (Cited on pages 30 and 116.)

[Pitsch et al., 2010] Pitsch, S., Holmberg, S., and Angster, J. (2010). Ventilation system design for a church pipe organ using numerical simulation and on-site measurement. *Building and Environment*, 45(12):2629–2643. doi:10.1016/j.buildenv.2010.05.022. (Cited on pages 19 and 36.)

[Polack et al., 1992] Polack, J.-D., Meynial, X., Dodd, G., and Marshall, A. H. (1992). The midas system for all scale room acoustics measurements. In *Proc. Audio Engineering Society International Conference*. (Cited on page 176.)

[Postma et al., 2015] Postma, B., Tallon, A., and Katz, B. (2015). Calibrated auralization simulation of the abbey of Saint-Germain-des-Prés for historical study. *Proceedings of the Institute of Acoustics*, 37:9. (Cited on page 175.)

[Powell, 1961] Powell, A. (1961). On the edgetone. *The Journal of the Acoustical Society of America*, 33(4):395–409. doi:10.1121/1.1908677. (Cited on pages 22 and 38.)

[Powell, 1964] Powell, A. (1964). Theory of vortex sound. *The Journal of the Acoustical Society of America*, 36(1). (Cited on page 23.)

[Pàmies et al., 2011] Pàmies, T., Romeu, J., Genescà, M., and Balastegui, A. (2011). Sound radiation from an aperture in a rectangular enclosure under low modal conditions. *The Journal of the Acoustical Society of America*, 130(1):239–248, ISSN: `0001-4966`. doi:10.1121/1.3596465. (Cited on pages 113, 116, 121 and 250.)

[Rayleigh, 1894] Rayleigh, J. W. S. (1894). *The theory of sound*. Dover, New York, USA, second edition. (Cited on pages 22 and 23.)

[Rioux, 2000] Rioux, V. (2000). Methods for an objective and subjective description of starting transients of some flue organ pipes - integrating the view of an organ builder. *Acta Acustica united with Acustica*, 86(4):634–641. (Cited on pages 25, 36 and 39.)

[Rioux, 2001] Rioux, V. (2001). *Sound Quality of Flue Organ Pipes*. PhD thesis, Chalmers University of Technology, Göteborg, Sweden. (Cited on page 25.)

[Rochas, 1997] Rochas, P. (1997). *Le petit dictionnaire de l'orgue illustré*. Harmonia Mundi, Arles, France, ISBN: `0794881401222`. (Cited on pages 54 and 112.)

[Rohfritsch et al., 2019] Rohfritsch, A., Conoir, J.-M., Marchiano, R., and Valier-Brasier, T. (2019). Numerical simulation of two-dimensional multiple scattering of sound by a large number of circular cylinders. *The Journal of the Acoustical Society of America*, 145(6):3320–3329, ISSN: `0001-4966`. doi:10.1121/1.5110310. (Cited on page 121.)

[Rossi, 1988] Rossi, M. (1988). *Acoustics and electroacoustics*. Artech House, Norwood, USA, ISBN: `0-89006-255-2`. (Cited on pages 94, 97, 124, 126 and 250.)

[Ruiz, 1970] Ruiz, P. M. (1970). *A technique for simulating the vibration of strings with a digital computer*. PhD thesis, University of Illinois, Urbana-Champaign, USA. (Cited on page 24.)

[Sauter and Soroka, 1970] Sauter, A. and Soroka, W. W. (1970). Sound transmission through rectangular slots of finite depth between reverberant rooms. *Journal of the Acoustical Society of America*, 47(1A):5–11. doi:10.1121/1.1911442. (Cited on pages 30 and 116.)

[Savioja and Svensson, 2015] Savioja, L. and Svensson, U. P. (2015). Overview of geometrical room acoustic modeling techniques. *The Journal of the Acoustical Society of America*, 138(2):708–730, ISSN: `0001-4966`. doi:10.1121/1.4926438. (Cited on page 30.)

[Schroeder, 1996] Schroeder, M. R. (1996). The Schroeder frequency revisited. *Journal of the Acoustical Society of America*, 99(5):3240–41. doi:10.1121/1.414868. (Cited on page 138.)

[Sgard et al., 2007] Sgard, F., Nelisse, H., and Atalla, N. (2007). On the modeling of the diffuse field sound transmission loss of finite thickness apertures. *Journal of the Acoustical Society of America*, 122(1):302–313. doi:10.1121/1.2735109. (Cited on pages 30, 116, 117, 128 and 146.)

[Shampine, 2008] Shampine, L. F. (2008). Dissipative approximations to neutral DDEs. *Applied Mathematics and Computation*, 203(2):641–648. (Cited on page 80.)

[Sheaffer et al., 2014] Sheaffer, J., van Walstijn, M., and Fazenda, B. (2014). Physical and numerical constraints in source modeling for finite difference simulation of room acoustics. *Journal of the Acoustical Society of America*, 135(1):251–61. doi:10.1121/1.4836355. (Cited on page 151.)

[Smith, 2007] Smith, J. O. (2007). *Introduction to digital filters with audio applications*. W3K Publishing, ISBN: `978-0-9745607-1-7`. (Cited on page 77.)

[Sreekumar et al., 2022] Sreekumar, A., Triantafyllou, S. P., and Chevillote, F. (2022). Virtual elements for sound propagation in complex poroelastic media. *Computational Mechanics*, 69:347–82. doi:10.1007/s00466-021-02078-2. (Cited on page 31.)

[Stegen, 1967] Stegen, G. R. (1967). *On the structure of an edgetone flow field*. PhD thesis, Stanford, San Francisco, CA, USA. (Cited on pages 41 and 74.)

[Strikwerda, 2004] Strikwerda, J. C. (2004). *Finite difference schemes and partial differential equations*. Society for Industrial and Applied Mathematics. (Cited on page 70.)

[Svensson and Calamia, 2006] Svensson, U. P. and Calamia, P. T. (2006). Edge-diffraction impulse responses near specular-zone and shadow-zone boundaries. *Acta Acustica united with Acustica*, 92(4):501–12. (Cited on page 31.)

[Svensson et al., 1999] Svensson, U. P., Fred, R. I., and Vanderkooy, J. (1999). An analytic secondary source model of edge diffraction impulse responses. *Journal of the Acoustical Society of America*, 106(5):2331–44. doi:10.1121/1.428071. (Cited on page 31.)

[Ségoufin, 2000] Ségoufin, C. (2000). *Production du son par interaction écoulement/résonateur acoustique*. PhD thesis, Université Paris VI, Paris, France. (Cited on pages 24, 28, 41 and 72.)

[Ségoufin et al., 2000] Ségoufin, C., Fabre, B., Verge, M.-P., Hirschberg, A., and Wijnands, A. P. J. (2000). Experimental study of the influence of the mouth geometry on sound production in arecorder-like instrument: Windway length and chamfers. *Acta Acustica united with Acustica*, 86(4):649–661. (Cited on pages 25, 38, 39, 41 and 222.)

[Taflove et al., 2005] Taflove, A., Hagness, S. C., and Piket-May, M. (2005). *Computational electrodynamics: the finite-difference time-domain method*. Artech House, artech house antennas and propagation library edition. (Cited on pages 151 and 155.)

[Tateishi et al., 2019] Tateishi, S., Iwagami, S., Tsutsumi, G., Kobayashi, T., Takami, T., and Takahashi, K. (2019). Role of the foot chamber in the sounding mechanism of a flue organ pipe. *Acoustical Science and Technology*, 40(1):29–39, ISSN: `1346-3969, 1347-5177`. doi:10.1250/ast.40.29. (Cited on pages 19 and 70.)

[Taylor, 2016] Taylor, A. J. (2016). Effects of centrifugal blowers and reservoir resonance on organ pipe flutter. In *EuroRegio*, pages 1–8, Porto, Portugal. European Acoustics Association. (Cited on page 19.)

[Taylor, 2018] Taylor, A. J. (2018). *The effects of centrifugal blowers, control valves, attenuating devices and reservoir resonance on organ pipe flutter.* PhD thesis, University of Salford, Salford, United Kingdom. (Cited on page 19.)

[Terrien, 2014] Terrien, S. (2014). *Instruments de la famille des flûtes - analyse des transitions entre régimes.* PhD thesis, Aix-Marseille Université, Marseille, France. (Cited on pages 25, 27, 28, 69, 77, 172 and 221.)

[Terrien et al., 2012] Terrien, S., Auvray, R., Fabre, B., Lagrée, P.-Y., and Vergez, C. (2012). Numerical resolution of a physical model of flute-like instruments: comparison between different approaches. In *Acoustics 2012*, pages 1–8, Nantes, France. (url). (Cited on pages 69 and 70.)

[Terrien et al., 2015] Terrien, S., Blandin, R., Vergez, C., and Fabre, B. (2015). Regime Change Thresholds in Recorder-Like Instruments: Influence of the Mouth Pressure Dynamics. *Acta Acustica united with Acustica*, 101(2):300–316, ISSN: `16101928`. doi:10.3813/AAA.918828. (Cited on page 73.)

[Thistlewaite and Webber, 1998] Thistlewaite, N. and Webber, G., editors (1998). *Cambridge companion to the organ.* Cambridge University Press, Cambridge, UK, ISBN: `0-521-57309-2`. (Cited on page 112.)

[Tritton, 2007] Tritton, D. J. (2007). *Physical fluid dynamics.* Springer Science and Bsuiness Media. Oxford University Press, Oxford, UK, second edition, ISBN: `978-0- 19-854493-7`. (Cited on page 21.)

[Trompette et al., 2009] Trompette, N., Barby, J.-L., Sgard, F., and Nelisse, H. (2009). Sound transmission loss of rectangular and slit-shaped apertures: experimental results and correlation with a modal model. *Journal of the Acoustical Society of America*, 125(1):31–41. doi:10.1121/1.3003084. (Cited on pages 30 and 117.)

[Valimaki and Haghparast, 2007] Valimaki, V. and Haghparast, A. (2007). Fractional Delay Filter Design Based on Truncated Lagrange Interpolation. *IEEE Signal Processing Letters*, 14(11):816–819, ISSN: `1070-9908`. doi:10.1109/LSP.2007.898856. (Cited on page 82.)

[Valimaki et al., 1996] Valimaki, V., Hänninen, R., and Karjalainen, M. (1996). An improved-digital-waveguide-model-of-flute-implementation Implementation issues. In *Proceedings of the International Computer Music Conference*, pages 1–4. (Cited on page 69.)

[Valimaki et al., 1992] Valimaki, V., Karjalainen, M., Janosy, Z., and Laine, U. (1992). A real-time DSP implementation of a flute model. In *Proc. IEEE International Conference*, volume 2, pages 249–252, San Francisco, CA, USA. IEEE, ISBN: `978-0-7803-0532-8`. doi:10.1109/ICASSP.1992.226073. (Cited on page 69.)

[Valimaki and Laakso, 2000] Valimaki, V. and Laakso, T. (2000). Principles of fractional delay filters. In *2000 IEEE International Conference on Acoustics, Speech, and Signal Processing. Proceedings (Cat. No.00CH37100)*, volume 6, pages 3870–3873, Istanbul, Turkey. IEEE, ISBN: `978-0-7803-6293-2`. doi:10.1109/ICASSP.2000.860248. (Cited on page 82.)

[Van Valkenburg, 1974] Van Valkenburg, M. E. (1974). *Network analysis*. Prentice Hall. Inc.Engle. (Cited on page 76.)

[Verge, 1994] Verge, M.-P. (1994). Jet oscillations and jet drive in recorder-like instruments. *Acta Acustica*, 2(5):403–419. (Cited on pages 22, 23 and 222.)

[Verge, 1995] Verge, M.-P. (1995). *Aeroacoustics of confined jets : with applications to the physical modeling of recorder-like instruments*. PhD thesis, Eindhoven University of Technology, Eindhoven, Netherlands. Publisher: Technische Universiteit Eindhoven. (Cited on pages 24, 26 and 155.)

[Verge et al., 1994a] Verge, M.-P., Fabre, B., Caussé, R., Hirschberg, A., and Van Steenbergen, A. (1994a). Oscillation du jet dans les instruments à embouchure de flûte recherche d'un modèle analytique. *Le Journal de physique IV*, 4(C5):661–664, ISSN: `1155-4339`. doi:10.1051/jp4:19945143. (Cited on pages 24, 28 and 72.)

[Verge et al., 1997a] Verge, M.-P., Fabre, B., Hirschberg, A., and Wijnands, A. P. J. (1997a). Sound production in recorderlike instruments. I. Dimensionless amplitude of the internal acoustic field. *The Journal of the Acoustical Society of America*, 101(5):2914–2924, ISSN: `0001-4966`. doi:10.1121/1.418521. (Cited on pages 19, 38 and 54.)

[Verge et al., 1994b] Verge, M. P., Fabre, B., Mahu, W. E. A., Hirschberg, A., van Hassel, R. R., Wijnands, A. P. J., de Vries, J. J., and Hogendoorn, C. J. (1994b). Jet formation and jet velocity fluctuations in a flue organ pipe. *The Journal of the Acoustical Society of America*, 95(2):1119–1132, ISSN: `0001-4966`. doi:10.1121/1.408460. (Cited on pages 19, 27, 36, 38, 39, 42 and 222.)

[Verge and Hirschberg, 1995] Verge, M.-P. and Hirschberg, A. (1995). Turbulence noise in flue instruments. In *International Symposium of Musical Acoustics*, pages 93–99, Dourdan, France. (url). (Cited on pages 27 and 38.)

[Verge et al., 1997b] Verge, M.-P., Hirschberg, A., and Caussé, R. (1997b). Sound production in recorderlike instruments. II. A simulation model. *The Journal of the Acoustical Society of America*, 101(5):2925–2939, ISSN: `0001-4966`. doi:10.1121/1.419481. (Cited on pages 22, 38, 69 and 74.)

[Villegas Curulla et al., 2022a] Villegas Curulla, G., Canfield-Dafilou, E. K., Domenighini, P., d'Alessandro, C., and Fabre, B. (2022a). Pipe organ buffet radiation patterns under realistic excitation conditions. (Cited on page 157.)

[Villegas Curulla et al., 2022b] Villegas Curulla, G., Domenighini, P., Canfield-Dafilou, E. K., Fabre, B., d'Alessandro, C., and Katz, B. F. G. (2022b). Pipe organ buffet radiation patterns under different excitation strategies. In *Proc. 24th International Congress on Acoustics*, pages 1–8, Gyengju, Korea. (Cited on page 157.)

[Villegas Curulla et al., 2023] Villegas Curulla, G., Domenighini, P., and Fabre, B. (2023). Flue organ pipe modeling extensions: initialization and transient as a function of the pipe and supply system geometries. (Cited on pages 70 and 71.)

[Villegas Curulla et al., 2022c] Villegas Curulla, G., Domenighini, P., Katz, B. F. G., and Canfield-Dafilou, E. K. (2022c). Directivity of a small pipe organ buffet. In *Symposium of Ancient Theatres*, pages 1–4. (Cited on page 157.)

[Villegas Curulla and Fabre, 2022] Villegas Curulla, G. and Fabre, B. (2022). Incorporating the windchest reservoir and a foot model to the organ pipe time domain simulation. In *Congrès Français d'Acoustique*, pages 1–7, Marseille, France. (url). (Cited on page 44.)

[Välimäki et al., 1993] Välimäki, V., Karjalainen, M., and Laakso, T. I. (1993). Fractional Delay Digital Filters. In *Proc. IEEE International Conference*, pages 355–359. IEEE. doi:10.1109/ISCAS.1993.393731. (Cited on page 82.)

[Wang et al., 2021] Wang, S., Maestre, E., and Scavone, G. P. (2021). Acoustical modeling of the saxophone mouthpiece as a transfer matrix. *Journal of the Acoustical Society of America*, 149(3):1901–12. doi:10.1121/10.0003814. (Cited on page 25.)

[Weber, 2022] Weber, A. (2022). *Acoustics of Historic Buildings: Intercomparison of Numerical Methods for Coupled Spaces & Sound Scattering by Piers and Columns in Gothic and Classical Architecture*. PhD thesis, Sorbonne Université, Paris, France. (Cited on page 151.)

[Weber and Katz, 2022] Weber, A. and Katz, B. F. G. (2022). Sound scattering by gothic piers and columns of the cathedral Notre-Dame de Paris. *Acoustics (MDPI)*, 4:679–703. doi:10.3390/acoustics4030041. (Cited on pages 30 and 151.)

[Whitham, 2011] Whitham, G. B. (2011). *Linear and nonlinear waves.* John Wiley & Sons, New York, USA, second edition, ISBN: `0-471-35942-4`. (Cited on page 137.)

[Wilson and Soroka, 1965] Wilson, G. P. and Soroka, W. W. (1965). Approximation to the diffraction of sound by a circular aperture in a rigid wall of finite thickness. *Journal of the Acoustical Society of America*, 37(2):286–97. doi:10.1121/1.1909325. (Cited on page 116.)

[Woolley and Campbell, 2017] Woolley, A. and Campbell, M. (2017). A musical and mechanical study of tracker actions. *International Society of Organbuilders*, 56:7–40, ISSN: `1017-7515`. (Cited on pages 39, 51 and 63.)

[Woolley, 2006] Woolley, A. G. (2006). *The Physical Characteristics of Mechanical Pipe Organ Actions and how they Affect Musical Performance.* PhD thesis, University of Edinburgh, Edinburgh, United Kingdom. (Cited on page 18.)

[Zhang et al., 2022] Zhang, J., Luo, J., and Zhang, X. (2022). A trend extraction method based on logistic functions and envelopes. *Scientific Reports*, 12(1):1–9. doi:10.1038/s41598-021-04596-8. (Cited on page 44.)

Glossary

List of Abbreviations and Acronyms

BVP	boundary-value problem
CFL	Courant-Friedrichs-Levy number
DRT	dimensionless rise-time
$FDTD$	finite-difference time-domain
$FVTD$	finite-volume time-domain
$FVFDTD$	finite-volume finite-difference time-domain
GA	geometrical acoustics
GO	Great Organ
JSA	jet spatial amplification
LHS	left-hand side
LTI	linear time-invariant
NDP	Notre-Dame de Paris cathedral
ODE	ordinary differential equation
PRT	pressure rise-time
RJV	reduced jet velocity (jet inverse Strouhal number)
SS	steady-state
TMM	transmission matrix method

List of Symbols for Chapter 2

a_o, b_o, c_o	zero frequency mode coefficients (resonator)
c	speed of sound propagation in air
δ_{ij}	Kronecker delta
Δp_{jx}	jet-drive pressure source term
Δp_{loss}	pressure losses term at the labium
$\Delta p_{tot} = \Delta p_{jx} + \Delta p_{loss}$	total pressure sources
$\varepsilon_r = 1/Q_r$	damping factor of the mode r
$f(\mathbf{r}, t)$	forcing term in a velocity potential field
λ	dynamic viscosity
μ	shear modulus
∇	nabla operator
$\nabla\cdot$	divergence operator
ω	pulsation
ω_r	r^{th} modal pulsation
p	pressure
$p' = p - \langle p \rangle$	perturbational component of pressure
$\frac{\partial}{\partial x_i}$	partial derivative w.r.t. first spatial dimension
$\frac{\partial}{\partial x_j}$	partial derivative w.r.t. second spatial dimension
$\frac{\partial}{\partial t}$	partial derivative w.r.t. time
$\psi(\mathbf{r}, t)$	velocity potential field
q	mass source
Q_{in}	portion of jet flow entering the pipe at the mouth area
Q_{out}	portion of the flow going out at the mouth area
$\mathbf{r} = (x_i, x_j)$	spatial position vector
ρ	fluid (air) density
s	complex frequency in Laplace domain
σ_{ij}	velocity field stress tensor
T_{ij}	Lighthill stress tensor
$\mathbf{v} = (v_i, v_j)$	velocity field
v_o	acoustic velocity in the zero frequency mode
v_r	acoustic velocity of mode r
$Y_p(\omega)$	pipe input admittance

List of Symbols for Chapter 3

β	pressure rise growth rate parameter
c	sound propagation speed in air
D_p	pipe diameter (resonator)
η	jet displacement w.r.t. normal line at the flue exit
$f_1 = 1/T_1$	fundamental oscillating frequency (resonator)
h	flue height (thickness)
$H(t)$	Heaviside function
H_m	mouth width
l_{eff}	effective length (flue)
L_f	foot length
l_{in}	effective length of foot toe inlet
L_p	length of the pipe (resonator)
l_{pal}	effective length of channel slot (pallet-box to groove)
ν	pressure rise non-linear onset parameter
$\Delta p = \Delta p_{tot}$	total pressure sources in the jet-drive model
p_{ac}	acoustic pressure (pipe)
p_{grv}	groove (channel) pressure
$p_f = p_{foot}$	foot pressure
p_m	mouth pressure
p_p	pressure at the pipe
p_{pal}	pallet-box pressure
P_{wind}	constant approximation of steady pressure in the pallet-box
$Q_1 = \langle Q_1 \rangle + Q_1'$	pipe inwards source-generated flow
$Q_2 = \langle Q_2 \rangle + Q_2'$	pipe outwards source-generated flow
q_{groove}	flow starting at the groove towards the tone channel and foot
$\langle q_{in} \rangle$	flow rate entering the pipe foot
Q_n	quality-factor of the resonator's n mode admittance
$\langle q_{out} \rangle$	flow rate leaving the foot through the flue exit
$q_{pallet-box}$	flow rate from the pallet-box towards the pallet-valve slot
$\langle q_{res} \rangle$	generic flow rate from the reservoir
$R_{f,in}$	foot toe inlet radius
ρ	fluid (air) density
R_p	resonator radius
$S_j = hH_m$	cross-section of the flue exit
S_{in}	cross-section of toe inlet (foot)
S_{pal}	cross-section of pallet slot (smaller than pallet valve)
$\hat{\tau} = \tau_{10-90} f_1$	non-dimensional pressure rise-time (10%-90% of SS pressure)
$\hat{t} = t f_1$	non-dimensional time by the fundamental oscillating frequency
$u_{in} = \langle u_{in} \rangle + u_{in}'$	flow velocity going into the foot through the toe
u_j	jet center-line velocity
u_{pal}	flow velocity through the pallet valve slot
$V_f = V_{foot}$	volume of the foot
V_{grv}	groove (channel) volume
$v_{k,ac}$	acoustic pressure (pipe) of the k mode
V_{pal}	volume of the pallet-box
W_m	mouth cut-up (distance from the flue to the labium)
x	spatial position along the length of the resonator
$\theta = \frac{u_j}{W_m f_1}$	reduced jet velocity (inverse Strouhal)

List of additional Symbols specific to Chapter 4

α	wave number solving Rayleigh equation
$\alpha_i \sim \beta/h$	wave number imaginary part of instability's solution (Rayleigh)
α_{vc}	vena-contracta parameter
$b = 2h/5$	jet half-width (Bickley profile)
β	jet spatial amplification
$c_p = \gamma u_j$	
δ_d	conformal mapping distance between sources Q_1 and Q_2
$\delta_{t+}, \delta_{t-}, \delta_{t\cdot}, \delta_{tt}$	time difference operator (forwd, backward, centered, 2^{nd} order)
η_b	jet displacement normalized by the jet half-width b
e_{t+}, e_{t-}	time shift operator (forward and backward)
f_s	sampling frequency
γ	relative convection velocity
$k = 1/f_s$	time-step
κ	pressure growth rate parameter
λ_r	eigenvalue of the acoustic velocity of mode r
$l_j = l_{eff}$	effective length of the flue exit (jet)
$\mu_{t+}, \mu_{t-}, \mu_{t\cdot}, \mu_{tt}$	identity operator (forward, backward, centered, 2^{nd} order)
n	discrete time index
ΔP	total sources pressure in frequency domain
P_{ac}	acoustic pressure in frequency domain
ψ	stream function (solving Rayleigh equation)
p_o	pole of the resonator filter
R_m	equivalent mouth *wetted* radius
$\tau = W_m/c_p$	mouth convection delay
$U(y)$	jet velocity profile (solving Rayleigh equation)
$\mathbf{v} = (v_1, ..., v_N)$	vector of acoustic velocities
$\mathbf{v}^n$	vector of the modal acoutic velocities at time step n
V_{ac}	acoustic velocity in frequency domain (pipe)
$v_{ac,m}$	acoustic velocity at the mouth
$v_{ac,p}$	acoutic velocity in the pipe
$\mathbf{x}(t)$	vector of states
y_{off}	labium offset w.r.t. flue exit normal
$Y_{p,in}(\omega)$	pipe input admittance
Y_r	pipe input admittance for mode r
Z_m	mouth window impedance
Z_{rad}	radiation impedance

List of Symbols for Chapter 5

$a = R_{cyl}$	cylinder radius
$Bl = B \cdot l = B_l$	product of magnetic field in the speaker gap times coil length
c	speed of sound propagation in air
C_{ab}	speaker cabinet equivalent compliance as per air volume contained
C_{as}	speaker suspension compliance
C_{ms}	compliance of the speaker's suspension
$\vec{e} = (\vec{e}_r, \vec{e}_\varphi, \vec{e}_z)$	cylindrical coordinate basis
f_c	pass-band cutoff frequency
f_n	resulting forces exerted on the n^{th} speaker of the array
f_s	speaker's frequency of resonance
γ	gas heat capacity ratio
$H_m^{\pm}$	convergent/divergent Hankel function of order m
$i = i(t)$	electric current (time domain)
$I(\omega)$	electric current (frequency domain)
J_m	first kind Bessel function of order m
k	wave number
$k_w^2 = k^2 - k_z^2$	
k_z	wave number along the z axis
$K = 1/C_{ms}$	speaker's suspension stiffness
L_e	speaker's voice coil inductanve
M_{ms}	total mass of speaker's moving elements
N_m	second kind Bessel function of order m
ω	temporal pulsation
$p = p(r,t)$	pressure
$\mathcal{P}_{nom}$	speaker nominal power
$P(r,\theta)$	pressure at distance r and angle θ
$\Phi = \Phi(\varphi)$	spatial solution in the φ cylindrical coordinate (rotational)
Ψ	potential field
P_o	cabinet enclosed pressure at rest
Q_o	linear acoustic flux per unit length
$R = R(r)$	spatial solution in the r cylindrical coordinate (radial)
R_e	speaker's voice coil DC resistance
R_{ms}	speaker's suspension mechanical resistance
ρ_o	fluid (air) density at rest
S_d	speaker's membrane effective surface
$T(t)$	temporal solution in time t
U_{rms}	root mean square voltage
v	cylinder surface vibration velocity
V_d	speaker peak volume displacement (linear regime)
V_o	cabinet enclosed volume at rest
$\dot{x}$	speaker's membrane velocity
X_{max}	speaker's max cone excursion in linear regime
$X(\omega)$	speaker's cone excurion (frequency domain)
$Z(z)$	spatial solution along the cylindrical z axis(height)

List of Symbols for Chapter 6

$*$	convolution product
$A_{m,n}$	modal shapes' amplitude
β	admittance as per [Pàmies et al., 2011]
β_{jk}	indicator function (adjacency between cells)
c_o	sound propagation speed in air
$\delta(x)$	Dirac delta in time or space
$\delta_{t\circ}$	discrete time difference operator (centered)
$d = 2e$	cylinder-to-cylinder distance [Rossi, 1988]
$D(\theta)$	directivity factor
$2e$	cylinder-to-cyliner distance [Junger and Feit, 1993]
$f(t)$	Green's function forcing term
$f(\mathbf{r}, t)$	forcing function to the Helmhotz non-homogeneous problem
F_o	forcing function amplitude
f_s	sampling frequency
$f(\theta)$	shape function
γ_{jl}	indicator function (adjacency between cell and bounds)
$G(\mathbf{r}\|\mathbf{r}_o)$	Green's function at observation point $\mathbf{r}$ and excitation $\mathbf{r}_o$
$\Gamma(x)$	gamma function
$H_n^{(1)} = H_n^-$	n-order Hankel function of first kind
h_{jk}	center-to-center distance between cells j and k
J_n	first kind Bessel function of order n
k_o	wave number in free propagation
k_{eff}	effective wave number
k_{ISA}	wave number under independent scattering approximation
$k_{m,n}$	wave number of the m-n mode
λ	wave length
(L_x, L_y, L_z)	width, depth, and height of the enclosing cavity
$\mu_{t\circ}$	discrete time average operator (centered)
$\mathbf{n}$	normal unit vector
∇	nabla operator
n_o	scatterers density per unit area
N_{sl}	number of slits present in the façade
ϕ_{an}	analytic signal
ϕ_l	phase shift of the secondary source l
$\psi_{m,n}$	modal shape corresponding to m, n indices (2D)
$\psi_j^{\pm}$	half-step forward/backward shifted potential of cell j
Ψ_{tot}	total field
$\Psi_{inc}, \Psi_{wall}, \Psi_{ap}$	incident, wall, and aperture contributions to the field
$pv(x)$	principal value
$\mathbf{r}_o$	excitation location coordinate vector
$\mathbf{r}$	observation location coordinate vector
r	observation distance
ρ	fluid (air) density
∂_t	partial time derivative
Q_{vol}	volume acceleration
$q(\mathbf{r}_o, t)$	acoustic flux at input location and time t
q_r	acoustic flux of the secondary source r

List of Symbols for Chapter 6 (continuation)

$R_{cyl} = a$	scatterer radius (half-with of aperture)
r_l	distance to origin of the secodary source l
S_{jk}	cell face adjoining cells j and k
$\sigma_{jl,FV}$	loss term for the bound l sharing a face with cell j
T_n	diffusion coefficients (eigs of translation operator $\mathcal{T}$)
$T_s = 1/f_s$	sampling interval (time step)
$U(\omega)$	Heaviside function (frequency domain)
$v_{\perp,l}^{(m),n}$	normal velocity at bounding face l and time step n and mode m
V_j	volume of cell j
$X(x), Y(y), Z(z)$	solution functions along the Cartesian coordinates x,y, and z
ξ_{wall}	specific admittance of the cavity walls
ξ_{sl}	specific admittance of the slit aperture
Y_n	second kind Bessel function of order n
$(\zeta_x, \zeta_y, \zeta_z)$	specific acoustic impedances in x, y, and z directions
Z_r	radiation impedance